EONS: A new biogeochemical model of Earth's longterm evolution

by

Julia E. Horne
B.A., Colgate University, 2016

A Dissertation Submitted in Partial Fulfillment of the
Requirements for the Degree of

DOCTOR OF PHILOSOPHY

in the School of Earth and Ocean Sciences

University of Victoria

EONS: A new biogeochemical model of Earth's longterm evolution

by

Julia E. Horne
B.A., Colgate University, 2016

Supervisory Committee

Dr. Colin Goldblatt, Supervisor

(School of Earth and Ocean Sciences)

Dr. Dante Canil, Departmental Member

(School of Earth and Ocean Sciences)

Dr. Roberta Hamme, Departmental Member

(School of Earth and Ocean Sciences)

Dr. Jon Husson, Departmental Member

(School of Earth and Ocean Sciences)

Dr. Jon Willis, Outside Member

(Department of Astronomy and Physics)

Abstract

I present Earth's Oxygenation and Natural Systematics (*EONS*): a new, fully coupled biogeochemical model of the atmosphere, ocean, and their interactions with the geosphere, which can reproduce major features of Earth's evolution following the origin of life to the present day. The model includes an interactive biosphere, cycles of carbon, nitrogen, phosphorus, and oxygen, and climate. A nominal model run initialized in the Eoarchean resolves emergent surface oxygenation, nutrient limitations, and climate feedbacks. The modelled atmosphere oxygenates in stepwise fashion over the course of the Proterozoic; a nearly billion year lag after the evolution of photosynthesis at 3.5 Ga is followed by a great oxidation event (GOE) at 2.4 Ga, which appears to be caused by the gradual buildup of organic matter on the continents imposing nutrient limitation on the biosphere by removing key nutrients from the ocean system. The simple climate system shows significant temperature shifts punctuate the oxygenation process, implying that major biological transitions possibly destabilized Earth's climate. I expand upon this finding by adapting the climate system to include non-linearities such as ice-albedo and supergreenhouse feedbacks in order to investigate potential causes of Paleoproterozoic Snowball Earth events. My preliminary findings suggest that Paleoproterozoic glaciations may have preceded the GOE, and are more likely a result of perturbations to atmospheric CO_2 than from declining CH_4. This work demonstrates that forward modelling the entirety of Earth's history with relatively few imposed boundary forcings is feasible, that the Earth system is not at steady state, and that our understanding of coupled C-N-P-O cycling as it functions today can explain much of the Earth's evolution.

Plain language summary

The Earth is an interconnected system of biological, geological, and atmosphere-ocean chemical systems which respond to and influence one another. I have developed a new model of our planet's chemical evolution, Earth's Oxygenation and Natural Systematics (*EONS*); this first of its kind model encompasses the entire lifetime of Earth's biosphere and major evolutionary developments therein, including the emergence of oxygen producing organisms and the colonization of continental bodies by plants. A basic (nominal) model run, which starts 4 billion years ago and allows biogeochemical systems to dynamically evolve until the modern day, agrees well with geochemical evidence of oxygen's rise in the atmosphere in magnitude and timing. It also successfully reproduces atmosphere-ocean chemistry and geologic systems as they appear in the modern context. The model output implies that the delay in oxygen's rise after the evolution of photosynthesis is caused by gradual burial of organic matter onto continents, depriving biological system of key nutrients in the process. The nominal run also suggests that evolutionary developments in the biosphere significantly disrupted the Earth's climate. I delve into this result further by including additional climate systems that contribute to global glaciation; this allows us to better understand oxygenation's relationship with Paleoproterozoic glaciations. Results from this experiment suggest that climate oscillations can accelerate oxygen's rise by enhancing weathering and nutrient transport during hot interglacials. I also find that a decline in greenhouse forcing by atmospheric CH_4 is a less significant factor in destabilizing the climate than a decline in CO_2. The *EONS* model is a significant step forward in using coupled systematics to describe the Earth's long-term evolution. This work demonstrates that the planet we live on is an immensely intertwined web of chemical relationships in a constant state of change, but one that can be fundamentally disentangled and understood.

Contents

List of Tables

List of Figures

Acknowledgements

I am eternally grateful to:

My supervisor, Colin who helped me develop my research interests and did an excellent job navigating me out of intermittent fogs. Thank you for being confident in me when I was not, and for always having a good sense of humour.

University of Victoria's School of Earth and Ocean sciences and all therein who contribute to fostering a welcoming, personable, and thriving intellectual culture. Thank you all for your support.

My parents, Vicki and Eric who have supported me without reservation for my entire life, encouraged my interest in science and nature, and provided me with opportunities to flourish. Endless, futile arguments with you at the dinner table prepared me well for pursuing a PhD. For better or worse, you are responsible for all of this.

My brothers and sisters-in-law: Nick, Alec, Rachel, and Georgette who are forever my closest friends. I consider myself tremendously lucky, and in no small part because I have you as siblings. I know you always have my back, as I will always have yours.

My partner, Alexander Fyfe who has endured Herculean trials of his patience and compassion and yet emerged in excellent form. Thank you for believing in me, for putting up with my neuroses, and for reminding me to move.

My precious cat, Mojo Jojo who I adopted during a time of minor existential crisis; hitherto one of my best decisions. For the last six years, he has ardently supported my decisions as long as the wet food is served on time.

My friends everywhere who, not to brag, are too numerous to list here. Whether we met in graduate school or in the first grade, our friendship means a great deal to me. Thank you for supporting me, shaping me, and helping me occasionally blow off steam.

Of course it is exhausting, having to reason all the time in a universe that wasn't meant to be reasonable.

Kurt Vonnegut Jr., *Breakfast of Champions*, 1973

I live and work as an uninvited visitor on the unceded traditional territories of the ləkʷəŋən *peoples. I value and respect the* Songhees, Esquimalt *and* W̱SANEC *people who have historical and ongoing relationships with and have been steadfast stewards of this land.*

Chapter 1

Introduction

This dissertation is centred on the development, interpretation, and practical application of a new biogeochemical model of Earth's long-term surface chemical evolution: *EONS* (Earth oxygenation and natural systematics). This work focuses on, in a broad sense, how one can reconcile the Earth operating in its present chemical state with what the geologic record implies about earlier conditions. How exactly did Earth get from point A to point B? What components of the Earth system are required in order to reproduce Earth's evolutionary trajectory? This work aims to address these questions.

This chapter begins with a review of terminology and some background information that informs the modern interpretation of the geologic record (section 1.1). I then provide a succinct overview of Earth's long term surface evolution, focusing on key eons and eras that my model resolves, and which will be the centre of focus for latter chapters (section 1.2). I outline several feedback mechanisms which control the Earth's long-term evolution and are referenced throughout this work (section 1.3). I briefly review several biogeochemical models which have spurred the development of this project (section 1.4). This chapter concludes with my research goals for this project that are addressed within the remaining chapters (section 1.5) and an outline of the thesis (section 1.7).

1.1 Terminological and theoretical context

I give an overview of concepts and geologic theories that will be mentioned throughout this work, including the organization of the geologic time scale (section 1.1.1), long-term geological cycles (section 1.1.2), nutrient cycling (section 1.1.3), the carbon isotope record (section 1.1.4), atmospheric chemistry (section 1.1.6), key events in biological evolution (section 1.1.5), and the general evolution of Earth's climate (1.1.7).

1.1.1 Geochronology

The geologic timescale is broken into a hierarchy of stages demarcated by *chronostratigraphic units* (a body of rock which is taken to represent a specific interval of time), positioned between stratigraphic horizons of uniform formation age and are generally global in extent. Numerical assignments of time defined by these bodies of rock are known as *geochronologic units*. An important but somewhat unobvious distinction here between chronostratigraphic and geochronologic units is that the former is concerned with the material, stratal body of contemporaneously deposited rock (i.e. a tangible remanent from a specific point in time), while the latter is concerned with the age difference between two depositional events, which define boundary ages for the intervening stratal package (i.e. an intangible, inferred parcel of time; Zalasiewicz et al., 2013; Murphy & Salvador, 1999). Functionally, chronostratigraphic units are described as relative layer positions (i.e. Upper Cretaceous) while geochronologic units are described as temporal positions (i.e. Late Cretaceous). The start of the Earth's chronostratigraphic record is the earliest Archean Eon, about 3.8 billion years ago, when the first preserved rock strata were formed (Murphy & Salvador, 1999).

Rank and relative magnitude of geochronologic units are organized according to the duration of time they represent. From longest to shortest:

1. *Eons* span hundreds of millions to billions of years, and are defined by chronostratigraphic assemblages called *eonothems*, consisting of a group of *erathems*. There are 4 eons in Earth's history (Hadean, Archean, Proterozoic, Phanerozoic); the names of the younger two eons reference the biosphere (hence the use of "-zoic", which translates to "life"). Names for the two oldest eons reference mythology.

2. *Eras* span hundreds of millions of years, and are defined by chronostratigraphic assemblages called *erathems*, consisting of a group of *stages*. There are 10 eras in Earth's history (i.e. Eoarchean, Paleoproterozoic, Mesozoic, etc.). Eras typically have names that reference their temporal position within their broader

eon (i.e. Mesoproterozoic is the middle portion of the Proterozoic eon).

3. *Periods* typically span 30 to 80 million years (with the exception of the Quaternary), and are defined by chronostratigraphic assemblages called *systems*, which consist of a group of *series*. There are 22 periods in Earth's history, so named for signature localities, events, or formations that characterize the period, many of which are derived from greek and latin (i.e. Cryogenian, Ediacaran, Permian, Carboniferous, etc.)

4. *Epochs* and *Ages* (i.e. Late Devonian, Pleistocene, Maastrichtian, etc.) typically span 2 to 10 million years and will not be significantly referenced in the discussion of this work. Epochs are defined by chronostratigraphic assemblages called *series*, which consist of a group of *stages*. The duration of a *stage* defines an *age*, which is the shortest chronostratigraphic category.

Giga-annum (Ga) and mega-annum (Ma) are conventionally used by geologists to denote time before the present in units of billions or millions of years, respectively (i.e. 4 Ga or 4000 Ma is equivalent to 4 billion years ago). Mega-annum is used for the more recent periods of Earth's history, particularly in the Phanerozoic eon, which spans considerably less time than 1 billion years (541 million years).

1.1.2 Plate tectonics, Wilson cycles, and supercontinents

Since first posited by Alfred Wegener over a century ago as "continental drift" (Wegener, 1912) and following the last half century of extensive seafloor mapping and cross-continental terrane correlation, the theory of plate tectonics has become the cornerstone of modern geologic theory, and has revolutionized our understanding of how the Earth system has evolved. Plate tectonics (from the greek "tektonikos" for "pertaining to building") is the movement of crust (buoyant continents and dense ocean slabs) as an expression of convection occurring in the mantle. The totality of Earth's crust is broken into different plates, formed when upwelled mantle material cools at the surface. When plates meet they cause a variety of side effects ranging from building mountains (orogenesis), to forming chains of volcanoes (subduction of an oceanic slab beneath either another oceanic slab or continental crust), to causing earthquakes, among many other possibilities.

John Tuzo Wilson proposed cyclical plate behaviour to explain the phases of ocean basin formation and closure, which drive continental movements (Wilson, 1966, 1968). Wilson cycles, as they are known today, describe 5 phases: (1) continental extension, where the lithosphere begins to thin and extend in response to mantle forces pulling its ends in opposite directions; (2) rifting, when the lithosphere begins to split into two bodies, moving in opposing directions; (3) upwelling from the mantle forms new ocean crust in between the two bodies, which further seafloor spreading expands; (4) initiation of subduction of the oldest oceanic crust beneath continental lithosphere, beginning to close the ocean basin; (5) continent-continent collision as the ocean basin closes completely.

Increasing geochemical evidence of cyclic tectonic behaviour fosters a growing consensus that the Earth has experienced several supercontinent assemblages, the most recent being Pangea in the Phanerozoic (Nance & Murphy, 2013; Nance, Murphy, & Santosh, 2014; Rogers & Santosh, 2003; Rolf, Coltice, & Tackley, 2014). Supercontinental cycles significantly influence Earth's surface biogeochemistry and climate: accretion, uplift, and enhanced weathering during formation drive increased nutrient transport to the ocean and cooling, while extensive volcanism and eruption of large igneous provinces (LIPs) during dispersal periods result in increasing greenhouse gas levels and warming (Nance, 2022; Rogers & Santosh, 2009; Santosh, 2010). While continents are stable, limited orogenesis results in subdued weathering and declining phosphorus and other nutrient transport to the ocean, curtailing biology's effects on climate; this is coupled with lower volcanic outgassing at subduction zones and eruptive events as supercontinental bodies act as "stable lids" forcing volcanism and subduction to operate primarily on the periphery of the body, with mantle upwelling focused on the hotter centralized lithospheric base eventually causing it to breakup (Condie, 2002; Lowman & Jarvis, 1999). Some key indicators for periods of supercontinental assembly are clustered age distributions in granitic zircons, widespread greenstone deformation and metamorphism, and increasingly heavy seawater strontium isotope signature; all are evidence of collisional orogenesis and enhanced weathering (Bradley, 2011; Condie & Aster, 2010; Condie, Pisarevsky, & Puetz, 2021). Conversely, evidence of increased oceanic crust production and possibly eruptions of large igneous provinces (although the link between LIP events and formation or breakup of supercontinents is unclear; Condie, Davaille, Aster, & Arndt, 2015; Condie et al., 2021), dyke swarms, and increased prevalence of passive margins herald supercontinental breakup (Bradley, 2011; Nance et al., 2014).

The Wilson cycle does not correspond directly with supercontinental cycles, because it describes a local process in one basin whereas supercontinental formation (or breakup) requires the closure (or opening) of many ocean basins across the globe. Wilson cycles are the mechanism by which continental bodies aggregate and therefore may cause supercontinents to develop.

1.1.3 Nutrient cycles

Nutrient cycles occupy the boundary between the biosphere and geosphere. Nutrients are chemical and mineral components of biological organisms and their tools, such as enzymes. The availability of nutrients in an environment is a strong constraint over biosphere size and stability. There are many important nutrients that dictate the behaviour and constrain the evolution of the biosphere, called macronutrients; preeminent across geologic timescales are the cycles for phosphorus, nitrogen, and carbon. Iron is a particularly important component of proteins and enzymes but in ecological terms is considered to be a micronutrient, and so its cycle is not detailed here. All components of the following systems are described in more detail in sections of the model description chapter 2.

1.1.3.1 Redfield ratios

The ratio of the chemical components of biological organisms has been extensively studied, and is known to vary throughout time, between different species, and in response to environmental pressures (Deutsch & Weber, 2012; Lenton & Watson, 2000; Martiny, Vrugt, Primeau, & Lomas, 2013a; Martiny et al., 2013b; Tanioka & Matsumoto, 2017). Early work by Redfield (1958) measuring the ratios of carbon, nitrogen, and phosphorus within phytoplankton found that communities broadly exhibited ratios of 1 P : 16 N : 106 C (known as the "canonical ratio"); this persistent ratio of carbon, nitrogen, and phosphorus in phytoplankton is dictated by the formulation of organic matter, as conceived by Redfield, as $(CH_2O)_{106}(NH_3)_{16}(H_3PO_4)$. Measurements of ocean chemistry revised this ratio to 1 P : 16 N : 117 C (Anderson & Sarmiento, 1994), and Redfield's chemical composition for organic matter assumes too much O and H. Revisitations to the Redfield ratio continue, with particular interest on how anthropogenic climate change and manipulation of nutrient cycling is driving adaptation in the biosphere (Li et al., 2022; Masuda et al., 2023; Ouyang et al., 2022; Wachholz et al., 2023). Phosphorus is typically viewed as the ultimate limiting nutrient for primary producers, because of these three elements it is always the lowest, no matter what ratio is being used, and because N is made available by nitrogen fixers in the modern ocean. In this work, I reference the canonical ratio as a generalized biochemistry of organisms; this is a simplification of necessity, as the complexity and flexibility of true organic matter stoichiometric composition is a modelling question beyond the scope of this current work, and because the canonical ratio is used widely in long-term biogeochemical models that this work is based on.

1.1.3.2 Phosphorus cycle

Most phosphorus is sequestered in continental crust in mineral species such as carbonate fluorapatite ($Ca_{10}(PO_4)_6(OH, F, Cl)_2$); chemical weathering and riverine transport eventually transfer particulate-bound P to the ocean (Ruttenberg, 2003). Primary producers then use available orthophosphate (${PO_4}^{3-}$) to fuel photosynthesis, and this nutrient is regenerated when the organic matter is subsequently remineralized. Dissolved P in oxygenated sediments can be absorbed onto ferric iron oxides (Dijkstra, Kraal, Kuypers, Schnetger, & Slomp, 2014) which, if there is insufficient sulphate concentrations to convert all Fe-oxide to Fe-sulfates, will form vivianite ($Fe(II)_3(PO_4) \cdot 8\,H_2O$; Egger, Jilbert, Behrends, Rivard, & Slomp, 2015; Ruttenberg, 2003). When this iron oxide-bound P is exposed to anoxic conditions, it undergoes reductive dissolution which releases phosphate (Kraal, Dijkstra, Behrends, & Slomp, 2017). Dissolved sedimentary phosphate can also be incorporated into carbonate minerals during precipitation, which are then accreted onto the continent.

Global rates of primary production depend first and foremost on the availability of phosphorus in the environment; as such, evolutionary selection has resulted in several mechanisms by which phosphorus limitation can be subverted. On land, fungi and lichen have evolved enzymes that specifically dissolve mineralized phosphorus when it is depleted in soils (Lambers, 2022; Ruttenberg, 2003). In the ocean, anaerobic bacteria can selectively remove phosphorus species from organic matter when it is particularly limiting (Van Cappellen & Ingall, 1994).

1.1.3.3 Nitrogen cycle

The nitrogen system is characterized by a fast cycle dictated by biological uptake and processing and a slow cycle dictated by geological release. The global nitrogen cycle is biologically-mediated, with producers significantly contributing to the generation of a fixed nitrogen reservoir which can be incorporated into minerals and sequestered geologically (Johnson & Goldblatt, 2015; Zerkle & Mikhail, 2017). Broadly, sedimentary biological nitrogen remineralized as ammonium (NH_4^+) can be incorporated by hydrothermal alteration into potassium feldspars, clays, or micas, exchanging with potassium cations (Holloway & Dahlgren, 2002). Rocks containing these minerals may accrete or be otherwise deposited onto continents and thus grow the continental N reservoir through time (Johnson & Goldblatt, 2017). Subduction of sediments and crust, particularly in colder subduction zones (Elkins et al., 2006), returns nitrogen to the mantle. Primordial (present at the formation of the Earth) and recycled nitrogen returns to the surface at volcanoes and mid-ocean ridges primarily as volatile N_2. In the mantle, nitrogen may act similarly to noble gases, incompatible as N_2 in mineral phases, though pH and redox conditions can also be such that it is cycled as ammonium (Li & Keppler, 2014; Mikhail, Barry, & Sverjensky, 2017; Mikhail & Sverjensky, 2014).

Nitrogen is mostly found in the atmosphere as biologically unusable N_2, which organisms convert into bioavailable "fixed" nitrogen (NH_3 or NH_4^+; Berman-Frank, Lundgren, & Falkowski, 2003; Canfield, Glazer, & Falkowski, 2010; Thomazo & Papineau, 2013). Isotopic evidence of nitrogen fixation dates back to 3.2 Ga (Stüeken, Buick, Guy, & Koehler, 2015a); aided by lateral gene transfer, this ability spread to many lineages relatively quickly (Boyd & Peters, 2013). Nitrogen fixers use the nitrogenase enzyme (or versions thereof) to perform this action, and this enzyme requires a metal cofactor (iron, vanadium, or molybdenum). These metals, and thus the enzyme itself, are sensitive to oxygen levels and enzyme deactivation occurs in oxic conditions (Gallon, 1981). Modern nitrogen fixers have evolved techniques, temporal and physical, to separate the processes of nitrogen fixation from oxygen production in photosynthesis and circumvent this sensitivity (Boyd & Peters, 2013).

Following the rise in atmospheric oxygen in the Proterozoic eon, oxidized forms of fixed nitrogen (NO_3^-, nitrate) became readily available in ocean surface waters, replacing reduced nitrogen as the major N nutrient species (Berman-Frank et al., 2008; Canfield et al., 2010; Cheng et al., 2019) and additional metabolic pathways evolved to produce and utilize new forms of nitrogen in the production of energy, such as denitrification and nitrification. Evidence of ^{15}N enrichment in sediments, indicative of an aerobic nitrogen cycle, dates back 2.7 - 2.5 Ga (Godfrey & Falkowski, 2009; Thomazo, Ader, & Philippot, 2011). As a result of environmental oxidation, N_2-fixation has become disfavoured relative to other assimilation pathways utilizing available ammonia or nitrate because it requires significant energy input to break apart the triple bond between nitrogen atoms (Berman-Frank et al., 2003). Under oxygen limited conditions, nitrate is used in organic matter remineralization as an electron acceptor and reverted back to N_2 via denitrification (Gruber, 2008). Oxygenation may have led to enhanced denitrification and the decline of the fixed nitrogen reservoir (Fennel, Follows, & Falkowski, 2005).

1.1.3.4 Carbon cycle

The biological carbon cycle is more simple than that of nitrogen; dissolved inorganic carbon (DIC) is directly incorporated into biological material during assimilation, and regenerated as CO_2 by organic carbon remineralization under oxic conditions. Under anoxic conditions without available electron acceptors[1], remineralization of organic matter proceeds via methanogenesis, producing both oxidized CO_2 and reduced CH_4 in a 1:1 ratio (Hardison & Canuel, 2011). Methane in the ocean is either consumed by methanotrophs and oxidized to CO_2, or it diffuses to the atmosphere, where it will react with any available oxygen or be photolytically broken down by ultraviolet radiation producing CO_2 and free H^+ (Catling, Zahnle, & McKay, 2001).

Dissolved inorganic carbon in the ocean exists as carbon dioxide, bicarbonate, and carbonate (CO_2, ${HCO_3}^-$, and ${CO_3}^{2-}$, respectively) in equilibrium. The geologic carbon cycle begins when calcium carbonate ($CaCO_3$) is precipitated from DIC under ${CO_3}^{2-}$ saturated conditions, a state determined by temperature, pH, and pressure conditions (Millero, 1995; Zeebe & Wolf-Gladrow, 2001). In the modern ocean precipitation is biologically mediated by organisms which produce internally ${CO_3}^{2-}$ saturated conditions either to form shells (such as phytoplankton, Merz, 1992) or as byproduct of their metabolic processes (such as microbes). In general, carbonate saturation decreases with depth. As a result, carbonate minerals precipitated in the surface ocean begin to dissolve as they sink into the deep ocean, such that most precipitated $CaCO_3$ is not sequestered in geologic reservoirs (Wallmann & Aloisi, 2012). Calcium carbonate is also formed during hydrothermal alteration of seafloor basalts proximal to spreading centres, incorporating this

---

[1] Anaerobic remineralization pathways (ordered by their favourability as determined by energetic yield) include reduction by nitrate, manganese, iron, or sulfate.

mineral into oceanic crust (Coogan et al., 2013; Coogan & Gillis, 2018). Organic and inorganic carbon in sediments and ocean crust is transported to subduction zones by seafloor spreading, where it is either accreted onto continents or continues downward with the subducting slab. Flux melting of subducting slabs appears to liberate the majority of downgoing carbon as CO_2 in arc volcanoes (Fischer, 2008; Li, Li, Aubaud, & Muehlenbachs, 2020; Marty & Tolstikhin, 1998; Williams, Schaefer, Calvache, & Lopez, 1992), with a minor component continuing with the slab into the mantle[2] to be released later at mid-ocean ridges or by plume volcanism (Dasgupta et al., 2013; Zahnle & Sleep, 2002). Atmospheric CO_2 is removed during weathering in reaction with water and continental carbonate and silicate minerals (this is described in more detail in section 1.3.1). This weathering draw-down of CO_2 forms bicarbonate $HCO_3{}^-$, and riverine transport of this species to the ocean begins the cycle anew.

1.1.4 Isotopes

Isotopic fractionation is the "relative partitioning of the heavier and lighter isotopes of a species between two coexisting phases in a natural system" (Tiwari, Singh, & Sinha, 2015). Stable isotope composition is denoted by delta notation, $\delta^X E$ (eg. δ^{13}C) and typically measured in permil (‰, per thousand):

$$\delta^X E = \left(\frac{{}^X E/{}^x E_{\text{sample}}}{{}^X E/{}^x E_{\text{standard}}} - 1 \right) \times 1000$$

wherein E is the element of interest (N, C, etc.), X is the heavy isotope, and x is the light isotope. Standards used for isotopic reference have a value of 0‰ for the given element; the standard for nitrogen isotopes is N_2 in the atmosphere, for carbon isotopes the Vienna Pee Dee belemnite (VPDB), and for oxygen isotopes either VPDB or Vienna standard mean ocean water (VSMOW; Kendall & Caldwell, 1998). Isotopic signature is commonly referred to as "enrichment" or "depletion" with respect to the heavy isotope (i.e. a material with positive δ^{13}C is enriched in heavy ^{13}C relative to the standard). Isotopic evidence in the rock record provides a significant window into the characteristics of the Earth through deep time, although

---

[2] This is one view of geologic carbon recycling based on modern flux measurements; the rate of carbon subduction into the mantle is likely quite variable across the globe and through time, as C retention is largely a function of mineralogy, which itself is controlled by geothermal gradient, water content, redox conditions, and other factors in addition to variability of overall subduction rate (Liu, Chen, He, & Chen, 2019).

this record is not infallible. Diagenetic (post-depositional) reactions and thermal alteration can significantly alter the isotopic composition of a material; depending on the extent of alteration, signatures can be altered or completely erased (Ahm, Bjerrum, Blättler, Swart, & Higgins, 2018; Allan & Matthews, 1990).

1.1.4.1 Equilibrium fractionation

Equilibrium fractionation occurs during reactions operating at equilibrium (i.e. when the rate of the forward reaction is equal to the rate of the back reaction); the reversibility of the reaction allows for isotopes to redistribute between the two phases or compounds to achieve equilibrium. Generally, the heavier isotope tends to accumulate in the compound with a higher oxidation state (Kendall & Caldwell, 1998). Phase changes typically impart some equilibrium fractionation, as the heavier isotope preferentially remains in the less volatile phase (i.e. liquid water is isotopically heavier than water vapour). This fractionation effect is strongest at low temperatures because more heavy isotope can transition to the more volatile phase as temperature increases. The equilibrium fractionation signature of oxygen isotopes (δ^{18}O) is typically used as a paleothermometer.

1.1.4.2 Kinetic fractionation

Kinetic fractionation occurs when a unidirectional reaction separates isotopes according to their relative mass and vibrational energy (Kendall & Caldwell, 1998). This often results from biological processing of carbon and nitrogen by autotrophic organisms; in the process, the ratio of light to heavy isotopes within the produced organic materials is altered relative to the environment. Organisms generally use lighter isotopes because their bond strengths are weaker and easier to break, and kinetic isotopic fractionations tend to be larger than fractionations imparted by equilibrium reactions (Kendall & Caldwell, 1998). Since primary producers preferentially use light carbon, organic carbon tends to have negative (depleted) δ^{13}C signatures, whereas carbonate minerals precipitating from the residual ocean carbon pool will be isotopically heavier and tend to have positive (enriched) δ^{13}C signatures. Carbon isotopes in biological organisms ($^{13}C_{org}$) are on average -20 and -30 ‰ lower than oceanic bicarbonate ($\delta^{13}C_{carb}$), based on the relative contribution of different groups of primary producers (Schidlowski, 2001).

1.1.4.3 The carbon isotope record

The geologic record hosts an amazingly complete archive of carbon isotopes for the ocean and biosphere, starting in the early Archean (Saltzman & Thomas, 2012; Schidlowski, 2001). Since bicarbonate is the dominant form of carbon at Earth's surface, the isotopic signature of carbonate minerals is considered the gold standard for reliably estimating surface carbon cycling through time (Schidlowski, 2001). The mantle isotopic signature $\delta^{13}C_{carb}$ = -5 ‰ defines a reference for this signal. Deviations from baseline $\delta^{13}C_{org}$ and $\delta^{13}C_{carb}$ values, called excursions, are found throughout the geologic carbon record.

Organic and inorganic carbon isotope records reflect both the effect of uptake or sequestration of carbon at the surface of the Earth, and the primary signature of carbon at the surface as a function of mantle outgassing (Schidlowski, 2001); thus, both organic and inorganic carbon materials contribute to the isotope record through complimentary signals. Because organic carbon processing by heterotrophic organisms does not appear to drastically alter the initial isotopic signature imparted during primary production (Lepot, 2020; Pearson, 2010), foraminifera $\delta^{13}C$ is used as a proxy for nutrient cycling and primary productivity in the paleoceanic environment. This record also serves as a proxy for paleoclimate because of the temperature sensitivity of CO_2 solubility (Lynch-Stieglitz, Stocker, Broecker, & Fairbanks, 1995).

Carbon isotope excursions are sometimes discussed as evidence of expanding organic carbon burial fraction (f_{org}), which some believe may broadly explain the gradual oxygenation of Earth's surface (Bjerrum & Canfield, 2004; Karhu & Holland, 1996). This is somewhat controversial given that many interpret the carbon isotope record as indicting generally constant f_{org} through time (Hayes & Waldbauer, 2006; Marais, Strauss, Summons, & Hayes, 1992; Schidlowski, 1988). Along with being open to multiple interpretations, isotopic records are also prone to alteration (Derry, 2010), and even material that appears to be unaltered may have experienced depositional isotopic alteration that muddles its signature (Ahm et al., 2018). Organic carbon buried in anoxic conditions can produce a biased isotopic record that could be misinterpreted as higher primary production (Saltzman & Thomas, 2012); furthermore, shifts in the balance of carbonate, silicate, and organic carbon weathering can result in $\delta^{13}C$ excursions, and appear as anomalously high primary production in the rock record (Kump & Arthur, 1999). As such, there are typically multiple interpretations for any given positive excursion. Given that the carbon isotope record results from a balance of several simultaneous cycles, it is difficult to provide a singular mechanistic cause that can uniformly explain an isotopic signal.

1.1.5 Biological Origins

There is significant uncertainty regarding the composition of Earth's first biosphere. The earliest organisms were likely simple, single-celled prokaryotes (archaea and bacteria) that developed around 3.8 - 3.5 Ga in the Eoarchean (Altermann & Kazmierczak, 2003); evidence of early biology comes partially from phylogenetic reconstruction (Gaucher, Kratzer, & Randall, 2010). The last universal common ancestor (LUCA) from which all later life evolves is believed to have been a hyperthermophilic (having an optimal growing temperature between 45-80°C; Gaucher et al., 2010) bacteria, though different approaches to phylogenetic reconstruction of LUCA have resulted in conflicting conclusions regarding its supposed thermophilic nature (Di Giulio, 2003; di Giulio, 2000; Galtier, Tourasse, & Gouy, 1999). Graphite with depleted $\delta^{13}C$ from the 3.8 Ga Isua sequence, Greenland, has been interpreted by some as evidence of plankton evolving very early in the Archean (Ohtomo, Kakegawa, Ishida, Nagase, & Rosing, 2014; Rosing, 1999), but has also been dismissed as inconclusive biomarker evidence (van Zuilen et al., 2005). Evidence of stromatolitic microfossils from the 3.46 Ga Apex chert, Australia (Altermann & Kazmierczak, 2003; Schopf, Kudryavtsev, Czaja, & Tripathi, 2007) suggest life evolved beyond hydrothermal vent ecosystems by the end of the Eoarchean[3].

Stromatolites are sedimentary structures of thinly layered calcareous mats and are typically formed by communities of microorganisms, particularly photoautotrophic prokaryotes; the layered structure arises from the segregation of different functional groups of microorganisms. One result of these microbial metabolisms is calcite precipitation, which enhances the preservation of the mat structures (Stal, 2012). Stromatolitic forms are not exclusively caused by biology; this type of structure can also result from abiotic means like the accretion of carbonate sediments (Grotzinger & Knoll, 1999), so verifying that a stromatolite is indeed biogenic requires evidence beyond structure, such as the inclusion of microfossils and carbon

---

[3] The biogenicity of the Apex chert has also been questioned; the putative microfossils may have formed as a result of multiple factors including abiotic catalytic synthesis, and thus is not an unambiguous demarcation for the origin of life (Marshall, Jehlička, Rouzaud, & Marshall, 2014).

isotope signature (Lepot, 2020). Stromatolites are abundant in Archean and Proterozoic strata (Lepot, 2020, and references therein). Archean stromatolites do not always contain significant evidence of microfossils or other hallmarks of biogenic formation (Schopf et al., 2007); such compounding evidence of biologic origin is much more common in Proterozoic stromatolites (Knoll, Wörndle, & Kah, 2013). Cyanobacteria, or blue-green algae, are extant organisms that likely emerged early in the Archean; today, they are found in many different environments, and are common in microbial mat communities such as those forming modern stromatolites (Stal, 2012; Whitton, 2012).

When life first evolved in the Archean ocean, possibly near hydrothermal vents, it was most likely anaerobic/anoxygenic (non-oxygen producing) and chemolithoautotrophic (deriving energy from minerals in the environment). Kerogens (insoluble complex hydrocarbons produced by organic matter buried in anoxic environments; Durand, 1980, Selley, 2005) in organic-rich shale deposits dating back to 3.2 Ga are potential evidence of an active biosphere dependent on methane, hydrogen, and iron produced by serpentinization (McCollom & Seewald, 2013; Mével, 2003); this remnant organic material can be produced by both biotic and abiotic processes, and is not *de facto* evidence of a biosphere (Lepot, 2020).

The need for nutrients, particularly phosphorus, nitrogen, and iron, limited where life could flourish and how much life could be sustained by the environment. Phosphorus today is primarily made available for organisms in the ocean via weathering and transport that liberates it from minerals in continental rock and dissolves it into the ocean; given limited continental emergence and enhanced phosphorus sinks in an anoxic ocean (Alcott, Mills, Bekker, & Poulton, 2022; Bjerrum & Canfield, 2002), phosphorus availability is believed to have been substantially restricted during the Archean, though this is debated (Crockford & Halevy, 2022; Konhauser, Lalonde, Amskold, & Holland, 2007b; Planavsky et al., 2010; Schidlowski, 1988).

By similar logic, important metals like molybdenum (Mo) could have been difficult to come by in the Archean ocean, since this metal is concentrated in continental bodies today and primarily removed by oxidative weathering (Zerkle, House, Cox, & Canfield, 2006). Molybdenum is a key component in the enzyme nitrogenase; this enzyme allows primary producers to fix otherwise inert N_2 into NH_3. A lack of available Mo in the oceans may have been a severe limitation on the early biosphere's capacity to fix nitrogen (Zerkle et al., 2006). Alternate nitrogenase enzymes exist in modern N-fixers, and it is unclear which of the metal cofactor versions of the enzyme evolved first. The emerging consensus indicates that Mo-dependent nitrogenase is the ancestral lineage of all nitrogenase enzymes, and emerged in anoxic environments in association with methanogens (Boyd & Peters, 2013), so a lack of oxidative weathering source may not have inhibited nitrogen fixation significantly. Lightning-sourced fixed nitrogen may have been the earliest form of this nutrient, producing nitrous oxide (N_2O) and cyanide (HCN); the latter can be converted into NH_4^+ (Zahnle, 1986). Cyanide in the ocean may have spurred early evolution of nitrogenase as a detoxifying mechanism (Fani, Gallo, & Liò, 2000; Zerkle et al., 2006). Regardless of the initial mechanism, it does not seem that LUCA could fix nitrogen, given that many archaea lack the capacity to do so (Boyd, Hamilton, & Peters, 2011; Dos Santos, Fang, Mason, Setubal, & Dixon, 2012). This makes arguments for nitrogen fixation as a primordial functionality difficult to believe (Fani et al., 2000). But it is clear that the evolutionary pressure to develop a method by which to fix N was so great that once the technique evolved in one lineage, it was soon found everywhere (Falkowski, 1997; Stüeken, Buick, Guy, & Koehler, 2015b).

1.1.6 Atmospheric chemistry and oxidation evidence

The changing state of atmosphere and ocean oxidation is recorded in the speciation and fractionation of redox-sensitive proxies. One such proxy I will mention frequently is sulphur isotopes. Mass dependent fractionation of sulphur (MDF-S) occurs because of the preferential inclusion of lighter elemental isotopes in minerals and in biotic processes; most thermodynamic and kinetic processes result in mass dependent fractionation (Pavlov & Kasting, 2002). Conversely, mass independent fractionation of sulphur (MIF-S) occurs when high-energy photochemical reactions separate isotopes, without preference to isotopic mass; this happens when high-energy UV radiation can fully penetrate the atmosphere and photolytic reactions occur in the troposphere and at the surface of the planet (Farquhar, Bao, & Thiemens, 2000). Such MIF-S reactions do not occur at Earth's surface in the modern context as a result of radiative shielding by the stratospheric ozone layer (Farquhar, Savarino, Airieau, & Thiemens, 2001). Threshold oxygen level for preserving this signal, which depends on the stability of reduced sulphur species in the atmosphere, is around 1×10^{-5} PAL (present atmospheric level; Pavlov & Kasting, 2002). Thus, one may be able to determine whether or not an atmosphere is anoxic ($O_2 \leqslant 1\times10^{-5}$ PAL) or oxic ($O_2 > 1 \times 10^{-5}$ PAL) from the relative dominance of sedimentary sulphur isotopic fractionation patterns.

1.1.7 Climate

The persistence of life through 4 billion years of climate evolution suggests that the planet has not strayed too far from what is considered the "habitable zone" of average surface temperatures. The Earth's climate has thus been broadly stable through time, despite major changes in atmospheric composition and solar flux. Just after the Moon-forming impact and the cooling of Earth's crust at the start of the Hadean eon (4.5 Ga), it is likely that there existed a very hot climate beneath a massive CO_2 atmosphere, though this period probably only lasted a few million years (Sleep, Zahnle, & Neuhoff, 2001). During the Archean eon, it is presumed from geochemical evidence and climate modelling that the surface was at least temperate and possibly hot, and sustained by higher partial pressures of CO_2 (Nutman, Bennett, & Friend, 2017; Walker, 1985; Walker et al., 1983); it is debated whether or not oxygen isotopes in cherts evidence equilibrium fractionation of seawater and silica (indicating temperatures around 70°C; Knauth, 2005), or if they are evidence of hydrothermal alteration (van den Boorn, van Bergen, Nijman, & Vroon, 2007) or a natural decline in seawater oxygen isotope signature (Kasting et al., 2006), both options which allow for more clement temperatures. Deuterium fractionation in cherts suggests more moderate temperatures below 40°C (Ali et al., 2020). The Mesoarchean (3.2 - 2.8 Ga) may have contained a snowball event, or a large-scale glaciation, which is demarcated by the Pongola glacial diamictite in South Africa (de Wit & Furnes, 2016; Von Brunn & Gold, 1993; Young, Brunn, Gold, & Minter, 1998). When coupled with models of climate (Charnay, Le Hir, Fluteau, Forget, & Catling, 2017) and geochemical cycles (Krissansen-Totton, Arney, & Catling, 2018), there is growing consensus that the Archean was rather temperate.

The sun's luminosity has increased through time as nuclear fusion increases solar core density (Gough, 1981); therefore, the early Earth received less solar influx to heat its surface than it does today (Newman & Rood, 1977; Sagan & Mullen, 1972). The solar history implies colder surface temperatures, conflicting with the evidence that implies warm temperate conditions; this conflict is conventionally known as the "faint young Sun paradox". It is less a paradox than a question of precisely how different the early atmosphere was to our current composition, given that the heat deficit can be reconciled with higher levels of greenhouse gases (Goldblatt & Zahnle, 2011). As continents have gradually emerged as a result both of mantle eruptions and by accretion of seafloor sediments, carbon precipitated from within the ocean has accumulated into a large, stable reservoir separate from the atmosphere. This reservoir is the remnant of carbon originally outgassed from the mantle to the atmosphere, and as such the growth of continental carbon can be considered a "degrowth" of the atmospheric carbon reservoir. Nitrogen, which can be sequestered from the atmosphere after biological processing, shows similar signs of gradual accumulation in the continents; the surface geologic reservoir of N could potentially house a massive early N_2 atmosphere (Johnson & Goldblatt, 2017, 2018), which could have provided significant additional warming in the Archean via pressure-broadening of greenhouse gas absorption spectra (Goldblatt et al., 2009).

1.2 A brief history of the Earth

In the following sections, I will give a brief overview of the geologic eons that the model covers focusing on major events and geologic markers that characterize the era.

1.2.1 Hadean eon: 4.5 Ga - 4.0 Ga

Earth's tangible story begins approximately 4.5 billion years ago in the Hadean. This eon is the most recent addition to the geologic timescale, coined in 1972 to describe the period before the rock record began (Cloud, 1972). Other names for this period included "Priscoan" (after the latin *priscus*, meaning "ancient") and simply "Pre-Archean". The Hadean was so named after the Greek god of the underworld, Hades, because this portion of time including the formation of the Moon, the bombardment of Earth's surface by asteroids, and the cooling of the magma ocean into crust is, not unreasonably, considered to be the most hellish period of Earth's history.

Little is known about the Hadean Earth, given few surviving rocks (although sections of the Nuvvuagittuq greenstone belt in Quebec have reported ages ca. 4.2 Ga; O'Neil, Carlson, Francis, & Stevenson, 2008), a sparse record of surface conditions, and no robust evidence of biological life. The surface of the Earth at this time was anoxic (Pavlov & Kasting, 2002), with higher partial pressures of carbon dioxide (Walker, 1985) and abiotic methane (Kasting, 2005) that added additional radiative forcing to keep the surface warm enough to maintain liquid surface water (Catling & Zahnle, 2020; Sagan & Mullen, 1972). Oxygen isotopes recorded by the oldest zircons provide us with evidence of this state (Peck, Valley, Wilde, & Graham, 2001); δ^{18}O enrichment in these minerals is believed to be a product of assimilation or melting of enriched sediments which experienced low-temperature hydrothermal alteration, and the felsic materials hosting such zircons generally require water for their formation. Carbonate chemistry suggests that the Hadean ocean was relatively similar to today, and suitable for hosting life by the end of the eon (Morse & Mackenzie, 1998).

1.2.2 Archean eon: 4.0 Ga - 2.5 Ga

The name of this eon refers to the Greek $\alpha\rho\chi\eta$ (*arkhē* or "beginning") and is a reference to opening lines in the book of Genesis using "in archaea", or "in the beginning", as this was long the extent of the surviving record of Earth's surface. The Archean was initially defined by the age of the oldest surviving rocks (the Acasta Gneiss from the Northwest Territories), and thus is considered when the stratigraphic record begins.

The Earth at this time likely had some form of operational plate tectonics involving subduction, though it was likely very sluggish compared to modern day rates as evidenced by models of mantle thermal evolution (Korenaga, 2006), ancient passive margins (Bradley, 2008), and atmospheric radiogenic xenon (Padhi, Korenaga, & Ozima, 2012). Continental bodies gradually emerged and developed as island arcs collided; whether or not there is significant subaerial continental exposure at this point is still debated (Dhuime, Hawkesworth, Delavault, & Cawood, 2018; Johnson & Wing, 2020; Reimink, Davies, & Ielpi, 2021). It has been posited that this period saw the first "supercraton" assemblages named Vaalbara (Zegers, Wit, & Dann, 1998) and Kenorland (Lubnina & Slabunov, 2011; Williams, Hoffman, Lewry, Monger, & Rivers, 1991), but the existence of either is debated (Bleeker, 2003; Evans & Muxworthy, 2019).

This is also when life begins, most likely as thermophilic chemoautotrophs near hydrothermal vents, using iron or sulphur as an electron receiver (Kappler, Pasquero, Konhauser, & Newman, 2005). The Archean ocean was ferruginous (high concentrations of iron; Holland, 2006; Poulton & Canfield, 2011; Pellerin et al., 2023), and possibly transitioned to euxinic (high concentrations of dissolved sulphur) by the end of the eon (Scott et al., 2011). In the early Archean, high concentrations of reduced iron fuelled the deposition of massive banded iron formations (BIFs) that are found throughout the early rock record (Holland, 2003, and references therein). This plentiful reduced iron fuelled photoferrotrophy (Crowe et al., 2008), and this metabolism likely contributed significantly to the production of iron oxides found in BIFs (Kappler et al., 2005; Konhauser et al., 2002; Thompson et al., 2019).

The carbon isotope record from the Archean as reviewed by Schidlowski (1988) shows remarkable stability in both $\delta^{13}C_{\text{org}}$ (around -26‰) and $\delta^{13}C_{\text{carb}}$ (around 0‰); the similarity of this ancient signal with the modern carbon isotope record has been interpreted as evidence of a biosphere dominated by autotrophic carbon fixation and inhibited by constraints on nutrient availability similar to that of the modern ocean biosphere. Isotopically light graphite in the Isua sequence, aged 3.8 Ga, was initially interpreted as evidence of early oxygenic carbon fixation (Rosing, 1999), implying that the biosphere developed oxygenic metabolisms very early. However, this graphite is more likely the result of H_2-driven anoxygenic photosynthesis (Olson, 2006), and the Isua BIF $\delta^{13}C_{\text{carb}}$ signal is now interpreted as evidence of iron-reducing metabolisms (Craddock & Dauphas, 2011; Czaja et al., 2013; Nutman et al., 2017); coupled with strongly negative $\delta^{13}C_{\text{org}}$ values at the end of the Archean (interpreted as evidence of organic carbon recycling by methanotrophs; Hayes & Waldbauer, 2006), the carbon isotope record of this eon further solidifies the image of an anoxic early Archean biosphere.

Photosynthetic oxygen production is thought to have begun sometime in the Neoarchean (Czaja et al., 2012; Olson, 2006). MIF-S signatures in the Nauga and Mount McRae shales indicate low O_2 ($\leqslant$ 0.001% PAL) during the Neoarchean (2.8 - 2.5 Ga), further confirming that while oxygenic photosynthesis was active at this time, atmospheric oxygen was curtailed by the overwhelming abundance of reducing species (Kendall et al., 2010).

1.2.3 Proterozoic eon: 2.5 Ga - 541 Ma

The name “Proterozoic” means “early life”. Although life emerged in the preceding Archean, the biosphere at this time is dominated by prokaryotes; more complex eukaryotes evolve in the middle of this eon, so the name seems suitable. This eon represents the largest grouping of Earth's history, spanning nearly 2 billion years, and contains several dramatic climate events as well as a permanent shift in atmospheric composition that defines the trajectory of life on Earth: the Great Oxidation Event (GOE).

1.2.3.1 Paleoproterozoic era: 2.5 Ga - 1.6 Ga

This era is characterized by major developments in the geosphere and biosphere which together cause dramatic shifts in atmospheric chemistry and climate, reshaping the Earth to more closely resemble its modern state. Two large supercratons called Superia (a combination of Wyoming, Superior, Hearne, and Kola-Karelia cratons; Bleeker, 2003) and Kapvaal (a combination of South Africa and Australia cratons; Zegers et al., 1998) begin to amalgamate near the equator (Gumsley et al., 2017). Global tectonics may have started to slow down during the formation of these large landmasses, indicated by a punctuated decline in juvenile igneous materials and detrital zircons aged 2.45 - 2.2 Ga (Pehrsson, Buchan, Eglington, Berman, & Rainbird, 2014).

The expansion of oxygenic and aerobic metabolisms forced once dominant anaerobic organisms to gradually adapt to higher concentrations of oxygen in the surface ocean and atmosphere (Duan et al., 2010). Oxygen level in the atmosphere reached a bistable tipping point somewhere between 2.45 - 2.3 Ga (Gumsley et al., 2017); the precise timing of the GOE and whether or not it was a singular event or a sequence of events has been long debated, but the nature of this transition is becoming increasingly well-constrained by geochemical proxies. Recent evidence from the Transvaal Supergroup (South Africa) has led several researchers to propose an age of 2.33 Ga for the GOE (Bekker et al., 2004; Luo et al., 2016), but it seems that this date signifies the termination of what was a multi-step oscillation between anoxic and oxic conditions spanning a nearly 200 Myr interval (Gumsley et al., 2017; Poulton et al., 2021). Transient oxygenation events likely preceded the irreversible oxygenation of the surface (Anbar et al., 2007; Crowe et al., 2013; Czaja et al., 2012; Duan et al., 2010; Mukhopadhyay et al., 2014), and fluctuations in the MIF-S signal corresponding to the GOE likely resulted from climatic instability around the event (Asael, Rouxel, Poulton, Lyons, & Bekker, 2018; Garduño Ruíz, Goldblatt, & Ahm, 2023; Poulton et al., 2021).

There are many theories regarding the cause of the GOE, spanning from a decline in reduced gases emanating from the mantle (Holland, 2002), a change in volcanic gas oxidation state (Gaillard, Scaillet, & Arndt, 2011) potentially correlated with a massive LIP event (Ciborowski & Kerr, 2016), loss of hydrogen to space (Catling et al., 2001; Claire, Catling, & Zahnle, 2006), a tipping point between biological methane versus oxygen production (Goldblatt, Lenton, & Watson, 2006), significant organic carbon preservation on the emergent continents (Husson & Peters, 2017; Lee et al., 2016; Marais et al., 1992), changing phosphorus recycling (Alcott et al., 2022), or increasing weathering following a global glaciation (Gumsley et al., 2017), to name a few. The complete oxygenation of the Earth's surface may have directly preceded (Warke et al., 2020), or coincided with several widespread glacial events (Gumsley et al., 2017; Rasmussen, Bekker, & Fletcher, 2013), including at least one low-latitude glaciation (Snowball event; Kirschvink et al., 2000; Hoffman, 2013).

This transition also coincides with a peak in BIF deposition, and these formations were an early indicator of fluctuating ocean redox conditions that eventually led to the initial theory of a Proterozoic oxidation event (Cloud, 1968). The prevalence of BIFs decreases following the permanent oxygenation of the atmosphere, until they no long appear regularly in the record following 1.8 Ga (Holland, 2006, Isley & Abbott, 1999, and references therein); it has been theorized that this disappearance is caused by a transition to sulfidic deep ocean conditions (Canfield, 1998; Poulton, Fralick, & Canfield, 2004).

The GOE is followed by a global +10‰ $\delta^{13}C_{\text{carb}}$ pulse known as the Lomagundi excursion (Schidlowski, Eichmann, & Junge, 1976); the cause of this excursion has been linked with expanding organic carbon burial (Karhu & Holland, 1996), though other arguments have suggested that this signals a shift in the isotopic composition of carbon outgassed at volcanoes (Eguchi, Seales, & Dasgupta, 2020). However, this excursion and oxygenation can be linked by another possible mechanism: a switch to modern crustal subduction at this time could have led to increased recycling of carbon stored in sediments, which would increase the δ^{13}C signature of erupted materials as higher amounts of isotopically heavy carbonate are recycled at arc volcanoes relative to other eruptive settings (Eguchi et al., 2020).

1.2.3.2 Mesoproterozoic era: 1.6 Ga - 1 Ga

This era is colloquially known as the "boring billion" because of a lack of geologic evidence of major climatic or tectonic disruptions. Particularly when compared with the significant climatic and chemical disruptions of surrounding eras, the Mesoproterozoic is a standout quiescent stage in Earth's history. This is likely the result of one or more stable supercontinents positioned near the equator (Nance, 2022; Nance et al., 2014): supercontinent Nuna, or Columbia, (Rogers & Santosh, 2002; Zhang et al., 2012) followed by Rodinia (Torsvik, 2003). The stability of supercontinental bodies seems to cause periods of climate stabilization, which emerge gradually out of the amalgamation period of high tectonic activity and are abruptly ended when the supercontinent begins to break up and disperse (Nance, 2022). The carbon isotope record of this period reflects climatic and biospheric stability imposed by limited phosphorus recycling (Kipp & Stüeken, 2017), and has been interpreted as evidence of carbon fixation dominated by cyanobacteria (Hurley, Wing, Jasper, Hill, & Cameron, 2021). This interval, devoid of glaciations, mass extinctions, or major phosphorite deposits (the lack of which is suggestive of nutrient stability within the ocean) may have fostered stable climate conditions under which prokaryotic photosynthesizers symbiotically merged to create the first chloroplasts and eukaryotic autotrophs (Brasier & Lindsay, 1998).

1.2.3.3 Neoproterozoic era: 1 Ga - 541 Ma

This era includes the formation and breakup of Rodinia (1.0 Ga and 800 Ma, respectively; Nance et al., 2014; Torsvik, 2003), causing dramatic and temporarily catastrophic climate shifts that led to what is now understood to be a series of global glaciations. Rodinia may have been followed by the formation of another, short lived supercontinent Pannotia/Gondwana (ca. 620 - 580 Ma; Cordani, D'Agrella-Filho, Brito-Neves, & Trindade, 2003; Nance, 2022). Fungi and lichen may have colonized the continents around 800 Ma, as suggested by molecular clock estimates (Heckman et al., 2001; Lucking, Huhndorf, Pfister, Plata, & Lumbsch, 2009) and morphological developments (Lutzoni et al., 2018), and were likely present by the Ediacaran (circa 600 Ma) according to trace fossil evidence (Retallack, 2013); this colonization results in a massive expansion of nutrient flux to the oceans. Oxygen levels may have oscillated throughout this era (Krause, Mills, Merdith, Lenton, & Poulton, 2022), an expected result of extreme climatic perturbation (Garduño Ruíz et al., 2023).

The Cryogenian period (720 - 635 Ma) includes at least two distinct snowball Earth glaciations, which are characterized by massive glacial diamictites in South

Africa, North America, and Australia; in particular, basalts adjacent to (and sometimes intermingling with) these glacial deposits contain magnetic iron recording near-equatorial paleolatitudes (Hoffman, Kaufman, Halverson, & Schrag, 1998), strong evidence that glaciers spanned from the polar regions to the equator. Whether or not these were "hard" (where the entire ocean to the equator froze) or "slushy" (where the equatorial ocean is partially frozen; Hyde, Crowley, Baum, & Peltier, 2000; Lewis, Weaver, & Eby, 2007) snowballs is unclear, debated (Schrag & Hoffman, 2001), and perhaps indeterminable. Glacial deposits are overlain by massive cap carbonates (Hoffman et al., 1998), a signature of compensatory sequestration of extremely high CO_2 levels in the atmosphere, which rose unabated by continental weathering feedbacks when the surface was frozen (Kirschvink, 1992), as temperatures swung from extremely cold averages (250 to 240 K, approximately -30°C) to extremely high averages (over 300 K, approximately 30°C). The recurrence of BIF deposition after a nearly billion year hiatus, and in close association with glacial deposits (Holland, 2006; Isley & Abbott, 1999) signals that the deep ocean experienced a transient return to ferruginous conditions during this wide scale carbon cycle disruption (Kirschvink, 1992) as sulphur transport to the ocean was significantly curtailed by glaciations (Canfield & Raiswell, 1999). Following their return in the Cryogenian, BIFs disappear from the geologic record.

The extreme shifts in Neoproterozoic climate are reflected in extreme positive excursions in $\delta^{13}C_{\text{carb}}$ (Kaufman & Knoll, 1995). This has been interpreted as evidence of a major and unique decline in organic carbon burial (Hoffman et al., 1998) and extensive remineralization (Rothman, Hayes, & Summons, 2003); all potential hallmarks of significant destabilization in the biosphere. It has also been argued that the Neoproterozoic record does not reflect particularly unique conditions, and viewing these excursions alongside δ^{18}O indicates that the carbon system was operating according to the same mechanisms as in the later Phanerozoic (Knauth & Kennedy, 2009). An extremely negative carbon isotope excursion, the Shuram-Wonoka anomaly, coincides with the end of the Neoproterozoic era (the Ediacaran period, 635 - 541 Ma) when body sizes increase; this $\delta^{13}C_{\text{carb}}$ excursion has been suggested as a sign of major changes in global carbon cycling (Rothman et al., 2003), but has also been linked with diagenesis (Derry, 2010).

1.2.4 Phanerozoic eon: 541 Ma - 0 Ma

Larger eukaryotic organisms (which evolve in the preceding Ediacaran) developed the ability to mineralize skeletons, thus beginning the start of the geologic fossil record and making the name for this eon (meaning "visible life") quite apt. The impetus for biomineralization may have been predation (Porter, 2011), or an adaptation to changing ocean chemistry (Lowenstein, Timofeeff, Brennan, Hardie, & Demicco, 2001; Stanley, 2006). The Phanerozoic is dominated by one major supercontinent cycle, during which supercratons Gondwana and Laurasia form into Pangea (Nance et al., 2014; Wegener, 1912) and subsequently begin to break apart in the Mesozoic Jurassic period (circa 200 Ma; Bradley, 2011), dispersing into modern continental bodies.

Because skeletons greatly improved the preservation of biospheric diversity, the Phanerozoic is home to the clearest record of the biosphere-climate-carbon cycle interactions, particularly with respect to the 5 major extinction events interspersed throughout this eon. From oldest to youngest (excluding the current Anthropocene mass extinction event): (1) the Ordovician-Silurian ca. 445 Ma (associated with major climate changes, including the Hirnantian glaciation, driven by volcanic eruptions; Harper, Hammarlund, & Rasmussen, 2014; Bond & Grasby, 2020); (2) the end-Devonian ca. 372 - 355 Ma (see following paragraph); (3) the Permian-Triassic ca. 252 Ma (also known as the "Great Dying", this is the largest recorded extinction event, and is associated with major carbon cycle disruption by massive LIP eruptions in the Siberian traps; Erwin, 1994 and references therein); (4) the end-Triassic ca. 200 Ma (associated with ocean acidification following massive LIP eruption of the Central Atlantic magmatic province; Whiteside, Olsen, Eglinton, Brookfield, & Sambrotto, 2010); and (5) the end-Cretaceous ca. 65 Ma (this event resulted in the disappearance of non-avian dinosaurs, and is associated with climate disruption initiated by the Deccan trap flood basalts in India and exacerbated by a massive bolide impact on the modern day Yucatan peninsula; Hallam, 1987; Schulte et al., 2010). Many of these extinction events are correlated with positive $\delta^{13}C_{\text{carb}}$ isotope excursions, interpreted as reflecting rapid climate warming from volcanic CO_2 or clathrate CH_4 releases that in turn cause massive changes to nutrient availability, primary production, and ocean anoxia (Saltzman & Thomas, 2012, and references therein).

A major disruption to climate and weathering has been implicated in the third mass extinction event, at the end-Devonian. During the Silurian period (445 - 420 Ma), fungi and lichen on the continents are joined by vascular plants. Their rooting systems, combined with helpful fungal associates, lead to a massive increase in continental weathering; roots are able to break up rocks and concentrate acids to generate soils, liberating key nutrients from minerals in the process (Hoffland et al., 2004; Kelly, Chadwick, & Hilinski, 1998; Lenton et al., 2016). A huge influx in weathering lead to a spike in the availability of nutrients and rising productivity, causing both a rapid rise in oxygen above modern levels (Glasspool & Scott, 2010) and a rapid decline in CO_2 and temperature. The resulting shift into a glacial climate and global marine regression (decline in sea level) perturbed the carbon cycle, as evidenced by a large positive $\delta_{^{13}C_{\text{carb}}}$ excursion, and may have contributed to ocean eutrophication at the end of the Devonian (ca. 355 Ma; Kaiser, Aretz, & Becker, 2016 and references therein).

After reaching a maximum in the Carboniferous period (ca. 355 - 300 Ma) as trees formed massive coal swamps, atmospheric oxygen levels decline to modern day levels (Glasspool & Scott, 2010). Our current atmosphere is 78% nitrogen (as inert N_2) and 21% oxygen (as O_2) with the remaining 1% as everything else (i.e. argon, carbon dioxide, methane, etc.) and the current mean surface temperature of $15°C$ is maintained primarily by CO_2 and CH_4 partial pressures of 280 and 1 ppm, respectively (pre-industrial averages).

1.3 A brief review of Earth system feedbacks

The Earth system, here meaning the interactions between the biosphere, geosphere, and atmosphere-ocean through time, is horridly complex. The origin of this complexity are the numerous operating feedbacks within each subsystem, which communicate changes in one subsystem into changes in another subsystem and so on, *ad infinitum*. A feedback is simply a response to perturbation (change) in a system. Feedback loops are when a system reacts in a certain way to perturbation, which either reinforces (positive loop) or diminishes (negative loop) the original perturbation.

1.3.1 The carbon-silicate weathering feedback

This feedback is between atmospheric CO_2, temperature, and carbonate or silicate minerals on the continents. As atmospheric CO_2 rises, either by natural mantle outgassing, volcanism, or by anthropogenic sources, surface temperature rises because of CO_2 radiative effects. Rising temperatures increase precipitation, as a warmer atmosphere holds more water vapour. When precipitation occurs, CO_2 is dissolved in the water to create carbonic acid (H_2CO_3), which dissolves minerals on the continent (a reaction which is also enhanced by temperature). Dissolved minerals and carbon (as bicarbonate, $HCO_3{}^-$) are transported to the ocean; bicarbonate is an alkaline species, which means its presence increases ocean pH and makes it more likely that calcium carbonate will precipitate. Carbonate minerals are subsequently buried and eventually accreted onto continental bodies, where the cycle can start again.

This is well known among Earth system scientists as the *WHAK* feedback, after the authors Walker, Hays, and Kasting (Walker, Hays, & Kasting, 1981). In the process of enhancing weathering, alkalinity formation, and precipitation and burial of carbon in $CaCO_3$, an increase in CO_2 negates itself. This is therefore a negative feedback that stabilizes climate over long periods on the order or millions of years.

1.3.2 The ice-albedo feedback

The climatic importance of ice coverage was recognized in the latter portion of 20th century by Budyko (1969) and Sellers (1969). The reflectivity of a planet is primarily a function of the proportion of surface covered by ice versus water or rock. Bare rock and water have low albedo (reflectivity), and thus absorb most incoming solar radiation. This absorption shifts Earth's radiative in-out balance towards net influx, which heats the planet. Conversely, ice and snow have very high albedo and reflect most incoming radiation, shifting the radiative balance towards net outflux and causing planetary cooling. Colder average surface temperatures result in less snow melt in the polar regions (and at high elevations) and so year-over-year ice accumulation increases; glacial ablation is less than glacial accumulation. Over many years, the area covered by glaciers or sea ice increases and more of the Earth's surface becomes highly reflective. Conversely, warmer average temperatures result in more ice melt every summer, revealing the ground and water underneath, both of which are more radiatively absorptive. This absorption makes surface temperatures rise and incurs more ice melt, and planetary albedo declines until no ice is left.

This feedback is positive because the perturbation to ice coverage (in either direction) is amplified by response of the climate system; ice begets more ice. A curiosity of this feedback is that on the Earth there is a threshold latitude where ice coverage expansion (or retreat) accelerates rapidly. Once there is long-lived ice coverage at latitudes near 50°, the system enters into a bistable state that transitions very rapidly into the proximal extreme (Budyko, 1969). If ice is expanding into lower latitudes, this becomes a global glaciation. If ice is retreating to higher latitudes, it becomes a global deglaciation. This is a primary feedback mechanism that produces (and terminates) Snowball Earth events.

1.3.3 The water vapour (supergreenhouse) feedback

Radiative equilibrium requires that an increase in solar energy absorbed is balanced by increasing emittance from a planet. This generally holds for temperate regions, but in the tropics where the troposphere is hotter and more moist, equilibrium begins to break down (Dewey & Goldblatt, 2018). Water vapour strongly absorbs thermal radiation, making it a very efficient greenhouse gas. When surface temperatures rise, evaporation increases. As the atmosphere holds more water vapour, its thermal opacity (or optical depth, the ratio of incoming to retransmitted longwave radiation) increases such that surface temperatures heat up even faster, and more water is evaporated; heat increases linearly with water vapour in temperate regions but non-linearly in tropical regions. This is a positive feedback that promotes surface heating.

1.3.4 Runaway glaciations

A combination of these three feedbacks (silicate-weathering, ice-albedo, and supergreenhouse) are integral players in the runaway glaciation phenomenon known as Snowball Earth. Some component of global weathering balance changes to initiate the climatic feedbacks; this can be continental bodies drifting towards the equator, or extensive basalt eruptions introducing weatherable materials to the surface, or external forcings like planetary obliquity could alter the climate. Extensive silicate weathering leads to gradually declining surface temperatures as atmospheric CO_2 is sequestered. This results in increasing glaciation, starting from at the poles and extending to the equator as the average planetary temperature continues to decline (due to increasing albedo). Once ice extends into the mid-latitudes, the system rapidly transitions to a global glaciation.

In the absence of significant continental weathering during a global glaciation, volcanic and mantle outgassing leads to a gradual increase in atmospheric CO_2 (Hoffman et al., 1998; Kirschvink, 1992). This climate feedback, coupled with the rapid transition between icy to ice-free albedos, initiates a supergreenhouse feedback that warms the planet to extreme temperatures and results in the deposition of massive carbonate platforms on top of glacial diamictites; these are considered trademarks of Snowball Earth glaciations (Hoffman, 2013; Hoffman et al., 1998). The buildup of sufficient surface CO_2 in order to trigger deglaciation in the Neoproterozoic has been estimated to require 4 to 30 million years (Hoffman et al., 1998).

1.4 Earth system models

The Earth has managed to maintain astonishing habitability through 4.5 billion years of existence, albeit with dramatically disruptive moments. Two major theories emerged to explain this observation, both of which colour the following work: First, the *Gaia* hypothesis posited long-term climate and carbon system stabilization caused by biological feedbacks, an "adaptive control system to maintain the Earth in homeostasis" (Lovelock, 1972; Lovelock & Margulis, 1974). Second, the *WHAK* feedback explained climate stabilization via coupling between atmospheric carbon dioxide, temperature, and continental silicate weathering, wherein increases to atmospheric CO_2 and surface temperature enhance mineral dissolution and continental weathering in a process that sequesters carbon from the atmosphere as carbonate minerals (Walker et al., 1981). In the decades since the development of these theories for Earth's evolution, models attempting to recreate the Earth system have continued to grow in complexity and in breadth of systems involved, yet all of these models are fundamentally in agreement: the Earth system as we understand it is the result of multifarious intertwined biological, geological, and climatic systems.

Modelling the Earth system in all its complexity is difficult. Many models of the Earth system attempt to recreate the carbon isotope record, as this is essentially a record of the coupled inorganic-organic carbon system. Thus, there has been significant focus on modelling oxygen and carbon systems through the Phanerozoic eon (Bergman, Lenton, & Watson, 2004; Berner, 2009; Lenton, Daines, & Mills, 2018; Zeebe, 2012) where the record is quite robust, with some models covering the Proterozoic (Alcott, Mills, & Poulton, 2019; Fennel et al., 2005) and Archean (Claire et al., 2006; Kharecha, Kasting, & Siefert, 2005) where records are much more sparse. Higher resolution biogeochemical box models of the coupled C-N-O-P-S systems resolve ocean chemical evolution over geologic timescales, but exclude mantle-surface interactions and anaerobic cycles applicable to the Archean (Ozaki, Cole, Reinhard, & Tajika, 2022). All have added to the growing wealth of knowledge regarding the ultimate controls on Earth's evolutionary trajectory. These models are broadly similar in form; they generally utilize fixed fluxes and numerous external forcings to evolve their chosen systems. None have spanned all of Earth's history.

This current work has been heavily influenced by other biogeochemical box models; particularly the COPSE (Bergman et al., 2004) and its later updates (Lenton et al., 2018), GEOCARB (Berner & Kothavala, 2001), LOSCAR (Zeebe, 2012), and the unnamed model of Sleep and Zahnle (2001). The latter two models are concerned primarily with carbon geochemical cycling and atmospheric CO_2, while the former two models (COPSE and GEOCARB) include more feedbacks with biology to resolve the Phanerozoic carbon isotope record. I borrow heavily from all four models in both a functional as well as philosophical sense, and the existence of this model is indebted to those authors, and all who influenced their work.

1.5 Research Goals

My modelling philosophy is to dynamically evolve the Earth's surface system through time by including as many feedbacks as possible and by imposing as few external forcings as possible. The resulting *EONS* model is a first of its kind, fully coupled interactive biogeochemical box model of the evolution of the surface through the majority of Earth's history. I employ a forward modelling approach similar to that of the COPSE model (Bergman et al., 2004) but starting from Eoarchean conditions and using limited external forcings mainly focused on biosphere evolutionary transitions. The exchange of mass between the modelled atmosphere-ocean and geosphere reservoirs is described by fluxes in units of moles per year for the major elements I track (C, N, P, O, Fe, H) progressing the system of coupled ordinary differential equations (ODEs) through time into the preindustrial contemporary period. The entire model consists of 257 unique fluxes between 96 unique chemical reservoirs.

The *EONS* model has been designed to test scenarios of Earth's early evolution. The transition between the late Archean to Paleoproterozoic eons is marked by increasing atmospheric oxidation, evidenced by the disappearance of the MIF-S signal (Pavlov & Kasting, 2002). This transition directly preceeded and develops into the GOE, occurring around 2.3 billion years ago (Gumsley et al., 2017; Luo et al., 2016), during which atmospheric oxygen levels rapidly increased and the Earth's surface switched between low-oxygen to high-oxygen steady states (Goldblatt et al., 2006). The cause of the GOE is debated, with some authors arguing for it being primarily driven by chemical transitions (Catling et al., 2001; Holland, 2002) or the growth of continental bodies (Ciborowski & Kerr, 2016; Eguchi et al., 2020; Gaillard et al., 2011; Husson & Peters, 2017; Lee et al., 2016), among others. The *EONS* model nominal run presents a scenario by which the emergence of the biosphere and subsequent evolutionary developments can result in this oxygenation transition and produce the oxygen proxy record.

Several theories surround the nature of the GOE and what it meant for the biosphere. My model can help address several of these, including the question of whether nitrogen became a limiting nutrient and led to a productivity collapse (Fennel et al., 2005), or whether the transition from an anoxic to oxic biosphere led to a change in the burial fraction of organic carbon; geochemical evidence suggests organic carbon burial is nearly constant at about 0.2 total carbon burial throughout the geologic record (Hayes & Waldbauer, 2006; Schidlowski, 1988), though that interpretation is debated (Bjerrum & Canfield, 2004). The *EONS* model allows for nutrient-biosphere feedbacks across this transition, providing insight into the nitrogen system dynamics and organic carbon burial as they may have evolved across the GOE.

The GOE is associated with Paleoproterozoic snowball glaciation events (Hoffman, 2013; Kirschvink et al., 2000). The relationship between the GOE and these glaciations is unclear; some argue that the collapse of atmospheric methane greenhouse caused rapid climate cooling (Kopp, Kirschvink, Hilburn, & Nash, 2005), but in theory there are many ways to initiate snowball events (Goddéris et al., 2003; Mills, Watson, Goldblatt, Boyle, & Lenton, 2011). Because oxygen level can oscillate as a result of changing temperature (Garduño Ruíz, Goldblatt, & Ahm, 2022, 2023), it is unclear whether fluctuations in the MIF-S record result from glaciations producing rising O_2 or because rising O_2 produces glaciations. The *EONS* model is here used to test the theory of GOE-precipitated snowball glaciation, as well as glaciations caused by other means.

1.6 Modelling the Earth system

The *EONS* model described herein is a work of coalescence; it brings together the different fields of geology, chemistry, biology, and physics in order to better understand how the Earth operates.

The *EONS* model is interpretive. It contains many assumptions and simplifications of horrendously complex systems in order to work. It excludes many systems and species that may drastically affect these results if included. Each theory tested, equation used, and component included is just one of many options from the literature. Throughout the model description (chapter 2), I have outlined the logic behind each flux parameterization; why it was included, why it is significant, where the equations originate, and, in some instances, why I have opted not to use a more precise formulation. This type of model allows us to test a few selections of theories as to how systems work and interact; that one theory was used over another is not to suggest that said theory is taken as fact.

Where I have made simplifications, I have done so using a conservative interpretation of how that system behaves (i.e. using logistic functions for the expansion of the biosphere). For equations, I have opted to use similar functions as those employed by previous modellers since one goal is for this model to be easily comparable to others of its ilk. While I have compiled many systems into this model and endeavoured to make each one as dynamic and realistic as possible, the immense complexity of the Earth system compared to my comprehensive capabilities requires me to make some components as simple as possible for ease of interpretation. This is particularly true of my treatment of the biosphere and mantle, but is of course a blanket statement for all parts of this work. This model, as much as it includes, is inexorably incomplete. Its biases are my biases. It does and will always get some things wrong; the ultimate challenge of modelling systems is to try to get the least wrong answer possible, a low and yet very difficult bar.

The following work attempts to say something about how Earth systems may interact through time, and ultimately posits one possible way the Earth may have evolved. It allows us to glimpse into how the Earth operates, as a neurosurgeon may poke around in a patient's brain. While I can draw some interesting conclusions from this exercise, the truth is still very obscured.

1.7 Thesis structure

This thesis consists of five chapters, including this introduction. Chapter 2 details the components of my model: all included species and systems, the relationships and interactions in between reservoirs and species, and the structure of the equations which comprise the model itself. Chapter 3 reviews the outcome of a nominal run of the model: detailing how individual systems evolve through time in response to biological and geological forcings, how this reproduced evolution matches with the available geologic record, and why the intertwined Earth system evolves as it does. Chapter 4 presents a new example case use for this model: I aim to resolve Paleoproterozoic Snowball Earth glaciations using additional climate feedbacks, to better understand how surface chemistry and climate respond to punctuated changes in geologic and biologic systems. Chapter 5 concludes with a review of my key findings. Appendices contain key information regarding model constants, initial conditions, a summary of key stoichiometries, the treatment of chemical equilibria, and derivations of climate parameters.

Chapters 2 and 3 of this dissertation have been submitted as a single manuscript for publication to the AGU journal *Geochemistry, Geophysics, Geosystems*. The *EONS* model is available for download on GitHub:

https://github.com/juliahorne/EONS.git

Chapter 2

Model Description

This chapter contains a comprehensive description of the *EONS* model, and is organized into the following sections:

1. Conventions and notation
2. Reservoirs, species, and structure
3. Boundary forcings
4. Fluxes
    (a) Biosphere
    (b) Atmosphere-ocean chemistry
    (c) Geosphere
    (d) Mass movement
5. Climate
6. Initial conditions
7. Differential equations and implementation

2.1 Conventions and notation

My notation uses subscripts indicating x flux name, j for species, and i for reservoir. Fluxes are represented $F_{x,j,i}$ in units of mol/yr. Where stoichiometric constants vary, I specify a species for clarity (e.g. mol C/yr). Fluxes affecting only one or two species or occurring only in one reservoir drop the j and i terms.

Fluxes sensitive to environmental conditions or availability of reactants include half-saturation limitations, $L_{x,j,i}$, defined:

$$L_{x,j,i} = \frac{[j]_i}{[j]_i + k_{x,j}} \tag{2.1}$$

for half-saturation uptake values, $k_{\mathrm{x,j}}$ (table A.1).

Reservoirs are denoted by $R_{j,i}$ in units of mol. Reference sizes for reservoirs (typically modern) are denoted $R_{j,i,0}$ (table A.1).

Fractions, denoted by f_x or f_j, range between 0 and 1. The atmospheric fraction of certain species, particularly O_2 and CO_2, are measured in units of present atmospheric levels (PAL), defined by the model reservoir over the modern day reservoir:

$$f_j = \frac{R_{j,\mathrm{a}}}{R_{j,\mathrm{a},0}} \tag{2.2}$$

I do not use the f_j notation (i.e. f_{O_2}) to denote fugacity.

Multiples of modern day values (which may exceed 1) are χ_x, and are used to denote forcings in this model.

2.2 Reservoirs, species, and structure

The *EONS* model quantifies the transfer of carbon, nitrogen, oxygen, and phosphorus species between relevant biological and geological reservoirs on the Earth. The reservoirs are: (1) atmosphere, *a*; (2) surface ocean, *s*; (3) continental shelf (neritic) reactive sediments, *n*; (4) deep ocean, *d*; (5) pelagic reactive sediments, *z*; (6) unreactive abyssal sediments, *u*; (7) ocean crust, *o*; (8) continents, *c*; and (9) upper mantle, *m*.

Species are included in table 2.1. I assume that charged nutrient species (i.e. NO_3^- and PO_4^{3-}) are assimilated in association with protons by primary producers to maintain electro-neutrality within their cells following the "nutrient-H$^+$–compensation principle" as described by Wolf-Gladrow, Zeebe, Klaas, Körtzinger, and Dickson (2007).

Organic carbon, nitrogen, and phosphorus are contained within a single molecule in Redfield ratio (106:16:1; see section 2.4.1). I track these species in individual reservoirs as phosphate may vary from this ratio in sediments because of scavenging by decomposers in P-limited conditions (see section 2.5.6). Organic C, N, and P also experience different effects of volcanism and metamorphism (see sections 2.6.2.2 and 2.6.3), requiring more precise accounting in geologic boxes.

As with any conceptual model of Earth system evolution, numerous assumptions and simplifications have been made. I explain these wherever possible through this section. However, several underpinning assumptions are implicit in my judgement of what to include or exclude; realistic limitations on the scope of the first version of a new model mean that not every cycle, process, or record can be included. For example: I neglect the sulphur cycle, even though I know that to be important; I do not output carbon or nitrogen isotope records from the model, even though these would be a useful constraint; and most mantle processes and species are omitted. I include a very simple iron cycle that serves a singular purpose: introducing reductant power to the surface from the geosphere. I do not include fluxes that return oxidized iron to the mantle, nor made any attempt to resolve how the redox state of the upper mantle iron reservoir changes through time, because those questions are beyond the scope of this work. I anticipate that future versions of *EONS* will include more nuanced treatment of these systems and cycles.

2.2.1 Nitrogen and Carbon speciation

Reservoirs in the ocean boxes (*s* and *d*) as well as in the shelf and deep reactive sediments (*n* and *z*) for DIC (dissolved inorganic carbon), TA (total alkalinity), and RN (reduced nitrogen) are "aggregate" reservoirs, consisting of several species.

2.2.1.1 Reduced nitrogen (RN)

Reduced nitrogen includes ammonium and ammonia in equilibrium.

$$\mathrm{NH_4}^+ \rightleftharpoons \mathrm{NH_3} + \mathrm{H}^+ \tag{2.3}$$

2.2.1.2 Dissolved inorganic carbon (DIC)

The DIC reservoir includes carbon dioxide, bicarbonate, and carbonate in equilibrium:

$$[\mathrm{DIC}] = [\mathrm{CO_2}] + [\mathrm{HCO_3}^-] + [\mathrm{CO_3}^{2-}] \tag{2.4}$$

$$\mathrm{CO_2} + \mathrm{H_2O} \rightleftharpoons \mathrm{H}^+ + \mathrm{HCO_3}^- \rightleftharpoons 2\,\mathrm{H}^+ + \mathrm{CO_3}^{2-} \tag{2.5}$$

Table 2.1: Model species summary A list of all of the species within the *EONS* model, and the reservoir boxes which they inhabit. Reservoir boxes include atmosphere, *a*; surface ocean, *s*; continental shelf (neritic) reactive sediments, *n*; deep ocean, *d*; pelagic reactive sediments, *z*; unreactive abyssal sediments, *u*; ocean crust, *o*; continents, *c*; and upper mantle, *m*. Water reservoirs are included to maintain mass balance of O and H atoms during the model run, and are otherwise non-functional reservoirs in the model.

Species	**Stochiometry**	**Reservoirs**								
		a	**s**	**n**	**d**	**z**	**u**	**o**	**c**	**m**
ammonia, organic nitrogen (ON)	NH_3	✓	✓	✓	✓	✓	✓		✓	
ammonium	NH_4^+		✓	✓	✓	✓		✓	✓	✓
total reduced nitrogen (RN)	$NH_3 + NH_4^+$		✓	✓	✓	✓				
nitrate	HNO_3		✓	✓	✓	✓				
dinitrogen	N_2	✓	✓	✓	✓	✓				
carbon dioxide	CO_2	✓								
methane	CH_4	✓	✓	✓	✓	✓				
dissolved inorganic carbon (DIC)	$CO_2 + HCO_3^- + CO_3^{2-}$		✓	✓	✓	✓				
total alkalinity (TA)	(equation 2.6)		✓	✓	✓	✓				
calcium carbonate	$CaCO_3$		✓	✓	✓	✓	✓	✓	✓	✓
organic carbon (OC), living biomass (LB)	CH_2O		✓	✓	✓	✓	✓		✓	
phosphoric acid, organic phosphorus (OP)	H_3PO_4		✓	✓	✓	✓		✓		
carbonate- and silicate-bound phosphate (CP, SP)	H_3PO_4						✓		✓	✓
oxygen	O_2	✓	✓	✓	✓	✓				
ferrous iron	FeO		✓		✓					✓
fayalite olivine	Fe_2SiO_4								✓	✓
iron hydroxide	$Fe(OH)_3$		✓	✓	✓	✓	✓	✓	✓	
Fe(III)-phosphate	$FePO_4$		✓	✓	✓	✓				
hematite	Fe_2O_3								✓	
silicates	SiO_3								✓	✓
water	H_2O	✓	✓	✓	✓	✓				

2.2.1.3 Total alkalinity (TA)

Total alkalinity reservoirs track the net anion concentration of an ocean/sediment box. Given the species tracked in the model, I adapt the explicitly conservative definition of total alkalinity from Dickson (1981) to include ammonia:

$$[\mathrm{TA}] = [\mathrm{HCO_3}^-] + 2[\mathrm{CO_3}^{2-}] + [\mathrm{B(OH)_4}^-] + [\mathrm{OH}^-] + [\mathrm{NH_3}] - [\mathrm{H}^+] \tag{2.6}$$

In reality, phosphorus species are also included in the definition of alkalinity; as I only track one such species in this model (H_3PO_4), and since phosphorus species are relatively minor constituents in the total alkalinity balance in ocean waters, I ignore alkalinity effects from phosphorus reactions. All species, with the exception of $B(OH)_4{}^-$, are tracked with explicit aggregate reservoirs in the model; for total dissolved borate, I assume a constant oceanic concentration ($[B_T]_i$) according to box salinity, also constant (approximately 35‰; Zeebe & Wolf-Gladrow, 2001).

2.2.1.4 Equilibrium speciation

The concentration of any species at a given time depends on the pH of the reservoir. Concentrations of the three carbon species as well as the two nitrogen species are found according to concentrations of hydrogen and hydroxyl ions ($[H^+]$ and $[OH^-]$) in each ocean and sediment box i.

$$[\mathrm{OH}^-]_i = \frac{K_{W,i}}{[\mathrm{H}^+]_i} \tag{2.7}$$

$$[\mathrm{CO_2}]_i = \frac{[\mathrm{DIC}]_i}{\left(1 + \frac{K_{1,i}}{[\mathrm{H}^+]_i} + \frac{K_{1,i}K_{2,i}}{[\mathrm{H}^+]_i^2}\right)} \tag{2.8}$$

$$[\mathrm{CO_3}^{2-}]_i = \frac{[\mathrm{DIC}]_i}{\left(1 + \frac{[\mathrm{H}^+]_i}{K_{2,i}} + \frac{[\mathrm{H}^+]_i^2}{K_{1,i}K_{2,i}}\right)} \tag{2.9}$$

$$[\mathrm{HCO_3}^-]_i = \frac{[\mathrm{DIC}]_i}{\left(1 + \frac{[\mathrm{H}^+]_i}{K_{1,i}} + \frac{K_{2,i}}{[\mathrm{H}^+]_i}\right)} \tag{2.10}$$

$$[\mathrm{NH_3}]_i = \frac{[\mathrm{RN}]_i}{\left(1 + \frac{[\mathrm{H}^+]_i}{K_{N,i}}\right)} \tag{2.11}$$

$$[\mathrm{NH_4}^+]_i = \frac{[\mathrm{NH_3}]_i[\mathrm{H}^+]_i}{K_{N,i}} \tag{2.12}$$

This system is solved using a sixth-order polynomial equation for the single set of positive roots, resolving the hydrogen concentration of box i (see appendix B.1.2). This polynomial has been modified from the fifth-order polynomial equation of Zeebe and Wolf-Gladrow (2001) in order to include the effects of ammonia-ammonium equilibrium on total alkalinity. The acid dissociation constants for protonation, hydration, boric acid, ion water product, and ammonia (K_1, K_2, K_B ,K_W, and K_N, respectively) for these equations are functions of water salinity (S_i) and temperature (T_i; Zeebe & Wolf-Gladrow, 2001).

2.2.2 Model structure

The *EONS* model is schematically represented in figure 2.1. The modelled ocean system is split into 4 reservoirs: surface ocean, deep ocean, neritic (shelf) sediments, and pelagic sediments. The surface ocean includes the euphotic zone (100 m depth) above the deep ocean, as well as the ocean overlying the continental shelf. The mid-point pressure of the surface ocean box is set at 5 bars (a full depth 100 m), while the deep ocean reservoir has a pressure of 200 bars (full depth of 4 km). In the reactive sediments, pressure is assumed to be equivalent to the overlying ocean box (10 bars for n, 400 bars for z).

The most productive portion of the surface ocean covers the continental shelf. Although the shelf occupies a small, fixed fraction of the overall ocean surface area ($f_{\mathrm{Ashelf}} = 0.08$), it hosts an outsized portion of total surface ocean productivity ($f_{\mathrm{Pshelf}} = 0.3$; Yool & Fasham, 2001). Thus, the apportionment of biologically mediated particulate species (organic matter, $\mathrm{CaCO_3}$, and $\mathrm{Fe(OH)_3}$) sinking out of the surface ocean into the shelf sediments or to deep ocean is controlled by this productivity fraction (see figure 2.2).

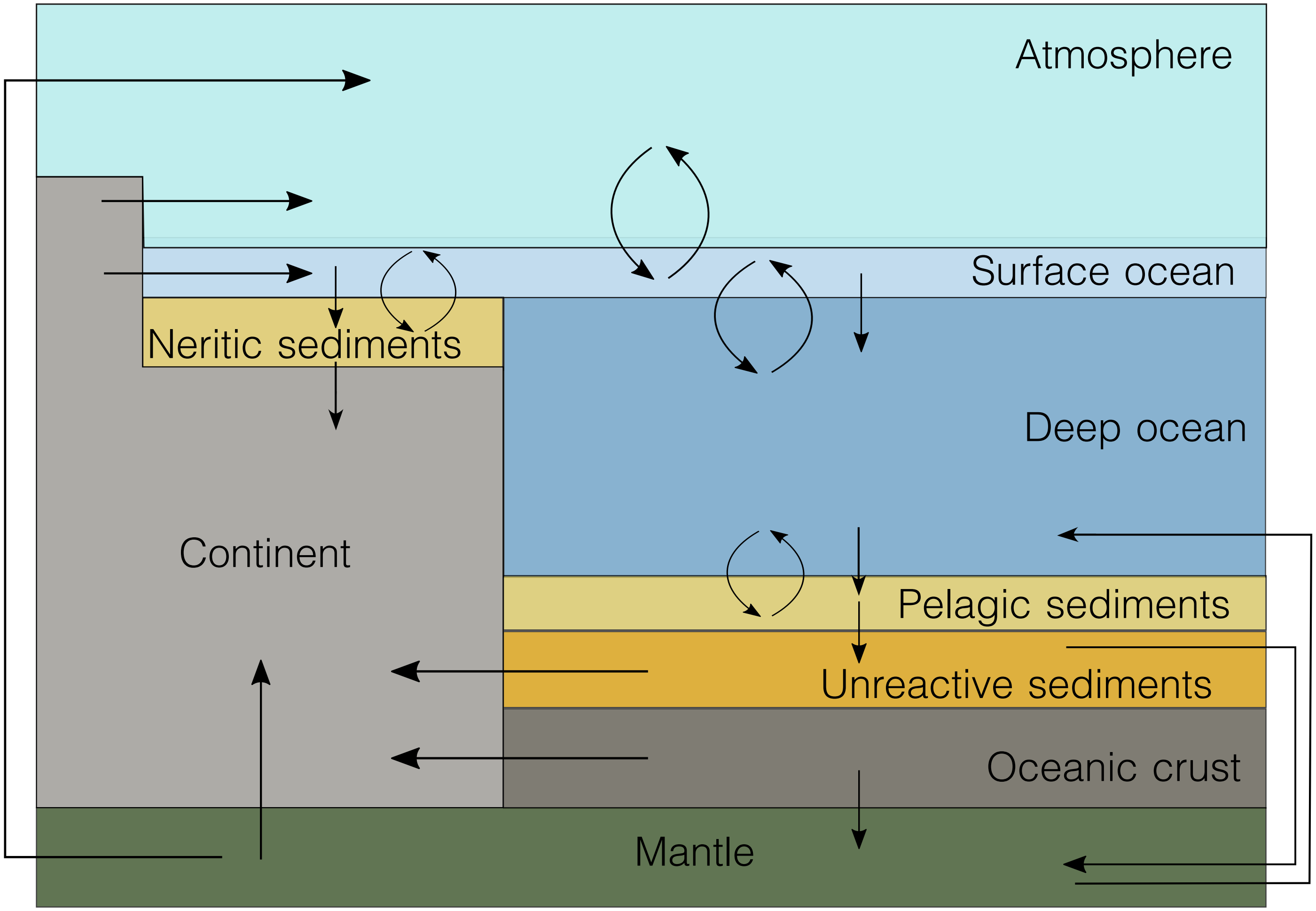

Figure 2.1: Model schematic Schematic representation of the *EONS* model structure. Arrows denote direct reservoir interaction via fluxes.

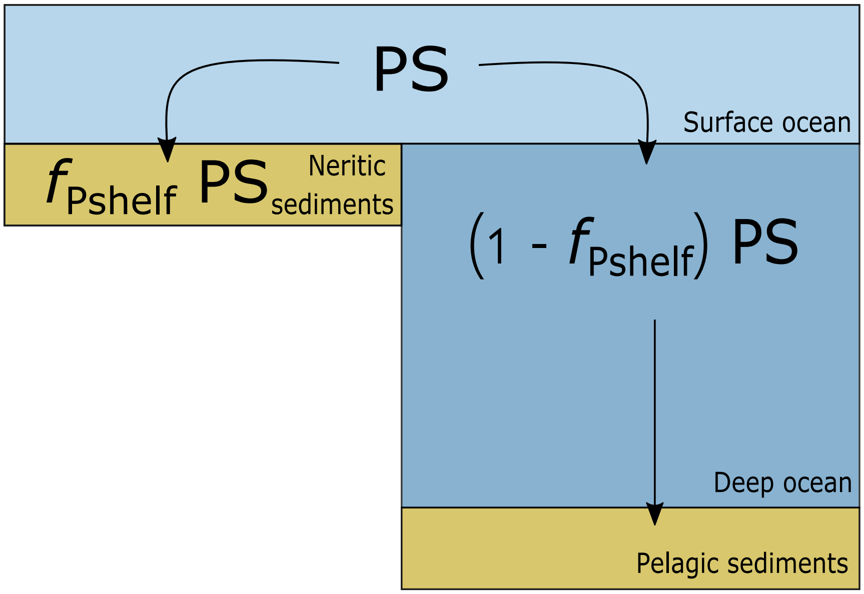

Figure 2.2: Shelf schematic Schematic representation of how export and sedimentation of particulate species *PS* (organic matter, $CaCO_3$, or $Fe(OH)_3$) is apportioned using the f_{PShelf} fraction.

2.3 Boundary Forcings

The *EONS* model evolves according to several time-dependent, imposed boundary forcings. These include mantle reductant (treated as FeO) outflux, continental erosion (emergence), solar flux, the evolution of oxygenic photosynthesis, the evolution of fungi, the emergence of large bodied organisms, and colonization of continents by plants. All time-dependent forcings are included figure 2.3. In the following subsections, t denotes model time in units of years; in terms of my forward modelling approach, $t = 0$ at the start of the Archean (4 Ga) and $t = 4 \times 10^9$ at the modern era (0 Ga).

2.3.1 Mantle reductant outflux

The flux of reducing species from the Hadean mantle was likely higher than at present, due to increased heat and faster convection (Blichert-Toft & Albarede, 1994; Sleep & Zahnle, 2001). Reduced iron enters the deep ocean at hydrothermal vents at a rate constrained by modern day mantle outgassing estimates ($F_{\mathrm{mantle,Fe,0}} = 3 \times 10^{11}$ mol Fe/yr; Holland, 2002). I impose a linear change in this forcing, decreasing from several times this value in the Archean (χ_{mantle}, see table A.1):

$$F_{\text{mantle,FeO}} = F_{\text{mantle,Fe,0}} \left(\chi_{\text{mantle}} + \frac{(1 - \chi_{\text{mantle}})t}{4 \times 10^9} \right) \tag{2.13}$$

2.3.2 Continental erosion

Over time, sediments sourced from continental erosion will accumulate in the deep ocean and cut off lower sediment layers from interacting with the water column; ergo, faster influx of sediments (higher erosion) results in shorter residence in the uppermost "reactive" layer. Sediment burial timescale affects the fraction of organic matter buried (and net oxygen production) as sedimentary burial competes with remineralization, making erosion an important factor to include in this model. Evidence indicates that erosional rates were lower in the Archean and increased to near modern rates with uplift by around 3 Ga (Reimink et al., 2021), and erosion is generally understood as a non-linear function of continental topography (Montgomery & Brandon, 2002). I relate erosion to continental emergence (the size of the continental silicate reservoir relative to modern) rather than topography, which I do not resolve:

$$\chi_{\text{eros}}(t) = \left(\frac{R_{\text{c,SiO3}}(t)}{R_{\text{c,SiO3,0}}} \right)^{-\frac{3}{2}} \tag{2.14}$$

2.3.3 Solar flux

Solar luminosity has increased from approximately 70% modern in the early Hadean at the initiation of nuclear fusion, a result of increasing solar core mass (Feulner, 2012; Gough, 1981; Sagan & Mullen, 1972). I approximate a quasi-linear function for solar flux through time with respect to modern value (S_0; see table A.1). The change in solar flux is formulated following Gough (1981) based on years from the present:

$$S = \left(1 - \frac{0.38(t - 4 \times 10^9)}{4.55 \times 10^9} \right)^{-1} S_0 \tag{2.15}$$

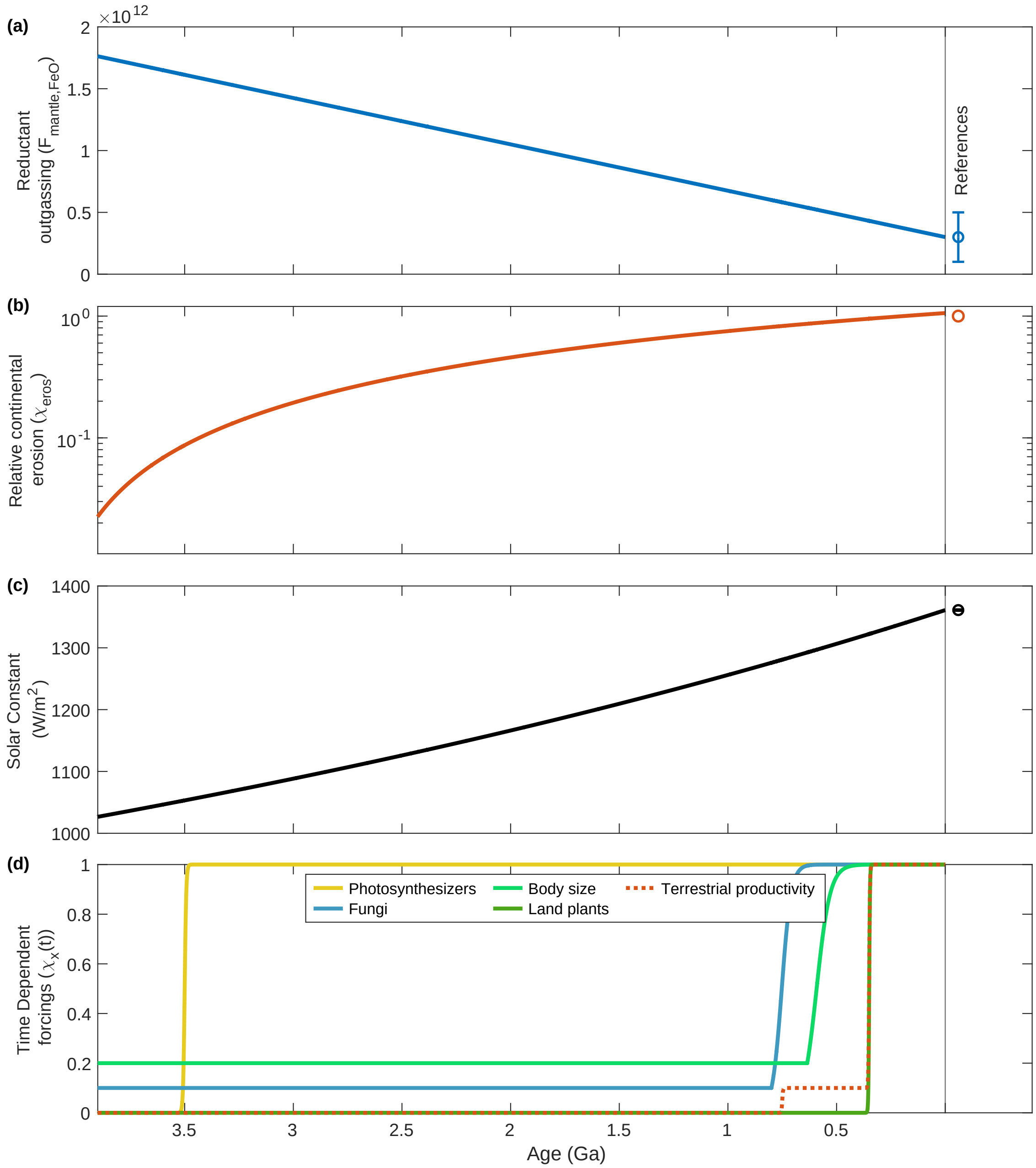

Figure 2.3: All model forcings a Mantle reductant outgassing flux ($F_{\text{mantle,FeO}}$), prescribed to linearly decrease through time in equation 2.13; **b** relative continental erosion rate, a function of continental size (equation 2.14); **c** the quasi-linear increasing solar flux function $S(t)$ in equation 2.15; **d** time-dependent biological transitions described in equations 2.16, 2.17, 2.18, 2.19, and 2.20. Modern estimates for reservoirs and fluxes are denoted as dots at the far right of each plot, with range estimates as vertical bars; the solid vertical line denotes the end of model output.

2.3.4 Timed evolution of Photosynthesis

Model runs begin with no operational oxygenic photosynthesis, which I assume evolves sometime in the Archean; estimates range from 3.8 Ga to 2.5 Ga (Crowe et al., 2013; Lyons, Reinhard, & Planavsky, 2014; Olson, 2006; Saito, Sigman, & Morel, 2003). Primary production in the biosphere via photo-ferrotrophy (section 2.4.1.2) prevails until the end of the Eoarchean (3.6 Ga), when oxygenic photosynthesis develops and rapidly becomes dominant. I force this flux to gradually increase over a few million years along a sigmoidal growth curve for global productivity by photosynthesizers with respect to the modern day, evolving from near zero to 1:

$$\chi_{\text{photo}}(t) = \begin{cases} 0 & t < 4 \times 10^8 \\ \dfrac{1}{1 + 10^{12} \exp\big(-\epsilon_{\text{photo}}(t - 4 \times 10^8)\big)} & t \geqslant 4 \times 10^8 \end{cases} \tag{2.16}$$

where the slope of the curve, ϵ_{photo}, is given in table A.1.

2.3.5 Timed evolution of fungi

Fungi, lichens, and plants selectively dissolve inorganic phosphate when it is depleted in soils or sorbed onto oxides, silicates, and calcium compounds (Lambers, 2022). The expansion of fungi after 800 Ma (3.2×10^9 years in model time; Heckman et al., 2001, Lucking et al., 2009) is approximated by a productivity growth curve:

$$\chi_{\text{fungi}}(t) = \begin{cases} \dfrac{1}{10} & t < 3.2 \times 10^9 \\ \dfrac{1}{\Big(1 + 9 \exp\big(-\epsilon_{\text{fungi}}(t - 3.2 \times 10^9)\big)\Big)} & t \geqslant 3.2 \times 10^9 \end{cases} \tag{2.17}$$

where the slope of the curve, ϵ_{fungi}, is given in table A.1. Prior to the evolution of fungi, inorganic phosphorus weathering is 10 times slower than its modern rate. After the forced 50 million year expansion of fungi, these fluxes operate on a typical silicate or carbonate weathering timescale.

2.3.6 Timed evolution of large-bodied organisms

I correlate faster sinking rates with the evolution of large organisms in the Ediacaran (circa 635 Ma, approximately 3.36×10^9 years in model time) and assume that smaller Precambrian organisms sank at one fifth the rate of modern primary producers.

$$\chi_{\text{sink}}(t) = \begin{cases} \dfrac{1}{5} & t < 3.36 \times 10^9 \\ \dfrac{1}{\Big(1 + 4\exp\big(-\epsilon_{\text{photo}}(t - 3.36 \times 10^9)\big)\Big)} & t \geqslant 3.36 \times 10^9 \end{cases} \tag{2.18}$$

The growth slow (ϵ_{photo}; see equation 2.16) is provided in table A.1.

2.3.7 Timed evolution of land plants

Vascular land plants enhance continental weathering in the breakdown of bedrock by root systems (Hoffland et al., 2004; Porder, 2019). This enhancement effects the silicate and carbonate weathering modifiers (section 2.6.4.1), and is formulated as a sigmoidal productivity expansion occurring at 400 Ma (approximately 3.6×10^9 years in model time). This curve is treated similarly to the rise of photosynthesizer populations:

$$\chi_{\text{plants}}(t) = \begin{cases} 0 & t < 3.6 \times 10^9 \\ \dfrac{1}{1 + 10^{12}\exp\big(-\epsilon_{\text{plant}}(t - 3.6 \times 10^9)\big)} & t \geqslant 3.6 \times 10^9 \end{cases} \tag{2.19}$$

where the slope of the curve, ϵ_{plant}, is given in table A.1. Prior to the evolution of land plants, weathering is not enhanced and has a weaker response to elevated atmospheric CO_2. After colonization in the Silurian period (443 Ma), all silicate and carbonate weathering fluxes are enhanced by a factor of 2 (Ibarra et al., 2019).

2.3.8 Timed evolution of the terrestrial biosphere

The modern terrestrial biosphere contributes approximately 50% of the global net primary productivity (Ciais et al., 2014). I represent the terrestrial biosphere as a fixed modern organic carbon burial flux that increases with two steps, the evolution of fungi and colonization of landmasses by plants, at approximately 700 Ma and

400 Ma respectively. I assume fungal evolution constitutes a 10% modern terrestrial biosphere, and land plants increase terrestrial productivity from that point to the modern level ($F_{\mathrm{terrprod},0} = 1 \times 10^{13}$ mol C/yr; Berner, 2009, Lenton et al., 2018). The fraction of modern terrestrial productivity is therefore a function of these other two forcings:

$$\chi_{\mathrm{terr}}(t) = \begin{cases} 0 & t < 3.2 \times 10^9 \\ \frac{1}{10}\chi_{\mathrm{fungi}} & 3.2 \times 10^9 \leqslant t < 3.6 \times 10^9 \\ \frac{1}{10}\chi_{\mathrm{fungi}} + \frac{9}{10}\chi_{\mathrm{plant}} & t \geqslant 3.6 \times 10^9 \end{cases} \tag{2.20}$$

The prescribed terrestrial biosphere flux is treated (in mol C/yr):

$$F_{\mathrm{terrprod}} = F_{\mathrm{terrprod},0} f_{\mathrm{CO_2}}^{\eta_{\mathrm{w}}} \chi_{\mathrm{terr}}(t) \tag{2.21}$$

where $f_{\mathrm{CO_2}}$ is the atmospheric level of CO_2 with respect to the modern day (PAL; see section 2.1) and the exponent η_{w} describes the CO_2 power-law relationship for physical weathering by vascular plants (see section 2.6.4.1). This limitation ensures terrestrial productivity decreases as CO_2 (and thus temperature) decreases. I assume 10% of the buried carbon is converted to methane in decomposition. Unlike productivity in the ocean, land productivity here is not considered to be nutrient limited, and the stoichiometry is assumed to be that of net productivity (i.e. the combined steps of photosynthesis and organic matter remineralization). Burial of terrestrial organic carbon is only a sink for CO_2, and does not affect continental reservoirs for N or P species.

2.4 Fluxes: Biosphere

2.4.1 Primary productivity

Organic matter (OM) in the ocean/sediment boxes is housed in two reservoirs: living biomass (LB) and dead biomass, or particulate organic carbon (OC). Primary produces utilize CO_2, NH_3, HNO_3, and H_3PO_4 to generate OM and byproducts, such as O_2, and exist only in the surface ocean. I assign OM and remineralization stoichiometry according to Redfield, Ketchum, and Richards (1963):

$$\begin{aligned} \mathrm{OM} &= (\mathrm{CH_2O})_{106}\,(\mathrm{NH_3})_{16}\,(\mathrm{H_3PO_4}) \\ &= \mathrm{C_{106}\,H_{263}\,O_{110}\,N_{16}\,P} \end{aligned} \tag{2.22}$$

More recent measurements of organic matter stoichiometry deviate from this older ratio, particularly with respect to oxygen and hydrogen content (Anderson & Sarmiento, 1994); I use this stoichiometry because it is still commonly used in biogeochemical modelling.

There are two pathways for primary production in the model: oxygenic and anoxygenic (photo-ferrotrophic) photosynthesis. The latter is confined to anoxic surface ocean conditions and thus only relevant for early Earth conditions (Crowe et al., 2008).

All biological production fluxes are limited by dimensionless nutrient sensitivities, defined by fixed nitrogen, phosphate, and carbon surface ocean concentrations and half-saturation uptake values for their assimilation ($k_{j,\mathrm{assim}}$; table A.1). Surface ocean fixed nitrogen (all "bioavailable nitrogen", reduced and oxidized; $R_{\mathrm{fixN}} = R_{\mathrm{HNO3,s}} + R_{\mathrm{RN,s}}$) and H_3PO_4 define a Redfield ratio sensitivity parameter:

$$L_{\mathrm{Redf}} = \frac{R_{\mathrm{fixN,s}}/R_{\mathrm{H3PO4,s}}}{R_{\mathrm{fixN,s}}/R_{\mathrm{H3PO4,s}} + k_{\mathrm{assim,NP}}} \tag{2.23}$$

where $R_{\mathrm{H3PO4,s}}$ is the surface ocean reservoir of phosphate, and $k_{\mathrm{assim,NP}}$ is a dimensionless half-saturation constant for the Redfield sensitivity, modified from the treatment used by Johnson & Goldblatt, 2018.

2.4.1.1 Oxygenic Photosynthesis

Nitrogen, carbon, and phosphate are incorporated into living biomass via photosynthetic biological assimilation, producing OM and oxygen. The stoichiometry of this assimilation flux depends on the source of nitrogen. When HNO_3 is used:

$$106\,\mathrm{CO_2} + 16\,\mathrm{HNO_3} + \mathrm{H_3PO_4} + 122\,\mathrm{H_2O} \xrightarrow{h\nu} (\mathrm{CH_2O})_{106}\,(\mathrm{NH_3})_{16}\,(\mathrm{H_3PO_4}) + 138\,\mathrm{O_2} \tag{2.24}$$

and when NH_3 is used:

$$106\,CO_2 + 16\,NH_3 + H_3PO_4 + 106\,H_2O \xrightarrow{h\nu} (CH_2O)_{106}\,(NH_3)_{16}\,(H_3PO_4) + 106\,O_2 \tag{2.25}$$

Phosphate is a limiting nutrient in the ocean. Therefore, the process of photosynthetic assimilation depends foremost on the surface reservoir of H_3PO_4:

$$F_{\text{assim}} = \frac{R_{\text{H3PO4,s}}}{\tau_{\text{assim}}} L_{\text{assim,DIC}} L_{\text{Redf}} \mathrm{r}_{\frac{C}{P}} \chi_{\text{photo}}(t) \tag{2.26}$$

where $\mathrm{r}_{\frac{C}{P}}$ is the Redfield ratio of carbon to phosphate (106:1), converting this flux to units of mol C/yr. Photosynthesis evolves after 3.6 Ga according to the population growth curve $\chi_{\text{photo}}(t)$; before this time, the term $\chi_{\text{photo}}(t) = 0$.

2.4.1.2 Photoferrotrophy

In anoxic surface waters, ferrous iron (Fe(II)) can be oxidized by iron-oxidizing bacteria. This is considered a possible source of the iron oxides (here simplified to iron hydroxide, $Fe(OH)_3$) which comprise the Archean BIFs, and may have been a significant component of early marine primary productivity (Crowe et al., 2008; Kendall, Anbar, Kappler, & Konhauser, 2012). This is also a pathway for transference of reducing power from iron to organic carbon, which can then be oxidized and recycled by biological systems.

$$\begin{gathered} 4\,FeO + CO_2 + \tfrac{16}{106}NH_3 + \tfrac{1}{106}H_3PO_4 + 11\,H_2O \\ \xrightarrow{h\nu} \\ 4\,Fe(OH)_3 + \tfrac{1}{106}(CH_2O)_{106}(NH_3)_{16}(H_3PO_4) + 5\,H_2O \end{gathered} \tag{2.27}$$

Photoferrotrophic production takes the form:

$$F_{\text{ferrotrophy}} = \frac{R_{\text{FeO,s}}}{\tau_{\text{assim}}} L_{\text{assim,DIC}} L_{\text{assim,fixN}} L_{\text{assim,H3PO4}} (1 - L_{\text{anox,O2,}s}) \tag{2.28}$$

This pathway requires anoxic conditions, and so has additional sensitivities to the degree of anoxicity of the reservoir ($L_{\text{anox,O2,}s}$), defined by the upper limit for dissolved oxygen concentration in an anoxic zone ($[O_2] < 6.2 \times 10^{-3}$ mol/m^3; Crowe et al., 2008) and availability of reduced fixed nitrogen ($L_{\text{assim,fixN}}$).

2.4.1.3 Nitrogen Fixation

Atmospheric nitrogen is made available for biological incorporation via nitrogen fixation when biologically utilizable reduced nitrogen (NH_3) is depleted. I parameterize nitrogen fixation by oxygenic photosynthesizers (cyanobacteria) as:

$$N_2 + 3\,H_2O \longrightarrow 2\,NH_3 + \tfrac{3}{2}O_2 \tag{2.29}$$

Newly fixed ammonia produced in this reaction is assumed to be immediately assimilated into biomass, via either photosynthetic assimilation pathway (equations 2.25 or 2.27). The two-step process of fixation and assimilation yields a net reaction sequence:

$$106\,CO_2 + 8\,N_2 + H_3PO_4 + 130\,H_2O \longrightarrow (CH_2O)_{106}(NH_3)_{16}(H_3PO_4) + 118\,O_2 \tag{2.30}$$

Photosynthetic fixation depends on the surface ocean reservoir of phosphate, DIC, and N_2, and is inversely proportional to surface ocean N:P ratio. In units of mol N/yr:

$$F_{\text{fix,newN}} = \frac{R_{\text{H3PO4,s}}}{\tau_{\text{fix}}} L_{\text{assim,DIC}} L_{\text{fix,N2}} (1 - L_{\text{Redf}}) \chi_{\text{photo}}(t) \mathrm{r}_{\frac{N}{P}} \tag{2.31}$$

where $\mathrm{r}_{\frac{N}{P}}$ is the Redfield ratio of nitrogen to phosphorus uptake (16:1), τ_{fix} is the timescale for nitrogen fixation (estimated to be approximately 5 times longer than assimilation; Fennel et al., 2005). Uptake (or release) of other species (j = CO_2, H_3PO_4, O_2 and H_2O) associated with assimilation of newly fixed N is:

$$F_{\text{fix,j}} = F_{\text{fix,newN}} \mathrm{r}_{\left(\frac{j}{\text{newN}}\right)} \tag{2.32}$$

Where $\mathrm{r}_{\left(\frac{j}{\text{newN}}\right)}$ is the ratio of the other species to the moles of assimilated new NH_3 (table A.1).

Prior to the evolution of oxygenic photosynthesis, nitrogen fixation (equation 2.29) occurs simultaneously with photoferrotrophy (equation 2.27) using excess iron:

$$\begin{gathered} 472\,FeO + 106\,CO_2 + 8\,N_2 + H_3PO_4 + 1322\,H_2O \\ \xrightarrow{h\nu} \\ 472\,Fe(OH)_3 + (CH_2O)_{106}(NH_3)_{16}(H_3PO_4) + 484\,H_2O \end{gathered} \tag{2.33}$$

Anoxygenic fixation is measured in mols Fe/yr, and formulated:

$$F_{\text{fixation,FeO}} = \frac{R_{\text{FeO,s}}}{\tau_{\text{fix}}} L_{\text{assim,DIC}} L_{\text{assim,H3PO4}} L_{\text{fix,N2}} (1 - L_{\text{Redf}})(1 - \chi_{\text{photo}}(t)) \tag{2.34}$$

The uptake of other species ($j = \mathrm{N_2}, \mathrm{CO_2}, \mathrm{H_3PO_4}$, and $\mathrm{H_2O}$) in this reduction process is treated:

$$F_{\text{fixation,j}} = F_{\text{fixation,FeO}} \mathrm{r}_{\frac{j}{\text{FeO}}} \tag{2.35}$$

where $\mathrm{r}_{\frac{j}{\text{FeO}}}$ is the ratio of the other species to the moles of iron (table A.1).

2.4.2 Nitrification

Nitrifiers use O_2 to convert NH_4^+ into HNO_3 (Gruber, 2008).

$$\begin{array}{l} \mathrm{NH_4{}^+ + \tfrac{3}{2}O_2 \longrightarrow NO_2{}^- + 2\,H^+ + H_2O} \\ \mathrm{NO_2{}^- + \tfrac{1}{2}O_2 \longrightarrow NO_3{}^-} \\ \hline \mathrm{NH_4{}^+ + 2\,O_2 \longrightarrow HNO_3 + H^+ + H_2O} \end{array} \tag{2.36}$$

Nitrification cannot occur in acidic conditions ($\mathrm{pH} \leqslant 6$) and full nitrification requires an environmental pH of 7.2 (Hiatt & Grady, 2008). Thus, the nitrification flux depends on $[O_2]$, $[H^+]$, and $[NH_4{}^+]$ within a given ocean or reactive sediment box i (s, d, n, or z):

$$F_{\text{nit},i} = \frac{[\mathrm{NH_4{}^+}]_i M_{\text{oc},i}}{\tau_{\text{nit}}} L_{\text{nit,O2},i} (1 - L_{\text{nit,H},i}) \tag{2.37}$$

where $M_{\text{oc},i}$ is the mass of water in reservoir i (kg), and τ_{nit} is the timescale in years for nitrification (table A.1).

2.4.3 Death of living biomass

Organic matter is transferred to the particulate organic carbon reservoir when it dies.

$$F_{\text{death}} = \frac{R_{\text{LB}}}{\tau_{\text{death}}} \tag{2.38}$$

Biomass living and dead is tracked in units of moles of carbon.

2.4.4 Organic matter remineralization

Remineralization, or respiration, occurs in every ocean and sediment box containing OM (i = s, d, n, or z). This transformation follows either aerobic or anaerobic pathways depending on oxygen availability; these include ammonification, denitrification, and methanogenesis.

2.4.4.1 Aerobic Remineralization: Ammonification

In aerobic remineralization, particulate organic carbon is oxidized by dissolved O_2 and returned to its nutrient components in Redfield ratio (Froelich et al., 1979), a reversal of oxygenic photosynthesis (equation 2.25):

$$(\mathrm{CH_2O})_{106}\,(\mathrm{NH_3})_{16}\,(\mathrm{H_3PO_4}) + 106\,\mathrm{O_2} \longrightarrow 106\,\mathrm{CO_2} + 16\,\mathrm{NH_3} + \mathrm{H_3PO_4} + 106\,\mathrm{H_2O} \tag{2.39}$$

Aerobic remineralization occurs when the ocean or sediment box i is sufficiently oxygenated, taking the form (in mol C/yr):

$$F_{\mathrm{ammon},i} = \frac{R_{\mathrm{OC},i}}{\tau_{\mathrm{oxrm},i}} L_{\mathrm{ammon,O2},i} \tag{2.40}$$

where $\tau_{\mathrm{oxrm},i}$ denotes the timescale for aerobic remineralization (table A.1). In oxygenated waters, this remineralization pathway (ammonification) will dominate over the anaerobic pathways.

2.4.4.2 Anaerobic Remineralization: Denitrification and Methanogenesis

In the case of ocean anoxia, remineralization proceeds anaerobically along two different pathways. When it is available, nitrate is used by heterotrophic denitrifiers to oxidize organic matter (Berman-Frank et al., 2008; Froelich et al., 1979):

$$\begin{gathered}(\mathrm{CH_2O})_{106}\,(\mathrm{NH_3})_{16}(\mathrm{H_3PO_4}) + \tfrac{424}{5}\mathrm{HNO_3}\\ \longrightarrow \\ 106\,\mathrm{CO_2} + \tfrac{212}{5}\mathrm{N_2} + 16\mathrm{NH_3} + \mathrm{H_3PO_4} + \tfrac{742}{5}\mathrm{H_2O}\end{gathered} \tag{2.41}$$

In the case that nitrate is not readily available, anaerobic remineralization is by methanogenesis:

$$(CH_2O)_{106}\,(NH_3)_{16}\,(H_3PO_4) \longrightarrow 53\,CO_2 + 53\,CH_4 + 16\,NH_3 + H_3PO_4 \tag{2.42}$$

Both anaerobic remineralization fluxes return nutrients to the water column in similar fashion as aerobic remineralization, except that they occur over longer timescales ($\tau_{\mathrm{oxrm},i} < \tau_{\mathrm{axrm},i}$) approximating reduced energetic yield.
My model quantifies the denitrification flux in an ocean/sediment box i (in mol C/yr):

$$F_{\mathrm{denit},i} = \frac{R_{\mathrm{OC},i}}{\tau_{\mathrm{axrm},i}}\left(1 - L_{\mathrm{ammon,O2},i}\right)L_{\mathrm{denit,HNO3},i} \tag{2.43}$$

The uptake ratio for denitrification (r_{denit}), in terms of mol HNO_3 per mol OC, is 84.8:106.

The model quantifies the methanogenesis flux (in mol C/yr) for box i:

$$F_{\mathrm{methgen},i} = \frac{R_{\mathrm{OC},i}}{\tau_{\mathrm{axrm},i}}\left(1 - L_{\mathrm{ammon,O2},i}\right)\left(1 - L_{\mathrm{denit,HNO3},i}\right) \tag{2.44}$$

2.4.5 Methanotrophy

Methane is oxidized in ocean or sediment boxes by methanotrophs, converting it to CO_2 (Goldblatt et al., 2006):

$$CH_4 + 2\,O_2 \longrightarrow CO_2 + 2\,H_2O \tag{2.45}$$

Methanotrophy is limited by the reservoir of CH_4 and dissolved oxygen in a box i (s, d, n, or z):

$$F_{\mathrm{mtrophy},i} = \frac{R_{\mathrm{CH4},i}}{\tau_{\mathrm{mtrophy}}}L_{\mathrm{mtrophy,O2},i} \tag{2.46}$$

2.5 Fluxes: Atmosphere-ocean chemistry

2.5.1 Ammonia photo-oxidation and photolysis

Ammonia is irreversibly destroyed by high-energy UV radiation in the atmosphere, generating N^{3-} and H^+:

$$\begin{aligned} NH_3 &\xrightarrow{h\nu} NH_2{}^- + H^+ \\ NH_2{}^- &\xrightarrow{h\nu} NH^{2-} + H^+ \\ NH^{2-} &\xrightarrow{h\nu} N^{3-} + H^+ \end{aligned} \tag{2.47}$$

When oxygen is available, the produced hydrogen ions will react to generate water, with a net reaction:

$$2\,NH_3 + \frac{3}{2}O_2 \xrightarrow{6h\nu} N_2 + 3\,H_2O \tag{2.48}$$

I parameterize ammonia photo-oxidation:

$$F_{\text{ammox}} = \frac{R_{\text{NH3,a}}}{\tau_{\text{ammox}}(O_2)} \tag{2.49}$$

Photo-oxidation timescale ($\tau_{\text{ammox}}(O_2)$) is a function of oxygen level, such that the lifetime of NH_3 is extended in anoxic conditions:

$$\tau_{\text{ammox}}(O_2) = \tau_{\text{ammox,0}}\frac{R_{\text{O2,a}}}{n_{\text{a}}} \tag{2.50}$$

Under anoxic conditions, I treat the stoichiometry of ammonia photodissociation (photolysis) as:

$$8\,NH_3 + 3\,CO_2 \xrightarrow{12h\nu} 4\,N_2 + 3\,CH_4 + 6\,H_2O \tag{2.51}$$

Ammonia photolysis is treated similarly to photo-oxidation, but without the sensitivity to oxygen and over a longer timescale:

$$F_{\text{pholys}} = \frac{R_{\text{NH3,a}}}{\tau_{\text{pholys}}} \tag{2.52}$$

2.5.2 Methane Photo-oxidation

Methane is photo-oxidised through a variety of pathways (Claire et al., 2006; Garduño Ruíz et al., 2023; Pavlov, Brown, & Kasting, 2001), with a net stoichiometry of:

$$CH_4 + 2\,O_2 \xrightarrow{4h\nu} CO_2 + 2\,H_2O \tag{2.53}$$

This reaction is slowed by orders of magnitude once an ozone layer provides photochemical shielding (Claire et al., 2006; Garduño Ruíz et al., 2023; Goldblatt et al., 2006; Gregory, Claire, & Rugheimer, 2021). I parametrise this as:

$$F_{\text{methox}} = K_{\text{eff}}([CH_4][O_2])^{\frac{1}{2}} \tag{2.54}$$

The effective rate constant (K_{eff}) is fitted to model results from Garduño Ruíz et al. (2023) and is a product of CH_4 and O_2 atmospheric mixing ratios:

$$K_{\text{eff}} = 3 \times 10^{20} \left(4 \times 10^{3\left(\frac{-[O2]}{[O2]+10^{-4}}\right)^{\frac{2}{5}}} \right) \tag{2.55}$$

K_{eff} has units of mol O_2 yr^{-1}. This new parametrisation is recommended over that used in Goldblatt et al. (2006) as it avoids a polynomial fit, which performed poorly outside of the fitted range.

2.5.3 Hydrogen Escape

My model considers mildly reducing to oxidising atmospheres, in which hydrogen-bearing species are minor atmospheric constituents. Hydrogen escape is therefore diffusion limited, and depends on the total hydrogen mixing ratio at the homopause (Hunten, 1973). I consider hydrogen escape to derive only from non-condensible species, CH_4 and NH_3, with stoichiometry:

$$\begin{array}{c} CH_4 \xrightarrow{4h\nu} C + 4\,H\uparrow \\ C + H_2O \longrightarrow \frac{1}{2}\,CO_2 + \frac{1}{2}\,CH_4 \\ \hline CH_4 + H_2O \xrightarrow{4h\nu} \frac{1}{2}CO_2 + \frac{1}{2}CH_4 + 4\,H\uparrow \end{array} \tag{2.56}$$

and

$$\begin{array}{c} NH_3 \xrightarrow{3h\nu} N + 3\,H\uparrow \\ 2\,N \longrightarrow N_2 \\ \hline 2\,NH_3 \xrightarrow{6h\nu} N_2 + 6\,H\uparrow \end{array} \tag{2.57}$$

These species are well-mixed, so the mixing ratio at the homopause is the general mixing ratio and hydrogen escape can be treated for gas j (in units of mol N/yr or mol C/yr, for NH_3 and CH_4 respectively):

$$F_{\mathrm{Hesc},j} = k_{\mathrm{Hesc}}[j]\tfrac{1}{\mathrm{H}_j} \tag{2.58}$$

where H_j is the number of H molecules per mole of gas j (i.e. $\mathrm{H}_{\mathrm{NH3}} = 3$) and k_{Hesc} is the average diffusion constant for H (in mol H/yr):

$$k_{\mathrm{Hesc}} = \frac{(5 \times 10^{13}\ \text{molecules cm}^{-2}\ \text{s}^{-1})(3.15 \times 10^{7}\ \text{s yr}^{-1})(100^{2}A_E)}{N_{\mathrm{Av}}} \tag{2.59}$$

where A_E is the surface area of Earth (m^2) and N_{Av} is Avogadro's constant (6.02×10^{23} molecules mol^{-1}). See table A.1 for the value of k_{Hesc}.

I do not consider hydrogen escape derived from water, as in temperate atmospheres water is cold-trapped at the tropopause, so the homopause mixing ratio will be negligible. If the climatology of the model was expanded to consider hot and moist atmospheres, then a term for water-derived hydrogen escape would need to be added.

2.5.4 Calcium Carbonate Precipitation and Dissolution

Calcium carbonate ($CaCO_3$) is precipitated when an ocean reservoir is oversaturated with respect to the carbonate ion (${CO_3}^{2-}$) and dissolves when undersaturated. In modern oceans this process is mediated by biology; abiotic precipitation requires much higher carbonate saturation, whereas organisms are capable of altering their internal fluid chemistries to precipitate at much lower ambient [${CO_3}^{2-}$]. In order to keep the link between the biosphere and inorganic carbon cycle as simple as possible, I have opted to assume modern biotic carbonate saturation requirements while not explicitly linking biotic precipitation to productivity in this model version. In the future, an additional forcing to carbonate saturation state could be added to shift from purely abiotic to biotic carbonate precipitation in addition to altering ocean [Ca^{2+}] to resolve a more comprehensive evolution for the marine carbonate system.

$$\mathrm{Ca}^{2+} + 2\,\mathrm{HCO_3}^{-} \underset{\Omega<1}{\overset{\Omega\geqslant 1}{\rightleftharpoons}} \mathrm{CaCO_3} + \mathrm{CO_2} + \mathrm{H_2O} \tag{2.60}$$

Precipitation and dissolution fluxes are driven by $[\mathrm{CO_3}^{2-}]$ and $[\mathrm{CaCO_3}]$, respectively, in a given ocean or reactive sediment box ($i = s, d, n$, or z):

$$F_{\mathrm{precip},i} = \begin{cases} \dfrac{\left(\Omega_i - 1\right)^{\eta_{\mathrm{calc}}}[\mathrm{CO_3}^{2-}]_i M_{\mathrm{oc},i}}{\tau_{\mathrm{precip}}} & \Omega_i \geqslant 1 \\ 0 & \Omega_i < 1 \end{cases} \tag{2.61}$$

$$F_{\mathrm{diss},i} = \begin{cases} 0 & \Omega_i \geqslant 1 \\ \dfrac{\left(1 - \Omega_i\right)^{\eta_{\mathrm{diss}}} R_{\mathrm{CaCO3},i}}{\tau_{\mathrm{diss}}} & \Omega_i < 1 \end{cases} \tag{2.62}$$

where $R_{\mathrm{CaCO3},i}$ is the reservoir of $\mathrm{CaCO_3}$ (in mol C), $M_{\mathrm{oc},i}$ is the mass of the box (kg), τ_{precip} and τ_{diss} are reaction timescales, and η_{calc} and η_{diss} are the thermodynamic rate powers of the calcification and dissolution reactions, respectively (modified from Ridgwell et al., 2007 and Zeebe, 2012; see table A.1). Calcium carbonate saturation state is calculated:

$$\Omega_i = \frac{[\mathrm{Ca}^{2+}]_{i,0}[\mathrm{CO_3}^{2-}]_i}{K_{\mathrm{sp},i}(T,S,P)} \tag{2.63}$$

where $[\mathrm{Ca}^{2+}]_{i,0}$ is a fixed concentration (mol/kg) and K_{sp} is an acid dissociation constant (Zeebe & Wolf-Gladrow, 2001; appendix B.1.2, table A.1). Carbonate ion concentration is considered in both the reaction equation (2.61) as well as in the Ω sensitivity (2.63); in the latter instance, the concentration determines whether or not precipitation or dissolution are operating, whereas in the former the concentration acts as a reservoir rate limit on the precipitation reaction. Given that $\mathrm{CO_3}^{2-}$ availability is taken into account by Ω, one could also use the DIC reservoir in place of carbonate ion concentration in equation 2.61; future versions of *EONS* will likely use this alternative formulation.

2.5.5 Iron photo-oxidation

In an oxygenated surface ocean, reduced iron is converted into iron hydroxide (Braterman, Cairns-Smith, & Sloper, 1983):

$$4\,\mathrm{FeO} + \mathrm{O_2} + 11\,\mathrm{H_2O} \xrightarrow{4h\nu} 4\,\mathrm{Fe(OH)_3} + 5\,\mathrm{H_2O} \tag{2.64}$$

This flux is limited by ferrous iron availability and oxygen level:

$$F_{\text{Fephotox}} = \frac{R_{\text{FeO,s}}}{\tau_{\text{photox}}} L_{\text{O2,anox},s} \tag{2.65}$$

where τ_{photox} is a timescale for the photo-oxidation reaction (see table A.1). This is unlikely a major source of iron oxides comprising Archean banded iron formations (BIFs; Konhauser et al., 2007a) but is still an important pathway for abiological iron oxidation.

2.5.6 Organic phosphate scavenging

Some anaerobic bacteria are capable of selectively remineralizing phosphate from particulate OM (Van Cappellen & Ingall, 1994).

$$(CH_2O)_{106}\,(NH_3)_{16}\,(H_3PO_4) \longrightarrow (CH_2O)_{106}\,(NH_3)_{16} + H_3PO_4\,\mathit{(aq)} \tag{2.66}$$

In laminated (anoxic) sediments, deviations from Redfield ratio C:P can exceed 10 times the regular ratio of 106:1 (Alcott et al., 2019; Van Cappellen & Ingall, 1994), implying that this scavenging is more energetically favoured in anoxic sedimentary settings. I assume scavenging is primarily limited by the amount of available organically bound phosphate, and increases proportionally with the phosphorus supply limitation on primary production. For i = sediment boxes n or z:

$$F_{\text{scav,i}} = \frac{R_{\text{OP},i}}{\tau_{\text{sink},i}} \left(1 - L_{\text{H3PO4,assim}}\right)\left(1 - L_{\text{O2,anox},i}\right) f_{\text{scav}} \tag{2.67}$$

where f_{scav} is the maximum fraction of organic phosphorus scavenged (0.1).

2.5.7 Phosphate adsorption onto iron

Phosphate can be adsorbed onto and buried within iron oxide deposits (Bjerrum & Canfield, 2002; Reinhard et al., 2017):

$$Fe(OH)_3 + H_3PO_4 \longrightarrow FePO_4 + 3\,H_2O \tag{2.68}$$

This reaction depends heavily on low pH (allowing the speciation of orthophosphate, ${PO_4}^{3-}$), iron oxide reservoir, the concentration of phosphate (in mol kg^{-1}), and a speciation constant (k_{ads}, in units of kg mol^{-1}; Bjerrum & Canfield, 2002). For ocean boxes ($i = s, d, n$ or z):

$$F_{\text{sorb},i} = \frac{R_{\text{FeOH3},i}}{\tau_{\text{sorb}}}[\text{H}_3\text{PO}_4]_i k_{\text{ads}}(1 - L_{\text{pH,sorb},i}) \tag{2.69}$$

As pH increases above neutral, the speciation (and thus absorption) of orthophosphate decreases. In reality, this reaction is also dependent on the dissolved silica concentration, which competes with phosphate for adsorption sites (Konhauser et al., 2007b). I do not resolve a silica cycle in this model, so I ignore that dependency in this formulation.

2.6 Fluxes: Geosphere

2.6.1 Sediment Burial

Reactive sediments (i) are eventually buried by overlying material and cut off from porewater; species buried in pelagic (z) sediments are transferred to "unreactive" sediments (u) cut off from ocean-atmosphere interaction, while species buried in shelf (n) sediments become part of the continent (c). Burial of particulate species (j = $CaCO_3$, $Fe(OH)_3$, $FePO_4$, OC, ON, SP, and OP) is treated:

$$F_{\text{burial},j,i} = \frac{R_{j,i}}{\tau_{\text{sink,i,0}}\chi_{\text{eros}}(t)} \tag{2.70}$$

where $\tau_{\text{sink,i,0}}$ is the modern residence time (yr) of reactive sediments. I do not track $FePO_4$ as a mineral species in the continent, instead burying this species as silicate-bound phosphate and iron oxide separately.

$$\text{FePO}_4 + 3\,\text{H}_2\text{O} \longrightarrow \text{Fe(OH)}_3 + \text{H}_3\text{PO}_4 \tag{2.71}$$

Dissolved H_3PO_4 is buried after first being incorporated into apatite, via:

$$5\,\text{Ca}^{2+} + 3\,\text{H}_3\text{PO}_4 + 10\,\text{HCO}_3{}^- + \text{H}_2\text{O} \longrightarrow \text{Ca}_5(\text{PO}_4)_3\text{OH} + 10\,\text{H}_2\text{O} + 10\,\text{CO}_2 \tag{2.72}$$

I avoid creating a separate carbonate reservoir and alkalinity effects during phosphorus speciation by simplifying equation 2.72 to a mass movement flux only affecting phosphate:

$$\text{H}_3\text{PO}_4\,(\text{aq}) \longrightarrow \text{H}_3\text{PO}_4\,(\text{s}) \tag{2.73}$$

Phosphate's incorporation into apatite in the sediments proceeds at a rate proportional to its dissolved concentration, generating a long-term sink for inorganic phosphorus (Kraal et al., 2017). This flux is primarily controlled by the burial of carbonate, a small portion of which contains absorbed apatite minerals. For $i = n$ or z:

$$F_{\mathrm{burial,PO4},i} = F_{\mathrm{burial,CaCO3},i} \frac{[\mathrm{H_3PO_4}]_i}{[\mathrm{H_3PO_4}]_0} f_{\mathrm{apatite}} \tag{2.74}$$

Co-precipitation of calcite and apatite requires specific environmental conditions (Knudsen & Gunter, 2002); as such, I use a conservative fraction ($f_{\mathrm{apatite}} = 0.01$) for estimating the portion of carbonate buried with apatite. $[\mathrm{H_3PO_4}]_0$ is a modern concentration of dissolved phosphate (1-2 μM; Koltermann, Gouretski, & Jancke, 2011, Talley, 2007).

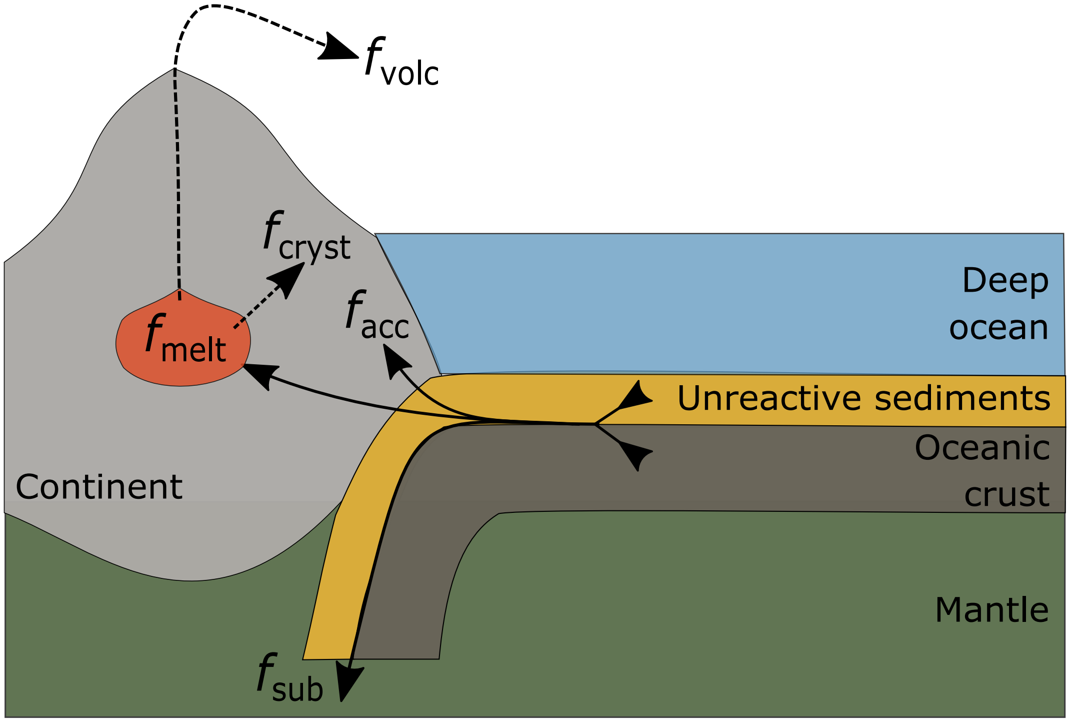

Figure 2.4: Subduction zone schematic A schematic representation of model subduction zones, highlighting slab subduction, accretion, and melt fractions (f_{acc}, f_{sub}, and f_{melt}, respectively). Melt fraction is split into either a volcanic ($f_{\mathrm{volc},j}$) or crystalline ($f_{\mathrm{cryst},j}$) fraction, depending on the volatility of species j.

2.6.2 Downgoing material

At the intersection of oceanic and continental crust, three major pathways emerge for species in the ocean crust and unreactive sediments: accretion, subduction, or melting ($f_{\text{acc}} + f_{\text{sub}} + f_{\text{melt}} = 1$; see table 2.2 and figure 2.4). Melted materials are then either volatilized at arc volcanoes (section 2.6.2.2) or recrystallized onto the continent (section 2.6.2.3; $f_{\text{volc}} + f_{\text{cryst}} = f_{\text{melt}}$); thus, distribution is species dependent. Sediments are twice as likely to be scraped off and accreted compared to the underlying oceanic slab[1]; correspondingly, ocean slab reservoirs are twice as likely to be subducted as overriding sediments.

Table 2.2: Subduction zone summary The apportionment of downgoing materials in the unreactive sediments and oceanic slab.

Box	**Accretion**	**Subduction**	**Melting**
Unreactive sediments	$f_{\text{acc,u}} = 0.1$	$f_{\text{sub,u}} = 0.05$	$f_{\text{melt}} = 0.85$
Ocean crust	$f_{\text{acc,o}} = 0.05$	$f_{\text{sub,o}} = 0.1$	$f_{\text{melt}} = 0.85$

I keep subduction timescale equal to that of modern seafloor spreading (approximately 10^8 years at present, based on the average age of modern oceanic crust; Müller, Sdrolias, Gaina, & Roest, 2008) which dictates species residence time in the ocean crust and unreactive sediments and apply this timescale to all subduction zone processes (i.e. subduction, accretion, volcanism, and recrystallization). This assumption ensures that seafloor generation (which is not strictly resolved here, but could be added in a future version) is equal to seafloor destruction; the subduction/spreading rate could be modified from a constant in a future version of the model to reflect evolving mantle heat flow.

2.6.2.1 Subduction and accretion

Subduction of oceanic lithosphere requires, at least in part, negative buoyancy resulting from thermal contrast between the overriding ocean slab and the upper mantle; as such, a hotter younger lithosphere would be more difficult to subduct, perhaps up to a factor of 2 in the Archean (Korenaga, 2006). Rather than try to capture the complexities of rheology and mantle evolution that truly control subduction for these species, I simply assume small, fixed fractions of the downgoing

---

[1] This is based on an estimate for some modern subduction zones, which have 20-70% of sediments forming accretionary prisms, though this estimate is highly location dependent (Von Huene & Scholl, 1991; Wong et al., 2019)

slab and sediments are subducted.

Both subduction and accretion fluxes are simply residence-dependant mass transfers; for a species hosted in the unreactive sediments (j = OC, ON, OP, CP, SP, and $Fe(OH)_3$) these fluxes (x = *sub* or *acc*) are:

$$F_{x,j} = \frac{R_{\mathrm{j,u}}}{\tau_{\mathrm{sub}}} f_{x,\mathrm{u}} \tag{2.75}$$

where τ_{sub} is seafloor spreading/subduction timescale. For NH_4^+ hosted only in the oceanic crust, subduction and accretion are:

$$F_{x,\mathrm{NH4}} = \frac{R_{\mathrm{NH4,o}}}{\tau_{\mathrm{sub}}} f_{x,\mathrm{o}} \tag{2.76}$$

As it is hosted in both reservoirs, the total accretion/subduction flux for calcium carbonate includes the fraction from unreactive sediments and the fraction from the ocean slab:

$$F_{x,\mathrm{CaCO3}} = \frac{f_{x,\mathrm{u}} R_{\mathrm{CaCO3,u}} + f_{x,\mathrm{o}} R_{\mathrm{CaCO3,o}}}{\tau_{\mathrm{sub}}} \tag{2.77}$$

2.6.2.2 Volcanism

The downgoing slab and the accompanying unreactive sediments[2] are exposed to flux melting and an assumed fraction of that melt ($f_{\mathrm{volc},j}$) can be volatilized at the arc front, releasing gases to the atmosphere. Organic matter in the unreactive sediments releases CO_2, CH_4, and NH_3 to the atmosphere (residual H_3PO_4 is recrystallized; see section 2.6.2.3):

$$(CH_2O)_{106}(NH_3)_{16}(H_3PO_4) \xrightarrow{heat} 53\,CO_2\uparrow + 53\,CH_4\uparrow + 16\,NH_3\uparrow + H_3PO_4\,(c) \tag{2.78}$$

Calcium carbonate in both the sediments and the slab releases CO_2:

$$CaCO_3 + SiO_2 \xrightarrow{heat} CO_2\uparrow + CaSiO_3 \tag{2.79}$$

Silicate-bound ammonium in the slab releases NH_3:

$$(NH_4)_2SiO_3 \xrightarrow{heat} 2\,NH_3\uparrow + SiO_2 + H_2O \tag{2.80}$$

---

[2] In reality, flux melting primarily mobilizes volatiles within the overriding lithosphere rather than in the slab itself. Since I do not resolve specific lithospheric or upper mantle provinces in this zero dimensional model, this nuance is not captured.

Volcanism occurs along an assumed timescale of subduction (τ_{sub}). Organic species (j = OC, ON) are hosted in the unreactive sediments and not in the slab, therefore:

$$F_{\text{volc},j} = \frac{R_{j,\text{u}}}{\tau_{\text{sub}}} f_{\text{volc},j} \tag{2.81}$$

Organic carbon fully volatilizes ($f_{\text{volc,OC}} = f_{\text{melt}}$) whereas ON is only partially volatilized. Calcium carbonate exists in both the sediments and the slab and fully volatilizes:

$$F_{\text{volc,CaCO3}} = \frac{R_{\text{CaCO3,u}} + R_{\text{CaCO3,o}}}{\tau_{\text{sub}}} f_{\text{volc,CaCO3}} \tag{2.82}$$

Silicate-bound $NH_4{}^+$ is only in the slab and is assumed to be partially volatilized, therefore:

$$F_{\text{volc,NH4}} = \frac{R_{\text{NH4,o}}}{\tau_{\text{sub}}} f_{\text{volc,NH4}} \tag{2.83}$$

Fully volatilizing here means that the entire portion of the slab and sediments which are melted at the subduction zone are returned to the atmosphere rather than recrystallized onto the continent. There is still a portion of the both the slab and sediments that escapes melting entirely and is subducted or accreted. All species in the oceanic slab and sediments are in some amounts returned to the upper mantle.

2.6.2.3 Recrystallization

Species in the slab and sediments without volatile components, and those assumed only partially volatilized, are recrystallized onto the continent rather than outgassed to the atmosphere when exposed to flux melting. For species j in the unreactive sediments ($Fe(OH)_3$, SP, CP, OP, ON), this is formulated:

$$F_{\text{cryst},j} = \frac{R_{j,\text{u}}}{\tau_{\text{sub}}} f_{\text{cryst},j} \tag{2.84}$$

All of these species except ON are assumed to be exclusively recrystallized ($f_{\text{cryst},j} = f_{\text{melt}}$); CP and OP are transferred to the silicate-bound (SP) reservoir. Organic-bound N is assumed partially recrystallized with the same fraction as $NH_4{}^+$; for $NH_4{}^+$ in the oceanic crust:

$$F_{\text{cryst,NH4}} = \frac{R_{\text{NH4,o}}}{\tau_{\text{sub}}} f_{\text{cryst,NH4}} \tag{2.85}$$

2.6.3 Metamorphism

Metamorphism from tectonic activity (uplift) or from exposure to intrusive pluton emplacement volatilizes compounds from the continental reservoirs (j = $CaCO_3$, OC, ON, OP, or NH_4) along an assumed timescale (τ_{meta}, assumed to be 10^9 years):

$$F_{\text{meta},j} = \frac{R_{\text{j,c}}}{\tau_{\text{meta}}} \tag{2.86}$$

The species associated with organic matter (CO_2, CH_4, and NH_3) are volatilized in Redfield ratio, with the exception of H_3PO_4, which I assume is instead transferred from the organic to the carbonate-bound reservoir (Ruttenberg, 2003). As these organic species are tracked in separate sediment and continental reservoirs, I remove the carbon and nitrogen volatiles from them separately. Organic carbon is volatilized as both CO_2 and CH_4, in a 50/50 split (the same stoichiometry used in volcanism, equation 2.78). Inorganic carbon and nitrogen metamorphism assumes the same stoichiometry as volcanism (equations 2.79 and 2.80).

2.6.4 Continental crust weathering

Weathering of continental reservoirs introduces DIC, alkalinity, RN, and H_3PO_4 to the surface ocean. Continental weathering reactions respond interactively to temperature and atmospheric composition.

2.6.4.1 Weathering modifiers

Weathering fluxes are enhanced by atmospheric CO_2 and temperature (Bergman et al., 2004; Brady & Carroll, 1994; Rushby, Johnson, Mills, Watson, & Claire, 2018; Walker et al., 1981; Zeebe, 2012). The transfer of CO_2 from the atmosphere to the ocean (as DIC and alkalinity) via weathering is a vital negative feedback stabilizing the climate on geologic timescales (Walker et al., 1981). Temperature controls weathering by enhancing precipitation (runoff), dissolution rates for silicate and carbonate minerals (Brady & Carroll, 1994), as well as subsequent precipitation of $CaCO_3$ which ultimately sequesters atmospheric carbon (Walker et al., 1981). Terrestrial weathering is further driven by the formation of weak carbonic acid (biologically and abiologically) in soils, enhanced by higher pCO_2 and biological activity (Berner, 1991; Brady & Carroll, 1994).

I adapt the treatment of chemical weathering used in the COPSE (Bergman et al., 2004) and GEOCARB (Berner, 1991) models such that weathering here responds interactively to higher CO_2 and temperatures. For my purposes, it is important to consider the effects of plant vegetation (enhancing weathering); in the GEOCARB and COPSE models, pre-plant weathering sensitivity is assumed higher than weathering after plants evolve. I assume the same pre-plant CO_2 sensitivity used in those models, but allow evolution of plants to enhance weathering up to a factor of 2 times the pre-plant modifier (Ibarra et al., 2019). Thus, weathering modifiers are also time-dependent, and take the form $m_j(t, T, \mathrm{CO_2})$, for j indicating carbonate, subaerial (granitic), and seafloor (basaltic) reactions:

$$m_j = \Theta_j(T) f_{\mathrm{CO_2}}^{\eta_{\mathrm{w}}} \Big(1 + \chi_{\mathrm{plants}}(t)\Big) \tag{2.87}$$

where $f_{\mathrm{CO_2}}$ is the atmospheric level of CO_2 with respect to the modern day (PAL) and the exponent η_{w} describes the CO_2 power-law relationship for weathering (between 0.2 and 0.5 for weak or strong control, respectively; Bergman et al., 2004, Berner, 1991, Sleep & Zahnle, 2001). Temperature-sensitive mineral dissolution, $\Theta_j(T)$, is an Arrhenius equation:

$$\Theta_j = \exp\left(\frac{E_j}{R}\Big(\frac{1}{290} - \frac{1}{T}\Big)\right) \tag{2.88}$$

where the term R is the gas constant and E_j is the activation energy of mineral dissolution (table A.1). I use specific minerals to characterize dissolution properties; continental carbonate dissolution uses dolomite (Herman & White, 1985), continental silicates uses diopside (Brady & Carroll, 1994; Schott, Berner, & Sjöberg, 1981), and seafloor basalts are enstatite and olivine (Schott et al., 1981; Wogelius & Walther, 1992).

Seafloor basalt weathering involves low-temperature off axis hydrothermal fluids (Coogan & Gillis, 2018) and depends on dissolved CO_2 levels:

$$f_{\mathrm{dCO_2}} = \frac{[\mathrm{CO_2}]_z}{[\mathrm{CO_2}]_{z,0}} \tag{2.89}$$

This term replaces $f_{\mathrm{CO_2}}$ in equation 2.87 (table A.1). Bottom waters are kept at a constant temperature in this model, therefore I ignore the temperature sensitivity term.

Weathering enhancement from continental vegetation is modified from Bergman et al. (2004):

$$W_{\text{plant}}(t, \text{CO}_2) = \begin{cases} 0 & t \leqslant 3.6 \times 10^9 \\ f_{\text{plants}}(t) \left(\dfrac{2 f_{\text{CO}_2}}{1 + f_{\text{CO}_2}} \right)^{\eta_{\text{w}}} & t > 3.6 \times 10^9 \end{cases} \tag{2.90}$$

where $f_{\text{plant}}(t)$ is an imposed sigmoidal growth curve for land plant population fraction (section 2.3.7). I do not include the plant weathering enhancement in calculating the seafloor weathering modifier.

Terrestrial weathering is limited by exposure of fresh rock surfaces and access to leached cations (West, Galy, & Bickle, 2005); this implies that chemical weathering processes have a maximum rate they cannot exceed, perhaps up to 10 times modern rates (Mills et al., 2011). I normalize continental weathering modifiers with respect to modern CO_2, temperature, and vegetation conditions ($m_{j,0} = 1$ for 290 K and 280 ppm pCO_2), producing dimensionless weathering sensitivities:

$$S_j = a_w \frac{m_j}{m_j + b_w} \tag{2.91}$$

for species j being carbonate or silicate. The factors a_w and b_w are tuned to achieve a sensitivity range of 10 times the modern at higher temperatures and CO_2 levels (figure 2.5). Seafloor weathering is limited by the rate of hydrothermal fluid flow through the basaltic ocean crust (Sleep & Zahnle, 2001), which I do not resolve; I normalize this flux to a modifier of 1 for present day:

$$S_{\text{sfw}} = \frac{m_{\text{sfw}}}{m_{\text{sfw}} + 1} \tag{2.92}$$

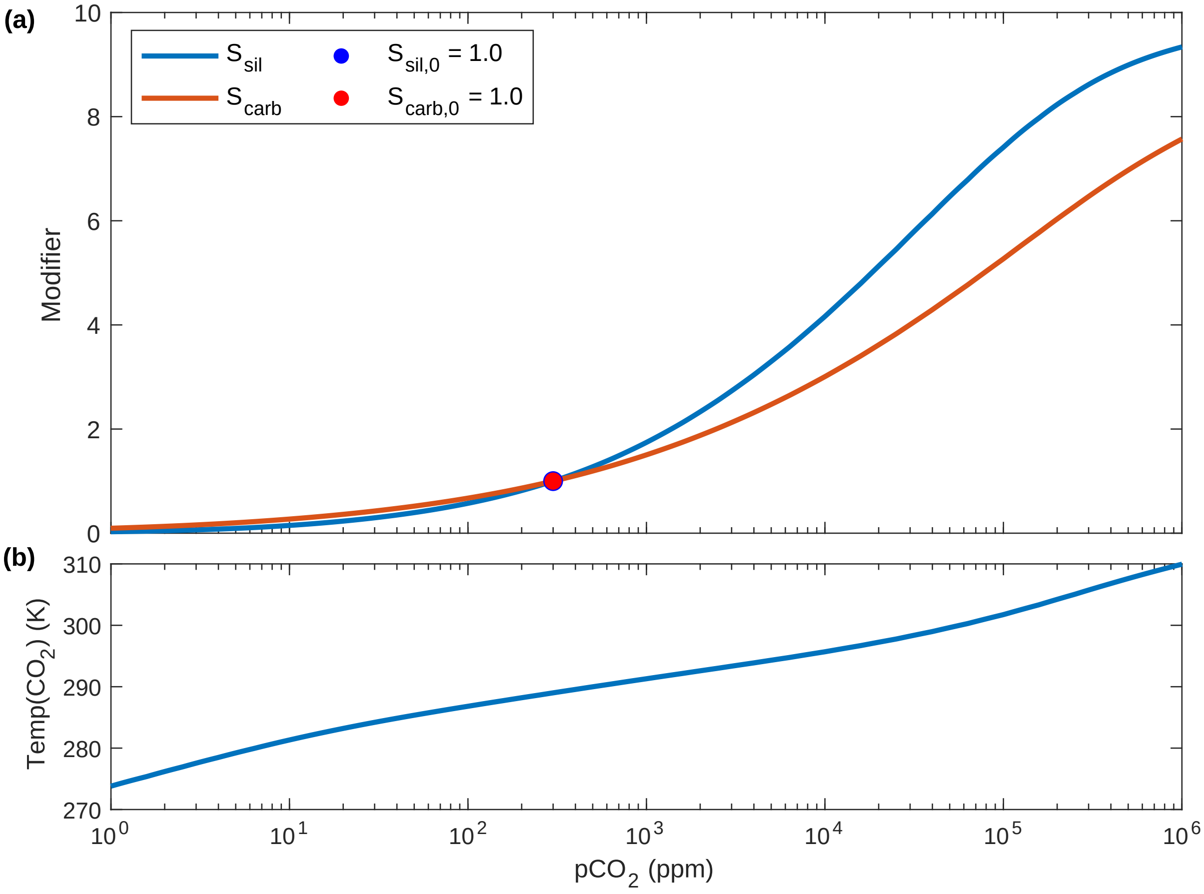

Figure 2.5: Weathering sensitivities a Carbonate and silicate weathering sensitivities, S_{carb} and S_{sil} for different pCO$_2$ conditions; **b** Temperature as a function of CO$_2$ partial pressure, calculated with equation 2.125 using modern solar constant and partial pressures for CH$_4$, N$_2$, and NH$_3$. General sensitivities are calculated using equations 2.87 - 2.91 and surface temperatures from CO$_2$ radiative forcing only. Reference modifiers for modern, pre-industrial pCO$_2$ (300 ppm) are plotted as dots.

2.6.4.2 Carbonate Weathering

Inorganic carbon and associated apatite minerals are weathered chemically by atmospheric CO_2 (Bergman et al., 2004; Zeebe, 2012):

$$\mathrm{CaCO_3(c) + H_2O + CO_2(a) \longrightarrow Ca^{2+} + 2\,HCO_3{}^{-}(aq)} \tag{2.93}$$

Carbonate-bound phosphate in apatite ($Ca_3(PO_4)_2$) weathers:

$$\mathrm{Ca_3(PO_4)_2 + 3\,H_2O + 3\,CO_2(a) \longrightarrow 3\,Ca^{2+} + 2\,H_3PO_4(aq) + 3\,CO_3{}^{2-}\,(aq)} \tag{2.94}$$

This is simplified to a transfer of phosphate from the continent to the oceans, without any affects on alkalinity in addition to regular carbonate weathering:

$$\mathrm{H_3PO_4\,(c) \longrightarrow H_3PO_4\,(aq)} \tag{2.95}$$

Carbonate weathering is generally:

$$F_{\text{wthr,CaCO3}} = \frac{R_{\text{CaCO3,c}}}{\tau_{\text{wcarb}}} S_{\text{carb}}(t, T, \mathrm{CO_2}) \tag{2.96}$$

where τ_{wcarb} is the lifetime of continental carbonates (yr), which is shorter than the canonical lifetime of continents.

Carbonate-bound phosphate weathering is formulated (in mol P/yr):

$$F_{\text{wthr,CP}} = \frac{R_{\text{CP,c}}}{\tau_{\text{wcarb}}/\chi_{\text{fungi}}(t)} S_{\text{carb}}(t, T, \mathrm{CO_2}) \tag{2.97}$$

Note that this weathering flux occurs over a modified carbonate weathering timescale which becomes equivalent to regular carbonate weathering only after the evolution of fungi late in the model run (see section 2.3.5).

2.6.4.3 Silicate Weathering

Continental silicates are weathered by CO_2, generating clay minerals and transferring atmospheric carbon to the ocean. I treat silicate weathering as alteration of igneous rocks (approximated here as wollastonite, $CaSiO_3$):

$$\mathrm{CaSiO_3(c) + H_2O + 2\,CO_2(a) \longrightarrow Ca^{2+} + 2\,HCO_3{}^{-}(aq) + SiO_2} \tag{2.98}$$

Igneous silicates contain significant NH_4^+, which substitutes for K^+ in muscovite and biotite ($KAl_2(AlSi_3O_{10})(OH)_2$) and alkali feldspars (Buddingtonite, $NH_4AlSi_3O_8$). I approximate this flux as buddingtonite weathering to kaolinite and silica, measured in units of mol N/yr:

$$\begin{aligned} 4\,\mathrm{NH_4AlSi_3O_8(c)} + 6\,\mathrm{H_2O} + 4\,\mathrm{CO_2(a)} &\longrightarrow 4\,\mathrm{NH_4AlSi_3O_8} + 4\,\mathrm{H_2CO_3} + 2\,\mathrm{H_2O} \\ &\longrightarrow 4\,\mathrm{NH_4}^+ + \mathrm{Al_4Si_4O_{10}(OH)_8} + 8\,\mathrm{SiO_2} + 4\,\mathrm{HCO_3}^- \end{aligned} \tag{2.99}$$

To reduce the use of untracked species (i.e. K and Al), I simplify to a stoichiometry that is broadly analogous to wollastonite weathering:

$$\mathrm{(NH_4)_2SiO_3(c)} + 2\,\mathrm{CO_2(a)} + \mathrm{H_2O} \longrightarrow 2\,\mathrm{NH_4}^+\,\mathrm{(aq)} + \mathrm{SiO_2} + 2\,\mathrm{HCO_3}^-\,\mathrm{(aq)} \tag{2.100}$$

Silicate-bound phosphorus weathering is treated the same as carbonate-bound phosphorus weathering (equation 2.95), transferring continental SP to H_3PO_4 in the ocean without any effects on alkalinity.

I assume that a large portion of Earth's surface reduced iron reservoir is confined in continental silicates as fayalite olivine; fayalite is weathered by CO_2 as with other silicates but also oxidized when atmospheric O_2 becomes available, producing hematite[3]:

$$\mathrm{Fe_2SiO_4} + \mathrm{CO_2(a)} + \mathrm{H_2O} + \frac{1}{2}\mathrm{O_2}\ \mathrm{(a)} \longrightarrow \mathrm{Fe_2O_3(c)} + \mathrm{H_2CO_3(aq)} + \mathrm{SiO_2} \tag{2.101}$$

The magnitude of subaerial silicate weathering is dictated by the size of the crustal silicate reservoir (i.e. the size of the continents, which is parameterized to grow directly from upper mantle input), and is in units of mols CO_2/yr:

$$F_{\mathrm{wthr,sil}} = 2\frac{R_{\mathrm{SiO3,c}}}{\tau_{\mathrm{wsil}}} S_{\mathrm{sil}}(t, T, \mathrm{CO_2}) \tag{2.102}$$

where τ_{wsil} is the timescale of silicate weathering, essentially the lifetime of the

---

[3] This assumed stoichiometry is another simplification of reality; magnetite (Fe_3O_4) is actually produced by this reaction. In order to limit the number of iron species in this version of the model, I opted for this stoichiometry using hematite, since that was already a species formed by photoferrotrophy and photo-oxidation in the ocean.

continents. Silicate-bound ammonium is similarly treated (in mol N/yr):

$$F_{\text{wthr,NH4}} = \frac{R_{\text{NH4,c}}}{\tau_{\text{wsil}}} S_{\text{sil}}(t, T, \text{CO}_2) \tag{2.103}$$

Silicate-bound phosphorus weathering is partially controlled by selective dissolution of silicate-bound phosphate by fungi, lichens, and plants (Lambers, 2022). Thus, phosphate weathering will be slower than modern rates prior to the evolution of fungi (circa 700 Ma; see section 2.3.5). In mol P/yr:

$$F_{\text{wthr,SP}} = \frac{R_{\text{SP,c}}}{\tau_{\text{wsil}}/\chi_{\text{fungi}}(t)} S_{\text{sil}}(t, T, \text{CO}_2) \tag{2.104}$$

In the modern context when $\chi_{\text{fungi}}(t) = 1$, this flux occurs over the same timescale as regular silicate weathering.

Reduced iron (fayalite) weathers along the canonical silicate timescale but is limited by the availability of oxygen:

$$F_{\text{wthr,Feox}} = \frac{R_{\text{Fe2SiO4,c}}}{\tau_{\text{wsil}}} \sqrt{f_{\text{O}_2}} S_{\text{sil}}(t, T, \text{CO}_2) \tag{2.105}$$

Unlike other weathering fluxes, this does not include transport of the product, hematite, to the oceans; rather, it remains in a new continental reservoir.

2.6.4.4 Oxidative Weathering

Organic matter is removed from the continental reservoir (c) via oxidative weathering when oxygen is plentiful in the atmosphere (Bergman et al., 2004).

$$(\text{CH}_2\text{O})_{106}(\text{NH}_3)_{16}(\text{H}_3\text{PO}_4)(\text{c}) + 106\,\text{O}_2(\text{a}) \longrightarrow 106\,\text{CO}_2 + 16\,\text{NH}_3 + \text{H}_3\text{PO}_4 + 106\,\text{H}_2\text{O} \tag{2.106}$$

Oxidative weathering occurs along a specific timescale (τ_{woxi}) and takes the form (for species j indicating OC, ON, OP):

$$F_{\text{wthr},j} = \frac{R_{j,\text{c}}}{\tau_{\text{woxi}}} \sqrt{f_{\text{O}_2}} \tag{2.107}$$

2.6.5 Reverse Weathering

Reverse weathering is essentially the reverse of silicate weathering (equation 2.98), forming authigenic clay at the expense of porewater alkalinity:

$$\mathrm{Ca^{2+}} + 2\,\mathrm{HCO_3}^- + \mathrm{SiO_2} \longrightarrow \mathrm{CaSiO_3} + 2\,\mathrm{CO_2} + \mathrm{H_2O} \tag{2.108}$$

I base my formulation for this reaction on that of Isson and Planavsky (2018) with a few simplifications[4]. For $i = n$ or z:

$$F_{\mathrm{revwthr},i} = 2k_{\mathrm{rw},i}(\mathrm{pH}_i)[\mathrm{Si}]_0 V_i \tag{2.109}$$

where V_i is the volume of reactive sediment porewaters (in m^3), $[\mathrm{Si}]_0$ is the concentration of silica in modern porewaters ($\leqslant 0.1$ mol/m^3; Isson & Planavsky, 2018), and term $k_{\mathrm{rw},i}(\mathrm{pH}_i)$ is the estimated modern rate of reverse weathering, determined by porewater pH (units yr^{-1}):

$$k_{\mathrm{rw},i} = 1.01 \times 10^{-19}\mathrm{pH}_i^{22.4} \tag{2.110}$$

Reverse weathering is multiplied by 2 to equate the moles of silica (not tracked) to moles bicarbonate consumed in the reaction. I assume a simpler sensitivity to silica concentrations than that of Isson and Planavsky (2018) since the pH-sensitivity of the rate parameter k_{rw} is a much stronger control on the overall reaction rate and I keep dissolved silica constant (see table A.1).

2.6.6 Seafloor Weathering

Dissolved $\mathrm{CO_2}$ reacts with seafloor basalts in hydrothermal settings, precipitating carbonate minerals in ocean crust (Sleep & Zahnle, 2001):

$$\mathrm{CO_2(aq)} + \mathrm{CaSiO_3} \longrightarrow \mathrm{CaCO_3} + \mathrm{SiO_2} \tag{2.111}$$

---

[4] I use $\mathrm{Ca^{2+}}$ as the cation in this reaction to mirror the stoichiometrically of silicate weathering; however, reverse weathering typically takes up other cations such as $\mathrm{Mg^{2+}}$, $\mathrm{Na^+}$ and $\mathrm{K^+}$. As these other cations are preferentially removed in this reaction, $\mathrm{Ca^{2+}}$ builds up in the ocean and can lead to declining pH and carbonate ion concentrations by promoting $\mathrm{CaCO_3}$ precipitation. I do not consider these conservative cations in the model, but this could be an important feedback to resolve in future versions of *EONS*.

Seafloor weathering here is based on an estimated modern rate (k_{sfw} in units of mol C/yr; Gillis & Coogan, 2011, Mills, Lenton, & Watson, 2014) and responds to pelagic sediment dissolved [CO_2] (section 2.6.4.1):

$$F_{\mathrm{sfw}} = k_{\mathrm{sfw}} S_{\mathrm{sfw}}(t, [\mathrm{CO_2}]_z) \tag{2.112}$$

This flux bolsters the silicate weathering climate feedback when continental surface area is lower, and at present is estimated to operate at a similar magnitude as carbon degassing at mid-ocean ridges (Coogan & Gillis, 2013). Therefore it is likely that this flux was a significant component of the carbon-silicate feedback in the Archean (Hayes & Waldbauer, 2006; Sleep & Zahnle, 2001).

2.6.7 Hydrothermal alteration

Ammonium is incorporated into silicate minerals- primarily biotite- during hydrothermal alteration (Holloway & Dahlgren, 2002). I treat this as cation exchange within ocean crust, where NH_4^+ replaces K^+ (untracked) and using the simplified N-silicate stoichiometry described in section 2.6.4.3. Stoichiometrically:

$$2\,\mathrm{NH_4}^+\,(\mathrm{aq}) + \mathrm{SiO_2} + 2\,\mathrm{HCO_3}^- \longrightarrow (\mathrm{NH_4})_2\mathrm{SiO_3} + 2\,\mathrm{CO_2}(\mathrm{aq}) + \mathrm{H_2O} \tag{2.113}$$

Hydrothermal incorporation depends on pelagic sediment porewater [NH_4^+], the rate of hydrothermal flow, and (because this is a symbolic alteration of silicates) is sensitive to CO_2 and temperature. My flux formulation is similar to that used by Johnson and Goldblatt (2018):

$$F_{\mathrm{hyd}} = [\mathrm{NH_4}^+]_z \rho_{oc} k_{\mathrm{hyd}} S_{\mathrm{sfw}}(t, [\mathrm{CO_2}]_z) \tag{2.114}$$

where ρ_{oc} is the density of ocean waters (in kg/m^3), and k_{hyd} is an estimated volumetric flow rate for hydrothermal vents, in units of m^3/yr.

2.6.8 Mantle outgassing and plumes

The entirety of modern continental reservoirs for N and C and 95% of silicate-bound phosphate, Fe_2SiO_4, and SiO_3 are initially contained within the upper mantle reservoir (m) and are gradually transferred to the surface either as outgassing volatiles (for carbon and nitrogen) or in the form of plume emplacement onto continental bodies (for phosphorus, iron, and silicate species). The flux of species j depends on the mantle overturn rate (τ_{mantle}):

$$F_{\text{mantle,j}} = \frac{f_{\text{m}} R_{j,\text{m}}}{\tau_{\text{mantle}}} \tag{2.115}$$

where $f_{\text{m}} = 0.1$ is a tunable parameter, here assuming that only 10% of the upper mantle is outgassing/erupting. Carbon and nitrogen species are released in both reduced (CH_4 and NH_3) and neutral forms (CO_2 and N_2). For species $j = CH_4$ or NH_3 and j^* = C or N:

$$F_{\text{mantle},j} = f_{\text{red}} F_{\text{mantle},j^*} \tag{2.116}$$

and for species $j = CO_2$ or N_2:

$$F_{\text{mantle},j} = (1 - f_{\text{red}}) F_{\text{mantle},j^*} \tag{2.117}$$

where $f_{\text{red}} = 0.01$ is the fraction of total element outgassed as a reduced species.

2.7 Fluxes: Exchanges

2.7.1 Air-sea gas exchange

Atmospheric gases (j = N_2, NH_3, CO_2, CH_4, and O_2) exchange via diffusion with the surface ocean (s) using the stagnant boundary approximation of Liss (1974)[5], following Johnson and Goldblatt (2018):

$$F_{\text{air-sea},j} = \frac{D_j}{d_{\text{sl}}} A_{\text{s}} \left(C_{j,\text{s}} - \kappa_j(T) P_j \right) \tag{2.118}$$

A positive flux is towards the atmosphere, and negative is into the ocean. D_j is the diffusion constant of each species and d_{sl} is the thickness of the stagnant boundary layer, thus giving the gas-phase transfer velocity (m/yr); A_{s} is the surface area of the ocean; $C_{j,\text{s}}$ is the concentration of species j in the surface ocean and is calculated by dividing the species reservoir (R_j, s) by the surface ocean volume (V_{s}); P_j is the

---

[5] The stagnant boundary approximation is slightly outdated, and incorrectly scales diffusivity, which should scale instead with the square root of the diffusivity constant.

partial pressure for gas j in the atmosphere, calculated (in Pa):

$$P_j = R_{j,\mathrm{a}} \frac{P_0}{n_0} \tag{2.119}$$

where $n_0 = 1.8 \times 10^{20}$ moles in present atmosphere and $P_0 = 101325$ pascals per atmosphere. A temperature dependent Henry's Law constant for species j ($\kappa_j(T)$; mol $\mathrm{m^3 Pa^{-1}}$) is calculated according to Sander (2015):

$$\kappa_j(T) = \kappa_{0,j} \exp\left(\nu_j \left[\frac{1}{T} - \frac{1}{T_0}\right]\right) \tag{2.120}$$

where T is the surface temperature in Kelvin, $\kappa_{0,j}$ is the Henry's Law constant at the reference temperature ($T_0 = 298.15$ K), and $\nu_j = -\Delta_{\mathrm{sol}} H/R$, a constant value for each species within relatively small temperature deviations from T_0 (see table A.1 for these values).

2.7.2 Ocean mixing

All dissolved species (j) in the ocean boxes ($i = s$ or d) are transferred between the two in accordance with concentration gradients via volumetric water flux (Johnson & Goldblatt, 2018):

$$F_{\mathrm{mix},j,i} = Q\left(\frac{R_{j,i}}{V_i} - \frac{R_{j,i^*}}{V_{i^*}}\right) \tag{2.121}$$

V_i is the volume of the ocean box ($\mathrm{m^3}$) and Q is the volumetric flow rate ($\mathrm{m^3/yr}$), which is calculated by dividing the deep ocean volume, V_{d}, by the deep ocean water lifetime, τ_{oc}.

2.7.3 Export

Particulate species in the surface ocean sink into the deep ocean according to the relative productivity fraction of the shelf versus the open ocean (f_{Pshelf}; see section 2.7.5). During their descent, OC and $\mathrm{CaCO_3}$ are susceptible to remineralization or dissolution, respectively. For species j (OC, $\mathrm{CaCO_3}$, and $\mathrm{Fe(OH)_3}$) this flux is generally:

$$F_{\mathrm{export},j} = \frac{R_{j,\mathrm{s}}}{\tau_{\mathrm{export},j}}(1 - f_{\mathrm{Pshelf}}) \tag{2.122}$$

Export timescales differ between these species: organic carbon sinking is modified here by the size of organisms relative to the modern day ($\tau_{\text{export,OC}} = \tau_{\text{sink,s}}/\chi_{\text{sink}}(t)$), a boundary forcing. Sinking calcium carbonate in the surface ocean is ten times faster than particulate organic carbon sinking, accounting for increased ballast ($\tau_{\text{export,CaCO3}} = \frac{1}{10}\tau_{\text{sink,s}}/\chi_{\text{sink}}(t)$); therefore nearly 90% of inorganic carbon escapes significant dissolution and is exported from the surface ocean (Emerson & Hedges, 2008). Particulate iron species sink at an average rate of 2×10^4 m/yr with no dependency on body size ($\tau_{\text{export,FeOH3}} = \frac{d_s}{2\times10^4}$; Thompson et al., 2019).

2.7.4 Diffusion into sediments

Dissolved species (j = N_2, RN, HNO_3, H_3PO_4, O_2, CH_4, TA, DIC) diffuse into and out of the porewaters of reactive sediments (i^* = n or z) from the overlying surface or deep ocean (i = s or d) according to the concentration gradient between those two reservoirs (Boudreau, 1996).

$$F_{\text{diff},j,i^*} = \left(\frac{[j]_i - [j]_{i^*}}{h_{\text{z}}}\right)\lambda_j A_{i^*} \tag{2.123}$$

where $[j]$ denotes a species concentration in units of (mol m^{-3}), λ_{j} is the diffusion coefficient (m^2/yr) for species j (table A.1), and h_z is the length of diffusion (0.01 m). A_{i^*} is either the surface area of the ocean (and pelagic sediments for diffusion into z) or the surface area of the continental shelf (for diffusion into n), in m^2.

2.7.5 Sedimentation

Particulate species (j = OC, $CaCO_3$, and $Fe(OH)_3$) suspended in the surface or deep ocean reservoirs (i = s or d) eventually settle into underlying sediments (neritic or pelagic, respectively; i^* = n or z) along depth-dependent timescales:

$$F_{\text{sed},j,i^*} = \frac{R_{j,i}}{\tau_{\text{sed},i,j(t)}} f_{\text{sed},i^*} \tag{2.124}$$

Sedimentation timescales differ between species similarly to export (section 2.7.3): organic carbon and carbonate sinking rates are modified by the size of organisms relative to the modern day ($\tau_{\text{sed},i,\text{OC}} = \tau_{\text{sink,i}}/\chi_{\text{sink}}(t)$ and $\tau_{\text{sed},i,\text{CaCO3}} = \frac{1}{10}\tau_{\text{sink,i}}/\chi_{\text{sink}}(t)$). Particulate iron sinks faster no dependency on body size ($\tau_{\text{sed},i,\text{FeOH3}} = \frac{d_i}{2\times10^4}$;

Thompson et al., 2019). All particulates in the deep ocean settle into the pelagic sediments ($f_{\mathrm{sed,z}} = 1$); neritic sediments gain the un-exported fraction of particulate matter sinking out of the surface ocean ($f_{\mathrm{sed,n}} = f_{\mathrm{Pshelf}}$).

2.8 Climate

I base my parameterization of surface temperature on a radiative equilibrium, grey atmosphere model (Goody & Yung, 1995), fitting the thermal optical depth to the strength of the greenhouse effect similar to Lenton (2000). I include linear water vapour feedback, but for simplicity do not include non-linearities such as the runaway greenhouse effect or ice-albedo feedback. The change in Earth's surface temperature associated with an increase in the partial pressure of greenhouse gases depends on the amount of greenhouse forcing (GF) that each gas exerts (in W/m^2). Greenhouse forcing is correlated to gas mixing ratio by interpolating onto the line-by-line radiative transfer data from Byrne and Goldblatt (2014); total greenhouse forcing is the sum of all greenhouse gases ($GF_t = GF_{\mathrm{NH_3}} + GF_{\mathrm{CO_2}} + GF_{\mathrm{CH_4}}$).

Radiative balance for the surface under a grey atmosphere is:

$$\sigma T^4 = \left(1 - \alpha\right)\left(\frac{S(t)}{4}\right)\left(1 + \frac{3}{4}\gamma_{IR}\right) \tag{2.125}$$

where σ is the Stefan-Boltzmann constant (W m^{-2}K^{-4}), T is surface temperature (K), α is planetary albedo, and $S(t)$ is solar flux forcing (Wm^{-2}), which increases quasi-linearly through time (see section 2.3.3; table A.1). I parameterize thermal optical depth:

$$\gamma_{IR} = f^{q}_{\mathrm{N2}}\Big(a_T(T - 250) + b_T GF_t\Big) \tag{2.126}$$

Constants a_T and b_T are fitted to the radiative transfer data from Byrne and Goldblatt (2014) by solving two simultaneous equations for surface temperature T = 289 K maintained by greenhouse forcing under (1) modern pCO$_2$ and solar flux (300 ppm and 1361 Wm^{-2}) and (2) Archean pCO$_2$ and solar flux (45,000 ppm and 1020 Wm^{-2} at 4 Ga; Goldblatt, McDonald, & McCusker, 2021). This fitting yields a climate sensitivity of 2.6 K per CO$_2$ doubling. Pressure broadening of absorption spectra, $f^{q}_{\mathrm{N_2}}$, is a function of the atmospheric N$_2$ level relative to modern, with constant q fitted to increase surface temperature by 4.4°C per pN$_2$ doubling at 2.5 Ga (Goldblatt et al., 2009; table A.1). Temperature change then relates to the difference in radiative fluxes, scaled by surface area (A_E, in m^2), ocean mass (M_{oc}, in kg), and water's specific heat capacity (c_p, in J kg^{-1} K^{-1}):

$$\left.\frac{\mathrm{d}T}{\mathrm{d}t}\right|_{\mathrm{GHF}} = \frac{A_E}{M_{\mathrm{oc}}c_p}\left((1-\alpha)\left(\frac{S(t)}{4}\right)\left(1+\frac{3}{4}\gamma_{IR}\right)-\sigma T^4\right) \tag{2.127}$$

Surface ocean temperature is assumed equal to the atmospheric temperature ($T_s = T$). The temperature of the neritic (shelf) reactive sediments (T_n) reflects surface ocean temperatures, but 5°C colder. The temperature of the deep ocean and underlying reactive sediments (T_d and T_z) are kept constant (277 K or 4°C in the deep ocean, 275.5 K or 2.5°C in sediments; Tromp, Van Cappellen, & Key, 1995).

2.9 Differential Equations

The *EONS* model is comprised of a series of ordinary differential equations (ODEs) that evolve the aforementioned surface reservoirs of the Earth system through time. The model is written in Matlab and uses the in-built ode15s solver for stiff systems.

The model is run in two steps because the transition to operational oxygenic photosynthesis is rather dramatic. The model is run initially with initial conditions for the Eoarchean for 400 million years without oxygenic photosynthesis. I then restart the model run with the output from the first 400 million years as initial conditions, this time allowing operational photosynthesis. This restarted model run then proceeds for 3.6 billion years, and then the two runs are spliced together to create one continuous evolutionary curve.

2.9.1 Atmosphere

$$\begin{aligned}\frac{\mathrm{d}R_{\mathrm{NH3,a}}}{\mathrm{d}t} &= F_{\text{air-sea,NH3}} + f_{\mathrm{red}}F_{\mathrm{mantle,N}} + F_{\mathrm{volc,NH4}} + F_{\mathrm{meta,NH4}} + \tfrac{16}{106}F_{\mathrm{volc,OC}} \\ &\quad + \tfrac{16}{106}F_{\mathrm{meta,OC}} - F_{\mathrm{photo,NH3}} - F_{\mathrm{Hesc,NH3}}\end{aligned} \tag{2.128}$$

$$\frac{\mathrm{d}R_{\mathrm{N2,a}}}{\mathrm{d}t} = F_{\text{air-sea,N2}} + \tfrac{1}{2}\big((1-f_{\mathrm{red}})F_{\mathrm{mantle,N}} + F_{\mathrm{photo,NH3}} + F_{\mathrm{Hesc,NH3}}\big) \tag{2.129}$$

$$\begin{aligned}\frac{\mathrm{d}R_{\text{CO2,a}}}{\mathrm{d}t} &= F_{\text{air-sea,CO2}} + (1 - f_{\text{red}})F_{\text{mantle,C}} + F_{\text{meta,CaCO3}} + F_{\text{volc,CaCO3}} \\ &\quad + \tfrac{1}{2}(F_{\text{meta,OC}} + F_{\text{volc,OC}} + F_{\text{methox}} + F_{\text{Hesc,CH4}}) \\ &\quad - F_{\text{wthr,CaCO3}} - F_{\text{wthr,sil}} - F_{\text{wthr,NH4}} - F_{\text{wthr,Feox}} - \tfrac{19}{20}F_{\text{terrprod}}\end{aligned} \tag{2.130}$$

$$\frac{\mathrm{d}R_{\text{O2,a}}}{\mathrm{d}t} = F_{\text{air-sea,O2}} + F_{\text{terrprod}} - F_{\text{methox}} - F_{\text{wthr,oxi}} - \tfrac{3}{4}F_{\text{photo,NH3}} - \tfrac{1}{2}F_{\text{wthr,Feox}} \tag{2.131}$$

$$\begin{aligned}\frac{\mathrm{d}R_{\text{CH4,a}}}{\mathrm{d}t} &= F_{\text{air-sea,CH4}} + f_{\text{red}}F_{\text{mantle,C}} - F_{\text{Hesc,CH4}} \\ &\quad + \tfrac{1}{2}\left(F_{\text{meta,OC}} + F_{\text{volc,OC}} + \tfrac{1}{20}F_{\text{terrprod}} - F_{\text{methox}}\right)\end{aligned} \tag{2.132}$$

$$\begin{aligned}\frac{\mathrm{d}R_{\text{H2O,a}}}{\mathrm{d}t} &= F_{\text{methox}} + \tfrac{3}{2}F_{\text{photo,NH3}} + \tfrac{1}{2}F_{\text{meta,NH4}} + \tfrac{1}{2}F_{\text{volc,NH4}} - F_{\text{Hesc,CH4}} \\ &\quad - F_{\text{wthr,CaCO3}} - F_{\text{wthr,sil}} - \tfrac{1}{2}F_{\text{wthr,NH4}} - F_{\text{wthr,Feox}} - F_{\text{terrprod}}\end{aligned} \tag{2.133}$$

2.9.2 Surface ocean

$$\begin{aligned}\frac{\mathrm{d}R_{\text{N2,s}}}{\mathrm{d}t} &= F_{\text{mix,N2,s}} + \tfrac{42}{106}F_{\text{denit,s}} - F_{\text{fixation,N2}} - \tfrac{1}{2}F_{\text{fix,newN}} - F_{\text{air-sea,N2}} \\ &\quad - F_{\text{diff,N2,n}}\end{aligned} \tag{2.134}$$

$$\begin{aligned}\frac{\mathrm{d}R_{\text{RN,s}}}{\mathrm{d}t} &= F_{\text{mix,RN,s}} + F_{\text{wthr,NH4}} + F_{\text{wthr,ON}} - F_{\text{nit,s}} - F_{\text{air-sea,NH3}} \\ &\quad + \tfrac{16}{106}\left(F_{\text{ammon,s}} + F_{\text{denit,s}} + F_{\text{methgen,s}} - f_{\text{RN}}F_{\text{assim}}\right) \\ &\quad - \tfrac{4}{106}F_{\text{ferrotrophy}} - F_{\text{diff,RN,n}}\end{aligned} \tag{2.135}$$

$$\frac{\mathrm{d}R_{\text{HNO3,s}}}{\mathrm{d}t} = F_{\text{mix,HNO3,s}} + F_{\text{nit,s}} - \tfrac{16}{106}(1 - f_{\text{RN}})F_{\text{assim}} - \tfrac{84.4}{106}F_{\text{denit,s}} - F_{\text{diff,HNO3,n}} \tag{2.136}$$

$$\begin{aligned}\frac{\mathrm{d}R_{\text{H3PO4,s}}}{\mathrm{d}t} &= F_{\text{mix,H3PO4,s}} + F_{\text{wthr,OP}} + F_{\text{wthr,SP}} + F_{\text{wthr,CP}} - F_{\text{fix,H3PO4}} \\ &\quad + \tfrac{1}{106}(F_{\text{ammon,s}} + F_{\text{denit,s}} + F_{\text{methgen,s}} - F_{\text{assim}}) - F_{\text{fixation,H3PO4}} \\ &\quad - \tfrac{1}{424}F_{\text{ferrotrophy}} - F_{\text{sorb,s}} - F_{\text{diff,H3PO4,n}}\end{aligned} \tag{2.137}$$

$$\frac{\mathrm{d}R_{\mathrm{LB,s}}}{\mathrm{d}t} = F_{\mathrm{assim}} + F_{\mathrm{fix,CO2}} + F_{\mathrm{fixation,CO2}} + \tfrac{1}{4}F_{\mathrm{ferrotrophy}} - F_{\mathrm{death}} \tag{2.138}$$

$$\frac{\mathrm{d}R_{\mathrm{ON,s}}}{\mathrm{d}t} = \tfrac{16}{106}\left(F_{\mathrm{death}} - F_{\mathrm{ammon,s}} - F_{\mathrm{denit,s}} - F_{\mathrm{methgen,s}} - F_{\mathrm{export,OC}} - F_{\mathrm{sed,OC,n}}\right) \tag{2.139}$$

$$\frac{\mathrm{d}R_{\mathrm{OP,s}}}{\mathrm{d}t} = \tfrac{1}{106}\left(F_{\mathrm{death}} - F_{\mathrm{ammon,s}} - F_{\mathrm{denit,s}} - F_{\mathrm{methgen,s}} - F_{\mathrm{export,OC}} - F_{\mathrm{sed,OC,n}}\right) \tag{2.140}$$

$$\frac{\mathrm{d}R_{\mathrm{OC,s}}}{\mathrm{d}t} = F_{\mathrm{death}} - F_{\mathrm{ammon,s}} - F_{\mathrm{denit,s}} - F_{\mathrm{methgen,s}} - F_{\mathrm{export,OC}} - F_{\mathrm{sed,OC,n}} \tag{2.141}$$

$$\frac{\mathrm{d}R_{\mathrm{CaCO3,s}}}{\mathrm{d}t} = F_{\mathrm{precip,s}} - F_{\mathrm{diss,s}} - F_{\mathrm{export,CaCO3}} - F_{\mathrm{sed,CaCO3,n}} \tag{2.142}$$

$$\begin{aligned}\frac{\mathrm{d}R_{\mathrm{TA,s}}}{\mathrm{d}t} = {} & F_{\mathrm{mix,TA,s}} + F_{\mathrm{wthr,sil}} + 2F_{\mathrm{wthr,CaCO3}} + 2F_{\mathrm{diss,s}} + F_{\mathrm{wthr,NH4}} + F_{\mathrm{wthr,ON}} \\ & + \tfrac{16}{106}(1 - f_{\mathrm{RN}})F_{\mathrm{assim}} + \tfrac{16}{106}\left(F_{\mathrm{ammon,s}} + F_{\mathrm{denit,s}} + F_{\mathrm{methgen,s}}\right) \\ & + \tfrac{84.4}{106}F_{\mathrm{denit,s}} - \tfrac{16}{106}f_{\mathrm{RN}}F_{\mathrm{assim}} - \tfrac{4}{106}F_{\mathrm{ferrotrophy}} - 2F_{\mathrm{precip,s}} - 2F_{\mathrm{nit,s}} \\ & - F_{\mathrm{diff,TA,n}} - F_{\mathrm{air\text{-}sea,NH3}}\end{aligned} \tag{2.143}$$

$$\begin{aligned}\frac{\mathrm{d}R_{\mathrm{DIC,s}}}{\mathrm{d}t} = {} & F_{\mathrm{mix,DIC,s}} + 2F_{\mathrm{wthr,CaCO3}} + F_{\mathrm{wthr,sil}} + F_{\mathrm{wthr,oxi}} + F_{\mathrm{wthr,NH4}} \\ & + F_{\mathrm{wthr,Feox}} + F_{\mathrm{ammon,s}} + F_{\mathrm{denit,s}} + \tfrac{1}{2}F_{\mathrm{methgen,s}} + F_{\mathrm{mtrophy,s}} + F_{\mathrm{diss,s}} \\ & - F_{\mathrm{assim}} - F_{\mathrm{fix,CO2}} - F_{\mathrm{fixation,CO2}} - \tfrac{1}{4}F_{\mathrm{ferrotrophy}} - F_{\mathrm{precip,s}} \\ & - F_{\mathrm{air\text{-}sea,CO2}} - F_{\mathrm{diff,DIC,n}}\end{aligned} \tag{2.144}$$

$$\frac{\mathrm{d}R_{\mathrm{CH4,s}}}{\mathrm{d}t} = F_{\mathrm{mix,CH4,s}} + \tfrac{1}{2}F_{\mathrm{methgen,s}} - F_{\mathrm{mtrophy,s}} - F_{\mathrm{air\text{-}sea,CH4}} - F_{\mathrm{diff,CH4,n}} \tag{2.145}$$

$$\begin{aligned}\frac{\mathrm{d}R_{\mathrm{O2,s}}}{\mathrm{d}t} = {} & F_{\mathrm{mix,O2,s}} + \left(\tfrac{138}{106}(1 - f_{\mathrm{RN}}) + f_{\mathrm{RN}}\right)F_{\mathrm{assim}} + F_{\mathrm{fix}} - 2F_{\mathrm{nit,s}} - F_{\mathrm{ammon,s}} \\ & - 2F_{\mathrm{mtrophy,s}} - \tfrac{1}{4}F_{\mathrm{Fephotox}} - F_{\mathrm{air\text{-}sea,O2}} - F_{\mathrm{diff,O2,n}}\end{aligned} \tag{2.146}$$

$$\begin{aligned}\frac{\mathrm{d}R_{\mathrm{H2O,s}}}{\mathrm{d}t} = {} & F_{\mathrm{wthr,oxi}} + F_{\mathrm{wthr,Feox}} + F_{\mathrm{ammon,s}} + \tfrac{148.4}{106}F_{\mathrm{denit,s}} + F_{\mathrm{nit,s}} + 2F_{\mathrm{mtrophy,s}} \\ & + F_{\mathrm{precip,s}} + 3F_{\mathrm{sorb,s}} - \left(\tfrac{122}{106}(1 - f_{\mathrm{RN}}) + f_{\mathrm{RN}}\right)F_{\mathrm{assim}} - F_{\mathrm{fix,H2O}} \\ & - F_{\mathrm{fixation,H2O}} - \tfrac{7}{4}F_{\mathrm{ferrotrophy}} - \tfrac{6}{4}F_{\mathrm{Fephotox}} - F_{\mathrm{diss,s}}\end{aligned} \tag{2.147}$$

$$\frac{\mathrm{d}R_{\mathrm{FeO,s}}}{\mathrm{d}t} = F_{\mathrm{mix,FeO,s}} - F_{\mathrm{ferrotrophy}} - F_{\mathrm{fixation,FeO}} - F_{\mathrm{Fephotox}} \tag{2.148}$$

$$\begin{aligned}\frac{\mathrm{d}R_{\mathrm{FeOH3,s}}}{\mathrm{d}t} = {} & F_{\mathrm{ferrotrophy}} + F_{\mathrm{fixation,FeO}} + F_{\mathrm{Fephotox}} - F_{\mathrm{sorb,s}} \\ & - F_{\mathrm{export,FeOH3}} - F_{\mathrm{sed,FeOH3,n}}\end{aligned} \tag{2.149}$$

$$\frac{\mathrm{d}R_{\mathrm{FePO4,s}}}{\mathrm{d}t} = F_{\mathrm{sorb,s}} - F_{\mathrm{export,FePO4}} - F_{\mathrm{sed,FePO4,n}} \tag{2.150}$$

2.9.3 Neritic Sediments

$$\frac{\mathrm{d}R_{\mathrm{N2,n}}}{\mathrm{d}t} = F_{\mathrm{diff,N2,n}} + \tfrac{42}{106}F_{\mathrm{denit,n}} \tag{2.151}$$

$$\frac{\mathrm{d}R_{\mathrm{RN,n}}}{\mathrm{d}t} = F_{\mathrm{diff,RN,n}} + \tfrac{16}{106}\left(F_{\mathrm{ammon,n}} + F_{\mathrm{denit,n}} + F_{\mathrm{methgen,n}}\right) - F_{\mathrm{nit,n}} \tag{2.152}$$

$$\frac{\mathrm{d}R_{\mathrm{HNO3,n}}}{\mathrm{d}t} = F_{\mathrm{diff,HNO3,n}} + F_{\mathrm{nit,n}} - \tfrac{84.4}{106}F_{\mathrm{denit,n}} \tag{2.153}$$

$$\begin{aligned}\frac{\mathrm{d}R_{\mathrm{H3PO4,n}}}{\mathrm{d}t} = {} & F_{\mathrm{diff,H3PO4,n}} + \tfrac{1}{106}\left(F_{\mathrm{ammon,n}} + F_{\mathrm{denit,n}} + F_{\mathrm{methgen,n}}\right) + F_{\mathrm{scav,n}} \\ & - F_{\mathrm{sorb,n}} - F_{\mathrm{burial,PO4,n}}\end{aligned} \tag{2.154}$$

$$\frac{\mathrm{d}R_{\mathrm{ON,n}}}{\mathrm{d}t} = \tfrac{16}{106}\left(F_{\mathrm{sed,OC,n}} - F_{\mathrm{ammon,n}} - F_{\mathrm{denit,n}} - F_{\mathrm{methgen,n}}\right) - F_{\mathrm{burial,ON,n}} \tag{2.155}$$

$$\begin{aligned}\frac{\mathrm{d}R_{\mathrm{OP,n}}}{\mathrm{d}t} &= \tfrac{1}{106}\big(F_{\mathrm{sed,OC,n}} - F_{\mathrm{ammon,n}} - F_{\mathrm{denit,n}} - F_{\mathrm{methgen,n}}\big) - F_{\mathrm{burial,OP,n}} \\ &\quad - F_{\mathrm{scav,n}}\end{aligned} \tag{2.156}$$

$$\frac{\mathrm{d}R_{\mathrm{OC,n}}}{\mathrm{d}t} = F_{\mathrm{sed,OC,n}} - F_{\mathrm{ammon,n}} - F_{\mathrm{denit,n}} - F_{\mathrm{methgen,n}} - F_{\mathrm{burial,OC,n}} \tag{2.157}$$

$$\frac{\mathrm{d}R_{\mathrm{CaCO3,n}}}{\mathrm{d}t} = F_{\mathrm{sed,CaCO3,n}} + F_{\mathrm{precip,n}} - F_{\mathrm{diss,n}} - F_{\mathrm{burial,CaCO3,n}} \tag{2.158}$$

$$\begin{aligned}\frac{\mathrm{d}R_{\mathrm{TA,n}}}{\mathrm{d}t} &= F_{\mathrm{diff,TA,n}} + 2F_{\mathrm{diss,n}} + \tfrac{84.4}{106}F_{\mathrm{denit,n}} - 2F_{\mathrm{precip,n}} - F_{\mathrm{revwthr,n}} \\ &\quad + \tfrac{16}{106}\big(F_{\mathrm{ammon,n}} + F_{\mathrm{denit,n}} + F_{\mathrm{methgen,n}}\big) - 2F_{\mathrm{nit,n}}\end{aligned} \tag{2.159}$$

$$\begin{aligned}\frac{\mathrm{d}R_{\mathrm{DIC,n}}}{\mathrm{d}t} &= F_{\mathrm{diff,DIC,n}} + F_{\mathrm{ammon,n}} + F_{\mathrm{denit,n}} + \tfrac{1}{2}F_{\mathrm{methgen,n}} + F_{\mathrm{mtrophy,n}} \\ &\quad + F_{\mathrm{diss,n}} - F_{\mathrm{precip,n}}\end{aligned} \tag{2.160}$$

$$\frac{\mathrm{d}R_{\mathrm{CH4,n}}}{\mathrm{d}t} = F_{\mathrm{diff,CH4,n}} + \tfrac{1}{2}F_{\mathrm{methgen,n}} - F_{\mathrm{mtrophy,n}} \tag{2.161}$$

$$\frac{\mathrm{d}R_{\mathrm{O2,n}}}{\mathrm{d}t} = F_{\mathrm{diff,O2,n}} - 2F_{\mathrm{nit,n}} - F_{\mathrm{ammon,n}} - 2F_{\mathrm{mtrophy,n}} \tag{2.162}$$

$$\begin{aligned}\frac{\mathrm{d}R_{\mathrm{H2O,n}}}{\mathrm{d}t} &= F_{\mathrm{ammon,n}} + \tfrac{148.4}{106}F_{\mathrm{denit,n}} + F_{\mathrm{nit,n}} + 2F_{\mathrm{mtrophy,n}} + F_{\mathrm{precip,n}} \\ &\quad + \tfrac{1}{2}F_{\mathrm{revwthr,n}} + 3\big(F_{\mathrm{sorb,n}} - F_{\mathrm{burial,FePO4,n}}\big) - F_{\mathrm{diss,n}}\end{aligned} \tag{2.163}$$

$$\frac{\mathrm{d}R_{\mathrm{FeOH3,n}}}{\mathrm{d}t} = F_{\mathrm{sed,FeOH3,n}} - F_{\mathrm{sorb,n}} - F_{\mathrm{burial,FeOH3,n}} \tag{2.164}$$

$$\frac{\mathrm{d}R_{\mathrm{FePO4,n}}}{\mathrm{d}t} = F_{\mathrm{sed,FePO4,n}} + F_{\mathrm{sorb,n}} - F_{\mathrm{burial,FePO4,n}} \tag{2.165}$$

2.9.4 Deep ocean

$$\frac{\mathrm{d}R_{\mathrm{N2,d}}}{\mathrm{d}t} = F_{\mathrm{mix,N2,d}} + \tfrac{42}{106}F_{\mathrm{denit,d}} - F_{\mathrm{diff,N2,z}} \tag{2.166}$$

$$\frac{\mathrm{d}R_{\mathrm{RN,d}}}{\mathrm{d}t} = F_{\mathrm{mix,RN,d}} + \tfrac{16}{106}\big(F_{\mathrm{ammon,d}} + F_{\mathrm{denit,d}} + F_{\mathrm{methgen,d}}\big) - F_{\mathrm{nit,d}} - F_{\mathrm{diff,RN,z}} \tag{2.167}$$

$$\frac{\mathrm{d}R_{\mathrm{HNO3,d}}}{\mathrm{d}t} = F_{\mathrm{mix,HNO3,d}} + F_{\mathrm{nit,d}} - \tfrac{84.4}{106}F_{\mathrm{denit,d}} - F_{\mathrm{diff,HNO3,z}} \tag{2.168}$$

$$\begin{aligned}\frac{\mathrm{d}R_{\mathrm{H3PO4,d}}}{\mathrm{d}t} &= F_{\mathrm{mix,H3PO4,d}} + \tfrac{1}{106}\big(F_{\mathrm{ammon,d}} + F_{\mathrm{denit,d}} + F_{\mathrm{methgen,d}}\big) \\ &\quad - F_{\mathrm{sorb,d}} - F_{\mathrm{diff,H3PO4,z}}\end{aligned}$$

$$\frac{\mathrm{d}R_{\mathrm{ON,d}}}{\mathrm{d}t} = \tfrac{16}{106}\big(F_{\mathrm{export,OC}} - F_{\mathrm{ammon,d}} + F_{\mathrm{denit,d}} + F_{\mathrm{methgen,d}} + F_{\mathrm{sed,OC,z}}\big) \tag{2.169}$$

$$\frac{\mathrm{d}R_{\mathrm{OP,d}}}{\mathrm{d}t} = \tfrac{1}{106}\big(F_{\mathrm{export,OC}} - F_{\mathrm{ammon,d}} + F_{\mathrm{denit,d}} + F_{\mathrm{methgen,d}} + F_{\mathrm{sed,OC,z}}\big) \tag{2.170}$$

$$\frac{\mathrm{d}R_{\mathrm{OC,d}}}{\mathrm{d}t} = F_{\mathrm{export,OC}} - F_{\mathrm{ammon,d}} - F_{\mathrm{denit,d}} - F_{\mathrm{methgen,d}} - F_{\mathrm{sed,OC,z}} \tag{2.171}$$

$$\frac{\mathrm{d}R_{\mathrm{CaCO3,d}}}{\mathrm{d}t} = F_{\mathrm{export,CaCO3}} + F_{\mathrm{precip,d}} - F_{\mathrm{diss,d}} - F_{\mathrm{sed,CaCO3,z}} \tag{2.172}$$

$$\begin{aligned}\frac{\mathrm{d}R_{\mathrm{TA,d}}}{\mathrm{d}t} &= F_{\mathrm{mix,TA,d}} + 2F_{\mathrm{diss,d}} + \tfrac{84.4}{106}F_{\mathrm{denit,d}} - 2F_{\mathrm{precip,d}} - 2F_{\mathrm{nit,d}} \\ &\quad + \tfrac{16}{106}\big(F_{\mathrm{ammon,d}} + F_{\mathrm{denit,d}} + F_{\mathrm{methgen,d}}\big) - F_{\mathrm{diff,TA,z}}\end{aligned} \tag{2.173}$$

$$\begin{aligned}\frac{\mathrm{d}R_{\mathrm{DIC,d}}}{\mathrm{d}t} &= F_{\mathrm{mix,DIC,d}} + F_{\mathrm{ammon,d}} + F_{\mathrm{denit,d}} + \tfrac{1}{2}F_{\mathrm{methgen,d}} + F_{\mathrm{mtrophy,d}} + F_{\mathrm{diss,d}} \\ &\quad - F_{\mathrm{precip,d}} - F_{\mathrm{diff,DIC,z}}\end{aligned} \tag{2.174}$$

$$\frac{\mathrm{d}R_{\mathrm{CH4,d}}}{\mathrm{d}t} = F_{\mathrm{mix,CH4,d}} + \tfrac{1}{2}F_{\mathrm{methgen,d}} - F_{\mathrm{mtrophy,d}} - F_{\mathrm{diff,CH4,z}} \tag{2.175}$$

$$\frac{\mathrm{d}R_{\mathrm{O2,d}}}{\mathrm{d}t} = F_{\mathrm{mix,O2,d}} - 2F_{\mathrm{nit,d}} - F_{\mathrm{ammon,d}} - 2F_{\mathrm{mtrophy,d}} - F_{\mathrm{diff,O2,z}} \tag{2.176}$$

$$\begin{aligned}\frac{\mathrm{d}R_{\mathrm{H2O,d}}}{\mathrm{d}t} &= F_{\mathrm{ammon,d}} + \tfrac{148.4}{106}F_{\mathrm{denit,d}} + F_{\mathrm{nit,d}} + 2F_{\mathrm{mtrophy,d}} + F_{\mathrm{precip,d}} \\ &\quad + 3F_{\mathrm{sorb,d}} - F_{\mathrm{diss,d}}\end{aligned} \tag{2.177}$$

$$\frac{\mathrm{d}R_{\mathrm{FeO,d}}}{\mathrm{d}t} = F_{\mathrm{mantle,Fe}} + F_{\mathrm{mix,FeO,d}} \tag{2.178}$$

$$\frac{\mathrm{d}R_{\mathrm{FeOH3,d}}}{\mathrm{d}t} = F_{\mathrm{export,FeOH3}} - F_{\mathrm{sorb,d}} - F_{\mathrm{sed,FeOH3,z}} \tag{2.179}$$

$$\frac{\mathrm{d}R_{\mathrm{FePO4,d}}}{\mathrm{d}t} = F_{\mathrm{export,FePO4}} + F_{\mathrm{sorb,d}} - F_{\mathrm{sed,FePO4,z}} \tag{2.180}$$

2.9.5 Pelagic Sediments

$$\frac{\mathrm{d}R_{\mathrm{N2,z}}}{\mathrm{d}t} = F_{\mathrm{diff,N2,z}} + \tfrac{42}{106}F_{\mathrm{denit,z}} \tag{2.181}$$

$$\frac{\mathrm{d}R_{\mathrm{RN,z}}}{\mathrm{d}t} = F_{\mathrm{diff,RN,z}} + \tfrac{16}{106}\left(F_{\mathrm{ammon,z}} + F_{\mathrm{denit,z}} + F_{\mathrm{methgen,z}}\right) - F_{\mathrm{nit,z}} - F_{\mathrm{hyd}} \tag{2.182}$$

$$\frac{\mathrm{d}R_{\mathrm{HNO3,z}}}{\mathrm{d}t} = F_{\mathrm{diff,HNO3,z}} + F_{\mathrm{nit,z}} - \tfrac{84.4}{106}F_{\mathrm{denit,z}} \tag{2.183}$$

$$\begin{aligned}\frac{\mathrm{d}R_{\mathrm{H3PO4,z}}}{\mathrm{d}t} &= F_{\mathrm{diff,H3PO4,z}} + \tfrac{1}{106}\left(F_{\mathrm{ammon,z}} + F_{\mathrm{denit,z}} + F_{\mathrm{methgen,z}}\right) + F_{\mathrm{scav,z}} \\ &\quad - F_{\mathrm{sorb,z}} - F_{\mathrm{burial,PO4,z}}\end{aligned} \tag{2.184}$$

$$\frac{\mathrm{d}R_{\mathrm{ON,z}}}{\mathrm{d}t} = \tfrac{16}{106}\left(F_{\mathrm{sed,OC,z}} - F_{\mathrm{ammon,z}} - F_{\mathrm{denit,z}} - F_{\mathrm{methgen,z}}\right) - F_{\mathrm{burial,ON,z}} \tag{2.185}$$

$$\begin{aligned}\frac{\mathrm{d}R_{\mathrm{OP,z}}}{\mathrm{d}t} &= \tfrac{1}{106}\left(F_{\mathrm{sed,OC,z}} - F_{\mathrm{ammon,z}} - F_{\mathrm{denit,z}} - F_{\mathrm{methgen,z}}\right) \\ &\quad - F_{\mathrm{burial,OP,z}} - F_{\mathrm{scav,z}}\end{aligned} \tag{2.186}$$

$$\frac{\mathrm{d}R_{\mathrm{OC,z}}}{\mathrm{d}t} = F_{\mathrm{sed,OC,z}} - F_{\mathrm{ammon,z}} - F_{\mathrm{denit,z}} - F_{\mathrm{methgen,z}} - F_{\mathrm{burial,OC,z}} \tag{2.187}$$

$$\frac{\mathrm{d}R_{\mathrm{CaCO3,z}}}{\mathrm{d}t} = F_{\mathrm{sed,CaCO3,z}} + F_{\mathrm{precip,z}} + \tfrac{1}{2}F_{\mathrm{sfw}} - F_{\mathrm{diss,z}} - F_{\mathrm{burial,CaCO3,z}} \tag{2.188}$$

$$\begin{aligned}\frac{\mathrm{d}R_{\mathrm{TA,z}}}{\mathrm{d}t} &= F_{\mathrm{diff,TA,z}} + 2F_{\mathrm{diss,z}} + \tfrac{16}{106}(F_{\mathrm{ammon,z}} + F_{\mathrm{denit,z}} + F_{\mathrm{methgen,z}}) \\ &\quad + \tfrac{84.4}{106}F_{\mathrm{denit,z}} - 2F_{\mathrm{precip,z}} - F_{\mathrm{revwthr,z}} - 2F_{\mathrm{nit,z}} - F_{\mathrm{hyd}}\end{aligned} \tag{2.189}$$

$$\begin{aligned}\frac{\mathrm{d}R_{\mathrm{DIC,z}}}{\mathrm{d}t} &= F_{\mathrm{diff,DIC,z}} + F_{\mathrm{ammon,z}} + F_{\mathrm{denit,z}} + \tfrac{1}{2}F_{\mathrm{methgen,z}} + F_{\mathrm{mtrophy,z}} + F_{\mathrm{diss,z}} \\ &\quad - F_{\mathrm{precip,z}} - F_{\mathrm{sfw}}\end{aligned} \tag{2.190}$$

$$\frac{\mathrm{d}R_{\mathrm{CH4,z}}}{\mathrm{d}t} = F_{\mathrm{diff,CH4,z}} + \tfrac{1}{2}F_{\mathrm{methgen,z}} - F_{\mathrm{mtrophy,z}} \tag{2.191}$$

$$\frac{\mathrm{d}R_{\mathrm{O2,z}}}{\mathrm{d}t} = F_{\mathrm{diff,O2,z}} - 2F_{\mathrm{nit,z}} - F_{\mathrm{ammon,z}} - 2F_{\mathrm{mtrophy,z}} \tag{2.192}$$

$$\begin{aligned}\frac{\mathrm{d}R_{\mathrm{H2O,z}}}{\mathrm{d}t} &= F_{\mathrm{ammon,z}} + \tfrac{148.4}{106}F_{\mathrm{denit,z}} + F_{\mathrm{nit,z}} + 2F_{\mathrm{mtrophy,z}} + F_{\mathrm{precip,z}} + \tfrac{1}{2}F_{\mathrm{revwthr,z}} \\ &\quad + 3(F_{\mathrm{sorb,z}} - F_{\mathrm{burial,FePO4,z}}) + \tfrac{1}{2}F_{\mathrm{hyd}} - F_{\mathrm{diss,z}}\end{aligned} \tag{2.193}$$

$$\frac{\mathrm{d}R_{\mathrm{FeOH3,z}}}{\mathrm{d}t} = F_{\mathrm{sed,FeOH3,z}} - F_{\mathrm{sorb,z}} - F_{\mathrm{burial,FeOH3,z}} \tag{2.194}$$

$$\frac{\mathrm{d}R_{\mathrm{FePO4,z}}}{\mathrm{d}t} = F_{\mathrm{sed,FePO4,z}} + F_{\mathrm{sorb,z}} - F_{\mathrm{burial,FePO4,z}} \tag{2.195}$$

2.9.6 Unreactive Sediments

Note: the term $r_o = \frac{R_{CaCO3,o}}{R_{CaCO3,u}+R_{CaCO3,o}}$*, the ratio of* $CaCO_3$ *contained within the ocean crust versus the total* $CaCO_3$ *in both unreactive sediments and ocean crust.*

$$\frac{\mathrm{d}R_{\mathrm{SP,u}}}{\mathrm{d}t} = F_{\mathrm{burial,FePO4,z}} - F_{\mathrm{acc,SP}} - F_{\mathrm{subduct,SP}} - F_{\mathrm{cryst,SP}} \tag{2.196}$$

$$\frac{\mathrm{d}R_{\mathrm{CP,u}}}{\mathrm{d}t} = F_{\mathrm{burial,PO4,z}} - F_{\mathrm{acc,CP}} - F_{\mathrm{subduct,CP}} - F_{\mathrm{cryst,CP}} \tag{2.197}$$

$$\frac{\mathrm{d}R_{\mathrm{ON,u}}}{\mathrm{d}t} = F_{\mathrm{burial,ON,z}} - F_{\mathrm{acc,ON}} - F_{\mathrm{volc,ON}} - F_{\mathrm{subduct,ON}} - F_{\mathrm{cryst,ON}} \tag{2.198}$$

$$\frac{\mathrm{d}R_{\mathrm{OP,u}}}{\mathrm{d}t} = F_{\mathrm{burial,OP,z}} - F_{\mathrm{acc,OP}} - F_{\mathrm{subduct,OP}} - F_{\mathrm{cryst,OP}} \tag{2.199}$$

$$\frac{\mathrm{d}R_{\mathrm{OC,u}}}{\mathrm{d}t} = F_{\mathrm{burial,OC,z}} - F_{\mathrm{volc,OC}} - F_{\mathrm{acc,OC}} - F_{\mathrm{subduct,OC}} \tag{2.200}$$

$$\frac{\mathrm{d}R_{\mathrm{CaCO3,u}}}{\mathrm{d}t} = F_{\mathrm{burial,CaCO3,z}} - (1 - r_{\mathrm{o}})(F_{\mathrm{volc,CaCO3}} - F_{\mathrm{acc,CaCO3}} - F_{\mathrm{subduct,CaCO3}}) \tag{2.201}$$

$$\begin{aligned}\frac{\mathrm{d}R_{\mathrm{FeOH3,u}}}{\mathrm{d}t} &= F_{\mathrm{burial,FeOH3,z}} + F_{\mathrm{burial,FePO4,z}} - F_{\mathrm{acc,FeOH3}} \\ &\quad - F_{\mathrm{subduct,FeOH3}} - F_{\mathrm{cryst,FeOH3}}\end{aligned} \tag{2.202}$$

2.9.7 Continental crust

$$\frac{\mathrm{d}R_{\mathrm{NH4,c}}}{\mathrm{d}t} = F_{\mathrm{acc,NH4}} + F_{\mathrm{cryst,NH4}} + F_{\mathrm{cryst,ON}} - F_{\mathrm{wthr,NH4}} - F_{\mathrm{meta,NH4}} \tag{2.203}$$

$$\begin{aligned}\frac{\mathrm{d}R_{\mathrm{SP,c}}}{\mathrm{d}t} &= F_{\mathrm{mantle,P}} + F_{\mathrm{burial,FePO4,n}} + F_{\mathrm{acc,SP}} + F_{\mathrm{cryst,CP}} + F_{\mathrm{cryst,SP}} \\ &\quad + F_{\mathrm{cryst,OP}} - F_{\mathrm{wthr,SP}}\end{aligned} \tag{2.204}$$

$$\frac{\mathrm{d}R_{\mathrm{CP,c}}}{\mathrm{d}t} = F_{\mathrm{burial,PO4,n}} + F_{\mathrm{acc,CP}} + F_{\mathrm{meta,OP}} - F_{\mathrm{wthr,CP}} \tag{2.205}$$

$$\frac{\mathrm{d}R_{\mathrm{ON,c}}}{\mathrm{d}t} = F_{\mathrm{burial,ON,n}} + F_{\mathrm{acc,ON}} - \tfrac{16}{106}F_{\mathrm{wthr,oxi}} - F_{\mathrm{meta,OC}} \tag{2.206}$$

$$\frac{\mathrm{d}R_{\mathrm{OP,c}}}{\mathrm{d}t} = F_{\mathrm{burial,OP,n}} + F_{\mathrm{acc,OP}} - \tfrac{1}{106}F_{\mathrm{wthr,oxi}} - F_{\mathrm{meta,OP}} \tag{2.207}$$

$$\frac{\mathrm{d}R_{\mathrm{OC,c}}}{\mathrm{d}t} = F_{\mathrm{burial,OC,n}} + F_{\mathrm{acc,OC}} + \tfrac{9}{10}F_{\mathrm{terrprod}} - F_{\mathrm{wthr,oxi}} - F_{\mathrm{meta,OC}} \tag{2.208}$$

$$\frac{\mathrm{d}R_{\mathrm{CaCO3,c}}}{\mathrm{d}t} = F_{\mathrm{burial,CaCO3,n}} + F_{\mathrm{acc,CaCO3}} - F_{\mathrm{wthr,CaCO3}} - F_{\mathrm{meta,CaCO3}} \tag{2.209}$$

$$\frac{\mathrm{d}R_{\mathrm{Fe2SiO4,c}}}{\mathrm{d}t} = F_{\mathrm{mantle,Fe2SiO4}} - F_{\mathrm{wthr,Feox}} \tag{2.210}$$

$$\frac{\mathrm{d}R_{\mathrm{FeOH3,c}}}{\mathrm{d}t} = F_{\mathrm{burial,FeOH3,n}} + F_{\mathrm{burial,FePO4,n}} + F_{\mathrm{acc,FeOH3}} + F_{\mathrm{cryst,FeOH3}} \tag{2.211}$$

$$\frac{\mathrm{d}R_{\mathrm{Fe2O3,c}}}{\mathrm{d}t} = F_{\mathrm{wthr,Feox}} \tag{2.212}$$

$$\frac{\mathrm{d}R_{\mathrm{SiO3,c}}}{\mathrm{d}t} = F_{\mathrm{mantle,SiO3}} \tag{2.213}$$

2.9.8 Oceanic crust

$$\frac{\mathrm{d}R_{\mathrm{NH4,o}}}{\mathrm{d}t} = F_{\mathrm{hyd}} - F_{\mathrm{volc,NH4}} - F_{\mathrm{acc,NH4}} - F_{\mathrm{subduct,NH4}} - F_{\mathrm{cryst,NH4}} \tag{2.214}$$

$$\frac{\mathrm{d}R_{\mathrm{CaCO3,o}}}{\mathrm{d}t} = F_{\mathrm{sfw}} - r_{\mathrm{o}}(F_{\mathrm{volc,CaCO3}} - F_{\mathrm{acc,CaCO3}} - F_{\mathrm{subduct,CaCO3}}) \tag{2.215}$$

2.9.9 Upper Mantle

$$\frac{\mathrm{d}R_{\mathrm{N,m}}}{\mathrm{d}t} = F_{\mathrm{subduct,NH4}} + F_{\mathrm{subduct,ON}} - F_{\mathrm{mantle,N}} \tag{2.216}$$

$$\frac{\mathrm{d}R_{\mathrm{P,m}}}{\mathrm{d}t} = F_{\mathrm{subduct,CP}} + F_{\mathrm{subduct,OP}} + F_{\mathrm{subduct,SP}} - F_{\mathrm{mantle,P}} \tag{2.217}$$

$$\frac{\mathrm{d}R_{\mathrm{C,m}}}{\mathrm{d}t} = F_{\mathrm{subduct,CaCO3}} + F_{\mathrm{subduct,OC}} - F_{\mathrm{mantle,C}} \tag{2.218}$$

$$\frac{\mathrm{d}R_{\mathrm{Fe,m}}}{\mathrm{d}t} = F_{\mathrm{subduct,FeOH3}} - F_{\mathrm{mantle,FeO}} - 2F_{\mathrm{mantle,Fe2SiO4}} \tag{2.219}$$

$$\frac{\mathrm{d}R_{\mathrm{SiO3,m}}}{\mathrm{d}t} = -F_{\mathrm{mantle,SiO3}} \tag{2.220}$$

2.9.10 Temperature

$$\frac{dT}{dt} = \frac{A_E}{M_{\mathrm{oc}}c_p}\left((1-\alpha)\left(\frac{S(t)}{4}\right)\left(1+\frac{3}{4}\gamma_{IR}\right) - \sigma T^4\right) \tag{2.221}$$

2.9.11 Mass Conservation

These differential equations account for oxygen and hydrogen atoms lost and gained from fluxes including hydrogen escape to space, species that I do not explicitly track (such as SiO_2 or CaO) and speciation changes in the otherwise unresolved mantle reservoir. Species lost from resolved reservoirs are added and species gained from unresolved reservoirs are subtracted.

$$\begin{aligned}\frac{\mathrm{d}R_{\mathrm{H,x}}}{\mathrm{d}t} &= F_{\mathrm{Hesc,H}} - F_{\mathrm{cryst,ON}} + 2F_{\mathrm{subduct,OC}} + 3\big(F_{\mathrm{subduct,CP}} + F_{\mathrm{subduct,SP}} \\ &\quad + F_{\mathrm{subduct,OP}} - F_{\mathrm{mantle,P}} + F_{\mathrm{subduct,ON}} - f_{\mathrm{red}}F_{\mathrm{mantle,N}} + F_{\mathrm{subduct,FeOH3}}\big) \\ &\quad + 4\big(F_{\mathrm{subduct,NH4}} - f_{\mathrm{red}}F_{\mathrm{mantle,C}}\big)\end{aligned} \tag{2.222}$$

$$\begin{aligned}\frac{\mathrm{d}R_{\mathrm{O,x}}}{\mathrm{d}t} &= \tfrac{1}{2}(F_{\mathrm{revwthr,n}} + F_{\mathrm{revwthr,z}} + F_{\mathrm{hyd}} - F_{\mathrm{wthr,sil}} - F_{\mathrm{wthr,NH4}} - F_{\mathrm{meta,NH4}} - F_{\mathrm{volc,NH4}}) \\ &\quad + F_{\mathrm{subduct,OC}} + F_{\mathrm{volc,CaCO3}} + F_{\mathrm{meta,CaCO3}} - F_{\mathrm{sfw}} - F_{\mathrm{mantle,FeO}} \\ &\quad + 2(F_{\mathrm{wthr,Feox}} - (1-f_{\mathrm{red}})F_{\mathrm{mantle,C}}) + 3(F_{\mathrm{subduct,CaCO3}} + F_{\mathrm{subduct,FeOH3}}) \\ &\quad + 4(F_{\mathrm{subduct,CP}} + F_{\mathrm{subduct,SP}} + F_{\mathrm{subduct,OP}} - F_{\mathrm{mantle,P}} - F_{\mathrm{mantle,Fe2SiO4}})\end{aligned} \tag{2.223}$$

Chapter 3

A nominal run of EONS

I present a run of *EONS*, which is initialised for Eoarchean (4 Ga) conditions, and runs through Earth history. This run reproduces the major features of Earth's geochemical evolution with minimal forcings applied and ends with a good reproduction of preindustrial conditions. I refer to this as the nominal run.

The following sections detail tuning requirements for producing such a run, organized by major systems (biosphere, atmosphere, ocean, etc). I overview the model output for the system as it changes through time in stages, bracketed by the major transition events:

1. Eoarchean (4 - 3.5 Ga, up to initialization of photosynthesis)
2. Paleo- through Neo- Archean (3.5 - 2.3 Ga, up to the Great Oxidation Event)
3. Paleo- to middle Neo- Proterozoic (2.3 - 0.8 Ga, up to evolution of fungi)
4. Cryogenian (0.8 - 0.65 Ga, up to evolution of large organisms)
5. Ediacaran (0.65 - 0.4 Ga, up to evolution of vascular plants)
6. Devonian through modern (0.4 Ga - present)

I then discuss implications for understanding the Earth system as a whole. I highlight where the nominal run succeeds and falls short, and explain why key tuning choices were made and their implications for future experiments and further model refinement. Many of the chemical changes on the Earth's surface in the model run can be attributed to evolutionary developments; as such, I frame my discussion of the Earth system by first characterizing the evolutionary trajectory of the biosphere.

I use a consistent colour scheme for all evolution figures, where line colours correspond to species (either in the reservoir or produced/used in the flux being shown; table 3.1). A list of all modern references for fluxes and reservoirs denoted in each figure is included in appendix A. Model output excludes a 10 million year spin-up period, during which the atmosphere and oceans equilibrate.

Table 3.1: Figure colour scheme summary A list of all of the species and their corresponding colours used in the model output figures. In general: red/oranges = nitrogen; greens = carbon; blues = phosphorus; yellows = oxygen; purples = iron. Some colours represent multiple species which are not plotted in the same figures.

Species	Stochiometry	Colour
ammonia, organic nitrogen (ON)	NH_3	🟥
ammonium and total reduced N (RN)	NH_4^+	🟥
nitrate	HNO_3	🟧
dinitrogen	N_2	🟥
carbon dioxide and silicate	CO_2 and SiO_3	🟩
methane and organic carbon (OC)	CH_4 and CH_2O	🟩
dissolved inorganic carbon (DIC)	$CO_2 + HCO_3^- + CO_3^{2-}$	🟩
total alkalinity (TA)	(equation 2.6)	🟩
calcium carbonate	$CaCO_3$	🟩
dissolved phosphoric acid, organic phosphorus (OP)	H_3PO_4	🟦
silicate-bound phosphate (SP) and Fe(III)-phosphate	H_3PO_4 and $FePO_4$	🟦
carbonate-bound phosphate (CP)	H_3PO_4	🟦
oxygen	O_2	🟨
ferrous iron and hydrogen	FeO and H	🟪
fayalite olivine and hematite	Fe_2SiO_4 and Fe_2O_3	🟪
iron hydroxide	$Fe(OH)_3$	🟪

3.1 Biosphere evolution

The modelled biosphere is detailed in figure 3.1, and described in detail in the following sections. The relative availability of key nutrients is shown in figure 3.2.

3.1.1 Biosphere: chronology

3.1.1.1 Stage 1

The pre-oxygenic photosynthesis biosphere is limited by reduced iron availability. Reduced iron levels gradually decrease as photo-ferrotrophy balances with mantle influx (figure 3.1 a), bringing the Eoarchean biosphere to a pseudo-steady state production flux of nearly 1×10^{12} mol C/yr at the end of this stage (figure 3.1 b). Phosphorus levels increase as iron levels equilibrate and from increasing continental weathering influx (figure 3.1 a). Fixation grows the available fixed nitrogen reservoir to approximately one tenth the modern surface reservoir at pseudo-steady state (figure 3.1 a and c). Figure 3.2 shows relative nitrogen and phosphorus limitations: nutrient levels increase until the end of this stage due to photo-ferrotrophy being more strongly limited by reduced iron.

Remineralization is dominated by methanogenesis due to absent dissolved oxygen or nitrate (figure 3.1 d) returning most organic carbon produced in productivity back to the dissolved nutrient reservoirs, with very little carbon buried as organics (figure 3.1 e). During this stage, the fraction of carbon buried as organics versus as both organic and inorganic materials (f_{org}) is a function of extensive carbonate burial (discussed further in section 3.6.1.1) as well as extended residence timescales in the reactive sediments from lower continental erosion (section 2.3.2) and smaller organisms sinking more slowly out of the surface and deep oceans (section 2.3.6).

3.1.1.2 Stage 2

Oxygenic photosynthesis evolves and rapidly dominates the biosphere, causing significant nutrient limitation through to the GOE as organic matter is preferentially buried in anoxic sediments. When photosynthesizer productivity reaches its full extent following a growth period (section 2.3.4) the availability of nutrients drops precipitously, entering a stage of significant phosphorus limitation for the next billion years (figure 3.2). In this period, photosynthesis levels reach a pseudo-steady state level of approximately 1×10^{14} mol C/yr and organic carbon burial fraction rises to approximately 3% (figure 3.1 b and e). Nitrogen fixation responds to phosphorus availability and nitrogen levels correspondingly plateau (figure 3.1 c), but the production of oxygen allows nitrification to expand the nitrate reservoir, which rapidly grows to approximately 10% of the total fixed nitrogen reservoir (figure 3.1 a). A transient peak in HNO_3 appears as increasing phosphorus limitation leads to a decline in demand for fixed N. Nitrate then declines to a new pseudo-steady state as denitrification rises in response; the availability of dissolved oxygen expands remineralization beyond methanogenesis to include ammonification (figure 3.1 d).

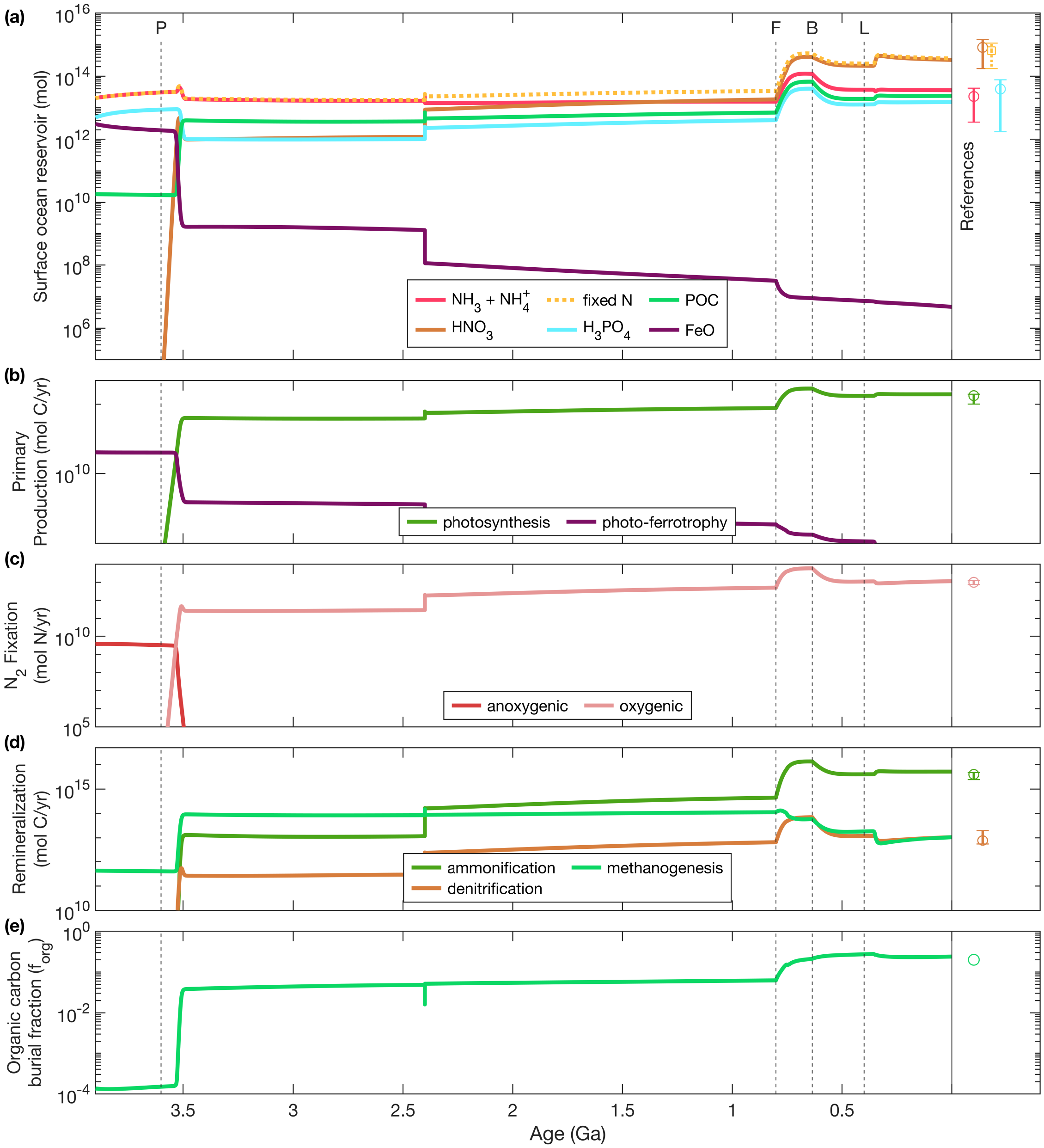

Figure 3.1: The evolution of biology. **a** All surface ocean nutrients; **b-d** primary production, nitrogen fixation, and remineralization fluxes (summed across all ocean/sediment reservoirs), respectively; **e** organic carbon burial fraction (f_{org}). Modern estimates for reservoirs and fluxes are denoted with symbols at the far right of each plot, with range estimates as vertical bars (citations in table A.3); the solid vertical line denotes the end of model output. Black dashed vertical lines denote forced evolutionary transitions: *P* for oxygenic photosynthesis, *F* for fungi, *B* for increased body sizes, and *L* for vascular land plants.

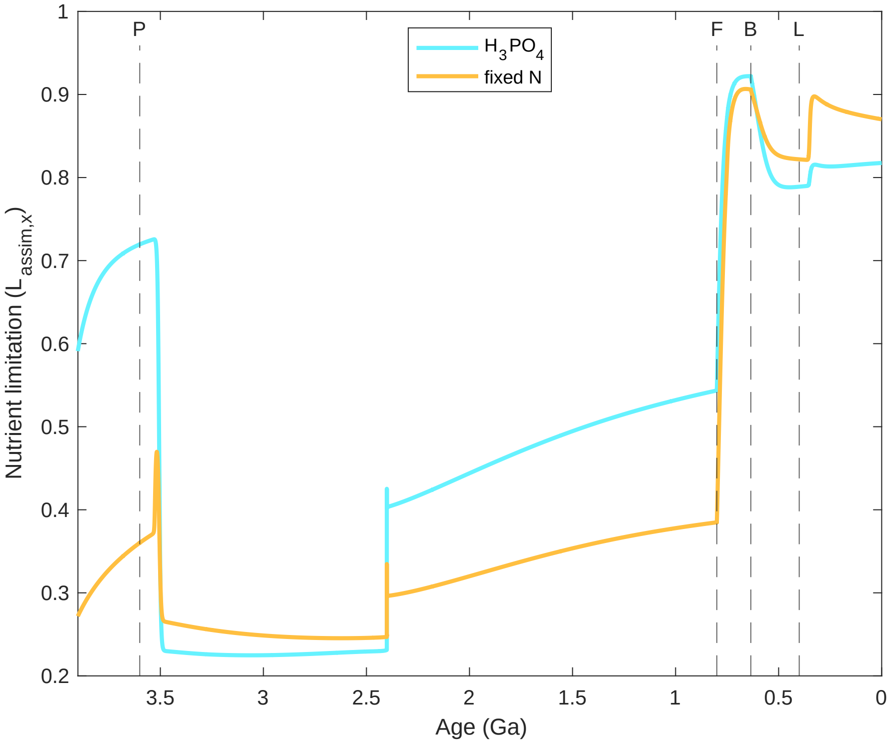

Figure 3.2: The evolution of nutrient limitations. Biological assimilation limitations by phosphorus and nitrogen surface ocean levels through time. Values indicate relative availability of the nutrient ($L_{\text{assim},x} = 1$ indicates no limitation). Black dashed vertical lines denote forced evolutionary transitions: *P* for oxygenic photosynthesis, *F* for fungi, *B* for increased body sizes, and *L* for vascular land plants.

3.1.1.3 Stage 3

The post-GOE biosphere is denoted by a rapid shift towards aerobic processes (ammonification) at the expense of anaerobic processes (photo-ferrotrophy, methanogenesis; see figure 3.1 b and d) with a corresponding rise in oxygenated nutrients (nitrate) over reduced nutrients (ammonia/ammonium, FeO; see figure 3.1 a). The oxygen transition is further demarcated by a transient dip in organic carbon burial (figure 3.1 e) as remineralization becomes more efficient along aerobic pathways (and because of perturbations within the carbonate system, discussed further in section 3.6.1.2). Nutrient limitation shifts from phosphorus to nitrogen over this transition as denitrification increases (figure 3.2 and 3.1 d). The post-GOE biosphere is characterized by a slow increase in nutrient availability (due to increased oxidative weathering) and a continuous decline in reduced nutrient reservoirs (figure 3.1 a). Organic carbon burial increases in lockstep with photosynthesis (figure

3.1 e), causing a persistent if slow expansion of the atmospheric oxygen reservoir (section 3.2.1.3). Oxygenic fixation, ammonification, and denitrification fluxes increase slightly across the 1.6 - 0.8 Ga period, coincident with a slow decline in anoxic processes such as photo-ferrotrophy and methanogenesis (figure 3.1 b-d). Nitrogen and phosphorus limit the biosphere to approximately 40-50% modern efficiency through the majority of this stage (figure 3.2).

3.1.1.4 Stage 4

The evolution of fungi at 0.7 Ga corresponds to a rapid influx of phosphorus with cascading effects for the biosphere. The post-GOE pseudo-steady state is disrupted by increased phosphorus influx to the ocean, boosting productivity beyond modern rates and resulting in extensive organic carbon burial. Photosynthesis and nitrogen fixation jump sharply; the latter easing nitrogen limitation (figure 3.1 a-c and figure 3.2). Phosphorus returns to being the primary limiting nutrient on the system because of progressive oxygenation in the deep ocean and sediments inhibiting P scavenging and allowing nitrogen levels to equilibrate (see section 3.3.1.4). Net primary productivity exceeds modern rates by the end of this stage (figure 3.1 b).

3.1.1.5 Stage 5

The evolution of large-bodied organisms in the Ediacaran increases export efficiency (figure 3.1 d), returning surface nutrient levels and productivity fluxes to near modern levels (3.1 a-c). Organic carbon burial continues its massive expansion (figure 3.1 e), increasing from near 5% to 20% at 0.65 Ga at the end of this stage.

3.1.1.6 Stage 6

Land colonization by vascular plants triggers the full oxygenation of the deep ocean and evolves the biosphere to its modern state. Additional oxygen production by the new terrestrial biosphere at 0.4 Ga increases deep ocean oxygenation (discussed further in section 3.2.1.6), resulting in nitrate dominating the fixed nitrogen reservoir (figure 3.1 a) and declining anaerobic remineralization fluxes (figure 3.1 d). Lowered denitrification reduces fixed N loss, and thus causes a slight decline in fixation and a jump in nitrogen availability as a nutrient (figure 3.1 c and figure 3.2).

Carbon burial fraction declines across this period from a high of 25% to 20% following this final evolutionary transition (figure 3.1 e). Vascular land plants enhance silicate and carbonate weathering fluxes, increasing ocean pH (discussed further in sections 3.2.1.6 and 3.6.1.6); the result is increased carbonate precipitation over dissolution, which contributes to the decline in organic carbon burial. This decline is also a function of the increasing oxygenation of the deep ocean, which expands ammonification to previously anoxic bottom waters and sediments and decreases burial efficiency.

3.1.2 Biosphere: tuning requirements

Early primary production by photo-ferrotrophy is highly sensitive to the influx of reduced iron from the mantle; a higher influx from a more reducing or faster convecting mantle would likely result in higher pseudo-steady state primary production. Assuming slower sinking rates prior to the evolution of large organisms is important in bolstering early primary production; faster sinking in the anoxic ocean would increase burial efficiency but also sequester more nutrients onto the continents and make the system less productive overall. Similarly, it is important for the early biosphere's productivity that residence time for particulate matter in the sediments is longer than at present (as controlled by erosional influx, χ_{eros}, a function of relative continent size); longer residence times in the sediments allows for more remineralization and returns nutrients more efficiently to their dissolved reservoir. Constant modern sediment residence timescales in an anoxic deep ocean would yield significantly higher f_{org} but also would inhibit primary production by sequestering key nutrients. Phosphorus weathering and burial flux balance is also key to the biosphere; I comment on this further in section 3.3.2.

3.1.3 Biosphere: implications

Biosphere productivity has increased through geologic time as more efficient pathways emerge. Characteristic of this model's design is a fundamental electron-donor limitation on primary productivity prior to the evolution of oxygenic photosynthesis; as the only anoxygenic pathway for primary production is photo-ferrotrophy, the biosphere is initially limited by FeO availability and is approximately 4 orders of magnitude lower than modern day. Fixation and remineralization are subsequently lower than modern rates by the same magnitude (figures 3.1 a, b, c, and d). Other organisms utilizing H_2S, H_2, and CO as electron donors have not been considered here and may very well have aided in maintaining higher primary productivity, perhaps even comparable to the modern level, during this stage (Kharecha et al., 2005). Additionally, higher or additional influxes of FeO into the system would allow for a higher level of primary production at pseudo-steady state. This model suggests that the Proterozoic biosphere had considerable levels of primary productivity, perhaps within two orders of magnitude of the modern biosphere.

Nitrogen and phosphorus limitations alternate across the GOE. Nutrient limitations primarily determine the efficiency of the ocean biosphere, and both nitrogen and phosphorus have been the ultimate limiting nutrient at different times. I do not see any indication that the onset of nitrification-denitrification causes a decrease in the fixed nitrogen reservoir, and I do not see an extensive nitrogen limited phase causing the delay between photosynthesis evolution and the GOE as predicted by other models (Fennel et al., 2005). I do, however, see nitrogen limiting conditions preceding photosynthesis evolution and in the post-GOE stage. The stalled expansion of the fixed N reservoir is apparently caused by lowered fixation, which itself is limited by the availability of phosphorus (section 2.4.1.3). Both nutrients are quite limiting in the period between 3.5 and 2.3 Ga, suggesting that burial of organic matter and removal of nutrients from the system is the ultimate reason for slow oxygen rise; this is not wholly inconsistent with the hypothesis that the GOE delay is a function of organic carbon accumulation onto continental bodies (Peters & Husson, 2017). Both nutrient limitation and the gradual increase of oxygen sources over sinks could plausibly contribute to the delay.

3.2 Atmosphere-ocean and climate evolution

The evolution of the modelled atmosphere and climate is shown in figure 3.3 and the ocean is shown in figure 3.4.

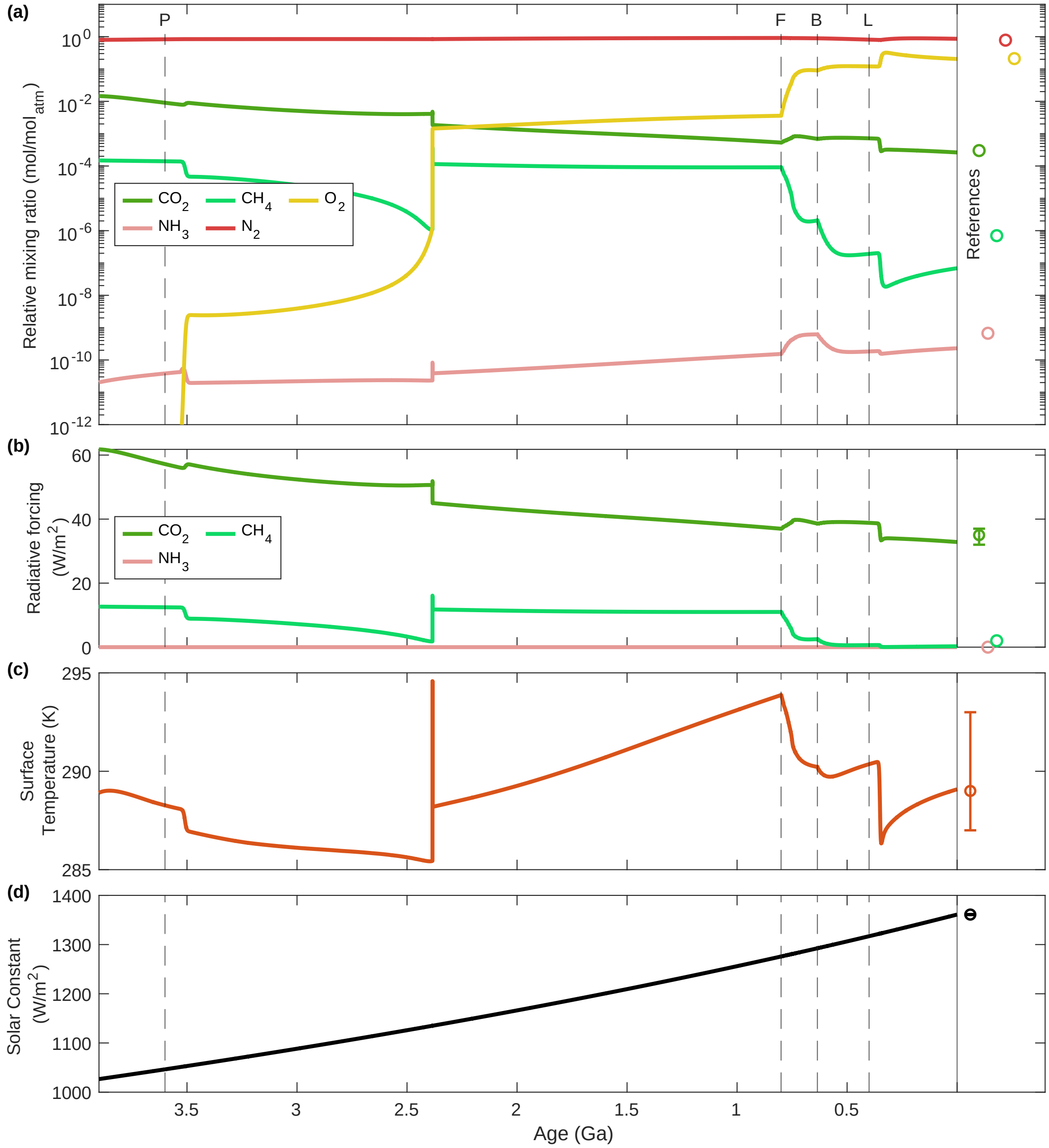

Figure 3.3: The evolution of the atmosphere and climate. **a** Atmospheric composition; note mixing ratios are moles of the gas divided by total moles in a 1 bar atmosphere. **b** Radiative forcing by greenhouse gases (Wm^{-2}); **c** surface temperature (K); **d** prescribed evolution of solar constant (Wm^{-2}). Modern estimates for reservoirs and fluxes are denoted with symbols at the far right of each plot, with range estimates as vertical bars (citations in table A.3); the solid vertical line denotes the end of model output. Black dashed vertical lines denote forced evolutionary transitions: *P* for oxygenic photosynthesis, *F* for fungi, *B* for increased body sizes, and *L* for vascular land plants.

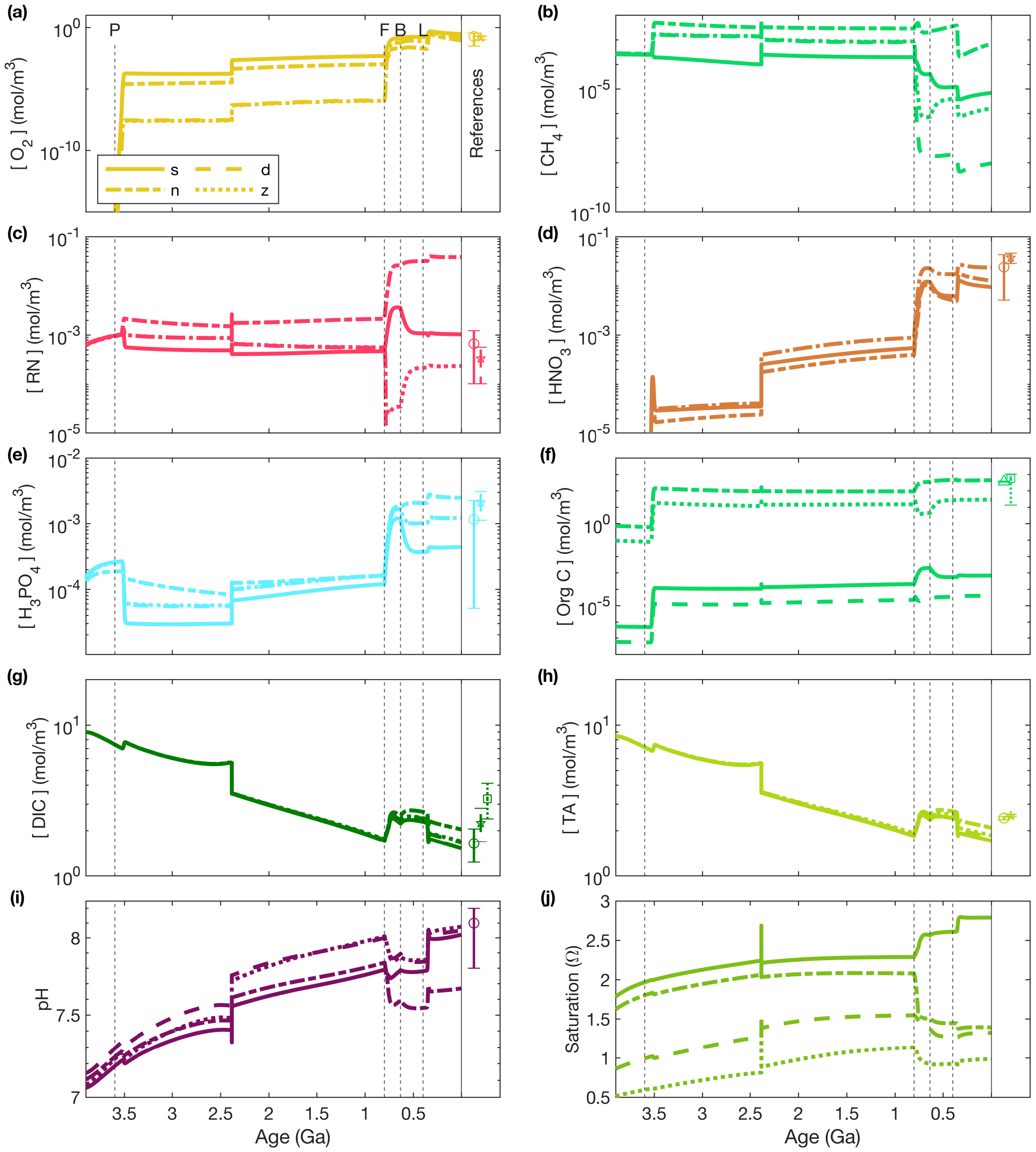

Figure 3.4: The evolution of ocean reservoirs. In the legend, *s*, *n*, *d*, and *z* denote surface ocean, neritic (shelf) sediments, deep ocean, and pelagic sediments, respectively. **a-f** Concentrations of reactive species (oxygen, methane, reduced nitrogen, nitrate, phosphate, and organic carbon, respectively; note that reduced nitrogen is comprised of NH_3 and NH_4^+ in equilibrium). **g-j** Inorganic carbon system parameters (dissolved inorganic carbon, total alkalinity, pH, and carbonate saturation, respectively). Modern estimates for reservoirs and fluxes are denoted with symbols at the far right of each plot, with range estimates as vertical bars (citations in table A.3); the solid vertical line denotes the end of model output. Black dashed vertical lines denote forced evolutionary transitions: *P* for oxygenic photosynthesis, *F* for fungi, *B* for increased body sizes, and *L* for vascular land plants.

3.2.1 Atmosphere-ocean: chronology

3.2.1.1 Stage 1

Ocean chemistry is in equilibrium with the atmosphere, with limited influxes from the continents. Dinitrogen and CO_2 rapidly become the largest components of the pre-photosynthesis atmosphere, owing to mantle outgassing and the limited draws of nitrogen fixation and continental weathering, respectively, in this period. Most CH_4 is biologically sourced (only 1% of mantle carbon outgassed is CH_4), and as such its atmospheric level is limited by biosphere production via methanogenesis. Ammonia sources are similarly primarily biological, bolstered by a small fraction of mantle nitrogen outgassing, and this species has the additional draw of biosphere uptake. Nutrient species (RN and H_3PO_4) gradually increase with fixation and silicate-bound phosphorus weathering, respectively (figures 3.4 c and e compared with figures 3.1 c and section 3.3.1.1); organic carbon is in pseudo-steady state (figure 3.4 f), reflecting photo-ferrotrophy levels (figure 3.1 b) and influencing dissolved RN and H_3PO_4 at the end of this stage. Relatively low ocean pH and high demand in productivity in this period (figures 3.2 and 3.4 i) limits NH_3 speciation and gas exchange into the atmosphere; for these reasons, NH_3 partial pressure is low throughout this stage and there is negligible radiative forcing from this greenhouse gas (figure 3.3 b).

Carbonate chemistry is in considerable flux as air-sea gas exchange and the initialization of the inorganic carbon pump gradually draws carbon from the atmosphere into the ocean and continents; the expansion of silicate weathering, which converts atmospheric CO_2 into alkalinity, also causes the gradual rise in ocean pH (figure 3.4 g-j; discussed further in section 3.6.1.1). Carbon dioxide equilibrates with the ocean to approximately 20 PAL at the start of this stage and maintains pseudo-steady state at this level, providing the majority of the radiative forcing for this period (figure 3.3 a-b).

3.2.1.2 Stage 2

The evolution of oxygenic photosynthesis is initially a minor disruption to atmospheric chemistry, introducing oxygen to the ocean and limiting the reservoirs of N and P. The evolution of photosynthesis initiates at the start of this stage; the gradual increase in oxygen following 3.4 Ga results from reductant sequestration via organic carbon burial (figure 3.1 e). As the fraction of carbon buried with organics is not a defined parameter but an output in my model, the timing of the GOE is primarily controlled by the surface reducing capacity as parameterized by relative mantle reductant outgassing (χ_{mantle}); I comment further on this control in section 3.2.2.

Oxygenic photosynthesis initiates a gradual rise in oxygen across the next billion years. Increased productivity boosts organic carbon reservoirs, especially in the neritic and pelagic sediments (figure 3.4 f) driving a rise in f_{org} (figure 3.1 e). Figure 3.4 (a) shows dissolved oxygen rising sharply in all ocean and sediment reservoirs immediately after photosynthesis evolution; this corresponds with an increase in nitrification and expansion of the dissolved nitrate reservoir (figure 3.4 d) and a decline in surface ocean methane (figure 3.4 b). Atmospheric methane is initially boosted by enhanced productivity inducing more methanogenesis but declines as more oxygen is produced until the GOE (figure 3.3 a and 3.1 d). Higher nutrient demand results in a sharp drop in surface ocean RN and H_3PO_4 in figures 3.4 c and e, intensifying biosphere limitation (figure 3.2); atmospheric NH_3 drops as demand on fixed N increases (figures 3.3 a and 3.1 c). Prior to the GOE, the carbonate system is in pseudo-steady state (figure 3.4 g-j), with near neutral pH.

3.2.1.3 Stage 3

Oxygen enters into the bistable range with methane around 2.3 Ga and rapidly transitions from around 10^{-6} PAL to almost 10^{-2} PAL; following the GOE, oxygen rises more slowly as productivity becomes nutrient limited (figure 3.2) and enters into a new pseudo-steady state with methane production. The ocean and sediments become increasingly oxygenated (although the deep ocean and pelagic sediments are still suboxic; figure 3.4 a). At the same time, methane in the surface ocean rebounds as methanogenesis experiences a slight, transient increase with higher productivity export to the suboxic deep ocean (figures 3.4 b and 3.1 d); this boosts atmospheric CH_4 levels to a pre-oxygenic photoysnthesis high and raises atmospheric temperature (figure 3.3 c). Nitrate continues to expand while reduced nitrogen levels stagnate (figures 3.4 c and d). The Mesoproterozoic "boring billion" in my model is characterized by little change in atmosphere-ocean chemistry, continuing pseudo-steady state across all reservoirs.

The climate shifts from cooling to rapid warming across the GOE transition. Atmospheric CO_2 is relatively stable going into the GOE, bolstered by increased methane oxidation (see section 3.5.1.3); the subsequent rise in CH_4 leads to a punctuated warming event that drives enhanced silicate weathering and stabilizes the climate at a higher temperature with increased CH_4 radiative forcing (figure 3.3 a-c; see section 3.6.1.3). The surface generally warms throughout this stage, with the exception of a brief cooling period coincident with the start of the GOE and CH_4 decline; gradual warming is generally a function of solar forcing parameter and should not be misconstrued as negating the reality of climate cooling events that may have arisen during this period due to ice-albedo feedbacks that are not resolved here.

Post-GOE warming accelerates the inorganic carbon cycle, triggering a sharp decline in DIC and alkalinity and disrupting carbonate saturation state across all ocean/sediment reservoirs as pH increases (figure 3.4 g-j). The temperature increase enhances continental weathering, alkalinity influx, and contributes to enhanced carbonate burial evidenced by spiking carbonate saturation corresponding to a dip in f_{org} (figures 3.4j and 3.1 e; discussed further in section 3.6.1.3). While the nutrient and oxygen levels in the ocean revert to a new pseudo-steady state in the aftermath of the GOE, the carbonate system continues it's longterm trend of CO_2 sequestration. Larger continents and higher temperatures slowly increase silicate and carbonate weathering's draw on atmospheric CO_2, transferring DIC and alkalinity to the ocean and continuing a rise in pH into the Neoproterzoic (figures 3.4 i and 3.3 a).

3.2.1.4 Stage 4

The evolution of fungi upends pseudo-steady state by boosting productivity and causing a major acceleration of oxygen's growth, significant climatic cooling, and shifting the limiting nutrient paradigm again. This finding is broadly consistent with theories surrounding the connection between land colonization by lichens and fungi and increasing oxygenation in the Neoproterozoic (Heckman et al., 2001; Lenton & Watson, 2004).[1] The influx of phosphorus spurs massive increases in primary production and a jump in atmosphere-ocean oxygen level that results in a nearly fully oxygenated ocean (figures 3.4 a-b, 3.3 a, and 3.1 b). Organic carbon levels in the surface ocean rise with productivity but decline in the pelagic sediments as increased dissolved oxygen there allows for extensive ammonification

---

[1] It has also been theorized that the Neoproterozoic oxygenation event resulted from changes in oxidative weathering of pyrite as the terrestrial biosphere evolved and started developing soils (Kanzaki & Kump, 2017; Kump, 2014); in a future version of *EONS* including a sulphur cycle, it may be possible to resolve this weathering transition and the potential effects on oxygen's rise.

and crashing methane production, causing a decline in all atmosphere-ocean CH_4 reservoirs (figures 3.4 b and f, 3.3 a, and 3.1 d). Dissolved RN and atmospheric NH_3 increase with fixation (figures 3.4 c, 3.3a and 3.1 c); I comment on the ammonia excursion further in section 3.4.1.3.

Carbonate saturation in the sediments and deep ocean declines sharply, resulting in widespread carbonate dissolution and leading to the massive expansion of f_{org} despite little change in total OC reservoirs (figures 3.4j and 3.1 e); as less carbon is buried as inorganic material, the fraction buried as organics rises. Declining pH and carbonate saturation and the corresponding bump in atmospheric CO_2 at 0.75 Ga (figures 3.4 i-j and 3.3a) are discussed in further detail in section 3.6.1.4. The small increase in CO_2 from this feedback partially compensates for the decline in CH_4 radiative forcing, such that the surface temperature drops only a few degrees (3.3 b-c).

3.2.1.5 Stage 5

The evolution of large bodied organisms causes a decline in organic carbon in the surface ocean as export efficiency increases and a shift in nutrient limitations (figures 3.4 c, e, and f, and 3.2), discussed earlier in section 3.1.1.5. Faster OC export and declining carbonate saturation lead to increasing f_{org} following this transition (figures 3.4 f and j and 3.1 e).

3.2.1.6 Stage 6

The Phanerozoic atmosphere-ocean system is a function of colonization of land by vascular plants, which completes the rise of oxygen to beyond 1 PAL and full oxygenation of the deep ocean during the Carboniferous as the terrestrial biosphere emerges (figures 3.4 a-b and 3.3 a). Nutrients and organic carbon reach their modern levels during this period as the biosphere becomes aerobic and continental influxes reach modern rates (figure 3.4 c-f); enhanced silicate/carbonate weathering and productivity causes a drop in CO_2 and a corresponding rise in pH (figures 3.3a, 3.4i, and 3.1 b and section 3.6.1.6). After a sharp temperature decline at the 0.4 Ga transition, warming resumes following increasing solar flux (figures 3.3 c-d). Atmospheric methane ends up lower than modern levels even with additional production in the simple terrestrial biosphere; this indicates a missing component or perhaps over-simplification in either the biological methane cycle or photochemical interactions, particularly methane oxidation.

3.2.2 Atmosphere-ocean: tuning requirements

This model interactively resolves the GOE, but timing and tempo of this transition can be significantly modified by two key parameters: mantle reductant outgassing flux and continental emergence. This nominal tuning arises from trying to fit these parameters as best as possible to their modern references and to evolve them within conservative limits. The relationship between mantle reductant outgassing tuning, organic carbon burial, and atmospheric oxygenation is shown in figure 3.5; many different GOE scenarios can occur, depending on the relative outflux of mantle reductants at the onset of photosynthesis.

Lower reductant flux requires less long-term organic carbon burial for net oxygen production to overwhelm surface reducing capacity. The GOE could have occurred at 2.3 Ga with a constant outflux of reductants, but only at a level 6-7x the modern rate (figure 3.5 c). Tuning χ_{mantle} depends mostly on the desired timing of the GOE, and acts to counteract the slow expansion of f_{org}. From the perspective of this model, constant $f_{\text{org}} = 0.2$ throughout geologic time, which is how some interpret the carbon isotope record (Hayes & Waldbauer, 2006; Marais et al., 1992; Schidlowski, 1988) is highly unlikely for many reasons, one being that such high burial would require significantly higher or more reducing mantle outgassing (or the emergence of the oxygenic biosphere much closer to the GOE) in order to result the tempo of surface oxygenation implied by the proxy record.

This atmosphere and climate history further depends on the treatment of continental growth; the initial atmospheric level of CO_2 and the overall trend of ocean pH and carbonate system behaviour depends on atmosphere-ocean equilibrium, which is in large part determined by the magnitude of silicate weathering with punctuated transitions reflecting significant changes in the biosphere (particularly the GOE, evolution of fungi, and land plants). Larger initial continents would draw out CO_2 rapidly via weathering and make the early Archean climate very cold (see section 3.6.2). Continental size further determines the initial ocean reservoir of phosphorus, which is exclusively sourced from the geosphere, and that in turn determines the pace of biosphere expansion (see section 3.3.3).

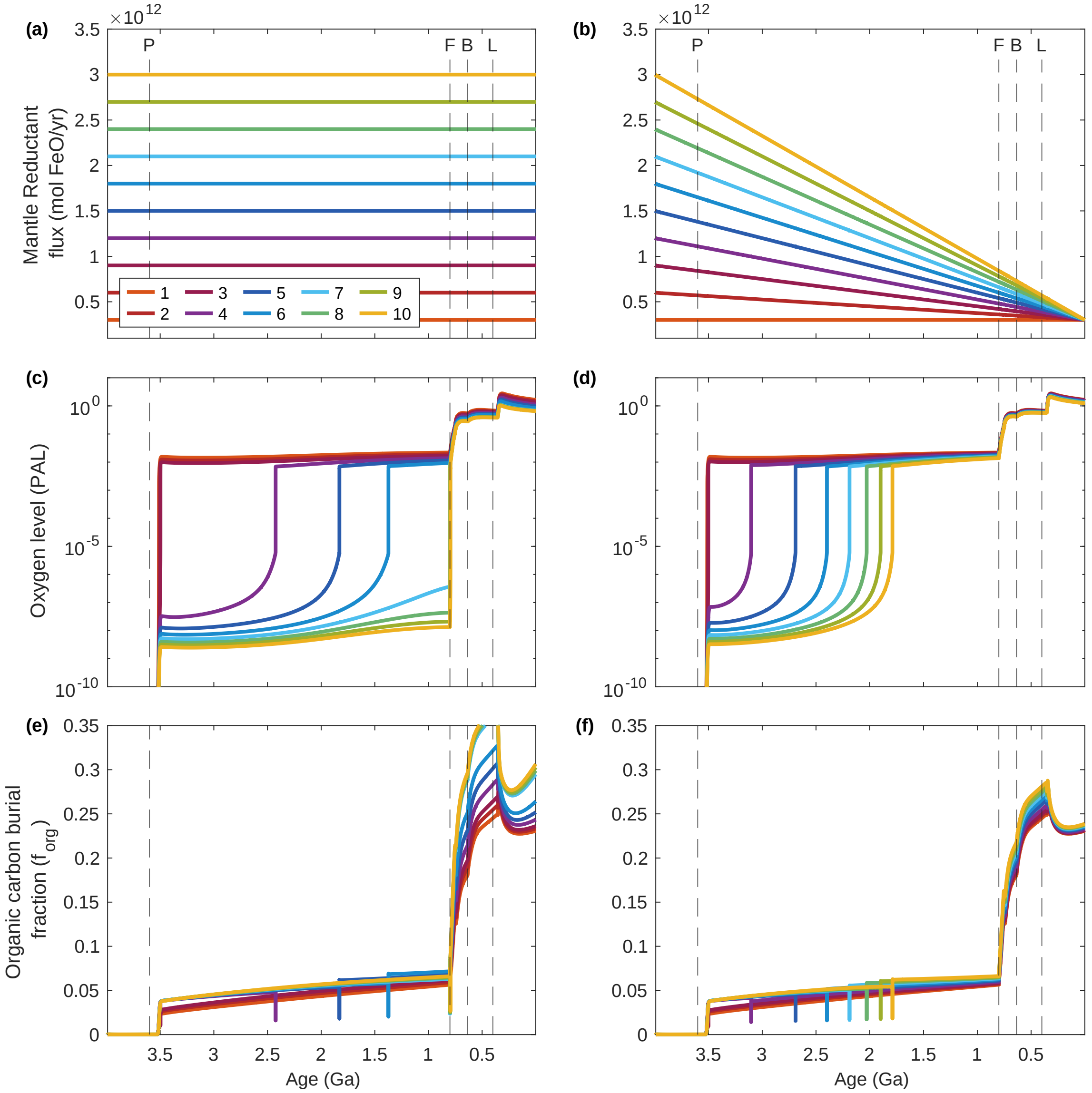

Figure 3.5: Timing the GOE by changing only $\chi_{\mathbf{mantle}}$ forcing. Left column (**a**, **c**, **e**) output from model runs with constant mantle reductant outflux, while right column (**b**, **d**, **e**) output from runs with linearly-decreasing mantle reductant outflux. Line colour denotes the value of χ_{mantle} (all other parameters in the model are kept the same). From top to bottom: **a** and **b** mantle reductant outfluxes (i.e. $\chi_{\text{mantle}}F_{\text{mantle,FeO,0}}$); **c** and **d** atmospheric oxygen levels (PAL); **e** and **f** fraction of total carbon buried as organic matter (f_{org}). Lower mantle reductant output is overwhelmed by lower net oxygen production (via the burial of organic carbon), resulting in earlier GOEs. Black dashed vertical lines denote forced evolutionary transitions: *P* for oxygenic photosynthesis, *F* for fungi, *B* for increased body sizes, and *L* for vascular land plants.

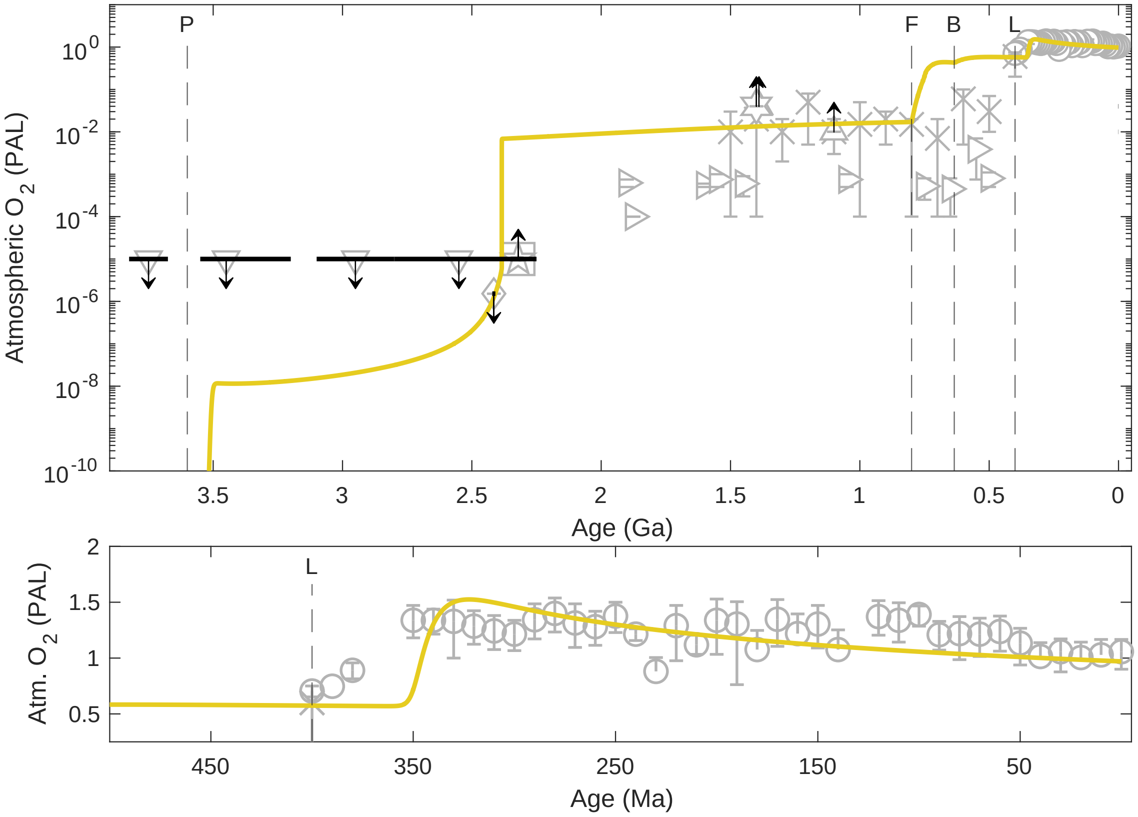

Figure 3.6: Oxygen curve and proxy compilation. Atmospheric oxygen through time in the model (yellow), constrained by literature estimates for atmospheric oxygen level (grey errorbars denote source's 1st standard deviation from mean). **a** Oxygen and estimates for the entire model run; **b** Phanerozoic period, which has a higher density of constraints. Arrows indicate maximums (↓) or minimums (↑) for oxygen based on existence mass independent fractionation of sulphur (MIF-S) signal, the duration of which is defined roughly by black bars. Symbols denote sources; △ = Canfield et al. (2018) and ✡ = Zhang et al. (2016), constraints from chromium isotopes; × = Krause, Mills, Merdith, Lenton, and Poulton (2022) estimates from δ^{13}C fractionation modelling; ◇ = Johnson, Gerpheide, Lamb, and Fischer (2014) constraints from uranite and pyrite; □ = Izon et al. (2022), ☆ = Luo et al. (2016), and ▽ = Claire et al. (2014) (and references therein), constraints from mass independent fractionation of sulphur isotopes; ○ = Glasspool and Scott (2010) constraints from charcoal; ◁ = Sperling et al. (2015) constraints from iron speciation; ▷ = Bellefroid et al. (2018) constraints from cerium anomalies (reading figure 4 data for 90 m chemocline). Black dashed vertical lines denote forced evolutionary transitions: *P* for oxygenic photosynthesis, *F* for fungi, *B* for increased body sizes, and *L* for vascular land plants.

My nominal run atmospheric oxygen curve is shown in figure 3.6 alongside constraints from different redox proxies in the literature; the timing and tempo of the rise of oxygen in this model fits extremely well within these constraints (figure

3.6). The evolution of photosynthesis initiates a gradual rise in oxygen that enters into the bistable range with methane around 2.3 Ga with secondary transition as fungi and terrestrial plants evolve around 0.7 Ga and 0.4 Ga, respectively. The Phanerozoic transition initiates a Carboniferous aged oxygen overshoot which gradually returns to modern levels, a finding predicted by other models focusing on the Phanerozoic (Bergman et al., 2004; Berner, 2009; Lenton et al., 2018).

3.2.3 Atmosphere-ocean: implications

Atmosphere-ocean chemistry is strongly controlled by biological transitions and complete surface oxygenation requires a terrestrial biosphere. This modelled atmosphere-ocean reflects major biological transitions and continental emergence. The impetus for adding in oxygen production in a terrestrial biosphere that evolves in two steps with fungi and then with land plants (see section 2.3.8) was an inability to achieve modern oxygen levels with modern ocean primary production and f_{org}; without this addition, oxygen in the atmosphere never exceeds 0.5 PAL, and the deep ocean and sediments remain anoxic. This tuning requirement is suggestive that the Phanerozoic started with suboxic deep oceans and that the modern ocean oxygen state was achieved relatively late, in the Devonian (Canfield, Poulton, & Narbonne, 2007; Krause et al., 2022).

The GOE and later expansion of the biosphere onto continents plausibly led to significant climate disruptions which may have resulted in mass extinctions. My results suggest that, from biological feedbacks alone, it is likely that the GOE was followed by a relatively warm period for the climate. An initial rise in oxygen might have caused a rise in atmospheric methane and surface temperature, whereas later rises (corresponding with oxygenation of the deep ocean) likely caused climate cooling, particularly as vascular plants and terrestrial biospheres evolve. Prior to the GOE, there is a marked decline in atmospheric CH_4 and temperature, corresponding well to the timing of the Paleoproterozoic snowball event (Hoffman, 2013; Kirschvink et al., 2000; Warke et al., 2020). The GOE is accompanied by a rapid rise in atmospheric temperature and CH_4, a result of increased surface aerobic remineralization and productivity followed by extensive anaerobic remineralization in the deoxygenated deep ocean. This reverses into a rapid decline as the silicate weathering feedback kicks in; a climate oscillation of this magnitude would have had severe consequences for the biosphere, which was also only beginning to cope with abundant oxygen. It is possible that this warming-cooling reversal, coupled with tectonic forcings, could have triggered significant global glaciation (Kopp et al., 2005).

The two-step oxygenation of the deep ocean caused by evolution of fungi (0.7 Ga) and land plants (0.4 Ga) also corresponds with major climatic cooling events. The temperature maximum prior to fungal evolution is followed by a rapid temperature crash as CH_4 production plummets; this feedback may have contributed to the Neoproterozoic snowball event (Hoffman et al., 1998). Even faster cooling occurs in the wake of vascular plant evolution, this time a perturbation to CO_2 (see section 3.6.1.6) correlates in time to the end-Devonian mass extinction (Kaiser et al., 2016). My model does not resolve very short term climate perturbations, punctuated events such as LIP eruptions, or global tectonic arrangements that undoubtably add to the complexity of the geologic oxygen record, particularly for the Phanerozoic portion of the record where more fine-scale oxygen oscillations are resolved.

3.3 Phosphorus cycle evolution

Figure 3.7 highlights the evolving global phosphorus cycle. Figure 3.8 highlights the C:P ratio of buried organic matter, a proxy for total phosphorus scavenging.

3.3.1 Phosphorus cycle: chronology

3.3.1.1 Stage 1

The early phosphorus cycle is dominated by influxes from continental reservoirs and outfluxes by sorption onto iron oxides. Continental expansion in the Eoarchean by mantle influx results in a silicate-bound phosphorus (SP) reservoir comparable to modern and significant weathering (figure 3.7 a and b). This influx is only 10% of the total modern P weathering flux, given the absence of terrestrial fungi and plants. The major outfluxes for $[H_3PO_4]$ are sorption onto iron-oxides and burial with apatite in sediments (figure 3.7 d-f). Oxide sorption declines until it broadly matches phosphorus influx, allowing dissolved phosphorus to rise to near-modern levels in the surface and deep ocean by the end of this stage (figure 3.7 c-d). Buried organic C:P declines steadily (figure 3.8); initially high rates of phosphate scavenging are in response to early biosphere P limitation (figure 3.2), but scavenging declines steadily as weathering transports more phosphorus to the ocean and P limitation eases. By the end of the stage, total OP export production remains several orders of magnitude lower than modern despite P availability (figure 3.7 b) as the pre-oxygenic photosynthesis biosphere achieves pseudo-steady state limited by FeO (section 3.1.1.1).

3.3.1.2 Stage 2

The emergence of oxygenic photosynthesis leads to increased phosphorus demand and biological influence over the phosphorus cycle. Biosphere expansion reduces ocean P reservoirs to a pseudo-steady state minimum at the end of this stage, bolstered by extensive scavenging (figure 3.8). Increasing burial spurs rapid growth of the continental OP reservoir (figure 3.7 a) as phosphorus sequestration shifts from oxide sorption to burial in organics and carbonates (figure 3.7 d-f). Sorption fluxes decline for the rest of the model run, mirroring declining iron oxide production by photo-ferrotrophy and increasing ocean pH (section 3.2.1.2); this flux is limited to lower pH conditions (section 2.5.7), and the trend in Fe-P reservoirs and sorption fluxes shown in figures 3.7 d-f broadly follows ocean pH (figure 3.4 i). The combination of higher production efficiency, high burial efficiency in anoxic sediments, and low oxidative weathering of sequestered OP (figures 3.7 b-f) pushes the system into a new pseudo-steady state with significantly lower dissolved P, severely limiting the oxygenic biosphere until the GOE (figure 3.2).

3.3.1.3 Stage 3

The phosphorus cycle is stabilized in the wake of the GOE, possibly because of feedbacks with the nitrogen system. Dissolved levels rebound slightly as oxidative weathering initiates (figure 3.7 b-c), easing both P limitation and scavenging (figures 3.8 and 3.2). Carbonate-bound P burial increases gradually throughout this period following progressive sequestration of atmospheric CO_2 by precipitation (section 3.2.1.3). The Mesoproterozoic therefore finds a new pseudo-steady state with relatively balanced phosphorus influxes and outfluxes, in response to a biosphere now limited by N (section 3.1.1.3).

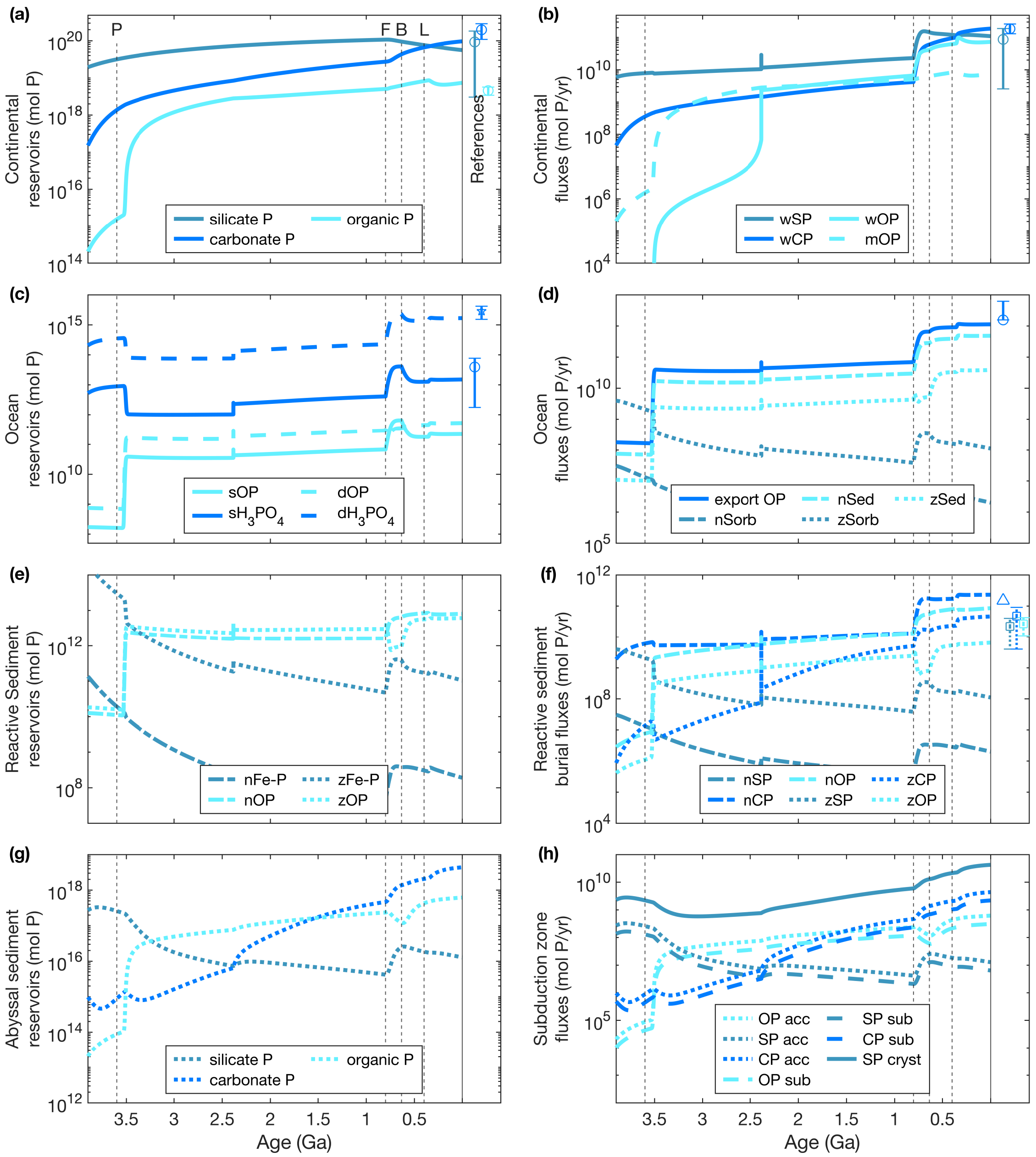

Figure 3.7: The evolution of phosphorus cycling. Left column (**a**, **c**, **e**, **g**) phosphorus geologic reservoirs; in the legends, *u* denotes unreactive pelagic sediments, *o* denotes oceanic crust (slab), and *s*, *n*, *d*, and *z* denote surface ocean, neritic (shelf) sediments, deep ocean, and pelagic sediments, respectively. Right column (**b**, **d**, **f**, **h**) phosphorus fluxes for each species out of the reservoirs in the corresponding left subplot (respectively: weathering (*w*) and metamorphism (*m*); export, sorption, and sedimentation; burial; accretion, subduction, and recrystallization). Modern estimates for reservoirs and fluxes are denoted with symbols at the far right of each plot, with range estimates as vertical bars (citations in table A.3); the solid vertical line denotes the end of model output. Black dashed vertical lines denote forced evolutionary transitions: *P* for oxygenic photosynthesis, *F* for fungi, *B* for increased body sizes, and *L* for vascular land plants.

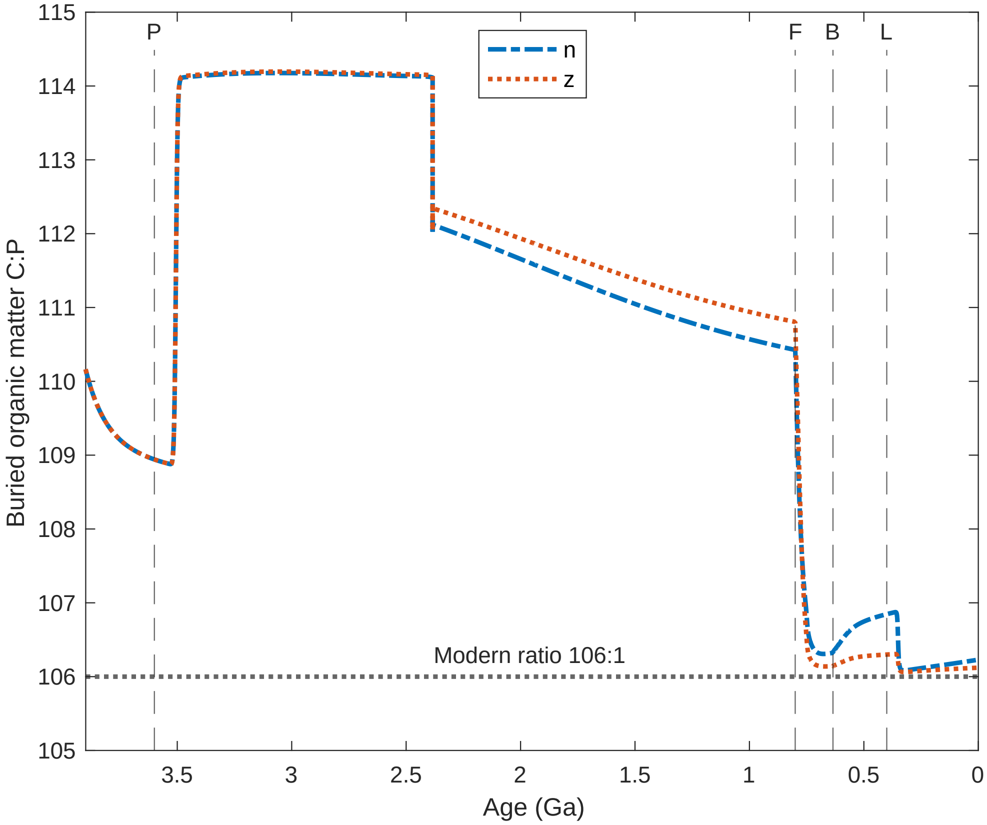

Figure 3.8: The evolution of organic matter C:P. The ratio of carbon to phosphate in buried organic matter. Line styles and colours correspond to the different sediment boxes: *n* is neritic (continental shelf) and *z* is pelagic sediments. Increased C:P in buried organic matter is a function of phosphate scavenging by decomposers in anoxic sediments, and is a function of bisophere P limitation and environmental oxygen level (see section 2.5.6). Black dashed vertical lines denote forced evolutionary transitions: *P* for oxygenic photosynthesis, *F* for fungi, *B* for increased body sizes, and *L* for vascular land plants. Dotted black horizontal line denotes modern day organic matter C:P ratio (106:1).

3.3.1.4 Stage 4

The P system is pushed out of pseudo-steady state following the evolution of fungi; this initiates a massive influx of inorganic P to the ocean, which in turn accelerates the biosphere (figure 3.7 b-d). Organic phosphorus in sediments again rises, and burial with apatite dominates outfluxes because of feedbacks in the inorganic carbon system (figure 3.7 e-f; discussed in more detail in section 3.6.1.4). A transient rise in iron-oxide sorption is likely related to the drop in pH coincident with this transition (section 3.2.1.4). Scavenging drops sharply as oxygen, and thus ammonification, rises in the pelagic sediments (figures 3.8 and 3.4 a), allowing nitrogen levels to equilibrate and pushing the system into a slightly P-limited regime (figure 3.2).

3.3.1.5 Stage 5

The development of large organisms in the Ediacaran decreases dissolved phosphorus to its modern level as remineralization in the water column becomes less efficient (figure 3.7 c). Faster sinking enhances export production (figure 3.7 d), causing a slight rise in scavenging as more organic matter is transported to suboxic sediments (figure 3.2). Geological phosphorus reservoirs are increasingly dominated by carbonate-bound P (figure 3.7 a), a function of increasing carbonate burial and the continuing decline of iron oxide sorption (figure 3.7 d-f; section 3.6.1.5).

3.3.1.6 Stage 6

The final transition phase into the modern phosphorus cycle follows the evolution of the terrestrial biosphere. Inorganic phosphorus weathering increases to its modern level (figure 3.7 b), pushing the oceanic phosphorus cycle into a new pseudo-steady state, excepting the continuous decline in iron-sorbed phosphorus reservoirs and fluxes. Ratios of C:P in buried organics return to Redfield ratio as the deep ocean oxygenates (figure 3.2). The modern geological P cycle is dominated by the balance in carbonate-bound P fluxes (figure 3.7 a-b, f-h).

3.3.2 Phosphorus cycle: tuning requirements

The balance between phosphorus weathering and burial partially determines whether the GOE occurs. The fraction of P buried with apatite (f_{apatite}) and the effect of fungi on P weathering timescales (χ_{fungi}) are two very important parameters controlling the balance of ocean P availability and thus the entire biological system. A very strong carbonate burial flux ($f_{\text{apatite}} > 0.1$) keeps the biosphere so nutrient limited after the evolution of oxygenic photosynthesis that oxygen production never overwhelms reductant input. If the effect of fungi on phosphorus weathering is weak prior to 3.5 Ga ($\chi_{\text{fungi}} > \frac{1}{10}$) then dissolved phosphorus exceeds 10x modern level and the GOE occurs very quickly after photosynthesis evolves; evidence for low Precambrian dissolved phosphorus precludes this scenario (Kipp & Stüeken, 2017).

3.3.3 Phosphorus cycle: implications

The climate has been sporadically destabilized by changes in phosphorus availability. During the period between evolution of oxygenic photosynthesis and fungi (3.5 - 0.7 Ga) there are huge shifts in phosphorus limitation and scavenging (figures 3.2 and 3.8). Surface temperature crashes broadly correlate with the rapid influxes of phosphorus to the ocean that define these shifts (figures 3.3 c and 3.7 c) by allowing large increases in biosphere productivity (figure 3.1 b). This has implications on organic matter burial efficiency through time as well; scavenging allows for phosphorus to be returned more efficiently to the ocean system in times of severe phosphorus limitation, but even so my modelled biosphere experiences periods of productivity very limited by P (figures 3.8 and 3.2). Nitrogen fixation's functional dependence on phosphorus further limits productivity in these conditions. As with high apatite burial, high organic matter burial in the Archean and Proterozoic oceans would severely restrict P (and hence fixed N) availability and would likely prevent a GOE from occurring, particularly because returning those sequestered nutrients to the ocean requires oxidative weathering, which only initiates after oxygen rises. Because of this, high organic matter burial efficiency in an anoxic ocean seems incompatible with the timing of the GOE.

3.4 Nitrogen cycle evolution

The evolution of the global nitrogen cycle is shown in figure 3.9.

3.4.1 Nitrogen cycle: chronology

3.4.1.1 Stage 1

The early nitrogen cycle includes significant sequestration into the continent and mantle. The inorganic and organic nitrogen cycles are intrinsically linked through nitrogen fixation, the singular pathway by which N_2 can be transferred to the continents and mantle. The nitrogen cycle "ramps up" as nitrogen fixation increases with phosphorus levels (see section 3.1.1.1). The rapid growth of the continental NH_4^+ reservoir (figure 3.9 c) is a testament to massive amounts of fixation and subsequent hydrothermal alteration (figure 3.9 h).

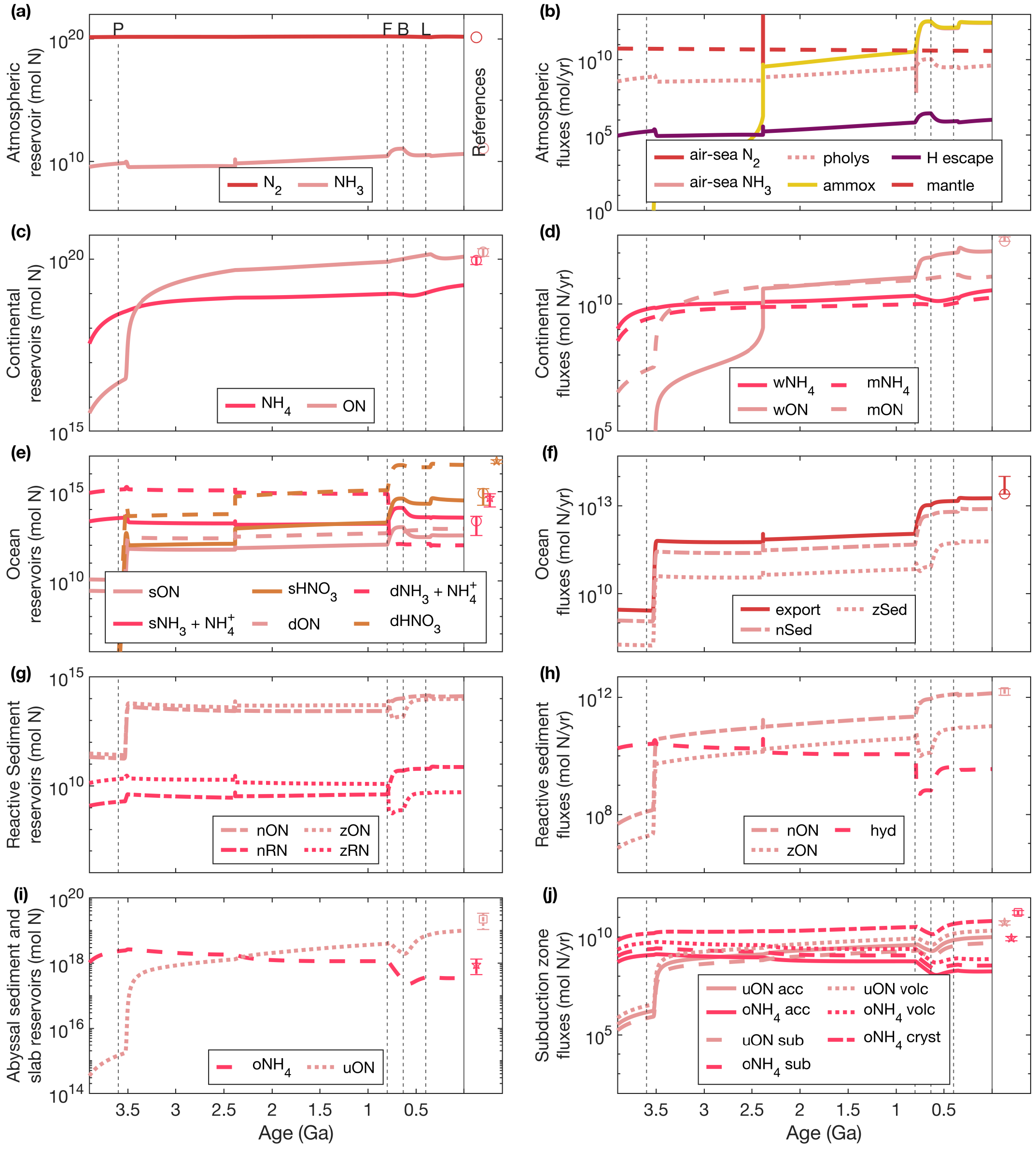

Figure 3.9: The evolution of nitrogen cycling. Left column (**a**, **c**, **e**, **g**, **i**) nitrogen reservoirs; in the legends, *u* denotes unreactive pelagic sediments, *o* denotes oceanic crust (slab), and *s*, *n*, *d*, and *z* denote surface ocean, neritic (shelf) sediments, deep ocean, and pelagic sediments, respectively. Right column (**b**, **d**, **f**, **h**, **j**) nitrogen fluxes for each species out of the reservoirs in the corresponding left subplot (respectively: air-sea gas exchanges, NH_3 photolysis, hydrogen escape, NH_3 photo-oxidation, and mantle outgassing; weathering (*w*) and metamorphism (*m*); export and sedimentation; burial and hydrothermal alteration; accretion, subduction, volcanism, and recrystallization). Silicate nitrogen is incorporated by hydrothermal alteration into the slab only, while organic nitrogen (NH_3) is buried in sediments from *n* and **z** reactive boxes and is not found in the slab. Modern estimates for reservoirs and fluxes are denoted with symbols at the far right of each plot, with range estimates as vertical bars (citations in table A.3); the solid vertical line denotes the end of model output. Black dashed vertical lines denote forced evolutionary transitions: *P* for oxygenic photosynthesis, *F* for fungi, *B* for increased body sizes, and *L* for vascular land plants.

As photo-ferrotrophy assumes pseudo-steady state at the end of this stage (figure 3.1 b), atmospheric NH_3 and dissolved RN reservoirs follow suit (figures 3.9 a and e); low ocean pH means RN is mainly NH_4^+, and therefore not exchanging with the atmosphere (figure 3.9 b-c); air-sea gas exchange is negative (into the ocean) and not visible throughout this stage, even with extremely high ocean RN levels. Readily available NH_4^+ is hydrothermally altered and accumulates in the oceanic crust, which is then mostly recrystallized onto the continent at subduction zones in a rapid expansion of the continental N reservoir (figure 3.9 c, h, and i). Meanwhile, subduction returns N to the mantle at a significant rate just lower than its mantle outgassing flux (figure 3.9 j).

3.4.1.2 Stage 2

The evolution of oxygenic photosynthesis and nitrogen fixation increases geologic N at the expense of dissolved reservoirs. Higher productivity following the evolution of oxygenic photosynthesis efficiently sequesters fixed nitrogen into the sediments and continents as organic matter (figures 3.9 c, f, g, and i). Hydrothermal sequestration into the oceanic crust declines as dissolved N reservoirs are increasingly taken up by the biosphere (figure 3.9 e, g and h). Nitrate emerges in the ocean as oxygen becomes available for nitrifiers (figure 3.9 e).

3.4.1.3 Stage 3

The GOE results in a rapid increase in atmospheric ammonia oxidation and oxidative weathering (figure 3.9 b and d). Nitrogen in the ocean is balanced between reduced and oxygenated species (figure 3.9 e). A massive spike in N_2 exchange to the atmosphere at the GOE corresponds with a significant increase in denitrification (figures 3.9 b and 3.1 d); this initiates a new period of ocean fixed N levels balanced by denitrification, which heralds the post-GOE period of N limited pseudo-steady state (figure 3.2).

3.4.1.4 Stage 4

The evolution of fungi and increasing oxygenation transitions the fixed N reservoir to primarily nitrate. The second jump in environmental oxygen results in further nitrification of the oceanic fixed N reservoir, which gets to a modern level during this stage (figure 3.9 e). Increasing productivity shifts the major sequestration pathway from hydrothermal alteration of NH_4^+ to the burial of organics (figure 3.9 h-i); this trend is slightly disrupted following the evolution of fungi at 0.7 Ga as remineralization fluxes increase and remove organic matter from the pelagic sediments more efficiently (figure 3.9 g-h; see section 3.1.1.3).

3.4.1.5 Stage 5

The evolution of larger organisms reinstates the trend of increasing organic N burial by the end of this stage. Nitrogen influxes to the mantle switch from being dominated by inorganic, silicate-bound N to organic-bound N (figure 3.9 j). Atmospheric ammonia rises to its highest level following this transition (figure 3.9 a), corresponding with a turn to positive air-sea gas exchange flux that categorizes the rest of the model run (3.9 b, partially covered by ammonia oxidation line); even so, this greenhouse gas remains of minor climatic import (figure 3.3 b). The end of biospheric N limitation coincides with a boost in fixation (figures 3.1 c and 3.2), thus ammonia is preferentially released to the atmosphere.

3.4.1.6 Stage 6

The modern N cycle appears to be in pseudo-steady state. The evolution of the terrestrial biosphere in the Phanerozoic finalizes the nitrification of the fixed N reservoir as the deep ocean and sediments become fully oxygenated (figure 3.4 a and e). Organic N weathering increases transiently across this transition with the oxygen overshoot (figures 3.9 d and 3.3 a).

3.4.2 Nitrogen cycle: tuning requirements

Because of the dependency of nitrogen fixation on phosphorus availability, the fixed nitrogen cycle is sensitive to phosphorus levels and therefore to the tuning of f_{apatite} (section 3.3.2). Perhaps the most significant controls on the nitrogen system are the treatment of hydrothermal alteration and the fraction of subduction zone melt that is recrystallized ($f_{\text{cryst,NH4}}$). As the only pathway for inorganic nitrogen sequestration is hydrothermal alteration, the continental silicate-bound N reservoir is quite sensitive to estimates for hydrothermal flow and the seafloor weathering sensitivity modifier (section 2.6.7). Assuming variable hydrothermal fluid flow would affect the amount of dissolved NH_4^+ passing through the ocean crust, while variable seafloor spreading would affect time spent at the hydrothermal ridge (not treated here); both could therefore change how much dissolved NH_4^+ could be sequestered in the ocean and continental crust through Earth history. I have assumed here that 75% of ocean crust NH_4^+ is recrystallized onto the continent. Higher recrystallization fraction, higher melt fraction, or even faster seafloor spreading (i.e. faster subduction) early in Earth's history would lead to faster accumulation of crustal N and could improve the fit of the model output to modern continental reservoir estimates (figure 3.9 c).

3.4.3 Nitrogen cycle: implications

The rise of geologic nitrogen reservoirs is entirely controlled by the biosphere through fixation, highlighted by the correlation between the growth of the silicate-bound N reservoir in continent and dissolved RN in the ocean (figure 3.9 c, e). Biological activity allows for the return of otherwise volatile nitrogen to the mantle, broadly stabilizing the size of the N_2 atmosphere through time (figure 3.9 a). Solubility and the biosphere's never-ending hunger for fixed nitrogen, absent a significantly higher reduced mantle outflux, effectively inhibit the growth of ammonia in the atmosphere and make a significant radiative contribution from this greenhouse gas extremely unlikely.

Biology is limited by nitrogen availability prior to oxygenic photosynthesis and following the GOE, which broadly corresponds with the nitrogen isotope record, suggestive of a "nitrogen crisis" throughout this period (Falkowski & Godfrey, 2008), though perhaps not for the reasons as previously proposed; the most important factor limiting N availability in *EONS* is sequestration (burial) outpacing fixation, and not nitrification-denitrification decreasing fixed N availability. The post-GOE period of N limitation does correspond to increased denitrification and N_2 outgassing to the atmosphere, but also a slow and unabated expansion of the dissolved nitrate and RN reservoirs (figure 3.9 e). My nominal run implies that surface nitrogen reservoirs have broadly grown over time, including fixed nitrogen in the ocean.

3.5 Organic carbon cycle evolution

The evolution of global organic carbon cycle is shown in figure 3.10.

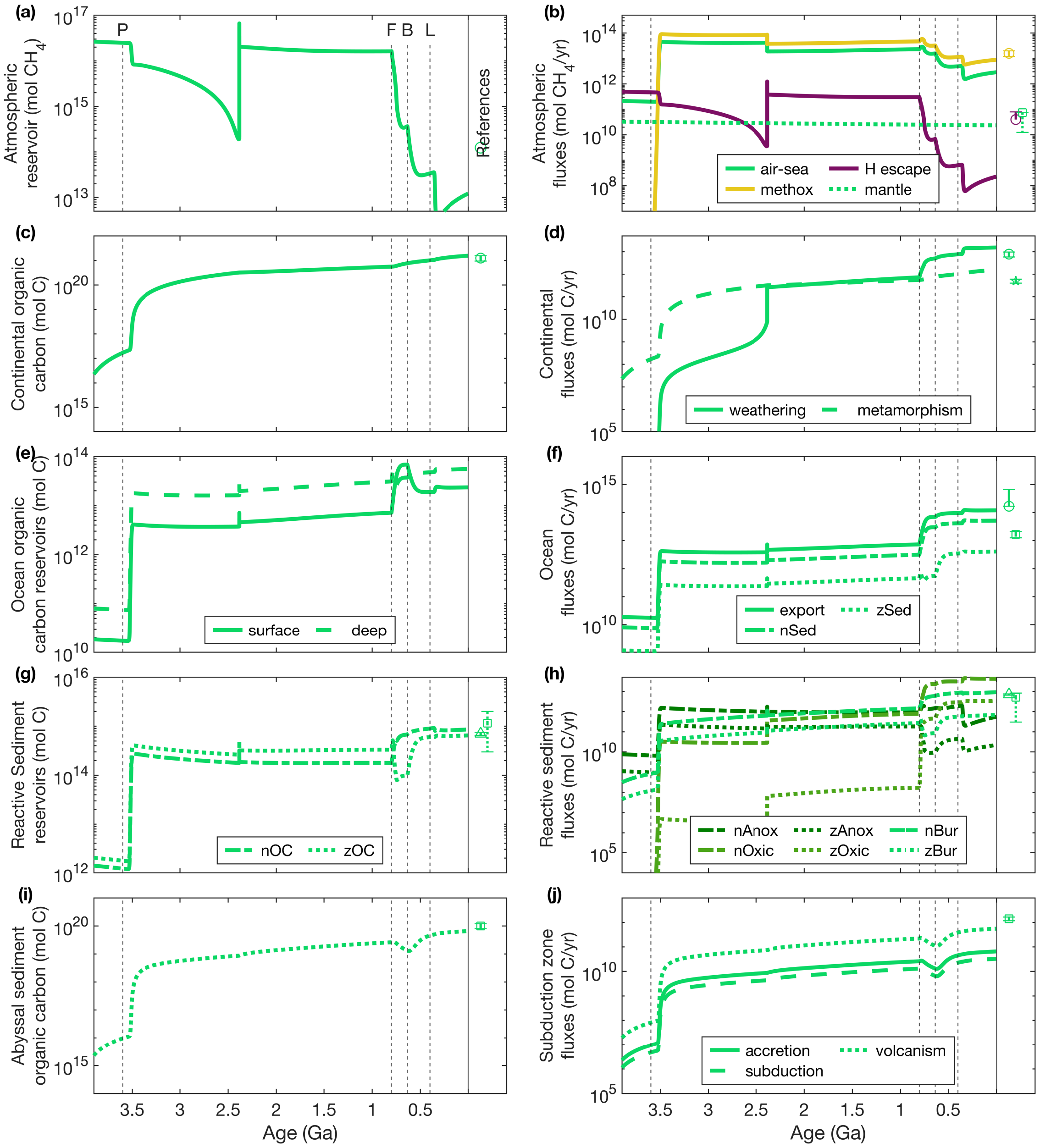

Figure 3.10: The evolution of organic carbon cycling. Left column (**a**, **c**, **e**, **g**, **i**) organic carbon reservoirs; in the legends, *u* denotes unreactive pelagic sediments, *o* denotes oceanic crust (slab), and *s*, *n*, *d*, and *z* denote surface ocean, neritic (shelf) sediments, deep ocean, and pelagic sediments, respectively. Right column (**b**, **d**, **f**, **h**, **j**) organic carbon fluxes for each species out of the reservoirs in the corresponding left subplot (respectively: air-sea gas exchange, hydrogen escape, methane oxidation, and mantle outgassing; weathering and metamorphism; export and sedimentation; remineralization (anoxic and oxic) and burial; accretion, subduction, and volcanism). Modern estimates for reservoirs and fluxes are denoted with symbols at the far right of each plot, with range estimates as vertical bars (citations in table A.3); the solid vertical line denotes the end of model output. Black dashed vertical lines denote forced evolutionary transitions: *P* for oxygenic photosynthesis, *F* for fungi, *B* for increased body sizes, and *L* for vascular land plants.

3.5.1 Organic carbon cycle: chronology

3.5.1.1 Stage 1

Biological activity rapidly expands organic carbon surface reservoirs. Though initialized at modern partial pressures, atmospheric CH_4 rapidly grows to approximately 100 times the modern level via ocean biosphere production outpacing hydrogen escape (figure 3.10 a-b). Photo-ferrotrophy adds a continuous influx of organic carbon to the continent, which ends this stage nearly 3 orders of magnitude smaller than its modern size (figure 3.10 c).

3.5.1.2 Stage 2

The evolution of oxygenic photosynthesis drives a massive rise in organic carbon production and significantly tempers atmospheric CH_4. The immediate aftermath of oxygenic photosynthesizer evolution is a nearly 100-fold increase in OC production, export, and burial (figure 3.10 e-h) that translates to a rapid growth in geologic reservoirs (figure 3.10 i and c, respectively). Anaerobic remineralization dominates in sediments (figure 3.10 h), but methane production cannot match rapidly increasing atmospheric oxidation, and CH_4 falls to near-modern levels by the end of this stage (figure 3.10 a-b).

3.5.1.3 Stage 3

The atmospheric methane decline ends with the initiation of the GOE, triggering oxidative weathering and partial oxygenation of the pelagic sediments (figure 3.10 d and h). Methane rebounds after this transition as oxygen levels come to a new steady state with surface reductants, leading to a temperature peak (figure 3.3 a and c). Geologic reservoirs of organic carbon continue growth (figure 3.10 c, e, g, and i).

3.5.1.4 Stage 4

The organic carbon cycle is disrupted again after the evolution of fungi, leading to a significant and lasting crash in atmospheric methane. The moderate oxygenation pseudo-steady state ends at fungal evolution circa 0.7 Ga; this transition sees the development of near-modern productivity and export that leads to a transient decline in pelagic sediment organic carbon as oxygenation in that reservoir proliferates aerobic remineralization (figure 3.10 f-h). The corresponding decline in anaerobic remineralization in the sediments (figure 3.10 h) is a death knell for atmospheric methane, which is further exacerbated by methane oxidation that increasingly outpaces air-sea gas exchange (figure 3.10 a-b).

3.5.1.5 Stage 5

The evolution of large bodied organisms in the Ediacaran leads to a secondary crash in atmospheric methane as production declines (figure 3.10 a); sedimentary anaerobic remineralization, which slightly rebounds here (figure 3.10 h) is dominated now by denitrification rather than methanogenesis (figure 3.1 d).

3.5.1.6 Stage 6

The evolution of the terrestrial biosphere solidifies atmospheric CH_4 decline and the full oxygenation of the pelagic sediments. The beginning of the Phanerozoic sees a slight increase in atmospheric methane (figure 3.10 a) that is quickly quashed by the evolution of land plants and the full development of the terrestrial biosphere. Complete oxygenation of the deep ocean and sediments (figure 3.4 a) at this point leads to a small rise in aerobic remineralization at the expense of anaerobic remineralization (figure 3.10 h), further decreasing oceanic methane production (figure 3.4 b). The rest of the organic carbon cycle reverts to a new pseudo-steady state for the remainder of the eon.

3.5.2 Organic carbon cycle: tuning requirements

Continental emergence strongly controls the organic carbon cycle. Reactive sediment burial timescale is evolved through the erosion parameter (χ_{eros}), which in turn effects the relative efficiency of sedimentary remineralization. More extensive remineralization, occurring when burial timescales are longer because of less continental erosion, means less organic carbon is buried and thus net oxygen production is lower. The nominal run is tuned such that the growth of continents via mantle influxes results in modern day surface reservoirs for C, N, P and SiO_3 at 0 Ga and reactive sediment residence times, using an inverse relationship with relative silicate reservoir size, evolve from approximately 100x modern in the Eoarchean (with 5% continental emergence) to modern day references.

3.5.3 Organic carbon cycle: implications

Continental organic carbon accumulation occurs in three major steps, and pre and post photosynthesis pulses in growth closely mirror oxygen's rise in the atmosphere (figure 3.3 a). Husson and Peters (2017) proffered that the punctuated accumulation of OC onto continental bodies was a major cause of the GOE timing and two-step rise, a theory validated by my nominal run which shows three major phases (figure 3.10 d): (1) slow productivity in the Archean results in slow early accumulation, (2) growth is thereafter accelerated by a more prolific oxygenic biosphere, eventually stabilizing throughout the Mesoproterozoic as oxidative weathering increases following the GOE. (3) A second jump in productivity following fungi evolution and enhanced P influx to the ocean results in the largest absolute growth of continental OC.

3.6 Inorganic carbon cycle evolution

The evolution of the inorganic carbon cycle is shown in figure 3.11.

3.6.1 Inorganic carbon cycle: chronology

3.6.1.1 Stage 1

The Eoarchean atmosphere-ocean inorganic carbon system is moderated by rapid growth of the continental carbonate reservoir. Atmosphere CO_2 level peaks in the first few million years of the Archean as mantle outgassing and eventually air-sea gas exchange equilibrate with DIC (figure 3.11 a-b, e). Minor subaerial silicate weathering and subsequent $CaCO_3$ precipitation in the surface ocean begins sequestering CO_2 from the atmosphere into the sediments and continent (figures 3.11 c-i); extensive inorganic carbon burial in neritic sediments significantly outpaces organic carbon burial (figures 3.11 h and 3.10 h) and helps maintain low f_{org} throughout this stage (figure 3.1 e). Seafloor weathering is nearly equal to continental silicate weathering for the first few million years and transfers significant carbon into the oceanic crust (figure 3.11 h-i); this flux declines later as pH rises. Sedimentary and ocean crust $CaCO_3$ is significantly recycled by volcanism, which helps maintain a high partial pressure of CO_2 through the end of this stage (figure 3.11 j). By that time, so much atmosphere-ocean carbon has been sequestered as $CaCO_3$ that the continental reservoir is within an order of magnitude of its modern size.

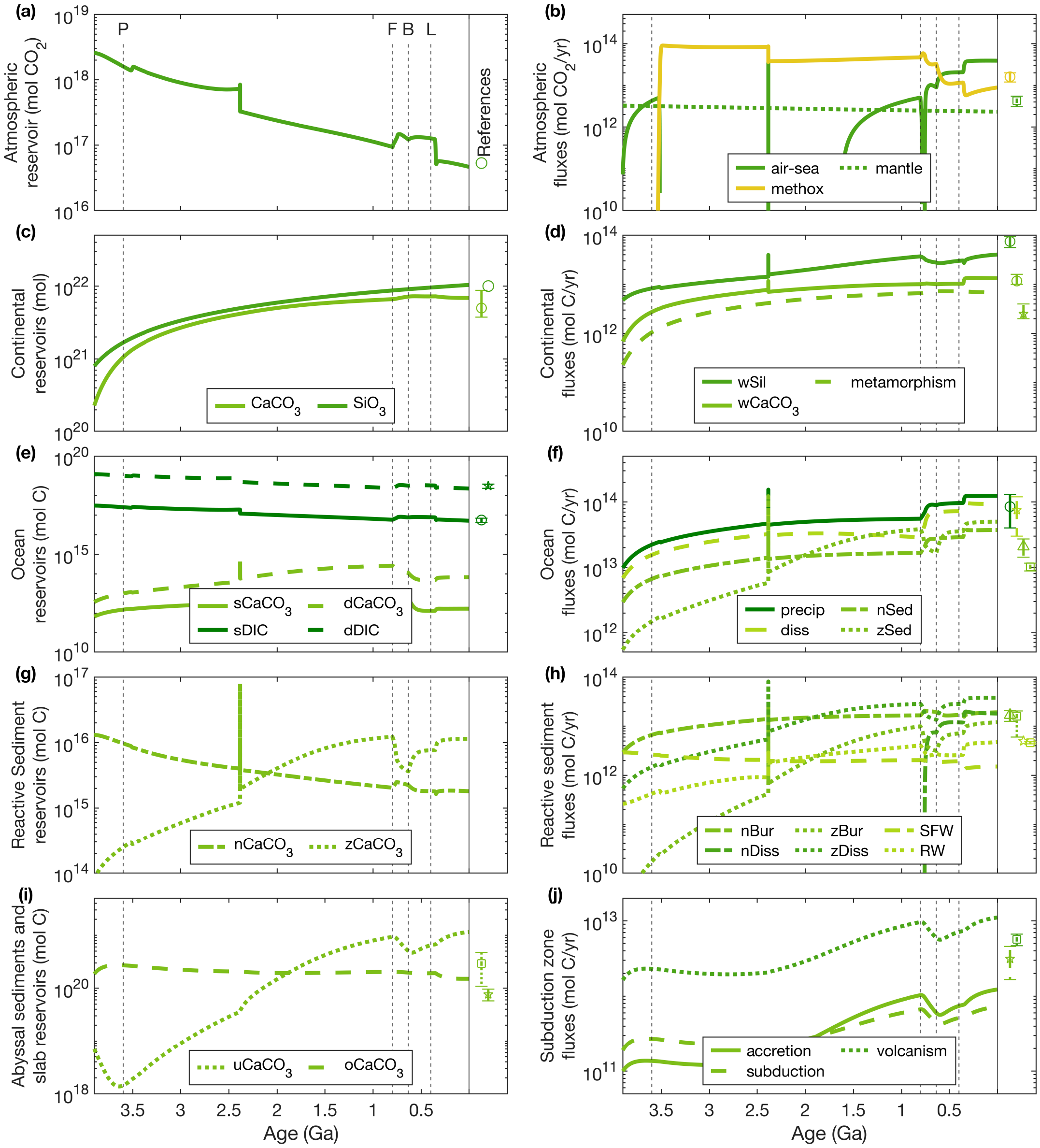

Figure 3.11: The evolution of inorganic carbon cycling. Left column (**a**, **c**, **e**, **g**, **i**) inorganic carbon (and continental silicate) reservoirs; in the legends, *u* denotes unreactive pelagic sediments, *o* denotes oceanic crust (slab), and *s*, *n*, *d*, and *z* denote surface ocean, neritic (shelf) sediments, deep ocean, and pelagic sediments, respectively. Right column (**b**, **d**, **f**, **h**, **j**) inorganic carbon fluxes for each species out of the reservoirs in the corresponding left subplot (respectively: air-sea gas exchange, mantle outgassing, and methane oxidation; silicate weathering, carbonate weathering and metamorphism; precipitation, dissolution, and sedimentation (export from surface ocean generally equals precipitation); dissolution, seafloor weathering, reverse weathering, and burial; accretion, subduction, and volcanism). Modern estimates for reservoirs and fluxes are denoted with symbols at the far right of each plot, with range estimates as vertical bars (citations in table A.3); the solid vertical line denotes the end of model output. Black dashed vertical lines denote forced evolutionary transitions: *P* for oxygenic photosynthesis, *F* for fungi, *B* for increased body sizes, and *L* for vascular land plants.

3.6.1.2 Stage 2

The inorganic carbon system is relatively stable following the evolution of oxygenic photosynthesis. Photosynthesis and increasing productivity initiates a massive draw of atmospheric CO_2 evidenced by negative air-sea gas exchange through the first part of this stage (figure 3.11 b). Just before the GOE, atmospheric CO_2 begins to rise in a mirror of methane's decline, a result of increasing production by oxidation (figures 3.11 a-b, and 3.3 a) ; this rise in CO_2 may also be a response to declining temperatures and limited silicate weathering 3.2.1.2). Continental weathering continues to rise with growing the silicate reservoir and somewhat stabilizes surface temperature (figures 3.11 c-d and 3.3 c).

3.6.1.3 Stage 3

The GOE causes a punctuated disruption in the inorganic carbon system. Declining CO_2 is partially compensated by outgassing of ocean DIC (figure 3.11 a-c); rising temperature from CH_4 decreases CO_2 solubility and reverses air-sea gas exchange (figures 3.3 a and c and 3.3 c). This coincides with a sharp rise in ocean pH and carbonate saturation state, enhancing $CaCO_3$ precipitation (figures 3.11 f and 3.4 i-j); this boon to the carbonate pump is a likely cause for the transient dip in f_{org} (figure 3.1 e). The ocean system returns to a pseudo-steady state after this transition, but the atmospheric CO_2 reservoir continues to decline as surface temperature and continental silicate reservoir steadily increase (figures 3.11 c-d and 3.3 c).

3.6.1.4 Stage 4

The crash in atmospheric methane following fungal evolution causes a massive restructuring of the inorganic carbon cycle. Proterozoic CO_2 trends downward until fungi evolve; this transition initiates a rise in atmospheric O_2 from enhanced productivity, transiently increasing atmospheric oxidation reactions producing CO_2 at the expense of CH_4, which correspondingly declines (figures 3.11 a-b, 3.3 a). Methane oxidation then crashes as the deep ocean becomes increasingly oxidized and methanogenesis slows (sections 3.1.1.4 and 3.2.1.4), which is mirrored by a steep rise in DIC and ocean CO_2 outgassing (figure 3.11 b and e) as deep ocean oxygenation accelerates methanotrophy (figure 3.4 a-b). Consequently, pH falls steeply in the deep ocean and sediments, widening the gap between surface and deep ocean saturation states (figure 3.4 i-j). Higher $CaCO_3$ precipitation and export from the surface and lower deep saturation contribute to enhanced dissolution particularly on the shelf (figure 3.11 f and h). This decline in pH is exacerbated by decreasing silicate weathering (figure 3.11 d), which also bolsters the expansion of atmospheric CO_2; weathering falls in response to temperature, yet another consequence of methane's crash (figure 3.3 a and c). Subduction zone fluxes peak at the start of this transition, and decline with $CaCO_3$ availability in the pelagic and unreactive sediments (figure 3.11 g and j).

3.6.1.5 Stage 5

Enhanced export slows the inorganic carbon cycle perturbation caused by the evolution of fungi. Increasing body sizes cause particulates to sink faster out of the surface and deep ocean, which in turn decreases dissolution in the water column (figure 3.11 f). Higher $CaCO_3$ export flux boosts sedimentary reservoirs and fluxes out of the subduction zone (figure 3.11 g, i, and j). Atmospheric CO_2 returns to its broad pattern of gradual decline as it is sequestered into the continent (figure 3.11 a and c).

3.6.1.6 Stage 6

The colonization of continents by vascular plants causes a significant atmospheric CO_2 crash. Continental carbonate and silicate weathering increase in immediate response to plant evolution, immediately drawing down CO_2 (figure 3.11 a and d); while silicate weathering slows as CO_2 falls, carbonate weathering increases with continental carbonates, which is boosted by the rapid influx of alkalinity spurring precipitation and deposition (figures 3.11 c, f, h, and i). Reverse weathering, which has tracked with sedimentary pH throughout the entire run, increases slightly in response to the alkalinity influx to maintain stable pH (figures 3.11 h and 3.4 i). In the aftermath of the CO_2 crash, the inorganic carbon system reverts to a new pseudo-steady state with significantly lower atmospheric CO_2; this reservoir continues its slow decline as solar constant increases surface temperature for the duration of the Phanerozoic (section 3.2.1.6).

3.6.2 Inorganic carbon cycle: tuning requirements

The inorganic carbon system in this model is sensitive to parameters controlling feedbacks between pH and reverse weathering. Because I do not resolve the global silicate cycle, the choice of fixed $[Si]_0$ in equation 2.109 is extremely important. Using the upper estimate for modern porewater dissolved silica yield a very strong feedback between reverse weathering and alkalinity that, while not broadly destabilizing to the inorganic carbon system, forces it into a lower pH steady state and subtly changes the history of atmospheric CO_2 sequestration. Precipitation and dissolution timescales are also controlling parameters for this system; I have tuned the model such that total precipitation and dissolution fluxes in the modern ocean correspond to literature estimates. My current choice to treat carbonate precipitation as continuous in terms of saturation requirements (see section 2.5.4) likely affects these results, and including a forcing for the evolution of widespread calcification by the biosphere would improve inorganic carbon cycling in *EONS*. The addition of this shift in carbonate chemistry may further affect how ocean pH and carbonate saturation state evolve through time. And the amount of carbon outgassing from the mantle strongly determines the stability of the Earth system, particularly in the Archean; a very large upper mantle carbon reservoir, or significantly faster mantle overturn, results in extremely high atmospheric CO_2. Under such conditions and with limited continental emergence, the system enters an extremely acidic state that rapidly becomes unstable.

3.6.3 Inorganic carbon cycle: implications

The climate has been broadly stabilized through geologic time by the long-term sequestration of atmospheric CO_2 into carbonate minerals. Carbon dioxide level and surface temperature essentially reflect one another, with the exception of a positive trend in temperature versus a negative trend in CO_2 (figures 3.3 c and 3.11 a), both of which are attributable in part to increasing solar constant and the growth of continental silicates (figures 3.3 d and 3.11 d). Temperature fluctuations, many of which are initiated by increases in biologically sourced atmospheric methane, are perfectly reflected in silicate, carbonate, and seafloor weathering curves (figures 3.3 c and 3.11 d and h). My modelled ocean pH agrees well with other models of gradual and monotonic pH increase (Krissansen-Totton et al., 2018). I omit the critical ice-albedo feedback, which would add a significant destabilizing force to this story.

A stabilized ancient climate requires extensive carbonate burial, which precludes constant f_{org}. High atmospheric CO_2 in the Eoarchean is required to keep temperatures above freezing (figure 3.3 a and c; Goldblatt & Zahnle, 2011; Walker, 1982), necessitating extensive carbonate burial through the Precambrian as continents grow and solar flux increases (figures 3.3 d and 3.11 d-h). Higher f_{org} results from either high organic carbon burial or low inorganic carbon burial; unless the biosphere was significantly more productive in the Archean-Proterozoic periods, in contradiction of conventional wisdom (Crockford et al., 2018; Kharecha et al., 2005), modern $f_{\text{org}} = 0.2$ at this time would require much lower carbonate burial. My model suggests that this is highly unlikely and that organic carbon burial increased slowly during these eons, and as a result led to the permanent oxygenation of the Earth's surface (figures 3.1e and 3.5).

3.7 Discussion and Conclusions

The Earth system is a massively interconnected web of biogeochemical feedbacks. Developing a comprehensive model of this system necessitates consideration of the coupled biogeochemical cycles and climate. This model demonstrates that understanding this planet as it evolved through time implicates systems operating on disparate timescales ranging seconds to billions of years. It further solidifies life's pervasive influence on our planet's evolution.

3.7.1 The origin of Earth's oxygen

While geologic forcings contribute to its precise timing, surface oxygenation is inevitable in the wake of the evolution of oxygenic photosynthesis. This model successfully produces a reasonable chemical evolution for the Earth's major surface systems. That this finding does not require a robust treatment of the terrestrial biosphere speaks to the overwhelming supremacy of the oceanic carbon pump in controlling the Earth's climate and surface chemistry. My model agrees with other recent models of the GOE, suggesting that this transition was stepwise (Alcott et al., 2019) and long lived, occurring gradually through the late Archean and Proterozoic, and completing in the early portion of the Phanerozoic with oxygen level reaching its maximum in the Carboniferous (Bergman et al., 2004; Lyons et al., 2014). These results suggest that while mantle reductant outflux influences the timing of the GOE, a major decline in geologic reductants is not necessary for surface oxidation (section 3.2.2). Furthermore, these results point to the delay in surface oxygenation after the evolution of oxygenic photosynthesis being exacerbated by gradual buildup of organic matter sequestering nutrients (section 3.2.3); while organic carbon burial is a major control allowing oxygen to rise, it is inextricably coupled with sequestration of nutrients, the affect of which is limited biosphere expansion. Explaining oxygen's rise as purely a result of increased organic matter burial appears insufficient to overcome this feedback. The fraction of carbon buried as organics must have evolved over time or the mantle must have been much more reducing (or outfluxes more than 10x higher) in order for this delay to occur (section 3.2.3); I believe the former is more realistic.

3.7.2 Expansion of organic carbon burial

The growth of f_{org} is a function of export and burial efficiency, both of which have increased as the biosphere expanded, weathering increased and nutrient limitations waned. Carbon isotope evidence and steady state models have suggested that f_{org} is broadly stable through time (Hayes & Waldbauer, 2006; Marais et al., 1992; Schidlowski, 1988), though interpretations of the Precambrian record are diverse. Rothman et al. (2003) modelled carbon isotope evolution in the Neoproterozoic through Phanerozoic and found these records inconsistent with steady state carbon cycling; these authors suggest that organic carbon remineralization became much more efficient at the Cambrian boundary, reducing the size the of ocean organic carbon reservoir and shifting the carbon system to a new steady state that has persisted ever since. A reconstruction of a possible Archean biosphere using more alternative anoxygenic production pathways suggest that the Archean biosphere may have had much lower burial efficiencies (Kharecha et al., 2005). Bjerrum and Canfield (2004) developed a carbon isotope mass balance model for the Precambrian and estimated organic carbon comprised 0-10% of total carbon buried, not significantly different from my model results. A recent study combining results from carbon isotope modelling and productivity estimates for the Archean suggest that constant $f_{\mathrm{org}} = 0.2$ would require burial efficiencies to be impossibly high until 3.5 Ga (Crockford, On, Ward, Milo, & Halevy, 2023). But it is possible that the carbon record itself is not helpful in constraining f_{org}, given significant uncertainty regarding the magnitude of inorganic carbon cycle fluxes in the Precambrian (Krissansen-Totton, Buick, & Catling, 2015), and the high potential for diagenetic alteration (Ahm et al., 2018; Derry, 2010) or authigenic carbonate formation (Schrag, Higgins, Macdonald, & Johnston, 2013) which can alter the carbon isotope record. It has also been suggested that changes in oxidative weathering may alter the isotope record (Daines, Mills, & Lenton, 2017; Derry, 2014), potentially obfuscating a rise in f_{org} (Krissansen-Totton, Kipp, & Catling, 2021; Planavsky et al., 2022). My findings support f_{org} evolving between several pseudo-steady states through Earth's history. Whether or not f_{org} reflects or produces a more oxidized surface is still unresolved; as it is not a fixed parameter in this model, a direct causal relationship to the GOE is impossible to determine. *EONS* includes all of the systems necessary to track carbon isotopes through time to further bolster this argument, although the addition of such components is beyond the scope of this current work; I hope to more directly address the carbon isotope record in the near future.

Producing the GOE under severely nutrient limited conditions requires lower organic matter burial efficiency. Decreased continental phosphorus influx, which further limits nitrogen fixation, is a major inhibiting factor for the Precambrian biosphere that must be overcome in order to sustain a biosphere which can eventually cause the GOE (section 3.1.3). The simplest pathway for nutrient resupply is remineralization under low burial efficiency. I have already discussed why high f_{org} in the Precambrian is unlikely based on the inorganic carbon system (section 3.6.3). My model suggests that the delay in oxygenation after the rise of biospheric oxygen production is in part a result of limitation imposed by deficient N and P supply. Higher pre-GOE burial efficiency ($f_{\mathrm{org}} > 0.05$) would invariably change the tempo of oxygenation; further exacerbation of nutrient supply could plausibly prevent oxygenation, or the faster accumulation of organic carbon could initiate a GOE even earlier. Fitting this model within geological oxygen constraints (section 3.2.2) suggests that a billion-year GOE delay requires lower efficiency. Were it the case that oxygenic photosynthesis evolved later than I assume here, higher burial efficiency would be more plausible.

3.7.3 Biospheric reworking of atmosphere, geosphere, and climate

Modern oxygen levels are achieved only when the deep ocean becomes fully oxygenated; in this model, that occurs when the terrestrial biosphere fully develops. This finding is consistent with other recent oxygen modelling which found that the evolution of land plants was key in stabilizing atmospheric oxygen (Krause et al., 2022). Model output also indicates rapid oxygenation and climate disruption coincident with biological expansion onto continents in the Neoproterozoic (sections

3.1.1.6 and 3.2.1.6), supporting a theory that enhanced phosphorus weathering by lichen and fungi contributed to the Neoproterozoic oxygenation event (NOE; Heckman et al., 2001, Lenton & Watson, 2004). Evidence indicates that the deep ocean became mostly oxygenated around the Ediacaran-Cambrian boundary, but that anoxia was still present (Canfield et al., 2007). My model produces ocean oxygen levels that are broadly consistent with these theories (section 3.2.1.4). The fact that the atmosphere-ocean does not achieve modern oxygen level without the addition of the terrestrial biosphere suggests that there were still significant portions of the deep ocean experiencing suboxia into Devonian (section 3.2.1.5).

The evolutionary trajectory of key geologic cycles is strongly influenced by transitions occurring in the biosphere. This can be most clearly demonstrated by observing the organic carbon continental reservoir growth curve and the corresponding expansion of oxidative weathering flux (figure 3.10 c and d, respectively), the latter of which is a nearly perfect reflection of the atmospheric O_2 curve, up to the point of the GOE when oxidative weathering begins (sections 3.2.1.3 and 3.5.1.3). The rise of geologic nitrogen reservoirs and the size of the continental N reservoir broadly correspond to the relative availability of fixed N in the ocean at any given time, and sequestration of biologically fixed N into the ocean crust and subsequent subduction into the mantle maintains surface atmospheric pressure within 20% of the modern level (section 3.4). Geologic phosphorus shifts from dominantly silicate to carbonate bound species, particularly in the Phanerozoic (section 3.3.1.5), as biology transitions from producing iron oxides and as increasing organic matter remineralization efficiency returns H_3PO_4 to sedimentary porewaters where it can be buried as apatite. Key perturbations in the inorganic carbon cycle result from atmospheric methane excursions and crashes exerting control over surface temperatures, activating the silicate weathering feedback (sections 3.5.1.3 and 3.6.1.3). Every geologic cycle in some way controls the tempo of biological evolution and becomes a product of biological influence.

The climate warms in response to the GOE rather than cools. My model shows that methanogenesis promotes a rise in atmospheric CH_4 in the aftermath of oxygen's rise which produces rapid climatic warming (sections 3.1.1.3, 3.2.1.3, and 3.5.1.3). This appears to contradict earlier theories that the permanent oxygenation of the surface would collapse the methane greenhouse and cause dramatic climate cooling (Pavlov, Kasting, Brown, Rages, & Freedman, 2000). Rather, while the GOE here coincides with rapid warming, it is preceded by a significant decline in CH_4 and cooling. Therefore it is possible that the same processes gave rise to both the GOE and the Paleoproterozoic snowball Earth. I will investigate this in a future version of *EONS* with a more developed climate system, including ice-albedo feedbacks.

3.7.4 Earth outside of steady state

Climate stabilization by the inorganic carbon cycle has its limitations. While Earth's long-term climate is relatively moderated by the silicate weathering feedback, the overall rising trend in surface temperature broadly reflects external forcings outside of steady state. The inorganic carbon system never achieves even pseudo-steady state between atmosphere-ocean and geologic reservoirs (section 3.6); while continental reservoirs rapidly grow to near-modern sizes, there is never a point in the model run when carbon reservoir size in any setting (atmosphere, ocean, crustal, or mantle) ceases to change, indicating that sources and sinks of surface carbon are never capable of true equilibration even if they broadly balance on shorter timescales. The continuous rise in solar constant forces a long-term decline in atmosphere-ocean inorganic carbon by influencing the rates of mineral dissolution and continental weathering (Walker et al., 1981). This system is susceptible to extreme perturbations caused by the biosphere, particularly when terrestrial plants emerge and directly influence the silicate weathering feedback; this causes a significant and rapid decline in surface temperature from an all-time high (section 3.6.1.6), strongly implicating terrestrial plants as the cause of the Devonian mass extinction.

The holistic Earth system is not at steady state. The presence of an active biosphere, coupled with progressive loss of hydrogen to space, means that our planet is becoming increasingly oxidized through time. From this perspective, it is unlikely that the Earth will return to a reducing atmosphere as long as sufficient atmospheric carbon remains available to fuel photosynthesis (Ozaki & Reinhard, 2021). My model shows that close coupling between biological and geological systematics, which puts expansive geologic cycles in a continuous feedback with short-term biological cycles, prevents planetary steady state. Punctuated pseudoequilibria arise between major biological transitions as primary production levels equilibrate with geologic influxes, but such distant timescales for system response prevent true stability. Earth's fundamental mutability arises from these inseverable systems; the whole of our planet is infinitely more complex than the sum of its parts.

Chapter 4

Paleoproterozoic glaciations and oxygenation

The nominal model run presented in chapter 3 implied that the Proterozoic was relatively warm, particularly in the wake of the GOE, and that methane levels in the atmosphere increased through time as a major contributor to the temperature trend. However, in the introduction chapter (1), I reviewed geochemical and stratigraphic evidence which indicates that the Proterozoic was not an eon of stable climate but one with the most extreme oscillations between glacial and hothouse climates in Earth's history. There is evidence of several glacial events occurring at nearly the same time as the GOE in the Paleoproterozoic. Hoffman (2013) stratigraphically correlated diamictites found in the Huronian (Superior craton, North America), Transvaal (Kaapvaal craton, South Africa), Turee Creek (Pilbara craton, Australia), and Sariolian (Kola-Karelia craton, Scandinavia) supergroups constraining at least three, perhaps four, distinct glacial episodes, one of which appears to be a global snowball glaciation (Evans, Beukes, & Kirschvink, 1997). These glacial events are well represented in the South African groups, and in this chapter I will reference these glaciations using the South African formation names (Makganyene, Duitschland, Rooihoogte, and Rietfontein).

As reviewed by Gumsley et al. (2017), oxygen levels recorded by MIF-S (mass independent fractionation of sulphur isotopes) vary across these glaciations, disappearing during interglacials (indicating high oxygen) and reappearing during glaciations (indicating low oxygen). The final glacial episode follows the permanent rise in oxygen, and terminates around the onset of the Lomagundi carbon isotope excursion (Bekker et al., 2004; Luo et al., 2016; Poulton et al., 2021; Rasmussen et al., 2013). The permanent rise in oxygen has been invoked as a primary driver of Paleoproterozoic glaciations, perhaps by causing a collapse in the methane greenhouse (Kirschvink et al., 2000; Kopp et al., 2005; Schrag, Berner, Hoffman, & Halverson, 2002). It has also been suggested that global glaciations are caused by changes in weathering and continental arrangement (Schrag et al., 2002). Changing patterns of continental weathering will result in fluctuations in nutrient transport to the ocean, productivity, and oxygen production, which means that changing oxygenation could be a consequence rather than a cause of glacial episodes. Additionally, there is evidence that significant tectonic changes, including a decline in volcanism, occurred around the same time as the GOE and glaciations (Pehrsson et al., 2014). Recent modelling work focusing on atmospheric chemistry through the GOE indicates a correlation between MIF-S reappearance and glaciations, implying that fluctuating oxygen level may be strongly controlled by climate and atmospheric water vapour (Garduño Ruíz et al., 2023); however, these authors still find that some of the Paleoproterozoic MIF-S signal cannot be explained by this mechanism alone.

The *EONS* model can resolve Paleoproterozoic climate instabilities by incorporating a few additional feedbacks into the climate system, with the goal of clarifying how climate, oxygen, and methane may relate during this chaotic period. By modelling such planetary glaciations, I can:

1. test potential scenarios causing snowball events
2. constrain a few major controls on glacial/interglacial timing and tempo
3. better understand the relationship between the GOE and snowball episodes

This chapter begins with a brief explanation of the changes to model climate feedback systems (section 4.1); I update the *EONS* model to include climatic nonlinearities in order to resolve climate instability arising in the early Proterozoic eon. I then compare the model output with and without added perturbations to elucidate how changing tectonics may affect glaciation (section 4.2). Using a few different parameters, I then perturb snowball oscillation timing and tempo to better constrain the strongest controls on the feedbacks within this model (section 4.3). I investigate how the parameterization of a key climatic tipping point governs the relationship between the great oxidation event, climate, and the occurrence of glacial events (section 4.5). This chapter concludes with a discussion of the implications of this exercise, and offers a suggestion for future inquiry (sections 4.6 and 4.7).

4.1 Climate feedbacks

The climate system in the nominal *EONS* model is controlled by the balance on incoming solar radiation and radiative forcing by greenhouse gases in the atmosphere. I assumed a fixed reflectivity (albedo) that was equal to the modern average with continental plants and minimal sub-polar ice coverage. I considered only a linear water vapour greenhouse feedback in my formulation of radiative balance, which is appropriate for temperate surface conditions.

The following subsections detail how parameterizations for albedo and thermal radiative retention are updated to resolve key climatological feedbacks. I approximate the effects of expanding ice sheets with changes to albedo, continental shelf area, and continental erosion. New parameterizations for albedo, shelf area fraction, and outgoing longwave radiation are included in figure 4.1 along with other temperature sensitive parameters in the model.

4.1.1 Ice-Albedo feedback

Ice coverage is a function of, and exists in a positive feedback loop with, average planetary surface temperature (see section 1.3). When glacial cover extends to mid-latitudes, the Earth rapidly transitions from mostly rock and water covered ($\alpha_{\text{rock}} = 0.3$) to mostly ice covered ($\alpha_{\text{ice}} = 0.6$; Hyde et al., 2000; Pollard, 2005; Hoffman & Schrag, 2002 and references therein). I approximate this transition using a hyperbolic tangent fit around a temperature threshold:

$$\alpha(T) = \left(\alpha_{\text{ice}} - \iota\right) - \iota \tanh\left(\tfrac{T - T_{\alpha}}{T_{w\alpha}}\right) \tag{4.1}$$

where T_{α} is the threshold temperature for albedo transition (K) $T_{w\alpha}$ is the width of the temperature response (K), and ι is half the difference between the two albedo states:

$$\iota = \tfrac{1}{2}\left(\alpha_{\text{ice}} - \alpha_{\text{rock}}\right) \tag{4.2}$$

This albedo parameterization results in endmember albedos stabilizing at 250 K and 290 K for icy and ice-free surfaces, respectively (see figure 4.1 a). This new albedo term is used in equation 2.9.10(describing surface temperature change from solar flux, greenhouse forcing, and black body radiative balance), replacing the fixed albedo term:

$$\left.\frac{\mathrm{d}T}{\mathrm{d}t}\right|_{\mathrm{GHF}} = \frac{A_E}{M_{\mathrm{oc}}c_p}\left(\left(1-\alpha(T)\right)\left(\frac{S(t)}{4}\right)\left(1+\frac{3}{4}\gamma_{IR}\right) - \sigma T^4\right) \tag{4.3}$$

This generates a feedback in which temperature declines result in increasing albedo, which then results in larger negative changes in temperature by allowing less solar flux ($S(t)$) to reach the planetary surface.

4.1.1.1 Effects on continental shelf

I assume an inverse relationship between flooded continental shelf and ice coverage, using albedo as a proxy for ice coverage (which is difficult to estimate in this type of model). As albedo increases towards α_{ice} and more ocean water is frozen in glaciers, sea level declines and exposes an increasing portion of shallow continental shelf (Kirschvink, 1992). Without overlying ocean, shelf sediments become inaccessible for ocean-sediment reactions and productivity ($\chi_{\mathrm{shelf}} \rightarrow 0$ as $\alpha(T) \rightarrow 0.6$).

$$\chi_{\mathrm{shelf}}(T) = \frac{\alpha_{\mathrm{ice}} - \alpha(T)}{\alpha_{\mathrm{rock}}} \tag{4.4}$$

See figure 4.1 b for this relationship with respect to surface temperature. The area fraction of shelf sediments as well as the fraction of primary productivity that is exported to and buried within shallow shelf sediments is affected by declining sea level, so both fractions (f_{Xshelf} denoting either f_{Pshelf} or f_{Ashelf}) assume the same relationship:

$$f_{\mathrm{Xshelf}}(T) = f_{\mathrm{Xshelf}}\chi_{\mathrm{shelf}}(T) \tag{4.5}$$

4.1.1.2 Effects on erosional influx

During planetary glaciation, the transport of eroded continental materials declines as the hydrologic cycle weakens; this is one explanation for generally slow rates of sediment accumulation during the Neoproterozoic Snowball Earth episodes (Hoffman, 2022; Partin & Sadler, 2016). As less particulate material is transported to the oceans, burial timescales increase (i.e. less sediment influx means it takes longer for reactive sediment reservoirs n and z to be buried and cut off from interactions with the overlying water column). I approximate this effect on burial timescales by modifying the erosional parameter χ_{eros}, which is otherwise a function of continental silicate reservoir size (see section 2.3.2):

$$\chi_{\text{eros}}(t,T) = \chi_{\text{eros}}(t)\chi_{\text{shelf}}(T) \tag{4.6}$$

4.1.2 Supergreenhouse feedback

Atmospheric water vapour increases with surface temperature due to increasing evaporation and increased capacity of warm atmospheres to hold water. Since water vapour acts as a strong greenhouse gas, this increasing moisture alters the radiative balance of the atmosphere. At temperatures exceeding approximately 300 K, there is a non-linear increase in the amount of water in the atmosphere, which causes outgoing longwave radiation to decrease as surface temperature increases (Dewey & Goldblatt, 2018). I therefore modify our equation for thermal optical depth (equation 2.126) using a hyperbolic tangent fit to temperatures exceeding the supergreenhouse threshold:

$$\gamma_{IR} = f_{\text{N2}}^{q}\left(a_T(T-250)\left(\frac{3}{2}+\frac{1}{2}\tanh\left(\frac{T-T_{\text{SG}}}{T_{w\text{SG}}}\right)\right)+b_T G F_t\right) \tag{4.7}$$

Where T_{SG} is the threshold for supergreenhouse warming (300 K), and $T_{w\text{SG}}$ is the width of the transition (in K).

Table 4.1: Snowball parameters Tunable model parameters for snowball glaciation feedback systems, denoting range tested and values used in presented glacial runs.

Parameter	Definition	Range	Value
T_α	Temperature for albedo transition (K)	265 - 275	270
$T_{w\alpha}$	Albedo transition width (K)	5 - 7	6.5
T_{SG}	Temperature for supergreenhouse transition (K)	295 - 305	300
$T_{w\text{SG}}$	Supergreenhouse transition width (K)	2 - 10	8
α_{ice}	Albedo for icy surfaces	0.55 - 0.65	0.6
α_{rock}	Albedo for ice-fee surfaces	0.3	0.3
η_{w}	Weathering power law CO_2 sensitivity	0.275 - 0.325	0.3
χ_{LIP}	Maximum LIP perturbation	2 - 25	25
χ_{spread}	Minimum spreading perturbation	0.1 - 0.5	0.1

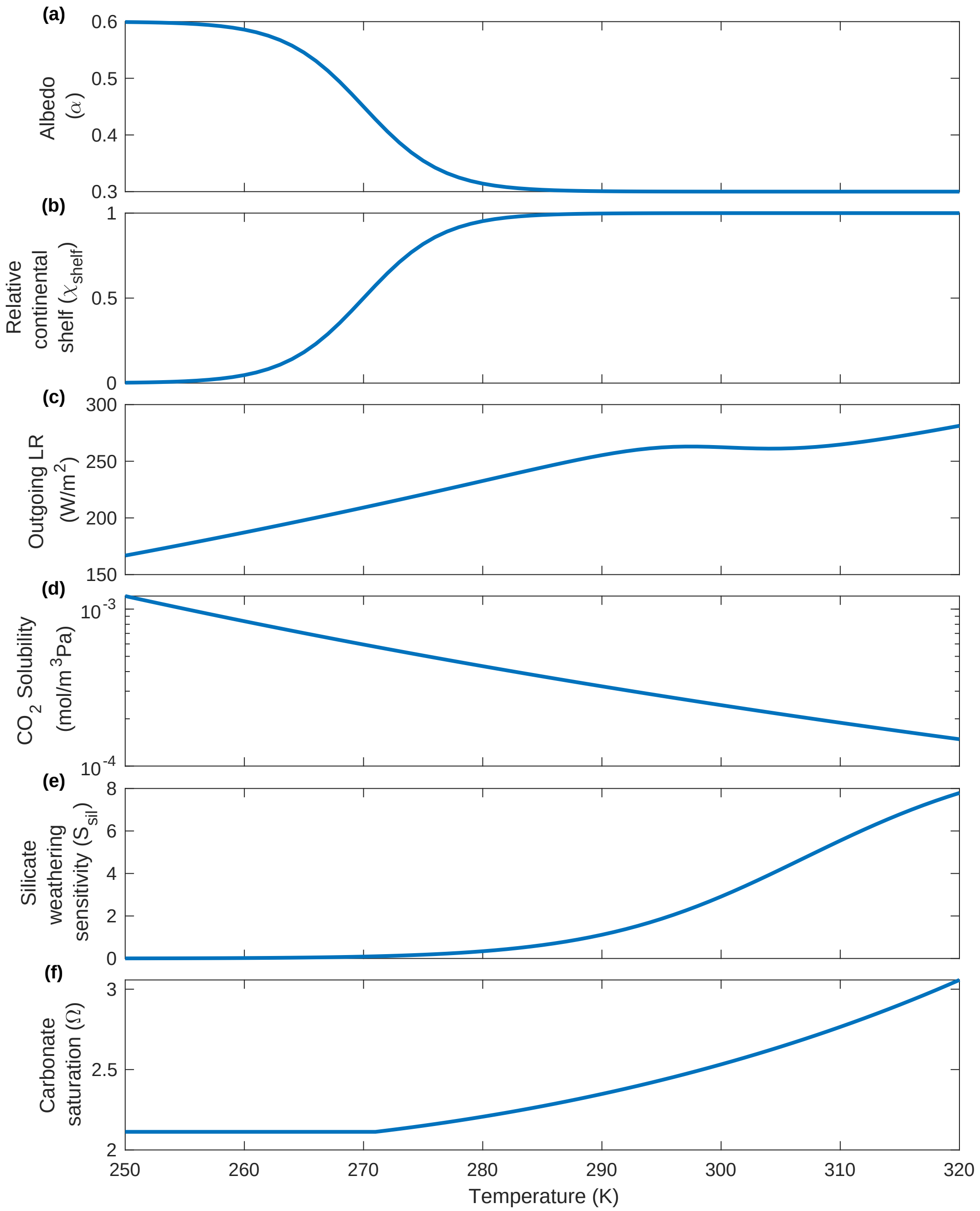

Figure 4.1: Temperature sensitive parameters Parameters varying with surface temperature: **a** surface albedo; **b** relative continental shelf fraction; **c** outgoing longwave radiation (γ_{IR} in equation 2.126); **d** CO_2 solubility; **e** silicate weathering sensitivity; **f** carbonate saturation state in the surface ocean for [TA] = 2400 μmol/kg and [DIC] = 2200 μmol/kg. The minimum surface ocean temperature is fixed at 271 K (-2° C), causing the discontinuity in declining carbonate saturation at very low temperatures shown in **f**.

4.2 Tectonic influences on Proterozoic glaciation

Adding in these climatic feedbacks allows testing for likely causes of the Paleoproterozoic snowball glaciations by comparing climate stability with and without perturbations. In particular, I investigate whether or not biological oxygen production and atmospheric methane decline alone are able to initiate global glaciation (Kirschvink et al., 2000; Schrag et al., 2002; Kopp et al., 2005; subsection 4.2.1). I consider the temperature thresholds for global glaciation and deglaciation to be 260 K and 280 K, respectively, corresponding to the boundaries for my albedo parameterization characterizing ice covered and ice free conditions.

Table 4.2: Geologic Perturbations A summary of the different fluxes affected by new tectonic perturbations, and the boundary forcing to mantle outgassing (χ_{mantle}) described in section 2.3, which is affected by the new mantle LIP eruption perturbation.

Parameter	Definition	Fluxes Affected	
χ_{spread}	Relative seafloor spreading rate	$F_{\text{volc,CaCO3}}$	$F_{\text{volc,OC}}$
		$F_{\text{volc,NH4}}$	$F_{\text{volc,ON}}$
		$F_{\text{subduct,CaCO3}}$	$F_{\text{subduct,OC}}$
		$F_{\text{subduct,NH4}}$	$F_{\text{subduct,ON}}$
		$F_{\text{subduct,SP}}$	$F_{\text{subduct,OP}}$
		$F_{\text{subduct,CP}}$	$F_{\text{subduct,FeOH3}}$
		$F_{\text{acc,CaCO3}}$	$F_{\text{acc,OC}}$
		$F_{\text{acc,NH4}}$	$F_{\text{acc,ON}}$
		$F_{\text{acc,SP}}$	$F_{\text{acc,OP}}$
		$F_{\text{acc,CP}}$	$F_{\text{acc,FeOH3}}$
		$F_{\text{cryst,CaCO3}}$	$F_{\text{cryst,NH4}}$
		$F_{\text{cryst,SP}}$	$F_{\text{cryst,OP}}$
		$F_{\text{cryst,CP}}$	$F_{\text{cryst,FeOH3}}$
		$F_{\text{mantle,C}}$	$F_{\text{mantle,N}}$
χ_{LIP}	Mantle plume eruptions	$F_{\text{mantle,SiO3}}$	$F_{\text{mantle,SP}}$
		$F_{\text{mantle,Fe2SiO4}}$	$F_{\text{mantle,FeO}}$
χ_{mantle}	Relative mantle reductant outflux	$F_{\text{mantle,FeO}}$	

I also test changes in tectonic systematics which may have contributed to causing snowball glaciations by applying two different perturbations which simulate a "Paleoproteozoic tectonic slowdown" (Pehrsson et al., 2014; see section 1.2.3.1). Parameterizations for these tectonic perturbations are evaluated separately and in conjunction (sections 4.2.2, 4.2.3, and 4.2.4). I opt to treat seafloor spreading and mantle LIP eruptions separately to more easily constrain the behaviour of the system under perturbations to outgassing and continental growth; in reality, mantle LIP events would be associated with extensive CO_2 outgassing. When I combine these perturbations in section 4.2.4, I do so in a way that allows outgassing to increase as mantle eruptions occur, in an attempt to capture a more realistic relationship between these two tectonic changes. I summarize all new climate parameters and perturbation values, denoting the baseline values used in runs shown throughout the rest of this chapter in table 4.1. I also summarize the fluxes affected by the tectonic perturbations outlined in this section in table 4.2.

4.2.1 No perturbations

For the "no forcing" endmember run shown in figure 4.2, I employ nominal model forcings (see section 2.3) and initial conditions with the updated climate system feedbacks, with an albedo transition threshold (T_α) of 270 K.

Without additional perturbations, the resulting climate and atmospheric chemistry evolution for the Paleoproterozoic is almost entirely unchanged from that of nominal model runs (see figure 3.3). The domination of oxygenic photosynthesizers over the biosphere around 3.5 Ga leads to a sharp decline in CH_4 as oxygen production begins, leading to a small decline in temperature. The GOE occurs around the same time with the same effects on the climate; rising O_2 and declining CH_4 cause gradual climate cooling until around 2.4 Ga when the GOE occurs. Atmospheric CH_4 rises sharply following the GOE, causing a rapid spike in surface temperature. The aftermath of the GOE has slightly declining CO_2, slowly rising oxygen levels, and a stable methane greenhouse that, in combination with rising solar constant, produces a gradually warming climate.

The initial result detailed in the nominal run appears robust; oxygenation of the atmosphere causes a rise in the CH_4 greenhouse and temperature, and maintains a stable, high level of atmospheric CH_4 after the GOE. These results suggest that Paleoproterozoic oxygenation does not result in a permanent decline of atmospheric methane, and that in this parameterization any decline in methane resulting from the GOE is insufficient to cause a global glaciation.

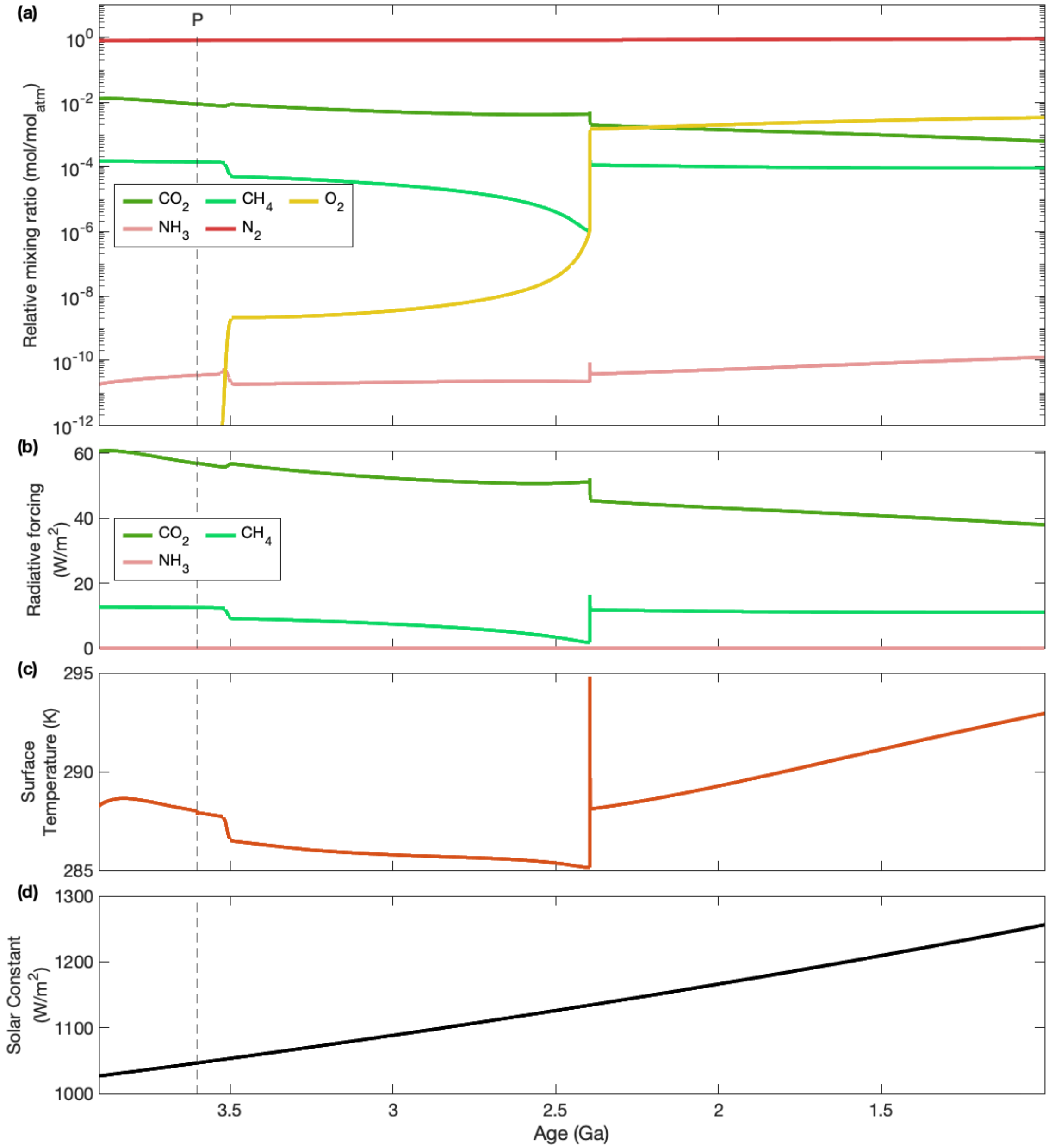

Figure 4.2: Nominal run with climate feedbacks Results from a nominally tuned model run (see chapter 3) with the updated climate described in section 4.1. **a** Atmospheric mixing ratios for gases; **b** radiative forcings by greenhouse gases; **c** surface temperature; **d** solar constant. A climate including more feedbacks fails to produce a snowball after the GOE.

4.2.2 Mantle plume eruptions, $\chi_{\mathbf{LIP}}$

I investigate how the eruption of large igneous provinces (LIPs) from the mantle may contribute to global glaciations via a new forcing to mantle-continent fluxes. The eruption of massive amounts of basalt in equatorial regions has been implicated as a possible mechanism for causing the Neoproterozoic Sturtian glaciation (Cox et al., 2016; Goddéris et al., 2003; Gumsley et al., 2017). In this model, I simulate elevated mantle eruption rate as a perturbation to mantle fluxes; this is applied as $\chi_{\mathrm{LIP}} F_{\mathrm{mantle},j}$ for j indicating SiO_3, SP, Fe_2SiO_4, or FeO, all fluxes of solid species from the mantle to the continent and deep ocean [1]. While LIP eruptions themselves drive transient increases in atmospheric CO_2, weathering of basalt erupted in LIP events causes a massive decline in CO_2 in the longer term (Cox et al., 2016). The LIP perturbation applied here does not include an increase in rate of mantle volatile outgassing, because the point of this perturbation is to constrain the effects of increased availability of weatherable material alone. I address a more realistic and complex scenario wherein LIP eruptions coincide with increased outgassing in section 4.2.4. The perturbations shown in figure 4.3 increase the rate of continental reservoir growth for SiO_3, SP, Fe_2SiO_4, and boosts mantle reductant outflux from hydrothermal vents for FeO. A rapid increase in continental silicate reservoirs leads to enhanced weathering and alkalinity flux to the ocean, drawing out atmospheric CO_2 and causing cooling (figure 4.3 a).

Increased weathering from continental emergence does not reduce atmospheric CO_2 enough in this dynamic system to cause significant temperature decline. Within the tested range of 2-25×, LIP eruptions fail to initiate significant global cooling. Early in the eruptions (pre-2600 Ma) O_2 declines due to increased outflux of reduced iron into the continents and oceans (see figure 4.3 a and b); declining O_2 allows for a temporary CH_4 rebound (not shown in this figure) that spurs the initial rise in surface temperature. As the perturbation begins to wane, the GOE initiates (around 2450 Ma) as enhanced productivity (boosted by an expanding continental reservoir of silicate-bound P) overwhelms the large surface reservoir of reduced iron.

---

[1] *EONS* has no silicate reservoir for the oceanic crust, so this perturbation emphasizes subaerial over submarine eruptions. However, the effects of LIP events should also include some submarine component and mantle reductant transport, so this perturbation also enhances the flux of FeO to the deep ocean. A future version of the model could include an ocean crust silicate reservoir to help this perturbation more closely resemble reality.

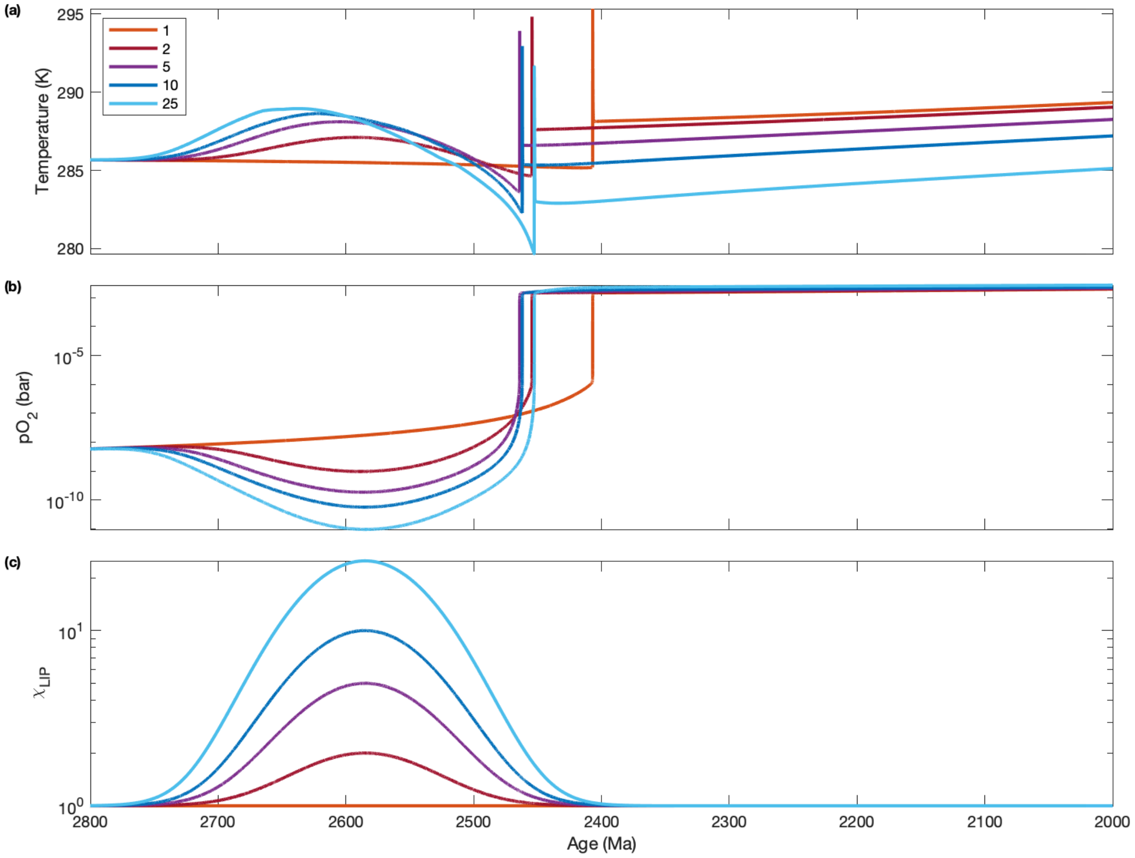

Figure 4.3: Perturbations to mantle eruptions. **a** Surface temperature; **b** oxygen level; **c** mantle eruption perturbation. Colours correspond to different mantle outflux perturbation maxima.

The largest magnitude perturbation, which is equivalent to modern continental emergence by the Mesoproterozoic, causes temperatures to fall below 280 K (figure 4.3 a). Nevertheless, climate remains stable and rebounds out of the decline as oxygen rises and precipitates the post-GOE jump in atmospheric CH_4. These results imply that while an increase in subaerially weatherable material will result in climatic cooling, the initiation of a snowball glaciation requires either more perturbations to the carbon system or perhaps a more unstable climate in addition to enhanced weathering. Results of earlier modelling done for the Neoproterozoic similarly suggest that multiple factors are necessary for such extreme climate disruption; Goddéris et al. (2003) suggested that the Sturtian glaciation was most likely caused by the compounding effects of weathering the Franklin LIP during the breakup of Rodinia and the near-equatorial position of landmasses, rather than basaltic weathering alone.

4.2.3 Seafloor spreading rate, χ_{spread}

I investigate how changing volatile outgassing may contribute to global glaciations via a new perturbation to spreading rate. Declining volcanic activity, particularly outgassing of CO_2, has been implicated as contributing to the initiation of the Neoproterozoic snowball events (Li, Evans, & Zhang, 2004). The new perturbation used here affects both mantle volatile fluxes to the atmosphere as $\chi_{\text{spread}} F_{\text{mantle,j}}$ (where j indicates either C or N, including both reduced and oxidized volatile species) and fluxes at subduction zones as $\chi_{\text{spread}} F_{\text{x,j}}$ (where x indicates the flux, either subduction, accretion, volcanism, or crystallization, and j indicates the species; all fluxes affected by changing seafloor spreading are detailed in table 4.2).

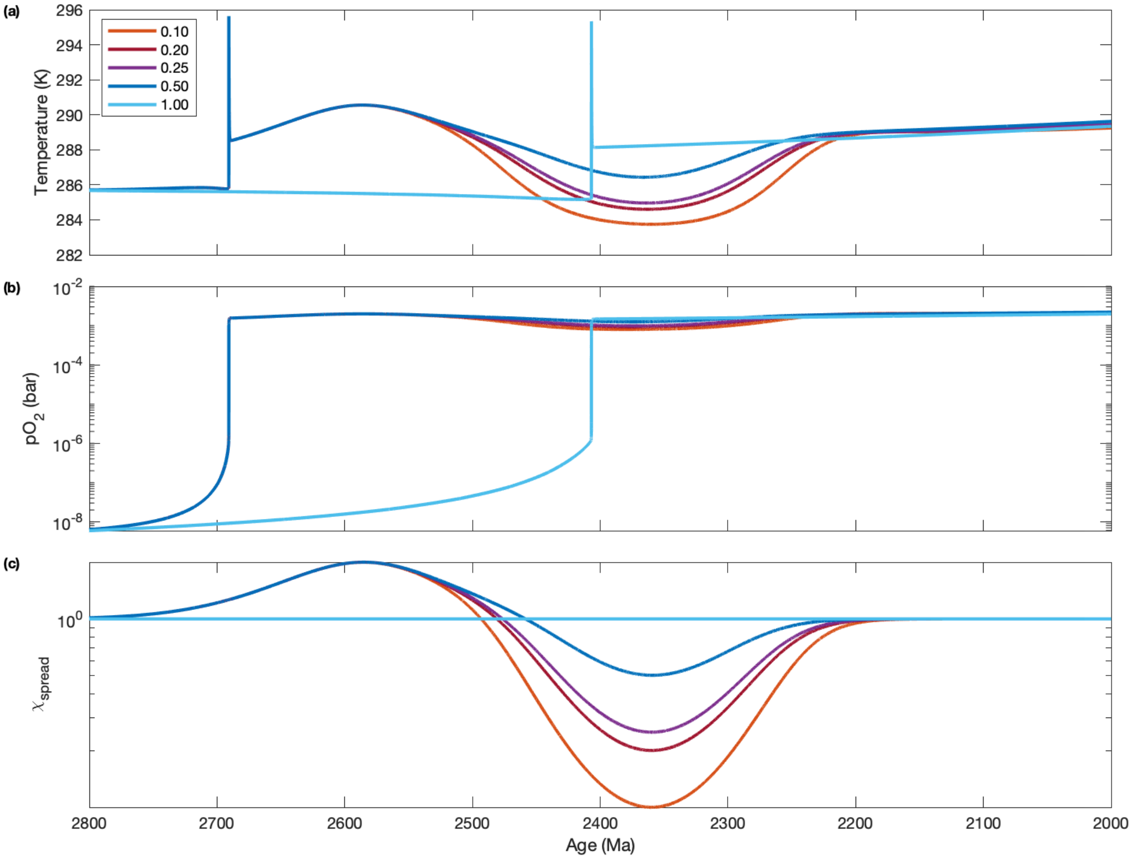

Figure 4.4: Perturbations to spreading rate. **a** Surface temperature; **b** oxygen level; **c** spreading rate perturbation. Colours correspond to different spreading rate perturbation minima.

The perturbation, shown in figure 4.4, is a sinusoidal increase and decrease to spreading rate mimicking the effects of increased mantle upwelling and subsequent outgassing quiescence during the initial amalgamation of a supercontinent. I use an asymmetrical form because increasing outgassing by a factor greater than 2 results in supergreenhouse conditions and generally unrealistic outgassing fluxes; thus all perturbations use the same maximum value and only vary in minima. Increasing outgassing (2750 - 2500 Ma) results in rising temperatures preceding the sinusoidal decline (2500 - 2200 Ma), during which mantle and volcanic outgassing are limited.

Changing rates of volatile carbon cycling alone do not cause enough temperature decline to initiate global glaciation. Initially, temperatures increase from faster outgassing of CO_2 and CH_4. Rising temperatures enhance continental weathering, causing an early GOE (ca. 2700 Ma) despite the perturbation's initial enhancement of reductant volatile (CH_4 and NH_3) outflux. The GOE is followed by a decline in temperatures as outgassing fluxes reach their minima (ca. 2350 Ma; see figure 4.4a). While the largest perturbation causes temperatures to decline below 284 K, climate remains within the temperate zone.

4.2.4 Combined perturbations

The modelled carbon system, because it is able to dynamically respond to changes in temperature, atmospheric CO_2, and pH, is not easily perturbed by a single change in the system. Because fluxes here are not fixed, a forced change in one flux will be balanced by a change in a corresponding flux, pushing the system back towards equilibrium. In the case of increased weathering, carbonate deposition increases and transports more carbon to subduction zones, where volcanism outflux increases. In the case of decreased volcanism, less available atmospheric CO_2 will cause a decline in weathering flux and alkalinity transport, thus decreasing CO_2 sequestration.

I combine the two tectonic perturbations in order to simulate some effects caused by the amalgamation and stabilization of Paleoproterozoic supercontinent Columbia/Nuna (Hawkesworth, Cawood, Kemp, Storey, & Dhuime, 2009; Nance et al., 2014). Increased volcanism, mantle outgassing, and mantle eruptions precedes continental collision and supercontinental aggregation[2]. Once stabilized,

---

[2] As mentioned in the introduction (section 1.1.2), the relationship between supercontinental formation or breakup and the prevalence of LIP events is not entirely clear. Condie et al., 2021 suggest that mantle plume activity (producing LIPs) is not essential in the formation of ocean basins during supercontinental breakup. They find that the age distribution of LIP events does not correlate uniformly to either supercontinental assembly or dispersal, and can occur at any

eruptions and volcanism enter a quiescent period where subduction is limited to the continental periphery and where mantle heat increases beneath the thick, stabilized continental lid (Condie, 2002). Combined tectonic perturbations such as these have been implicated in causing the Neoproterozoic glaciations (Li et al., 2004). Figure 4.5 encapsulates how the model climate reacts to a few combinations of these tectonic perturbations, focusing on the more extreme cases tested in sections 4.2.2 and 4.2.3. These results imply that both spreading and LIP perturbations are required in this model to destabilize the climate enough to resolve a sequence of Paleoproterozoic snowball glaciations coinciding with the GOE that broadly agrees with the record.

Combined perturbations to tectonic cycles work together and amplify the destabilization of the inorganic carbon system, which ultimately controls climate. LIP eruptions combined with moderate to high subsequent decline in spreading result in temperature fluctuations between 230 and 330 K (curves for χ_{LIP} = 25 χ_{spread} = 0.2 and for χ_{LIP} = 25 χ_{spread} = 0.1, respectively, in 4.5). The combination for χ_{LIP} = 25 χ_{spread} = 0.2 results in one short glaciation (ca. 40 Myr), while the combination of χ_{LIP} = 25 χ_{spread} = 0.1 results in three glaciations, the first and last lasting approximately 50 Myrs and the middle lasting nearly 100 Myrs (figure 4.5). Interglacials for the latter combination are on the order of 0.7 Myrs in duration. The combination of elevated CO_2 and more continental material leads to greatly enhanced weathering and a much more protracted decline in temperature than either forcing acting alone; when coupled with declining volcanism and outgassing depriving the surface of CO_2 to sustain a greenhouse, this protracted temperature decline results in a global glaciation.

---

point during the lifetime of the supercontinent. Orogenesis and uplift are generally correlated with supercontinental formation, though similarly are not specific to those periods alone (Condie et al., 2021). Since *EONS* has no way to simulate the effects of continental uplift, the LIP perturbation used here simulates both eruption of fresh material and growth of continental bodies. As such, I am making the assumption that during supercontinent formation weathering is going to be enhanced, either by eruption of new material from the mantle or by uplift and exposure of continental materials already present; the methodology used reflects the capabilities of the model, rather than settled science.

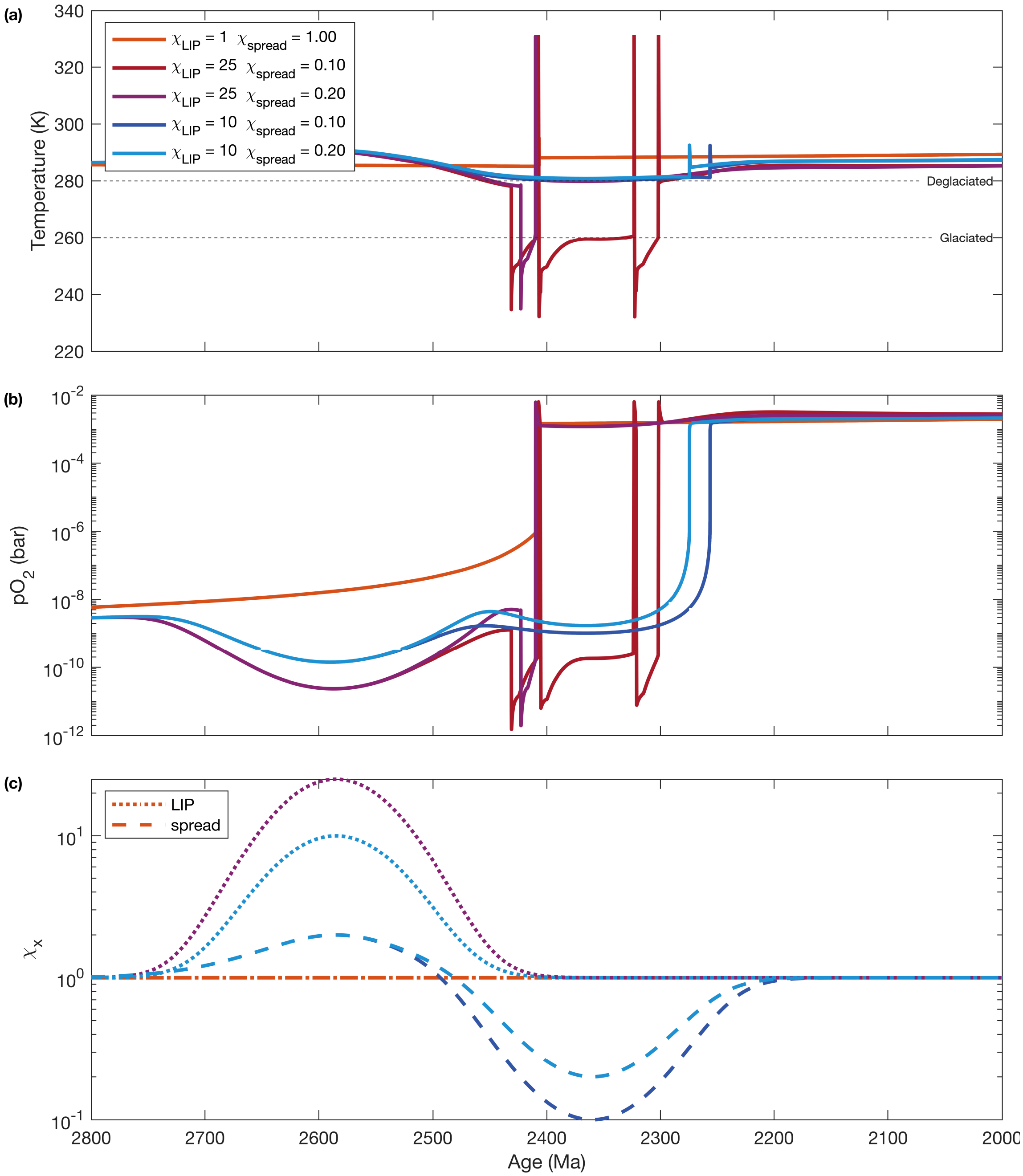

Figure 4.5: Combined perturbations resulting in glacial oscillations a Surface temperature (horizontal dashed lines denote glaciation and deglaciation thresholds); **b** oxygen level; **c** combined tectonic perturbations to mantle eruptions and spreading rate. Colours correspond to different perturbation combinations (χ_{LIP} by χ_{spread} in the legend).

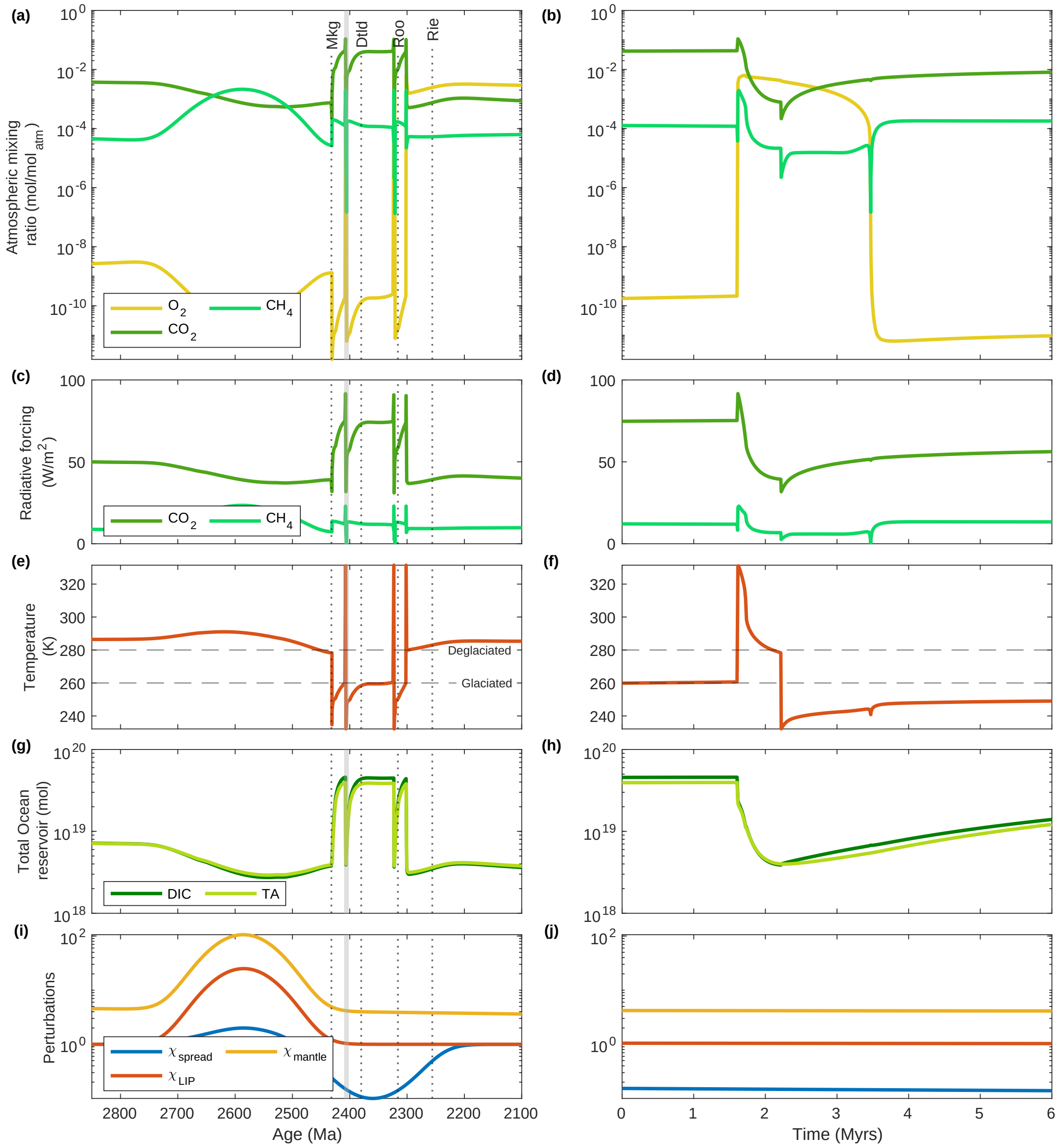

Figure 4.6: Surface conditions during oscillating glacial episodes Left column shows the full period of perturbation for selected systems and reservoirs (perturbations shown in bottom row subplots), with age in Ma. Right column shows zoomed in portion of highlighted grey zone, an interglacial event, with time since start of interglacial measured in millions of years. **a-b** Atmospheric mixing O_2, CO_2, and CH_4 mixing ratios; **c-d** radiative forcing of greenhouse gases CO_2 and CH_4; **e-f** surface temperature (horizontal dashed lines denote glaciation and deglaciation thresholds); **g-h** total ocean reservoirs for DIC and total alkalinity; **i-j** the perturbations applied, including χ_{mantle} forcing. Dotted vertical lines denote age estimates for Paleoproterozoic glacial diamictites from the South African Kapvaal craton and associated Superior craton diamictites compiled by Garduño Ruíz, Goldblatt, and Ahm (2023). We defer to using the South African formation names (*Mkg* for Makgayene, *Dtld* for Duistchland, *Roo* for Rooihoogte, and *Rie* for Rietfontein).

I examine how the carbon cycle responds to combined tectonic perturbations for a selected case of $\chi_{\mathrm{LIP}} = 25$ and $\chi_{\mathrm{spread}} = 0.1$; this combination of perturbations results in the longest period of glacial oscillations (figure 4.5), and as such provides the most material for analysis (although the magnitude of these perturbations are quite extreme; I comment on this further in section 4.5). Figure 4.6 shows how some surface reservoirs and fluxes react to this combination of perturbations in more detail, with a focus on atmosphere-ocean reservoirs and climate; geologic perturbations leading up to the GOE at 2400 Ma result in a temporary expansion of the CH_4 greenhouse by introducing reductants (χ_{LIP}) and increasing volatile outgassing from the mantle (χ_{spread}; figure 4.6 a and i). As oxygen begins rising again, there is a sharp decline in atmospheric CO_2 which seems to initiate glacial oscillations (figure 4.6 a, c, and e).

The rate of geologic carbon release is a major control on glacial cycles. The total duration of climate destabilization broadly matches the duration of χ_{spread} decline (figure 4.6 i). Figure 4.8 shows alkalinity controls and cap carbonate deposition throughout the three glacial cycles. All resulting glaciations are punctuated by short interglacial periods in which massive cap carbonate layers are deposited (figure 4.8 i through j)[3], which signifies that this model is simulating Snowball Earth glaciation events. Shelf cap carbonates average 300 m in thickness, approximately 10 times the size of recorded Paleoproterozoic cap carbonate platforms (Kennedy, 1996); pelagic carbonate deposition is not generally preserved in the geologic record, as most of this $CaCO_3$ is recycled at subduction zones.

The system falls into glacial oscillations when carbon influxes into the atmosphere-ocean decline to a critical low and atmospheric CO_2 enters into a temporary positive feedback loop with silicate weathering. I highlight the rapid transition into glacial conditions in figure 4.7. Volcanism slowed by the χ_{spread} perturbation causes atmospheric CO_2 to decline steadily until reaching a mixing ratio around 7×10^{-4} bar, corresponding to a peak in ocean pH (figure 4.7d and e). The initially shallow decline in CO_2 causes simultaneous declines in surface temperature and subaerial weathering fluxes, particularly silicate and carbonate weathering (4.7a through c). Alkalinity falls into a lasting period of net outflux as silicate weathering (now

---

[3] The carbonate layer thickness subplot only highlights the formation of cap carbonates during hot interglacials, and ignores regular depositional periods (during glaciations, there is no deposition on continental shelves due to declining sea level; see section 4.1.1.1). However, the gaps between the cap carbonate formations are not indicating a lack of $CaCO_3$ burial in pelagic sediments, but that these periods do not meet the climatic criteria for formation of cap carbonates.

starved of atmospheric CO_2) shuts down; following this crash, reverse weathering dominates as the major source of alkalinity loss, slightly outpacing $CaCO_3$ weathering (figure 4.7 c). Curtailed carbon supply (i.e. the spreading perturbation here causing a continuous decline in volcanism) thus initiates glaciation by disrupting the balance in alkalinity supply, which is intrinsically linked with atmospheric CO_2 level via silicate and carbonate weathering influxes. It appears that there is a short-term positive feedback that arises between atmospheric CO_2 and silicate weathering at this critical threshold: there is a lag in response time between alkalinity transport (via silicate weathering) and carbonate burial such that declining silicate weathering does not result in declining $CaCO_3$ precipitation until the pelagic sediments have turned over, which occurs on timescales of a few thousand years. With continuously declining CO_2, this relatively brief period of alkalinity outflux outpacing supply is enough to destabilize the climate; more carbon is sequestered than the system can handle. This lag in response time is illustrated by the sharp transition to negative net alkalinity flux in figure 4.8c, essentially a buffering period for the ocean carbonate system. After glaciation initiates, carbon influx stabilizes at a new high level as $CaCO_3$ burial shuts down (figure 4.7 b); this new imbalance will eventually cause the end of the glaciation.

Atmospheric CO_2 balance dictates when glaciations initiate and terminate. Glaciations start when CO_2 level drops below an atmospheric mixing ratio of approximately 8×10^{-4}, and terminate when CO_2 rises above a mixing ratio of approximately 2×10^{-2} (figures 4.7 d, 4.6 a and b, and 4.8 c and d). Glacial periods are characterized by increasing (or stable high) CO_2 levels, with declining (or stable low) O_2 (figure 4.6 a and b); high ocean DIC, alkalinity, and slightly acidic to neutral pH (figures 4.6 g and 4.8g); and a positive imbalance in both alkalinity and CO_2 atmosphere-ocean fluxes (influxes outpace outfluxes, figure 4.8 e and f). During glaciations, the ocean inorganic carbon system shuts down, allowing for massive reservoirs of DIC and alkalinity to accumulate; interglacial warm periods result in the rapid deposition of $CaCO_3$, which temporarily returns these reservoirs to their pre-glacial state (figure 4.6 g and h and 4.8 i and j). Glacial episodes are characterized by high levels of atmospheric CO_2, due to the cessation of weathering and carbonate precipitation (figures 4.6 a and 4.8 b).

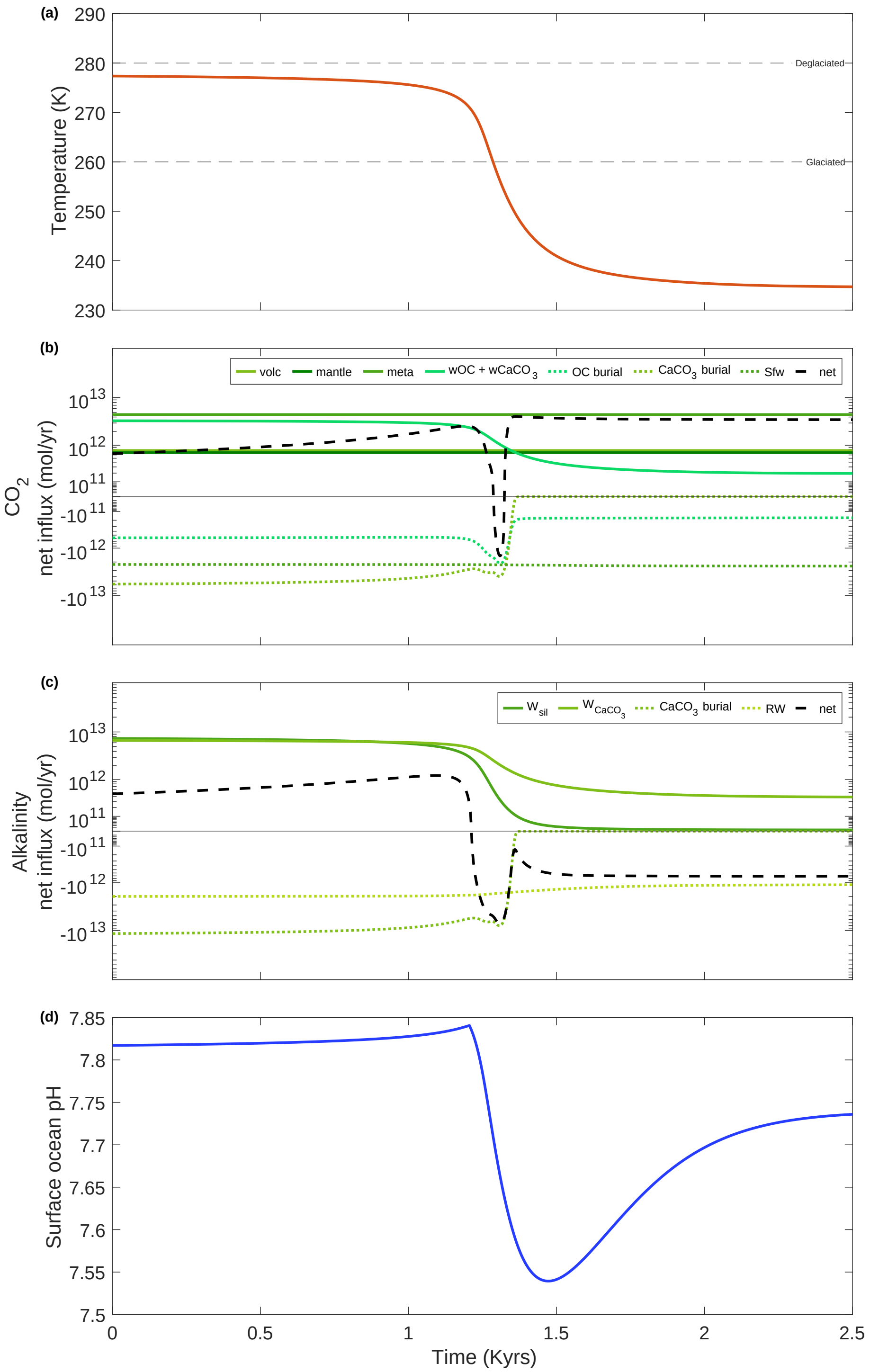

Figure 4.7: Alkalinity and CO_2 systematics at the initiation of glacial episodes. **a** Surface temperature (horizontal dashed lines denote glaciation and deglaciation thresholds); **b** net CO_2 influx to the atmosphere-ocean; **c** net alkalinity influx to the ocean; **d** atmospheric CO_2 mixing ratio; **e** surface ocean pH. Subplots **b** and **c** are shown on symmetric log y axis, with outfluxes represented as negative values; horizontal solid lines denote 0. Timescale is shown in kiloyears after the start of the glacial cycle at approximately 2425 Ma).

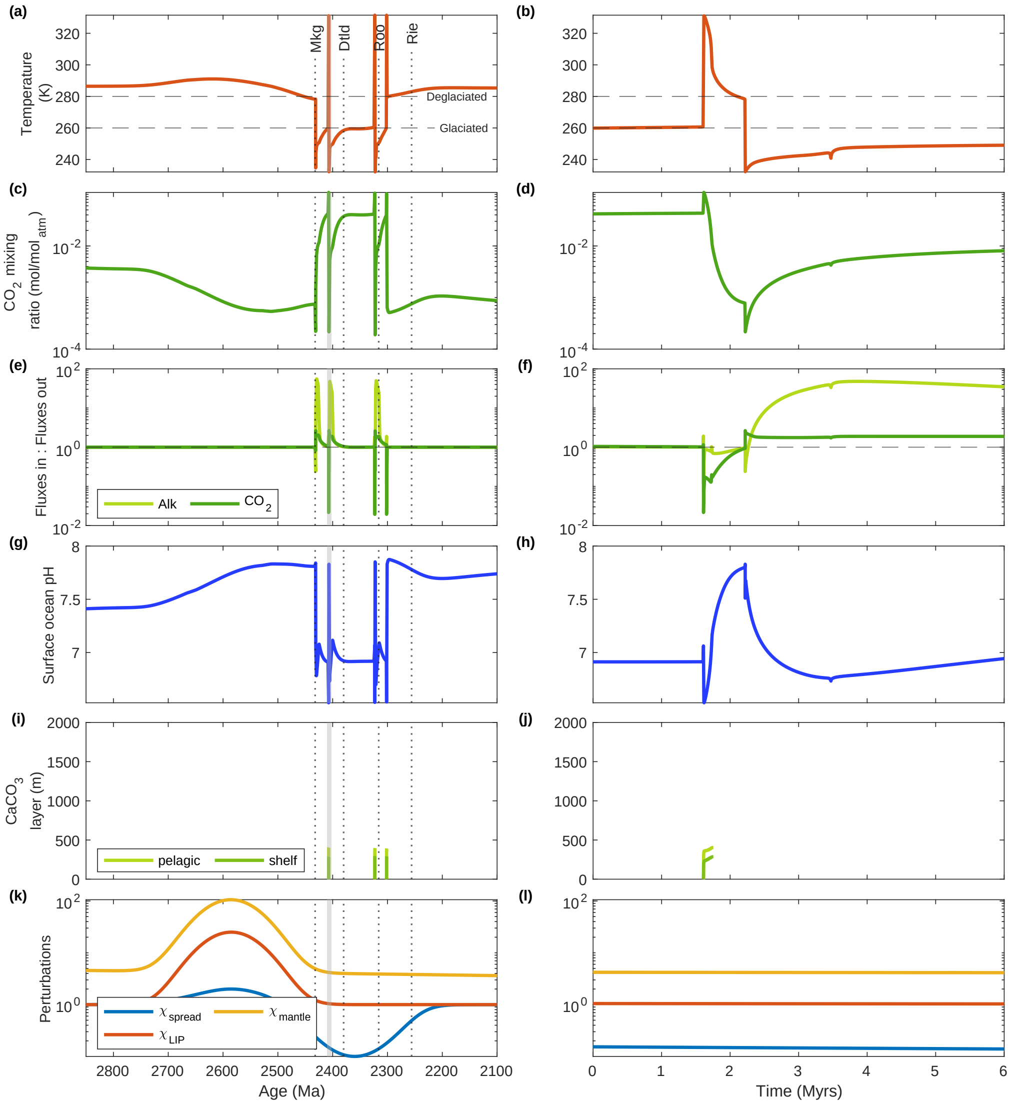

Figure 4.8: Alkalinity and CO$_2$ systematics during oscillating glacial episodes Left column shows the full period of perturbation for selected systems and reservoirs (perturbations shown in bottom row subplots), with age in Ma. Right column shows zoomed in portion of highlighted grey zone, an interglacial event, with time since start of interglacial measured in millions of years. **a-b** Surface temperature (horizontal dashed lines denote glaciation and deglaciation thresholds); **c-d** atmospheric CO$_2$ level; **e-f** ratio of total fluxes of alkalinity and CO$_2$ into and out of the atmosphere-ocean system (horizontal dotted line denotes 1); **g-h** surface ocean pH; **i-j** thickness of CaCO$_3$ layer deposited during the interglacial periods; **k-l** the perturbations applied, including χ_{mantle} forcing. Dotted vertical lines denote age estimates for Paleoproterozoic glacial diamictites from the South African Kapvaal craton and associated Superior craton diamictites compiled by Garduño Ruíz, Goldblatt, and Ahm (2023). We defer to using the South African formation names (*Mkg* for Makgayene, *Dtld* for Duistchland, *Roo* for Rooihoogte, and *Rie* for Rietfontein).

The results of this test suggest that interglacial periods can be much shorter than corresponding glacial periods, but such short interglacial durations contradict the geologic records for Snowball Earth events. The *EONS* model is producing interglacial periods lasting about 0.5-1 Myrs (figure 4.6), characterized by elevated O_2 with decreasing CO_2 and CH_4 (figures 4.6 b and 4.6c); sharply declining ocean DIC and alkalinity (figure 4.6 g) and rapidly increasing pH (figure 4.8g), which results in extensive deposition of $CaCO_3$ on the continental shelf (figure 4.8 i through j); and a slightly negative imbalance in both alkalinity and CO_2 atmosphere-ocean fluxes (where outfluxes outpace influxes, figure 4.8 f). Glacial episodes in the record transpire over intervals on the order of 10-60 Myrs punctuated by interglacials lasting 10-50 Myrs (Halverson, Hoffman, Schrag, Maloof, & Rice, 2005; Hoffman, 2013; Hoffman et al., 2017; Hoffman et al., 1998). Because of this discrepancy, I investigate the controls on interglacial timing in the *EONS* model in more detail.

4.3 Controls on glaciation timing and tempo

The initial success in generating glacial events through purely geologic perturbations indicates that the major controls on glacial timing and tempo lie in the balance of surface CO_2 and alkalinity fluxes. Previous work on modelling the Neoproterozoic glaciations (Mills et al., 2011) demonstrated that material transport limitation on the silicate weathering feedback (WHAK; Walker et al., 1981) exerted a strong control over glacial/interglacial timing, and demonstrated that a glacial episodes controlled by perturbations to weathering were on the order of tens of millions of years in duration, in agreement with the record. With the ability to resolve glacial oscillations using tectonic perturbations, I investigate the capability of geologic cycles in the *EONS* model to resolve longer interglacial cycles, and attempt to bridge the gap between my preliminary results and the geologic record.

4.3.1 Weathering CO_2 sensitivity, η_w

The sensitivity of subaerial carbonate and silicate weathering (η_w) is a tunable model parameter, with values estimated between 0.2 - 0.5 (for a weak and strong control, respectively; Sleep & Zahnle, 2001; Bergman et al., 2004; Berner & Kothavala, 2001). A lower value of η_w (i.e. weathering less sensitive to CO_2) will result in higher stable CO_2 levels. Figure 4.9 shows different glaciation tempos using a narrow range of values for η_w.

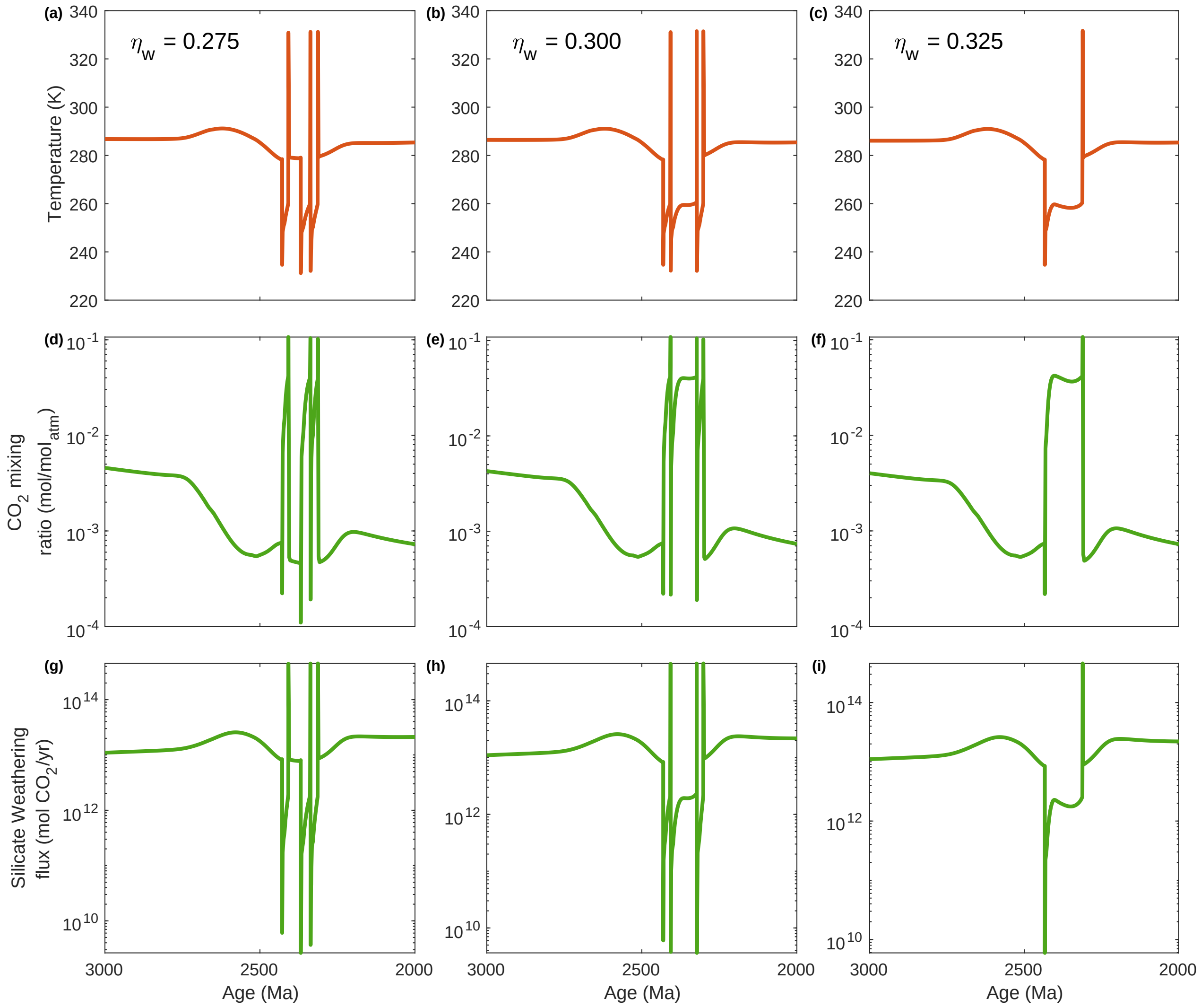

Figure 4.9: Glacial behaviour and weathering CO_2 sensitivity Effects of changing subaerial CO_2 sensitivity on the timing and number of glacial oscillations. Columns correspond to output for tested value of η_w, denoted in legends of top row plot. Top row (**a**, **b**, **c**) surface temperature; second row (**d**, **e**, **f**) atmospheric CO_2 mixing ratio; bottom row (**g**, **h**, **i**) silicate weathering flux.

Weathering CO_2 sensitivity is inversely correlated with number of glacial oscillations; higher sensitivity to CO_2 results in fewer snowball events. Systems with higher weathering sensitivity respond faster to changes in CO_2. In figure 4.10, the steeper response of $\eta_w = 0.5$ denotes higher weathering at $CO_2 > 1 \times 10^{-3}$ bar and lower weathering at $CO_2 < 1 \times 10^{-3}$ bar. This parameterization would result in a much more dynamic weathering range when compared with shallower slopes for less sensitive systems. Thus, less sensitive systems have relatively higher weathering at lower CO_2, which results in a more unstable oscillatory response. Because higher sensitivity results in a stronger weathering feedback, small increases in CO_2 incur more weathering at lower temperatures, which is why these systems are associated with longer stable glaciations (figure 4.9 c); glacial episodes in general correspond to high CO_2 level with low surface temperature, since silicate weathering ceases and CO_2 builds up rapidly on geologic timescales (see figure 4.8 c and d).

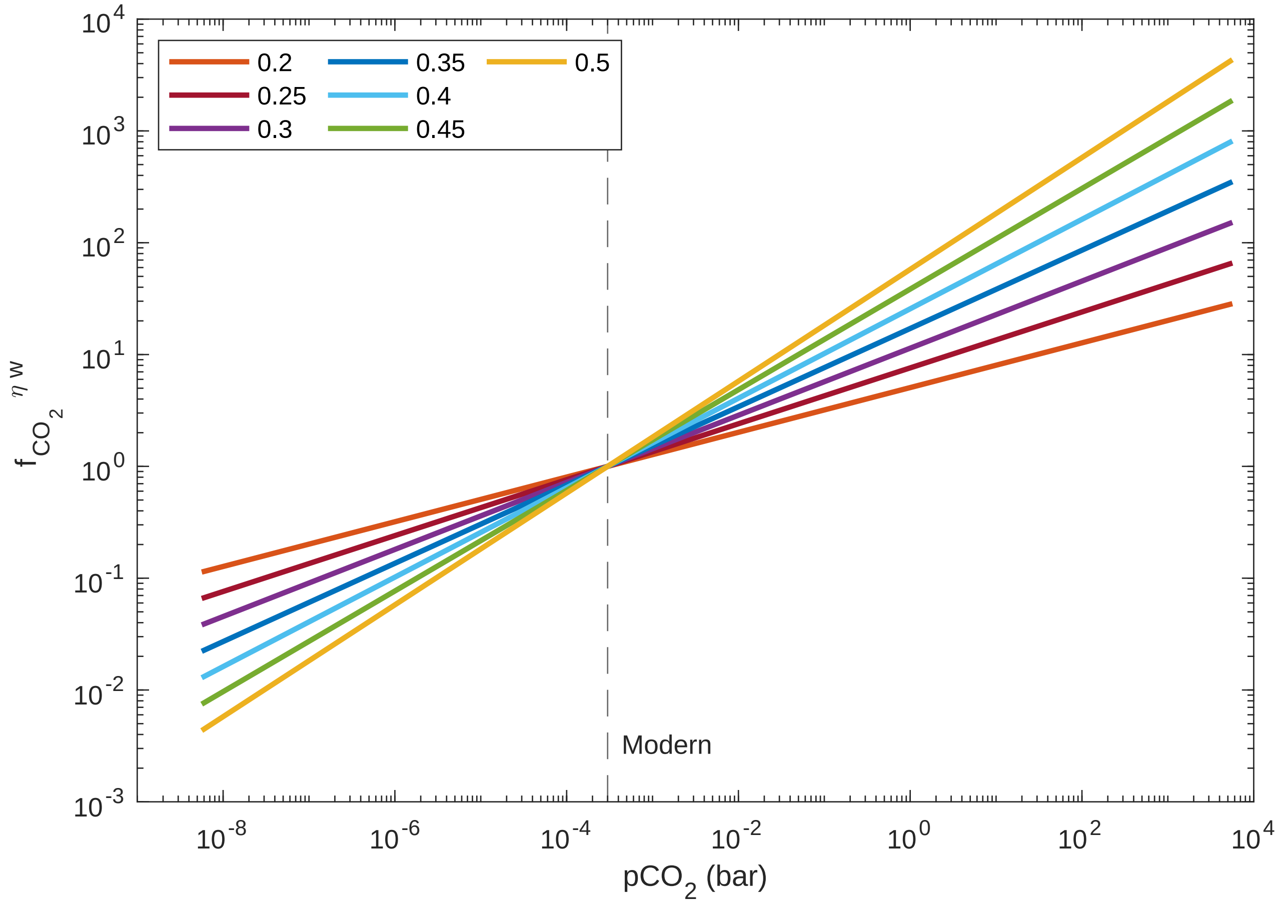

Figure 4.10: Parameter range of CO_2 weathering sensitivity How different atmospheric CO_2 levels and the value of CO_2 weathering sensitivity exponent η_w (given in legend) affect the magnitude of the subaerial carbonate and silicate weathering response (equation 2.87). The vertical dashed line denotes modern CO_2 concentration.

An interesting phenomenon arises when $\eta_w = 0.275$; the first interglacial period extends beyond 0.5 Myrs to approximately 40 Myrs in duration with low stable

CO_2 (figure 4.9 a and d). I investigate this long interglacial event further in sections 4.3.2 and 4.4.

4.3.2 Spreading perturbation, χ_{spread}

The duration of glacial-interglacial oscillations appears to a function of the duration of the decline in spreading, because this perturbation exerts a first order control on the geologic residence of carbon. Volcanism is the shortest pathway within the geologic carbon cycle for the return of sequestered carbon to the atmosphere, operating on a timescale of 100 million years in this model. In the previous test producing a long interglacial with less responsive CO_2 weathering (figure 4.9 first column), the occurrence of the interglacial did not correspond with the spreading perturbation minimum, rather with a slope declining towards the minimum. The nature of a sinusoidal perturbation means that the value being perturbed is constantly changing. In order to constrain how interglacials respond to a stable minimum χ_{spread}, I compare this baseline sinusoidal treatment to a new piecewise form. Figure 4.11a shows two different treatments for the spreading perturbation, both in runs using $\eta_w = 0.275$. I also evaluate runs with combinations of sinusoidal χ_{spread} and either linearized or gaussian (baseline) treatments for χ_{LIP}, shown in figure 4.11b.

Figure 4.11 compares how different treatments of the tectonic perturbations affect the duration of interglacial periods, and oxygen level; 4.11a shows different styles of perturbation to seafloor spreading (χ_{spread}) and 4.11b compares treatments of the perturbation of mantle LIP eruptions (χ_{LIP}). Changing to a linear shape for χ_{spread} erases the appearance of a single long interglacial (figure 4.11a-a, curve for piecewise), while a linear treatment of χ_{LIP} only appears to affect when glacial (and by extension, interglacial) events occur (figure 4.11b-a).

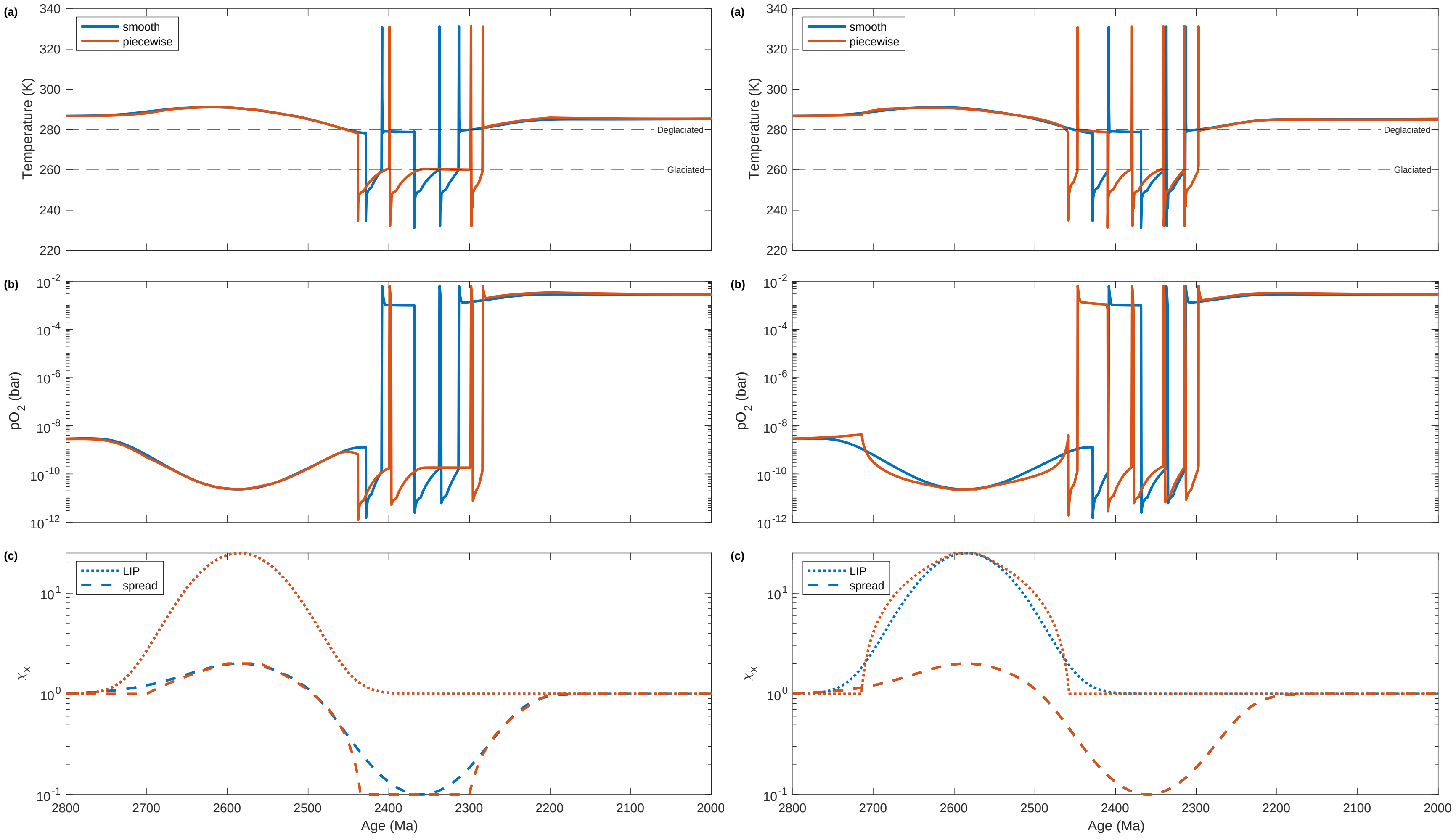

(a) **(b)**

Figure 4.11: Interglacial timing and treatment of $\chi_{\mathbf{spread}}$ and $\chi_{\mathbf{LIP}}$ **a** The basic sinusoidal treatment of χ_{spread} (blue) alongside a piecewise treatment of similar depth and duration. Perturbation to χ_{LIP} is the same in both runs. **b** The basic gaussian pulse treatment of χ_{LIP} (blue) alongside a piecewise treatment of similar height and duration. Perturbation to χ_{spread} is the same in both runs. Subplots for both figures: **a** Surface temperature (horizontal dashed lines denote glaciation and deglaciation thresholds); **b** oxygen level (PAL); **c** χ_{LIP} and χ_{spread} perturbations. Note both **c** subplots use logarithmic y-axis scaling.

4.4 Geologic controls on long interglacials

Interglacials in this dynamic model are dictated by the response of the atmosphere-ocean carbon cycle to changes in geologic cycles; therefore, interglacial duration reflects the timescales of atmosphere-ocean carbon cycling. This model generally produces interglacials between 2×10^5 and 7×10^5 years in duration for glacial events caused by purely tectonic factors. These durations are significantly shorter than interglacial episodes produced by earlier models (Mills et al., 2011), and in disagreement with the Paleoproterozoic glacial record (Halverson et al., 2005; Hoffman, 2013), which records interglacial episodes on the order of 10 Myrs in duration.

I am able to tune the model to produce a single longer interglacial episode, by using a particular combination of decreased weathering CO_2 sensitivity and χ_{spread} slope. I evaluate the sensitivity of interglacials to parameterizations of volatile outgassing, using consistent values for η_w and χ_{LIP} but with different slopes of declining χ_{spread}, shown in figure 4.12.

In this model, a specific confluence of geologic factors can cause a long-period interglacial event. The default parameterization of χ_{spread} is shown in figure 4.12 k as the intermediate (dotted purple) slope results in an interglacial approximately 40 million years in duration, while similar curves either result in longer stable glaciations (blue curve, shallower) or rapid termination of glacial cycles (red curve, steeper; figure 4.12a and b). The steepest curves produce stable low CO_2 states with high ocean pH and short atmosphere-ocean CO_2 residence (figure 4.12c through h). The red curve experiences a rapid interglacial that stabilizes into a long glacial period perpetuated by low outgassing flux, resulting in long atmosphere-ocean CO_2 residence time (figure 4.12g through j). Steeper declines in χ_{spread} correspond to higher outgassing, returning the system to truly stable conditions faster than shallow slopes with slightly lower outgassing. This implies that producing extended interglacial periods in *EONS* may be a matter of producing a perfectly tenuous, stable condition for atmosphere-ocean CO_2.

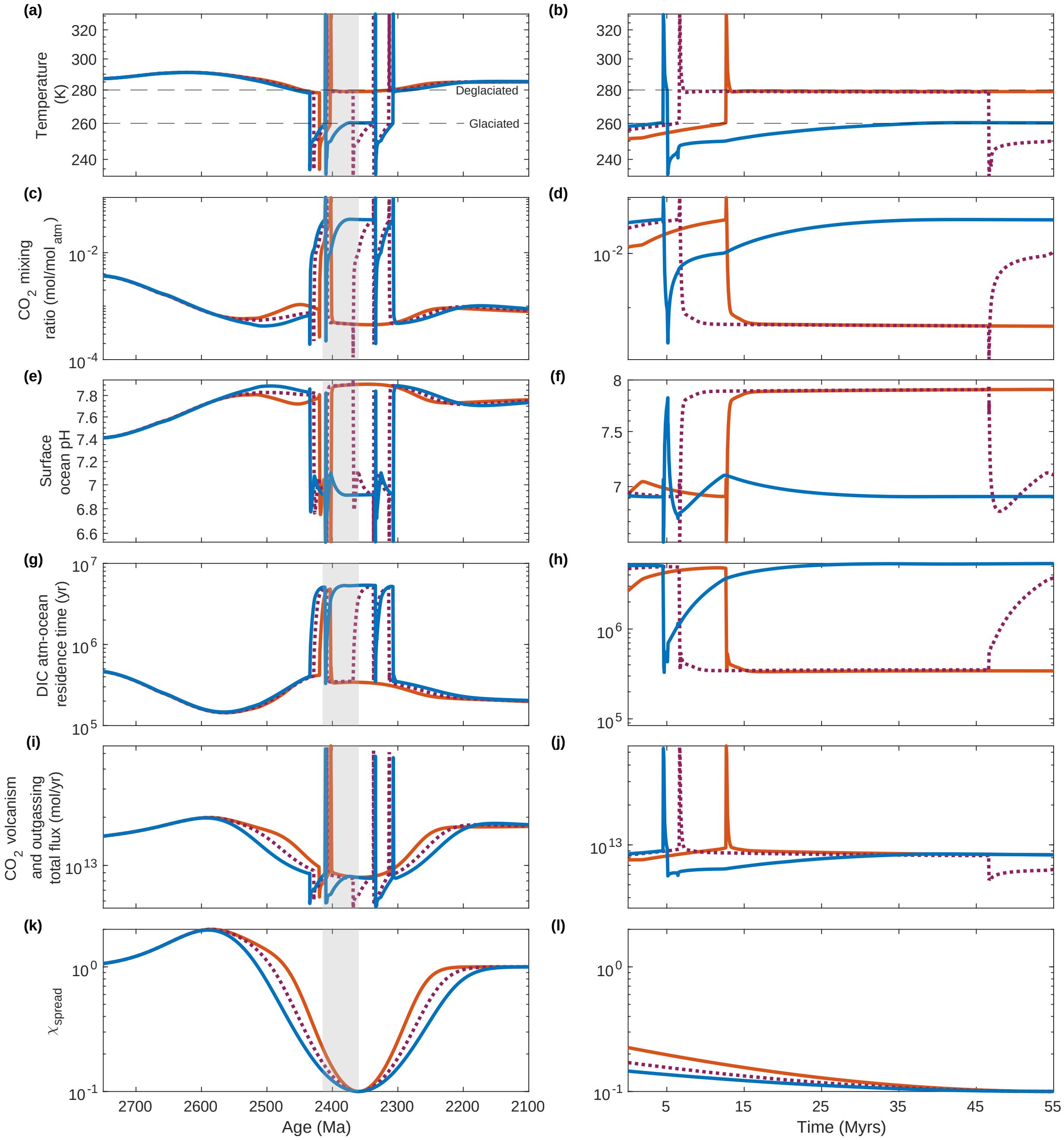

Figure 4.12: Glacial behaviour and width of spreading perturbation Left column shows the full period of perturbation for selected systems and reservoirs (perturbations shown in bottom row subplots), with age in Ma. Right column shows zoomed in portion of highlighted grey zone, an interglacial event, with time since start of interglacial measured in millions of years. Colours and linestyle correspond to the different treatments of the χ_{spread} decline (blue = shallower slope, red = steeper slope, dotted purple = baseline slope). **a-b** Surface temperature (horizontal dashed lines denote glaciation and deglaciation thresholds); **c-d** atmospheric CO_2; **e-f** surface ocean pH; **g-h** atmosphere-ocean residence time for DIC; **i-j** total volcanic and mantle CO_2 outgassing flux; **k-l** different treatments to χ_{spread} perturbation.

Fixing carbon outgassing in this dynamic model requires a constant perturbation, because of how the atmosphere-ocean system reacts in response to changing CO_2. Figure 4.13a shows alkalinity and atmosphere-ocean CO_2 balance (net flux into atmosphere-ocean) for a run with only short interglacial periods (produced by the piecewise χ_{spread} treatment shown in figure 4.11a). Figure 4.13b shows alkalinity and CO_2 balance in a run including a long interglacial period (produced by the sinusoidal χ_{spread} treatment shown in figure 4.11a). Note that in figure 4.13a-b volcanism and mantle outgassing are perturbed to a stable low value by χ_{spread} whereas in figure 4.13b-b the sinusoidal χ_{spread} perturbation causes volcanism and mantle outgassing to steadily decline; this is the key difference between these two results, particularly because of the role that CO_2 plays in regulating ocean pH and alkalinity balance. With a constant perturbation to volatile outgassing, the influx of CO_2 is not actually kept stable (figure 4.13a-b).

The ramifications of these different perturbations to spreading rate are better illustrated in figures 4.14a and 4.14b, which highlight the first interglacial period for both scenarios; the former lasting 0.7 million years, and the latter lasting 40 million years. Carbonate burial increases in response to elevated weathering and alkalinity transport (figure 4.14a-e and 4.14b-e), as a result of the rapid increase in surface temperature at the start of the interglacial. Elevated silicate weathering results in a rise in pH from increased alkalinity transport (figure 4.14a-d), which is rapidly deposited as $CaCO_3$, resulting in a sharp pH decline that shallows as $CaCO_3$ deposition slows (figure 4.14a-e). This pelagic $CaCO_3$ is eventually transported to subduction zones, leading to increased volcanism (figure 4.14a-b and 4.14b-b). The system becomes starved of CO_2 as silicate weathering is increasingly enhanced at higher CO_2 and temperatures, and enables enhanced $CaCO_3$ deposition. Through this response, increasing volcanism will prematurely terminate an interglacial unless suppressed by the correct amount.

Long interglacial periods result from long periods of stable ocean alkalinity and atmosphere-ocean CO_2. The short interglacial never achieves alkalinity balance, whereas the long interglacial is characterized by alkalinity influxes equalling outfluxes (figures 4.14a-c and 4.14b-c); the carbon system achieves similar balance (figure 4.14b-b) This corresponds to a stable period of CO_2 influx (figure 4.14b-b). Because less CO_2 is outgassed in this case, ocean pH gets slightly higher and results in higher reverse weathering. The fact that other slopes for χ_{spread} decline do not generate the same alkalinity balance indicates that the particular perturbation which generates a long interglacial is by coincidence increasing ocean pH by just the right amount to boost reverse weathering and balance alkalinity outfluxes.

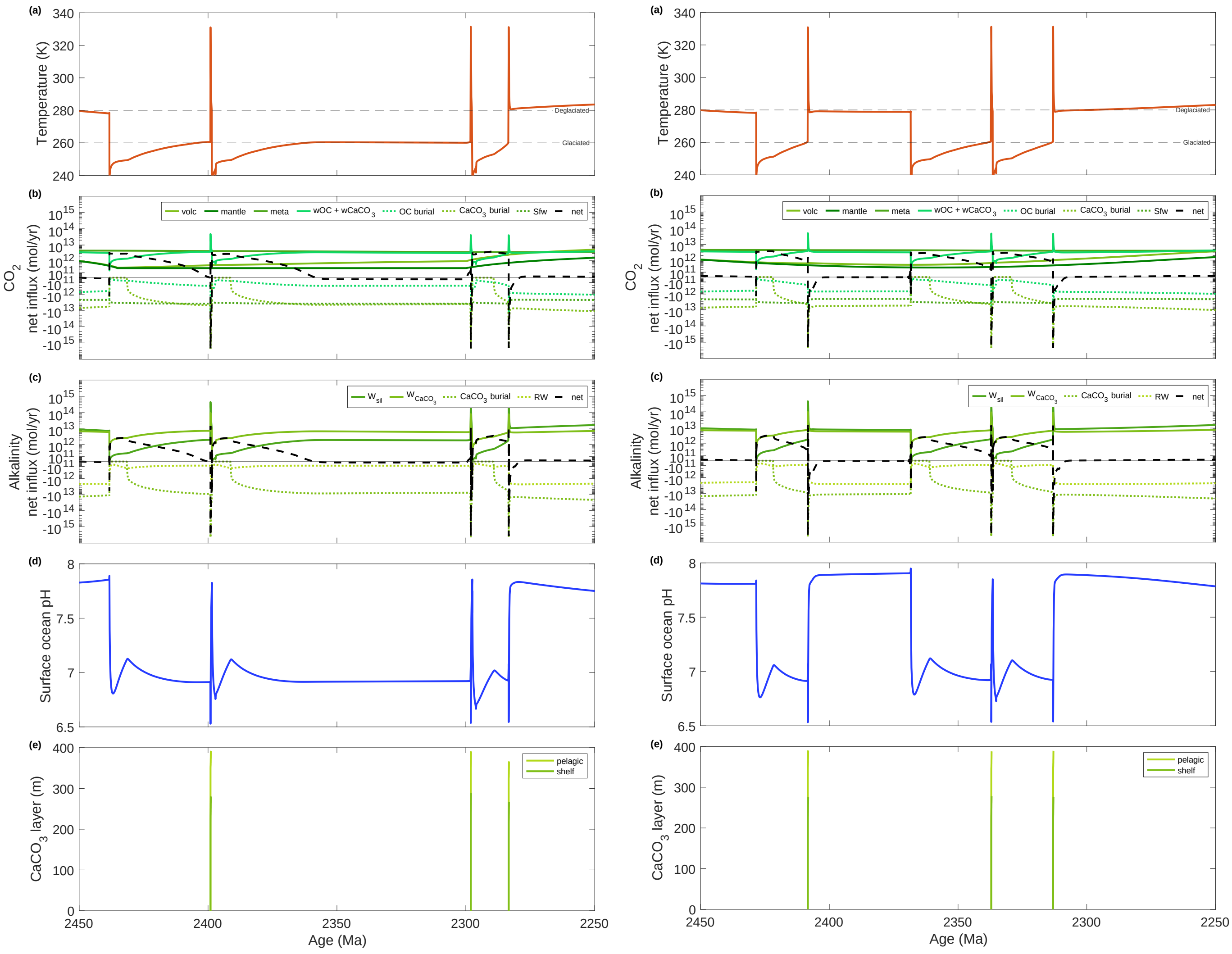

(a) **(b)**

Figure 4.13: Alkalinity and CO_2 balance during all glacial cycles 4.13a shows a run using piecewise χ_{spread} producing only short interglacials; 4.13b shows a run using sinusoidal χ_{spread} producing one long interglacial. In each subplot: **a** Surface temperature (horizontal dashed lines denote glaciation and deglaciation thresholds); **b** net CO_2 influx to the atmosphere-ocean; **c** net alkalinity influx to the ocean; **d** surface ocean pH; **e** thickness of sedimentary $CaCO_3$ layer deposited during hot interglacials. Subplots **b** and **c** are shown on symmetric log y axis, with outfluxes represented as negative values; horizontal solid lines denote 0.

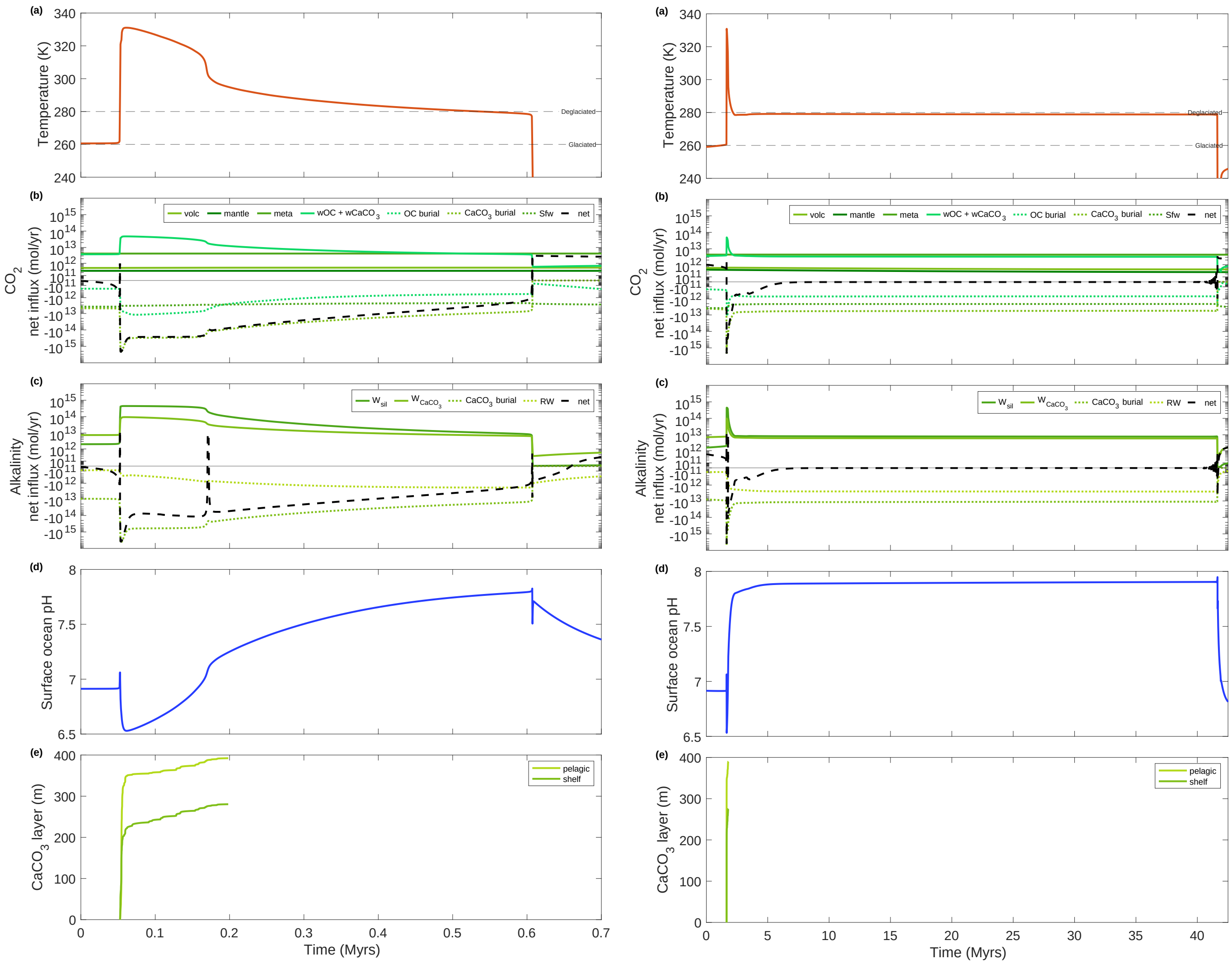

(a) **(b)**

Figure 4.14: Alkalinity and CO_2 balance during an interglacial 4.14a shows a short interglacial; 4.14b shows a long interglacial. In each subplot, **a** surface temperature (horizontal dashed lines denote glaciation and deglaciation thresholds); **b** net CO_2 influx to the atmosphere-ocean; **c** net alkalinity influx to the ocean; **d** surface ocean pH; **e** thickness of sedimentary $CaCO_3$ layer deposited during hot interglacials. Subplots **b** and **c** are shown on symmetric log y axis, with outfluxes represented as negative values; horizontal solid lines denote 0.

This model, as parameterized, routinely produces interglacial events that are significantly shorter than what is suggested by geologic evidence. The results of this model with regard to interglacial duration also contrast with the results from Mills et al. (2011). While my exploration of glacial/interglacial sensitivity broadly agrees with their findings, this model implies that interglacial durations on the order of tens of millions of years is highly unlikely. Mills et al. (2011) use fixed fluxes with only weathering responding to CO_2 and temperature, and they do not resolve ocean chemistry; in this model I employ dynamic fluxes and reservoirs, and a comprehensive treatment of ocean carbon cycling, which gives a fully coupled surface carbon system. This difference explains much of the discrepancy between our results. In Mills et al. (2011), geologic fluxes are responding to geologic forcings. In this model, atmosphere-ocean fluxes respond to geologic forcings and in turn affect changes in geologic reservoirs and fluxes (i.e. volcanism and weathering). The two models demonstrate the key interplay of timescales in the Earth system; Mills et al. (2011) demonstrate how purely geological systematics react with climate, and in turn resolve cycles on geologic timescales. In this model, I demonstrate how biogeochemical cycles interact in response to (and affect) both geology and climate, and so resolve cycles on oceanic cycling timescales. The tenure of interglacials in *EONS* is apparently dictated by ocean carbon and alkalinity balance and the time required for weathering to scrub the atmosphere of high CO_2 accumulated during glacial periods; as a result, this model produces interglacial periods lasting hundreds of thousands to millions of years, on the order of the general residence time of alkalinity and DIC in the ocean during temperate periods (figure 4.12 g and h).

4.5 Relationship between GOE and glaciation

The dynamic coupling of biogeochemical cycles and climate allows me to investigate how a dramatic change in atmospheric chemistry such as the GOE relates to the timing of glacial oscillations. Initial results imply that the GOE does not cause glaciations on its own, and the magnitude of tectonic perturbations required in order to tip the climate into a glacial state are quite extreme; a 90% decrease in seafloor spreading and a 2500% increase in mantle-surface flux. This implies that the climate parameterization in *EONS* is exceptionally stable, and such stability presumably affects the results of my previous tests. This may be a consequence of parameterization choices, particularly related to the albedo transition threshold

(T_α). In this section, I demonstrate how this parameterization choice affects the outcome of the GOE and the implied stability of Proterozoic climate.

4.5.1 Climate tipping point, T_α

The threshold temperature choice for glaciation is particularly important in this experiment; a lower threshold makes it more difficult to initiate glaciations, whereas a higher threshold makes it much easier to fall into glaciations. The choice of T_α = 270 K used in runs up to this point reflects a system that only glaciates when global mean surface temperature decreases below the freezing point of water. It is important to note that the true control on runaway glaciation is ice line progression to mid-latitudes; while this depends on temperature in a broad sense, it is also strongly controlled by the relative position of continents, topography, equator-pole thermal gradient, ocean circulation patterns, precipitation patterns, and many other variables that are not well constrained for the Proterozoic and in any case are not resolved in this model. Given this uncertainty, and because the pre-GOE does experience potentially significant cooling, I test how the system reacts to different values for T_α absent additional tectonic perturbations to constrain how my parameterization of climate affects the susceptibility of this system to fall into glaciation, as well as the timing and tempo of glaciations.

This parameter choice greatly affects how and when the GOE occurs, and the duration of glacial oscillations that arise as a result. The scenarios shown in figures listed in table 4.3 encompass a range of potential climate types, ranging from very stable ($T_\alpha \leqslant$ 276 K; figure 4.15), to moderately stable (276 K $< T_\alpha >$ 278 K; figure 4.16), to weakly stable ($T_\alpha \geqslant$ 278 K; figure 4.17).

Table 4.3: Albedo threshold parameterization and climate sensitivity Summary of the different albedo threshold parameterization values tested and the kinds of climates they produce.

T_α **range (K)**	**Climate type**	**Figure**
270 - 276	very stable, no glaciations	4.15
277	moderately stable, rare glaciations	4.16
278 - 279	weakly stable, frequent glaciation	4.17

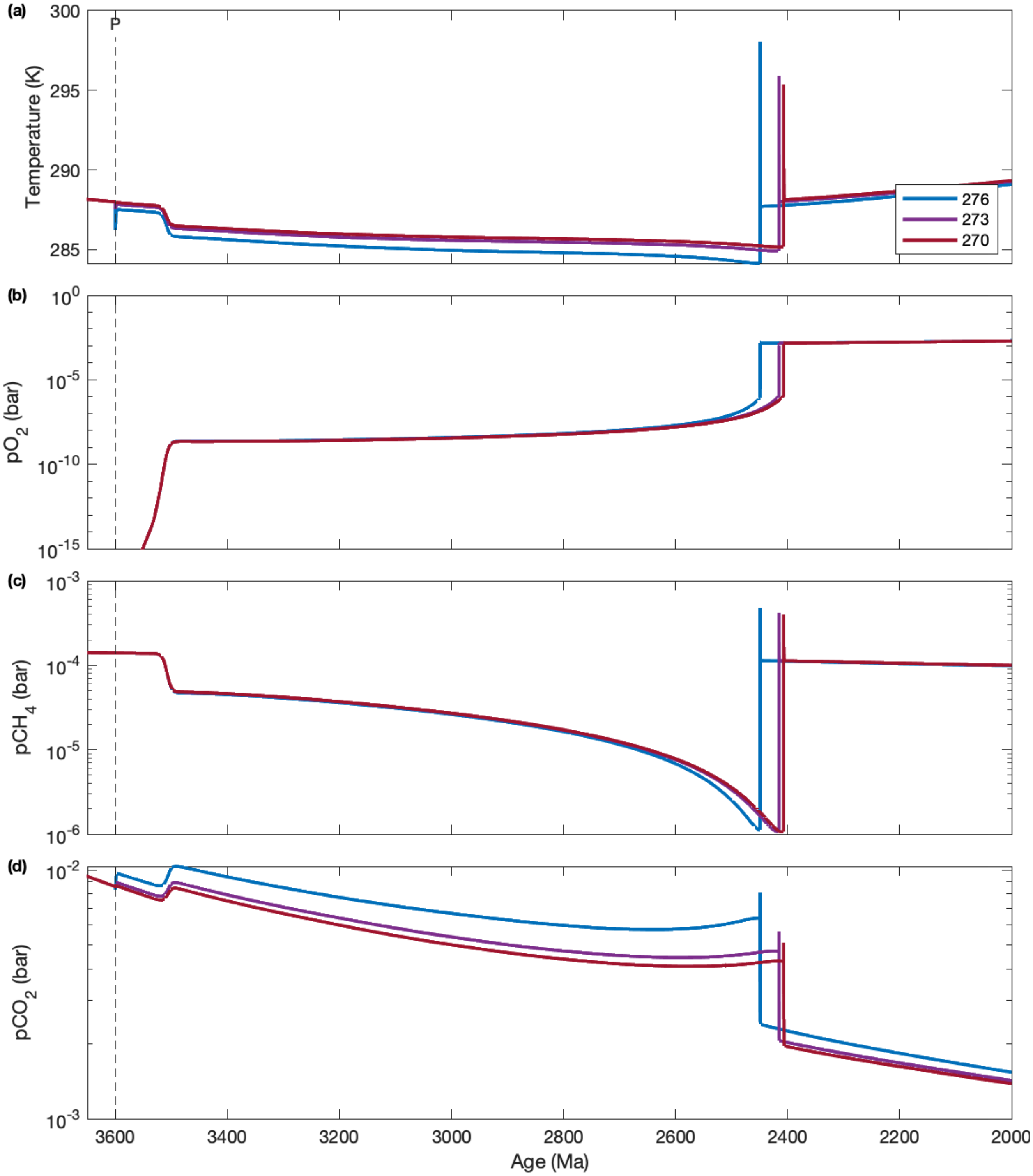

Figure 4.15: Comparing very stable parameterizations of T_α Changing the temperature threshold for albedo transition (T_α) between 270 - 276 K, simulating very stable climates. **a** Surface temperature; **b** atmosphere O_2 level; **c** atmosphere CH_4 level; **d** atmosphere CO_2 level. Transition to operational oxygenic photosynthesis is denoted by vertical dashed line labeled *P*.

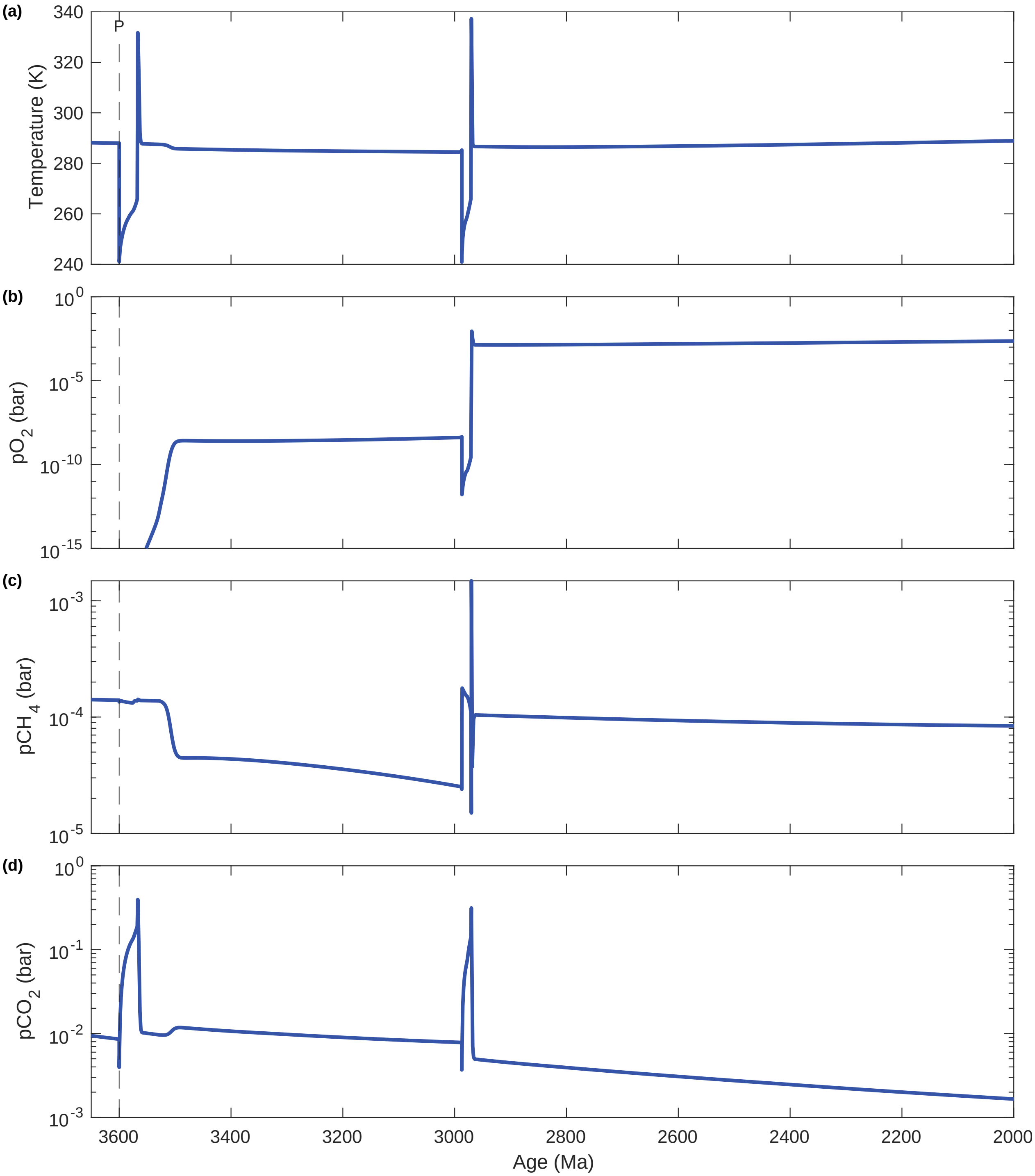

Figure 4.16: A moderately stable parameterization of T_α Changing the temperature threshold for albedo transition (T_α) to 277 K produces a moderately stable climate. **a** Surface temperature; **b** atmosphere O_2 level; **c** atmosphere CH_4 level; **d** atmosphere CO_2 level. Transition to operational oxygenic photosynthesis is denoted by vertical dashed line labeled *P*.

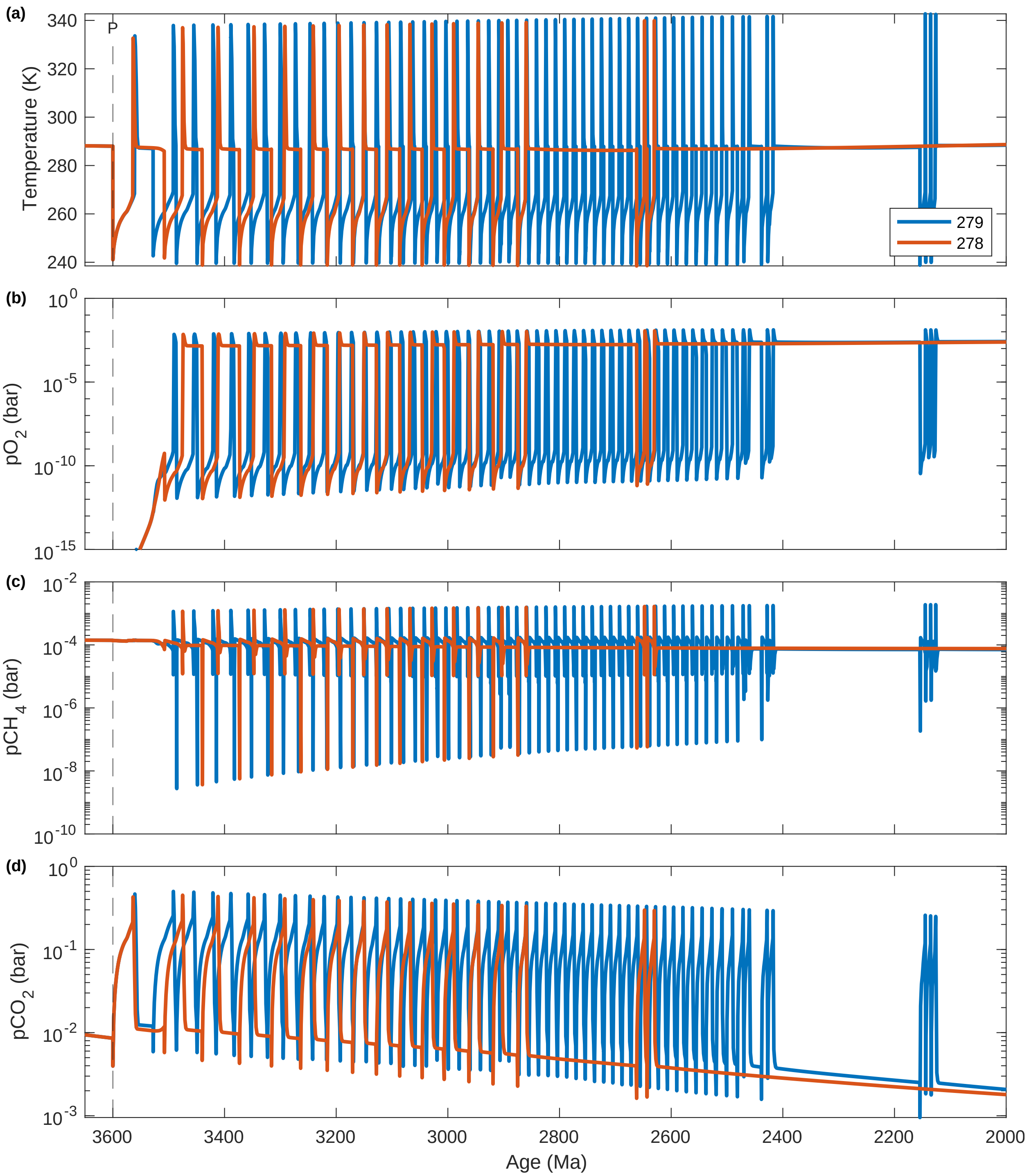

Figure 4.17: Comparing weakly stable parameterizations of T_α Changing the temperature threshold for albedo transition (T_α) between 278 - 279 K, which simulate weakly stable climates. **a** Surface temperature; **b** atmosphere O_2 level; **c** atmosphere CH_4 level; **d** atmosphere CO_2 level. Transition to operational oxygenic photosynthesis is denoted by vertical dashed line labeled *P*.

The model is insensitive to $T_\alpha \leqslant 276$ K; none of the very stable climates experience glaciation, even following the GOE. Making $T_\alpha > 276$ K drastically affects the timing and tempo of the oxygenation event itself, as shown in figure 4.16 which looks at $T_\alpha = 277$ K. Using $T_\alpha \geqslant 278$ K results in a climate that is far too sensitive to changes in radiative forcing, and falls easily into glacial oscillations, including numerous early glaciations that are apparently unaffiliated with significant O_2 level or declining CH_4.

The successful initiation of glacial oscillations by moderate and weakly stable climate parameterizations is a proof of concept that changes in the biosphere (in this case, the evolutionary development of oxygenic photosynthesis and the expansion of biosphere productivity) can destabilize climate and result in global glaciations. I discuss the behaviour of these glaciations and how they relate to oxygenation in more depth in the following section. These glaciations do not correlate at all in time or in absolute duration with the geologic record. The immediacy of the rise in oxygen in these scenarios is almost certainly a result of model tuning, and is not presented here as a contradiction of the Archean and Proterozoic rock record. Evidence from the Archean does suggest that transient oxygenation events occurred (Mukhopadhyay et al., 2014), but there is no evidence of Archean glaciations predating the Pongola diamictite (ca. 2900 Ma; Young et al., 1998). Given more time to adjust the model tuning with this updated climate treatment, I expect that the timing of the GOE could be shifted in time to better fit the record (see section 4.7).

4.5.2 Oxygen, methane, and glaciations

All moderate and weakly stable climate parameterizations experience an early glaciation associated with the evolution of photosynthesizers and the initial rise in oxygen, though O_2 remains significantly below the threshold of bistability (around 1×10^{-6} bar). This is shown in figures 4.16 and 4.17 (a and b). The initial rise in oxygen at 3500 Ma is actually preceded by a glacial episode initiated by decline in CO_2.

Initiation and termination of glacial oscillations seems to be dictated by atmospheric CO_2. In both weakly stable climates, a first episode of glacial instability is initiated by oxygen rising from 1×10^{-10} to 1×10^{-3} bar (figure 4.17d). This is then followed by a second cluster with no apparent link to changes in either oxygen or methane (I comment on this in section 4.5.3). Duration of the pseudo-stable period between these clusters is positively correlated with climate stability (for 277 K, a second glaciation occurs ca. 3000 Ma after a delay of 550 Myrs; for 278 K, two glaciations around 2750 Ma follow a delay of around 200 Myrs). These pseudo-stable periods differ in oxygen and methane atmospheric levels, but they correspond broadly in CO_2 level at time of initiation (below 1×10^{-2} bar; figures 4.16d at 3500 Ma and 4.17d curve for 278 K at 2900 Ma); more unstable climates require slightly lower CO_2 to transition into the pseudo-stable period.

Changes in atmospheric CH_4 and O_2 appear to follow, rather than drive, glacial events. The earliest spike in oxygen from near 0 to 1×10^{-8} bar is correlated with the longest glacial and interglacial periods (see figure 4.17). I highlight the first such event occurring in a weakly stable climate (T_α = 278 K) in figure 4.18, to illustrate how atmospheric chemistry drives and responds to this event. Methane does not decrease at the start of the first series of oscillations (around 3650 Ma); instead, CO_2 level drops as oxygenic photosynthesis evolves (and primary production becomes much more efficient). Methane levels do not crash until the end of the second glacial period, around 3475 Ma (figure 4.18 c). These glaciations don't appear to be primarily caused by CH_4 decline at all. On the contrary, they appear to cause temporary CH_4 decline when O_2 rises in the aftermath of hot interglacials (figure 4.18 a through d, between approximately 3550 and 3500 Ma). The culprit for instigating these glaciations appears to be the disruption to atmospheric CO_2 (figure 4.18 d), which also seems to dictate the behaviour of oscillations through time. I comment on the relationship between CO_2 and oscillations in more detail in section 4.5.3.

In these weakly stable climates, glaciation occurs before any GOE, which may contradict the record. As mentioned before, the timing of the GOE in these runs is very likely a result of model tuning, but an important implication of this preliminary investigation is that the climate must be at least moderately stable in the Archean as photosynthesizers evolve or glaciations resulting from the initial decline in atmospheric CO_2 will catalyze an early GOE. Even in the case of the moderately stable climate (T_α = 277 K) where an Archean glaciation does not result in immediate oxygenation (figure 4.16a and b), an early GOE follows the second glaciation around 3000 Ma; temporal correlations between the GOE and Paleoproterozoic glaciations are not straightforward, with some arguing that geologic evidence shows the GOE preceding glacials (Warke et al., 2020), and others finding that the GOE may have occurred between glacial episodes (Rasmussen et al., 2013). The results shown here suggest that glaciations in an unstable climate could reasonably occur prior to global oxygenation, and perhaps contribute to accelerating the pace of the GOE via weathering in interglacials. None of these scenarios show a GOE actually preceding glaciations, but these preliminary modelling results do not rule out that possibility.

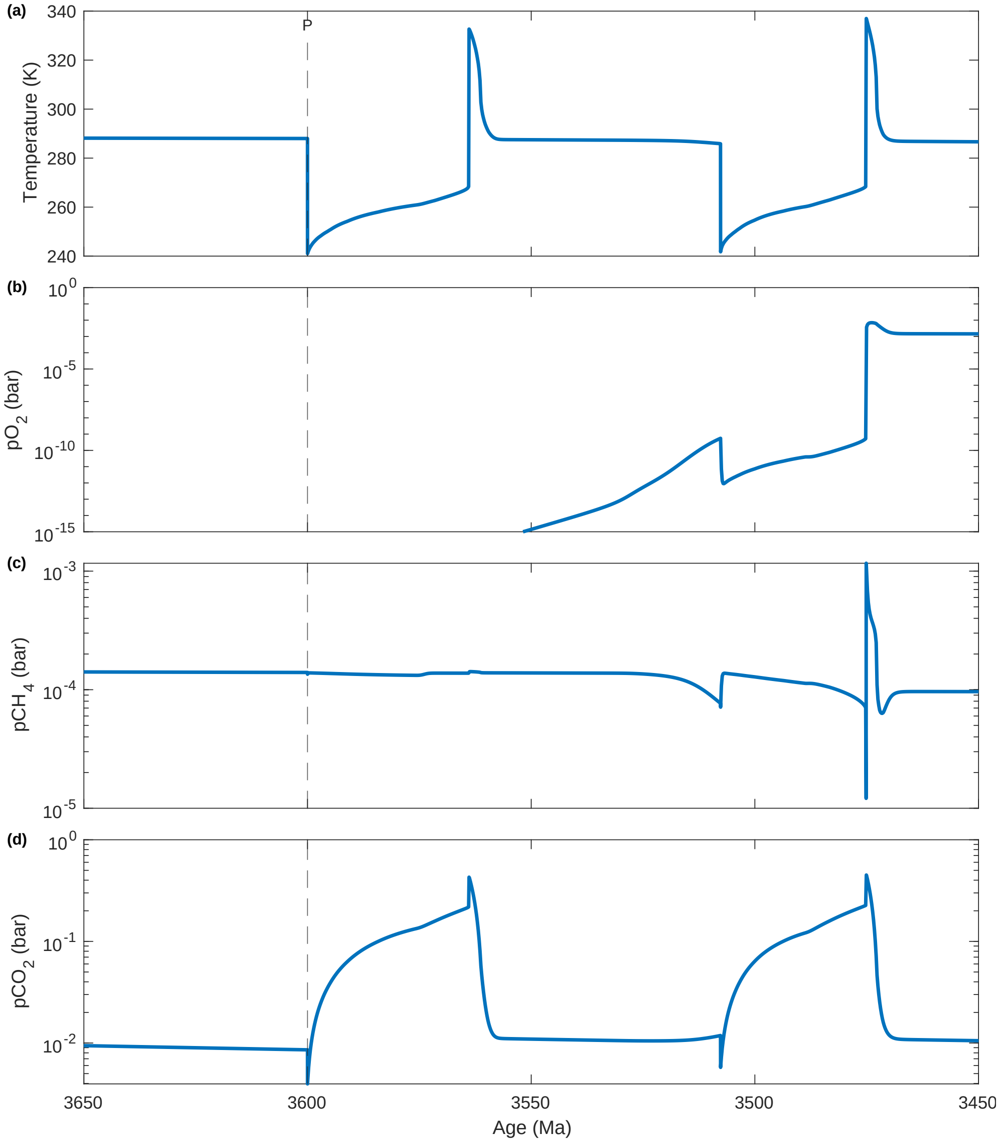

Figure 4.18: First glacial episode with T_α = 278 K The behaviour of the very first glacial-interglacial event, correlated with the rise of oxygenic photosynthesis, using T_α = 278 K (a weakly stable climate). **a** Surface temperature; **b** atmosphere O_2 level; **c** atmosphere CH_4 level; **d** atmosphere CO_2 level. Transition to operational oxygenic photosynthesis is denoted by vertical dashed line, labeled *P*.

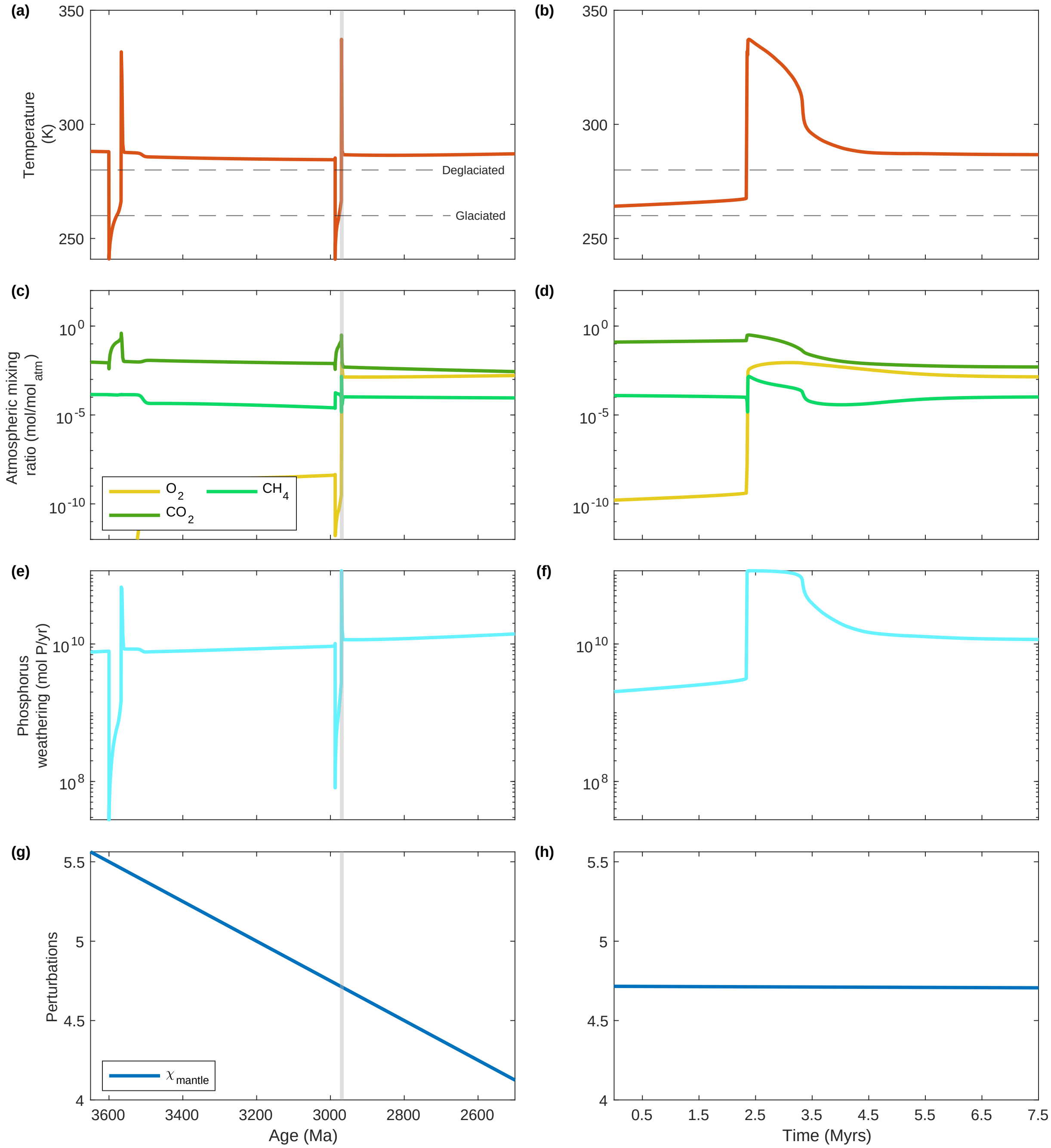

Figure 4.19: Phosphorus weathering and atmospheric composition during oscillating glacial episodes with T_α = 277 K Left column shows the full period of perturbation for selected systems and reservoirs (perturbations shown in bottom row subplots), with age in Ma. Right column shows zoomed in portion of highlighted grey zone, an interglacial event, with time since start of interglacial measured in millions of years. **a-b** Surface temperature (horizontal dashed lines denote glaciation and deglaciation thresholds); **c-d** atmospheric O_2, CH_4, and CO_2 mixing ratios; **e-f** total weathering flux of continental phosphorus; **g-h** nominal linear decline in mantle reductant output; no additional tectonic perturbations are applied in this scenario.

Crashing CH_4 is a consequence of glaciation rather than a cause, and CH_4 reverts back to stable high levels at the end of glacial oscillations. Rising O_2 levels still correspond to rapid spikes in atmospheric CH_4 following the termination of glacial instability (figures 4.16c and 4.18c), and in general the atmospheric methane reservoir in the Proterozoic appears extremely resilient. The results of this preliminary exercise seems to support the original finding in *EONS* nominal runs (chapter 3) that CH_4 levels increase dramatically after oxygen exceeds its bistable threshold (figure 4.19c and d). This entire exercise also suggests that methane's relationship to snowball events is more a reflection of oxygen levels perturbed by phosphorus weathering influxes (see figure 4.19b through f); as interglacials initiate and continental weathering resumes, the rapid influx of nutrients to the ocean spurs massive production of oxygen as well as methane as a result of export to the anoxic deep ocean.

4.5.3 Inorganic carbon cycling and glaciations

Unstable climates (higher T_α) are more likely to fall into glacial oscillations, have long-lasting glacial instability, and experience a recurrence of glaciations after a period of pseudo-stability because they maintain higher pCO_2 for longer. The weakly stable climates shown here all produce two main clusters of climate instability: for $T_\alpha = 278$ K, the first cluster occurs between 3500 and 2800 Ma, followed by a second cluster of two oscillations between 2550 and 2600 Ma (figure 4.17). The moderately stable climate similarly produces two single glaciations with a long intervening delay (figure 4.16). In all cases, the cause of the second cluster of glaciations is not immediately obvious, nor is the cause for the delay between the two clusters apparent. The duration of glacial instability (in both clusters) is positively correlated with T_α (comparing curves in figure 4.17a with 4.16a), whereas the length of pseudo-stability between glaciations (i.e. the delay following the end of the first cluster and the return of instability starting the second cluster) is inversely correlated with T_α (i.e. higher threshold results in shorter pseudo-stability). A higher threshold temperature for albedo transition requires less climate cooling, and a smaller decline in greenhouse gases, to tip into icy conditions; therefore it is reasonable to expect that the likelihood of falling into glaciation is greater in these climates, and that one should see shorter periods of stability between oscillation clusters. Even weakly stable climates seem to approach a stable state once atmospheric CO_2 declines to near 1×10^{-3} bar (figure 4.17d), suggesting that long-term decline in atmosphere-ocean CO_2 plays a key role in achieving stability. More unstable climates seem to take longer to achieve significant carbon sequestration, likely owing to the repeated disruption of the oceanic carbon cycle during glacial episodes.

Both moderately and weakly stable climates initially produce long interglacials, but the duration of interglacials through time is variable, and appears to decline steadily in correlation with declining CO_2 (figures 4.16 and 4.17). While early, higher pCO_2 interglacials in weakly stable climates are on the order of 75 Myrs in duration (figure 4.17a), later interglacials are closer to 1-5 Myrs, similar to interglacials caused by my tectonic perturbations (see figure 4.12 b). Figures 4.20 and 4.21 show alkalinity and CO_2 systematics for climates with T_α = 277 K or 278 K (moderate to weakly stable scenarios), while figures 4.23 and 4.24 show surface CO_2 controls in these climates. As with my tectonically produced interglacials (figure 4.14b), the balance in net influx of carbon and alkalinity within the atmosphere-ocean system dictates interglacial duration (figures 4.20 and 4.21e and f). Atmospheric CO_2 and the amount of $CaCO_3$ deposited during interglacials decline almost monotonically as oscillations progress (figures 4.20 and 4.21, c and i); the declining trend is most obvious in the weakly stable climate shown in figure 4.21. This decline suggests that increased long-term sequestration of surface CO_2 in the continents is a significant factor in climate regulation; the extended length of the earliest glaciations seems to result from the limited buffering capacity of the early Archean continents. Because continental bodies are smaller at 3500 Ma than at 2500 Ma, the silicate and carbonate weathering feedback is slightly weaker (see figures 4.23 and 4.24, b and c, between 3600 and 3400 Ma) and it takes longer for weathering to sufficiently draw down high CO_2. As the silicate and carbonate reservoirs grow, the residence time of CO_2 in the atmosphere ocean declines (figures 4.23 and 4.24i and j) and higher rates of CO_2 weathering results in more rapid termination of interglacials. This suggests that modifying the rate of continental emergence in the Archean-Proterozoic could affect the duration of glacial oscillations.

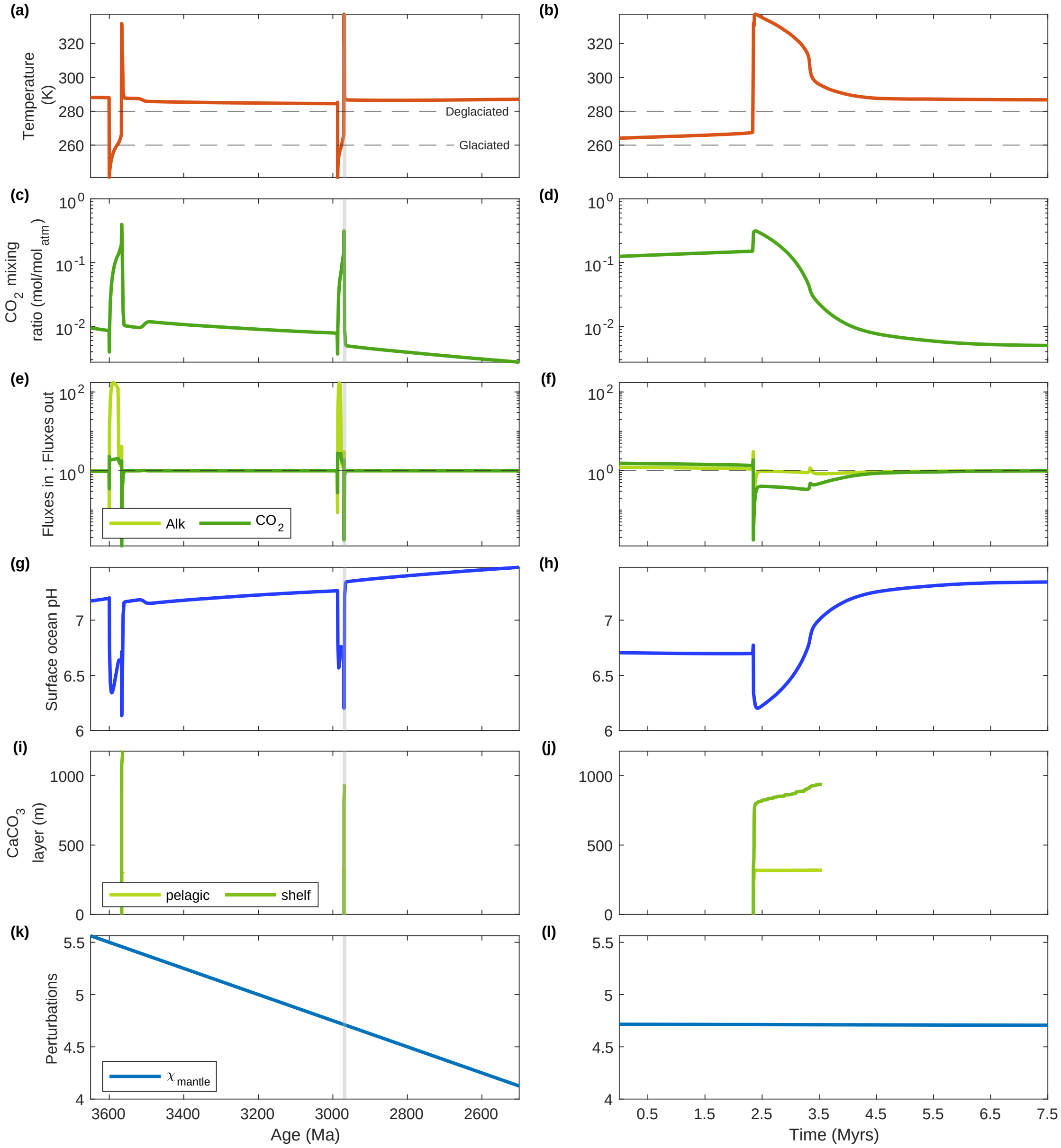

Figure 4.20: Alkalinity and CO_2 systematics during oscillating glacial episodes in a moderately stable climate (T_α = 277 K) Left column shows the full period of perturbation for selected systems and reservoirs (perturbations shown in bottom row subplots), with age in Ma. Right column shows zoomed in portion of highlighted grey zone, an interglacial event, with time since start of interglacial measured in millions of years. **a-b** Surface temperature (horizontal dashed lines denote glaciation and deglaciation thresholds); **c-d** atmospheric CO_2 level; **e-f** ratio of total fluxes of CO_2 and alkalinity into and out of the atmosphere-ocean system (horizontal dotted line denotes 1); **g-h** surface ocean pH; **i-j** thickness of sedimentary $CaCO_3$ layers deposited during the interglacial periods; **k-l** nominal linear decline in mantle reductant output; no additional tectonic perturbations are applied in this scenario.

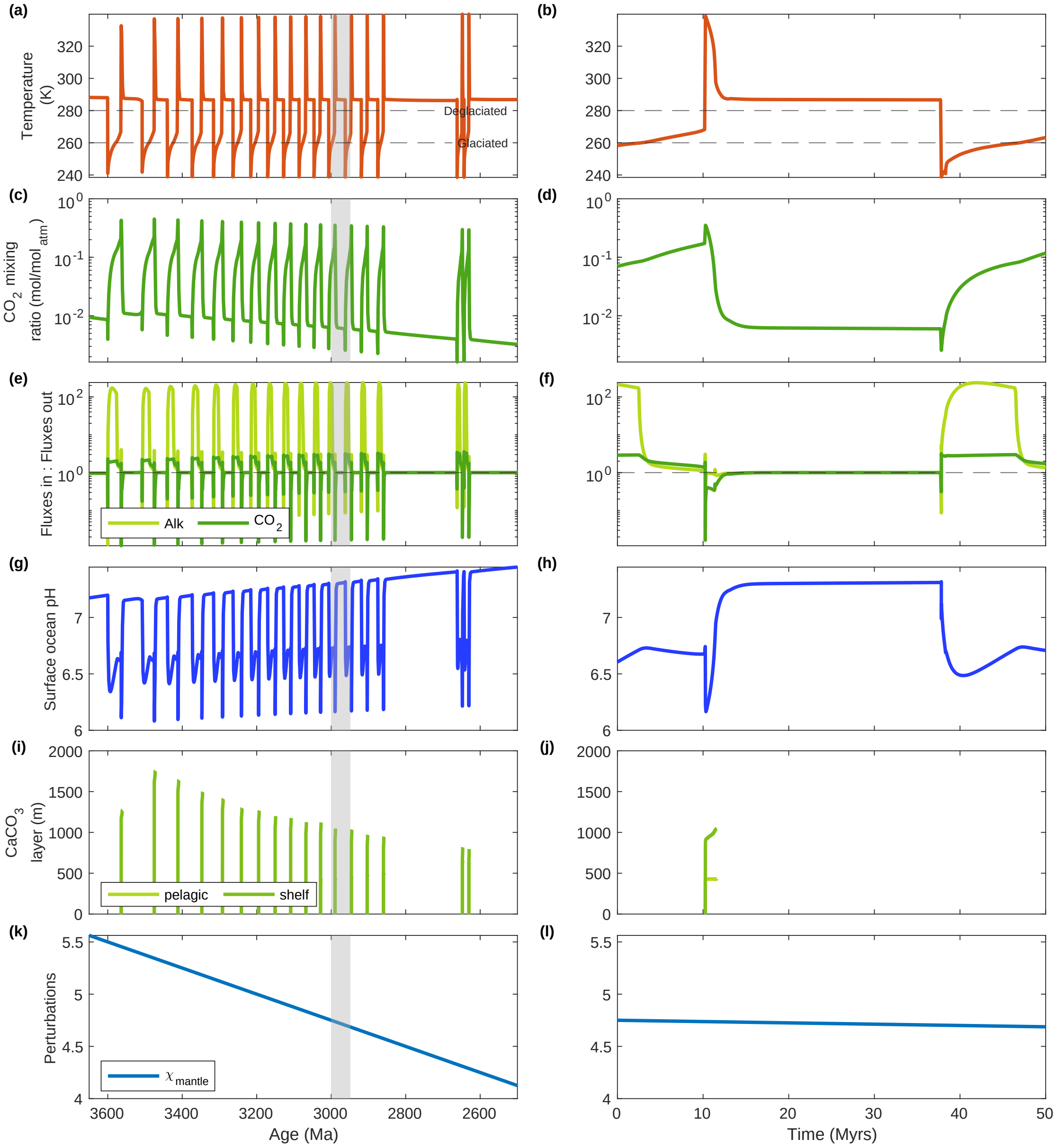

Figure 4.21: Alkalinity and CO_2 systematics during oscillating glacial episodes in a weakly stable climate (T_α = 278 K) Left column shows the full period of perturbation for selected systems and reservoirs (perturbations shown in bottom row subplots), with age in Ma. Right column shows zoomed in portion of highlighted grey zone, an interglacial event, with time since start of interglacial measured in millions of years. **a-b** Surface temperature (horizontal dashed lines denote glaciation and deglaciation thresholds); **c-d** atmospheric CO_2 level; **e-f** ratio of total fluxes of CO_2 and alkalinity into and out of the atmosphere-ocean system (horizontal dotted line denotes 1); **g-h** surface ocean pH; **i-j** thickness of sedimentary $CaCO_3$ layers deposited during the interglacial periods; **k-l** nominal linear decline in mantle reductant output. Time since start of the interglacial period is shown in thousands of years. No additional tectonic perturbations are applied in this scenario.

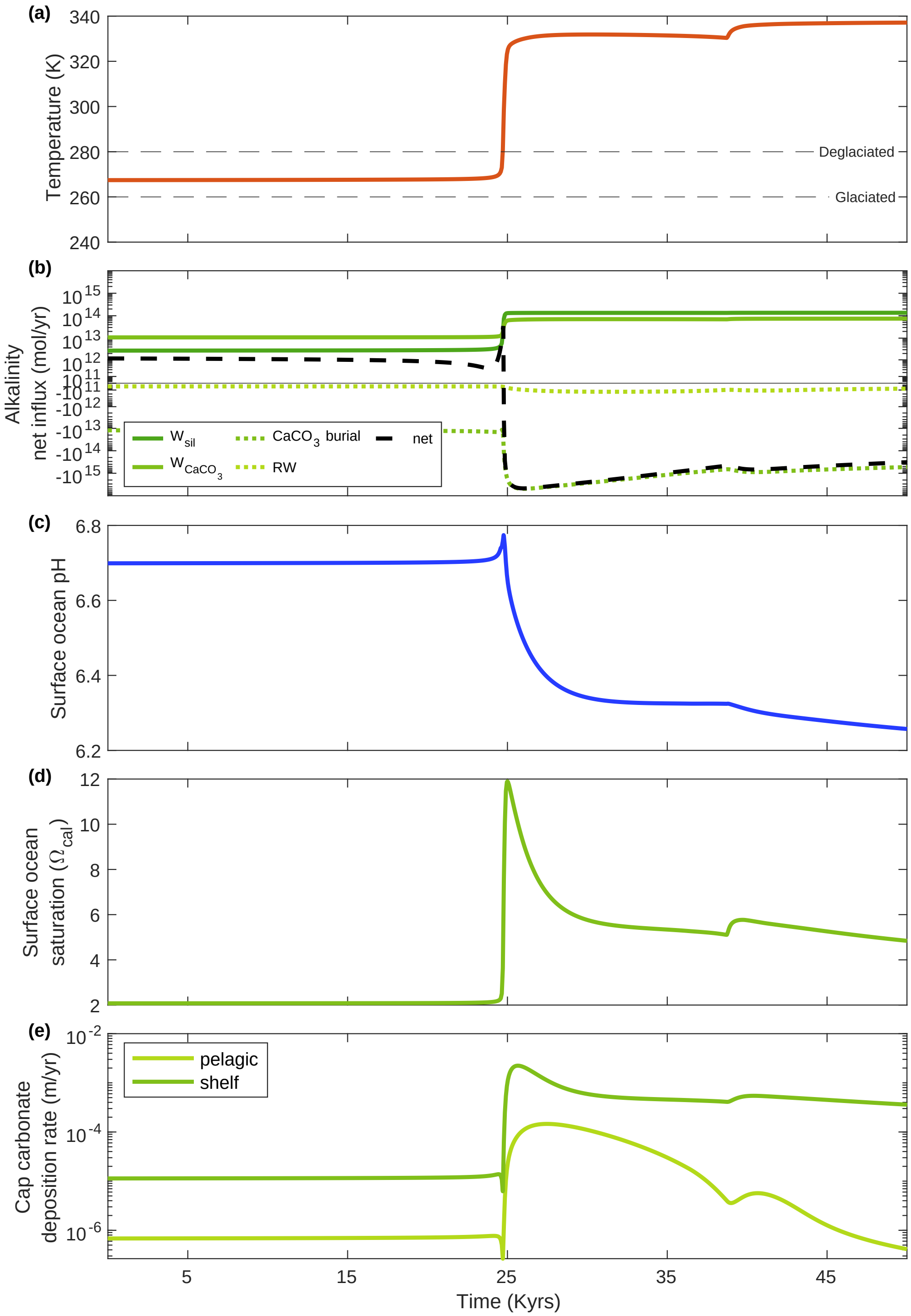

Figure 4.22: Alkalinity and CO_2 systematics at the start of an interglacial in a moderately stable climate ($T_\alpha = 277$ K) a Surface temperature (horizontal dashed lines denote glaciation and deglaciation thresholds); **b** net alkalinity influx to the ocean (horizontal line denotes 0); **c** surface ocean pH; **d** surface ocean $[CO_3^{2-}]$ saturation state; **e** rate of sedimentary $CaCO_3$ deposition; no additional tectonic perturbations are applied in this scenario. Timescale is shown in kiloyears after the start of the interglacial cycle.

As in scenarios caused by tectonic perturbations (section 4.4), the start of hot interglacial periods are characterized by alkalinity outflux from the ocean; figure 4.22 shows the start of the interglacial period highlighted in figure 4.20. The accumulation of massive amounts of atmospheric CO_2 during the preceding glaciation results in a supergreenhouse effect with extreme temperatures, which enables high continental weathering fluxes (figure 4.22a and b). Elevated weathering spurs a transient rise in pH and carbonate saturation (figure 4.22c and d). After a brief lag between alkalinity transport to the ocean from weathering and carbonate precipitation in sediments, $CaCO_3$ burial rate increases (figure 4.22e) and draws out the excess alkalinity faster than it is replenished. Carbonate deposition slowly decreases to balance weathering influxes and carbonate saturation state at this new high temperature (figure 4.22d and e), producing the shallowing growth trend seen in sedimentary $CaCO_3$ layer thicknesses in figures 4.20j and 4.21j. Carbonate burial sequesters alkalinity and leads to a decline in ocean pH until the end of the initial interglacial hot period (figures 4.22c and 4.20h), when cap carbonate deposition has sufficiently depleted atmospheric CO_2 supply (figure 4.20b).

Glacial oscillations arise as the carbon system transitions to a new pseudo-stable state, but this balance is derailed by volcanic recycling of cap carbonates. The disruptive effects of successive cap carbonate deposition are revealed by comparing moderate and weakly stable scenarios (figures 4.23 and 4.24, respectively). By 3000 Ma, the weakly stable climate has experienced nearly 500 Myrs of continuous glacial oscillations, while the moderately stable climate has experienced only one glacial event. At this time, both show similarly developed continental $CaCO_3$ reservoirs, atmosphere-ocean CO_2 residence time, silicate weathering fluxes, and ocean pH; additionally, interglacials in both climates result in the formation of similarly sized cap carbonates (figures 4.20 and 4.21 i and j).

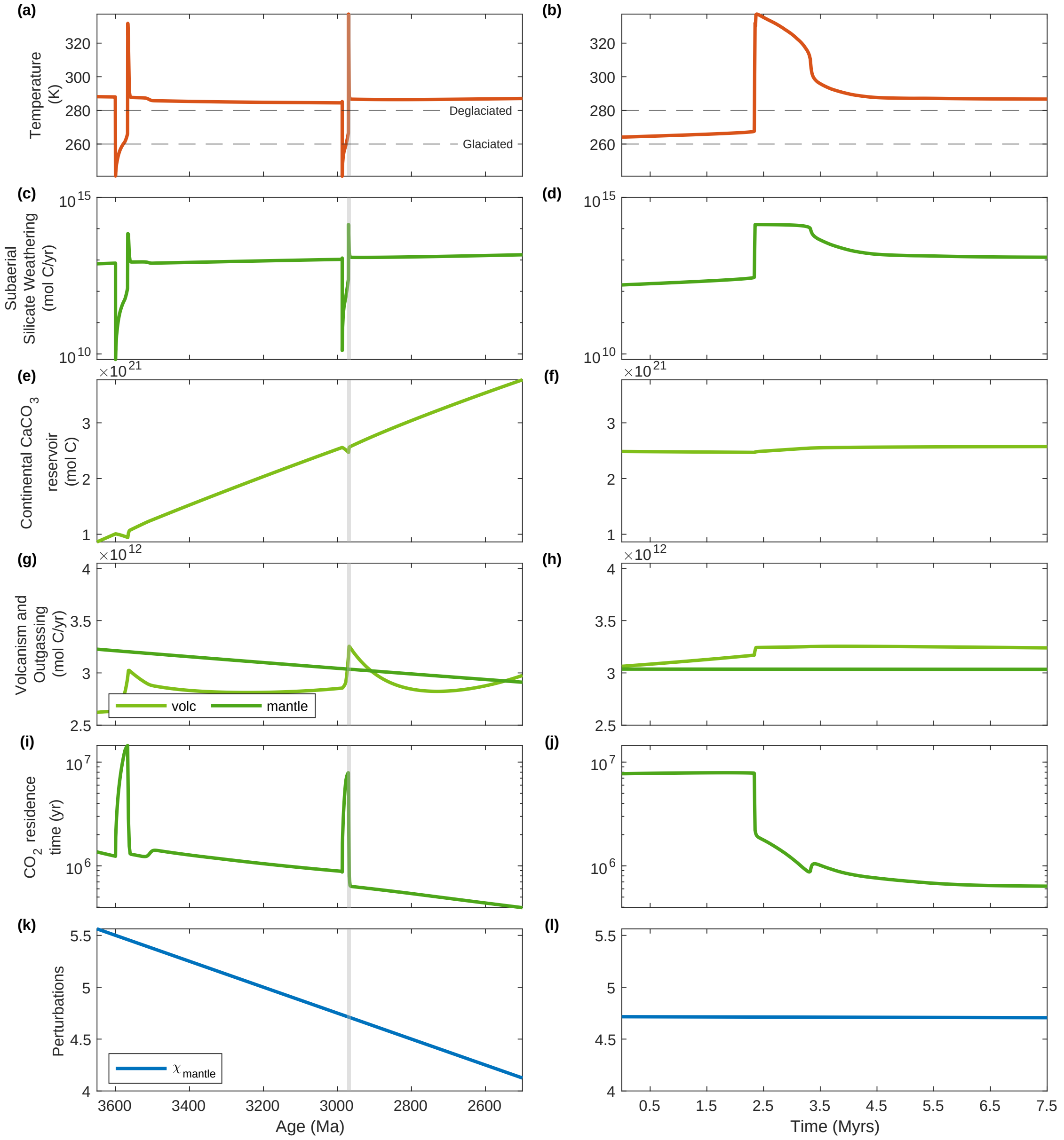

Figure 4.23: Controls on CO$_2$ level during oscillating glacial episodes in a moderately stable climate (T_α = 277 K) Left column shows the full period of perturbation for selected systems and reservoirs (perturbations shown in bottom row subplots), with age in Ma. Right column shows zoomed in portion of highlighted grey zone, an interglacial event, with time since start of interglacial measured in millions of years. **a-b** Surface temperature (horizontal dashed lines denote glaciation and deglaciation thresholds); **c-d** subaerial silicate weathering flux; **e-f** continental CaCO$_3$ reservoir size; **g-h** CO$_2$ volcanic and mantle outgassing fluxes; **i-j** residence time of CO$_2$ in the atmosphere-ocean system; **k-l** nominal linear decline in mantle reductant output; no additional tectonic perturbations are applied in this scenario.

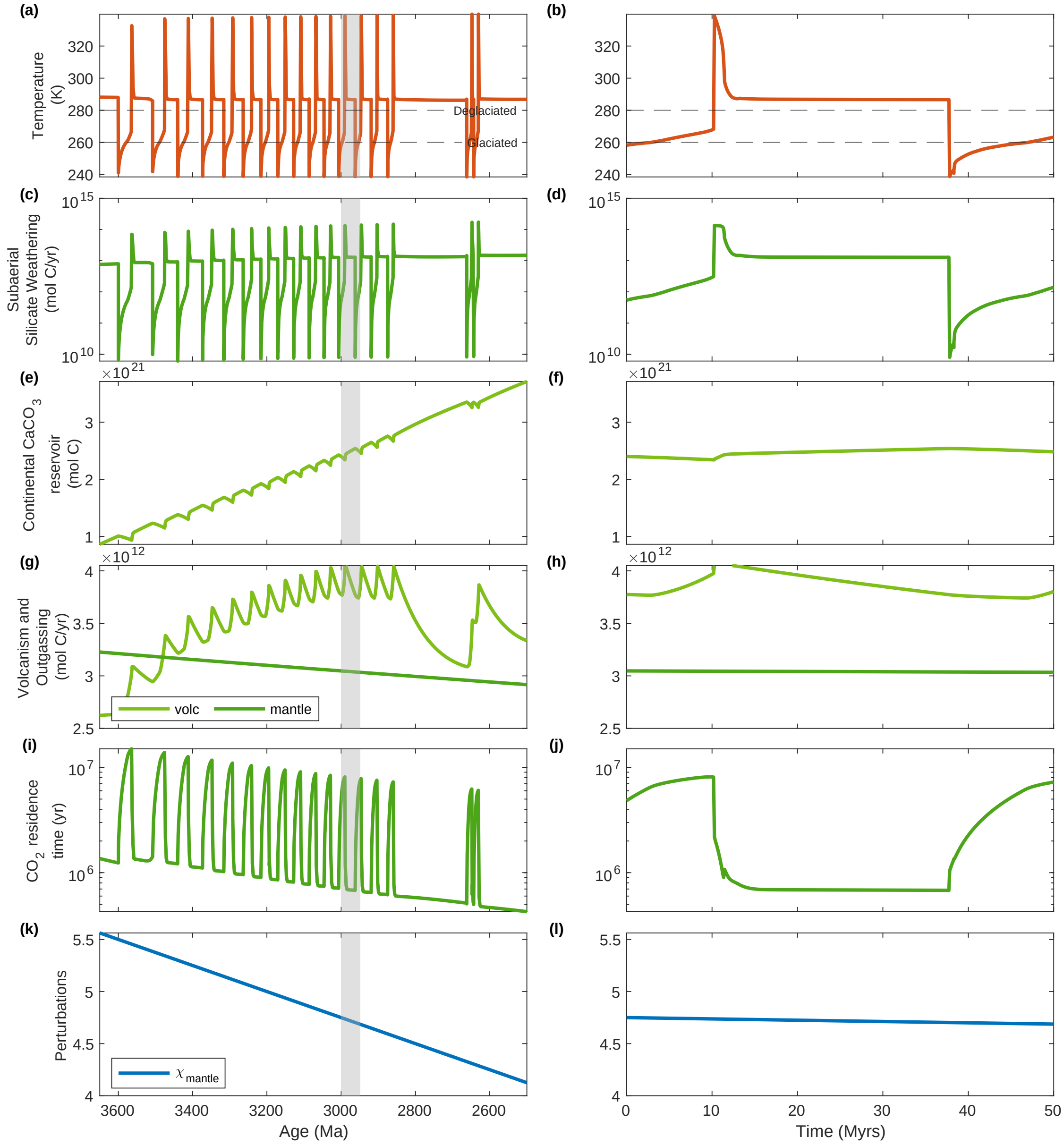

Figure 4.24: Controls on CO$_2$ level during oscillating glacial episodes in a moderately stable climate (T_α = 278 K) Left column shows the full period of perturbation for selected systems and reservoirs (perturbations shown in bottom row subplots), with age in Ma. Right column shows zoomed in portion of highlighted grey zone, an interglacial event, with time since start of interglacial measured in millions of years. **a-b** Surface temperature (horizontal dashed lines denote glaciation and deglaciation thresholds); **c-d** subaerial silicate weathering flux; **e-f** continental CaCO$_3$ reservoir size; **g-h** CO$_2$ volcanic and mantle outgassing fluxes; **i-j** residence time of CO$_2$ in the atmosphere-ocean system; **k-l** nominal linear decline in mantle reductant output; no additional tectonic perturbations are applied in this scenario.

The two scenarios differ most significantly in volcanic CO_2 outgassing flux (figures 4.20 and 4.21 g and h). Rapid formation of $CaCO_3$ stabilizes the climate after interglacials, but when buried pelagic carbonate is introduced to subduction zones it drives higher volcanic outgassing, and rapid release of CO_2 accelerates weathering and cooling which destabilize the climate. In the case of a moderately stable climate, volcanic CO_2 outgassing increases in fewer pulses, producing a lower maximum output flux when compared with the trend in a weakly stable climate because there are fewer incidences of massive carbonate deposition (figures 4.23 and 4.24 g and h); as a result, less carbon is returned to the surface as CO_2 in this scenario. It appears that glacial cycles are perpetuated by the formation, and subsequent recycling, of massive pelagic carbonate layers which result in massively destabilizing pulses of CO_2 volcanism.

4.6 Discussion

Initial results indicating climate warming by CH_4 following the GOE are robust. While the biosphere is capable of significant climate destabilization, these results suggest that methane and oxygen levels fluctuate in response to climatic shifts, rather than act as the primary control over climate. In all scenarios, both with and without glaciations and with variable parameterizations of climate stability, a rise in atmospheric oxygen is soon followed by a large increase in atmospheric CH_4 because of export to a stratified, anoxic deep ocean. After glaciations cease, the Mesoproterozoic climate appears to be warm and stable as a result of relatively high atmospheric CH_4. The idea of a Proterozoic climate warmed by considerable atmospheric CH_4 is not new (Pavlov, Hurtgen, Kasting, & Arthur, 2003) and does not contradict irreversible oxygenation. The scenarios explored here indicate that oxygenation during interglacials will temporarily collapse the CH_4 greenhouse. However, these results do not suggest that such a decline in methane will cause a global glaciation (Kirschvink et al., 2000; Kopp et al., 2005; Schrag et al., 2002).

Carbon dioxide, rather than methane, ultimately controls glacial initiation, timing, and duration. The long-term sequestration of atmosphere-ocean carbon is a major stabilizing force for Earth's climate, and is implicated in both tectonically driven (section 4.4) and climatically driven (section 4.5.3) glaciation scenarios explored in this work. My initial experiments with tectonic perturbations suggest that significant climate destabilization could arise as a consequence of changes to geologic carbon cycling. Experiments with more unstable climates similarly suggest that atmospheric CO_2 decline and the long-term sequestration of inorganic carbon is the ultimate control over climate stability. While reality is undoubtably more complex, this exercise demonstrates the first order control that the geosphere exerts over the climate, particularly with respect to the balance of surface carbon and ocean alkalinity.

The pacing of glacial oscillations in this model is primarily determined by atmosphere-ocean cycles and timescales, and on the level of atmospheric CO_2. The results of my investigation into tectonically produced glaciations (section 4.2) imply that interglacial periods are more likely to be hundreds of thousand or millions of years in duration. This result is in disagreement with earlier modelling (Mills et al., 2011), as well as the better preserved geologic record of Neoproterozoic Snowball Earth events (Halverson et al., 2005; Hoffman et al., 2017), which is characterized by interglacial intervals around 10-50 million years. This model builds upon that of Mills et al. (2011) by including a much more resolved atmosphere-ocean system and more dynamic weathering and outgassing fluxes. These results further support their conclusion that weathering and carbon-alkalinity balance dictate the tempo of glacial cycles. Both models are in agreement that geologic feedbacks strongly control climate; our different approaches result in disagreement on the precise pacing of geologic feedback responses. By applying long-term tectonic perturbations to my dynamic system, I can push the climate into an unstable, cooling state; however, it appears that the climate parameterization in this model is relatively stable against all but the most extreme long-term perturbations. My results suggest that tectonic changes can set in motion the preconditions for glaciation, but may be insufficient to tip the system into collapse. The short tempo of interglacials in this model ultimately arises because the main cause of interglacial stability is alkalinity balance in the ocean. It has been suggested by earlier studies, concerned with the Neoproterozoic cap carbonate negative $\delta^{13}C$ isotope excursion, that interglacial signals should be limited by timescales on the order of atmosphere-ocean carbon residence (Kennedy, 1996) but this is not a favoured view given well constrained estimates for the duration of interglacial carbonate platform deposition, and because the isotope record can also be explained by a decline in organic carbon burial (Hoffman et al., 1998). My findings present a new area for investigation and improvement: I do not consider additional tectonic factors that could have contributed to perpetuating long-term alkalinity balance, and the shapes of tectonic perturbations used here are simple and by no means capture all potential scenarios. Wilson cycles, shifting paleolatitude, variations in metamorphism during continental growth, submarine eruptions, or changes in the rate and chemical composition of volcanism as it emerges subaerially all would contribute to how geologic carbon influxes and outfluxes balance, how that balance evolves through time, and overlapping cycles could plausibly result in multiple long interglacial episodes. The interglacials caused by unstable climates similarly require further investigation, particularly with respect to the duration of interglacials in relation to surface and geologic carbon balance, which appears to be extremely important. I have yet to determine how cycle duration changes when oscillations initiate in the Proterozoic with larger continents and lower CO_2 instead of in the Archean.

A direct causal link between glaciations and the GOE is still murky, but both events seem to be related to significant changes in the geosphere, and may somewhat explain their simultaneity in the geologic record. My experiments with weakly stable climates generally support the interpretation of the geologic record by Gumsley et al. (2017), that global glaciation will cause a transient GOE that then collapses back into an anoxic state. As suggested by Garduño Ruíz et al. (2023), it does appear that oxygen history is strongly dictated by climate, and here I present some mechanisms which, in addition to atmospheric water vapour, could have contributed to the complexity of the Paleoproterozoic MIF-S record. The duration of glacial episodes shown here is primarily a function of limited carbon transfer from the geosphere to the atmosphere-ocean, and the emergence of large subaerial continents is a significant factor in the initiation of glacial events in a stable climate. These results suggest that geology-climate interaction exerts the strongest control over glacial occurrence and pacing. The link could be because large continents provide increased atmospheric CO_2 buffering, host larger reservoirs for long-term $CaCO_3$ and organic carbon storage, produce larger fluxes of nutrients to bolster high primary production, curtail the rate of volatile carbon recycling by acting as stable lids, and possibly because of combinations of these options. In addition, continental growth significantly contributes to the timing of oxygenation in the nominal version of this model because of how weathering drives the expansion of the biosphere (section 3.1.1.2; Gumsley et al., 2017); continental emergence may have influenced oxygenation in other ways, through changing the sedimentary capacity to store organic carbon (Husson & Peters, 2017), or by shifting volcanism to dominantly subaerial sources (Ciborowski & Kerr, 2016; Gaillard et al., 2011;

Kump & Barley, 2007) to name only a few. Arguments for a first order control of volcanism and mantle eruptions over the GOE are mostly predicated on changes in the redox state of emitted sulphur and as such addressing those scenarios directly is beyond the scope of this model. What this model can say is that the coincidence of LIP events and with the GOE and Paleoproterozoic glaciations can at the very least be causally linked by changing balances of weathering, outgassing, and mantle reductant outflux.

The initial rise of oxygenic photosynthesizers may have caused a glacial event in the Eoarchean. Results of tests with a weakly stable climate ($T_\alpha \geqslant 277$ K) suggest that the dip in atmospheric CO_2 associated with the proliferation of oxygenic photosynthesizers could have resulted in a global glacial event. There is little, if any, evidence of Archean glaciations predating the Pongola event at 2.9 Ga. Timing aside, the results of my exploration of different climate tipping points does suggest there is merit to the argument that CO_2 decline triggered glacial oscillations (Goddéris et al., 2003; Lowe & Tice, 2007) without invoking extreme Archean CO_2 levels. In unstable climates, the decline of atmospheric CO_2 as photosynthesizers evolve initiates glaciations, which in turn expedite the GOE because of the massive increase in continental nutrient flux in subsequent interglacials; this result suggests there that glacial events could actually lead to a rise in oxygen, and in the case of the moderately stable climate resulting from $T_\alpha = 277$ K this could still agree with evidence that full atmospheric oxygenation preceded later Paleoproterozoic glaciations (Warke et al., 2020). I have not yet found a scenario in which the GOE itself directly causes glacial events. That is not to say that it is not possible, but that I have not yet managed to resolve it using this particular model.

4.7 Looking forward

The climate feedbacks and parameterizations described here enable the *EONS* model to provide insights into the nature of oxygen's initial rise and how it functionally related to Paleoproterozoic glaciations. These results are preliminary and offer many areas for further investigation, particularly after addressing some results that may extend from model tuning choices; in particular, the early GOE caused by unstable climates results in an extended period of glacial oscillations. Because glacial-interglacial tempo appears related to surface carbon level (both declining over time), if these events occur in the Paleoproterozoic instead it might change how long interglacial intervals and total oscillation periods last.

The timing and tempo of Neoproterozoic snowball events are much better constrained (Hoffman et al., 1998) and similarly coincide with a significant increase in oxygen (Lenton & Watson, 2004; Mills et al., 2014). The *EONS* model nominal run resolves rapid oxygenation at this time coincidental with the expansions of lichen and fungi, which led to enhanced continental weathering and nutrient availability (section 3.1.1.4). Similarly to the runs shown here for the Paleoproterozoic, runs with a more responsive climate extending into the Neoproterozoic failed to show a causal relationship with this expansion of oxygen and climate destabilization. In my early attempts at initiating glaciations with tectonic forcings, the combination which is shown here successfully causing glaciations in the Paleoproterozoic fails to do so when repeated in the Neoproterozoic; this implies that the Neoproterozoic climate is even more resilient against destabilization as currently parameterized. My preliminary investigation using weaker climate parameterizations did not immediately show results in the Neoproterozoic, but because of time constraints I am not able to discern why. My investigation into the climate tipping point parameterization leads me to believe that my initial failures in the Neoproterozoic arise from an overly stable climate parameterization, which is further compounded by the growing stability of the Earth's climate through time as solar flux increases (and atmospheric carbon declines). An experiment using either tectonic forcings, a weakly stable climate, or perhaps combinations of both to cause Neoproterozoic glaciations would offer an interesting contrast to these preliminary results, as well as present scenarios with more potential for validation against geologic constraints.

Chapter 5

Conclusions

In this final chapter, I briefly review the major results of the *EONS* model presented in chapters 3 and 4 (section 5.1). Building off of these results, I suggest a few other questions the *EONS* model can currently address (section 5.2). I then comment on the model's caveats, where it can be improved, and what systems could be added in the future (section 5.3). I also summarize the model's major accomplishments and potential (section 5.4). I end this chapter, and this dissertation, with a reflection on the modelling process and my improved understanding of the Earth system (section 5.5).

5.1 Review of major findings

A significant finding from the Nominal run presented in chapter 3 is that the nearly billion year delay in oxygenation following the evolution of oxygenic photosynthesizers arises, at least in *EONS*, from nutrient limitations imposed by significant organic carbon burial in the anoxic ocean. The stepwise increase in oxygen reflects transitions between different nutrient limitations, vacillating from phosphorus to nitrogen limited and back again as the balance of in-out fluxes to the ocean shift between regimes dominated by remineralization, continental weathering, scavenging, and fixation-denitrification. When developments in the biosphere initiate rapid increases in phosphorus weathering, the system is forced out of the previous regime as fixed nitrogen production rises to meet demand. Just as the surface progressively oxygenates, nutrients become increasingly abundant as their continental reservoirs grow.

Because *EONS* resolves organic and inorganic carbon burial fluxes, these results suggest that the fraction of carbon buried as organics has increased in lockstep with oxygen through time. Carbonate sequestration dominates the Archean balance of f_{org} because the biosphere as resolved in this model is relatively restricted in scope by iron availability. As the surface ocean becomes more oxidized, increased remineralization there bolsters the Proterozoic biosphere, and exports a significant amount of organic carbon into a persistently anoxic deep ocean. *EONS* suggests biospheric expansion within a redox stratified Proterozoic ocean should result in increasing f_{org}.

The persistent anoxicity of the Proterozoic deep ocean in *EONS* results in my finding that the GOE likely resulted in a rebound in atmospheric methane rather than a crash. Extensive methanogenesis in the deep ocean seems to make up for the gradual decline in atmospheric CH_4 as O_2 levels rise in the prelude to the GOE. The post-GOE CH_4 greenhouse may have promoted a warm Mesoproterozoic, and lingered until the Neoproterozoic oxygenation event. This model highlights the extreme complexity of the relationship between the GOE and Paleoproterozoic climate, and does not suggest that oxygenation would cause glaciations. While I cannot offer a straightforward answer regarding the cause of the Paleoproterozoic glaciations, the *EONS* model suggests that oxygen level is subordinate to climate rather than a predominant influence over it.

EONS also suggests that the climate system is most strongly controlled by CO_2, and that the sequestration of a large Archean CO_2 atmosphere into continental carbonate reservoirs results in a stabilization of the climate over time. Furthermore, the balance of dissolved inorganic carbon and alkalinity in the oceans appears to be a major component of the resiliency of the Earth system to major climatic perturbations. The fast response of the *EONS* Paleoproterozoic atmosphere-ocean carbon system to climate destabilization suggests that Snowball Earth glaciations were complex events that likely arose as a result of multiple compounding factors.

I find in general that the Earth system is not at steady state. Rather, it is a system characterized by punctuated disequilibria interrupting pseudo-steady state periods. The stepwise evolution of atmospheric oxygen is not unique to that species alone, but instead reflects the stepwise evolution and deepening entanglement of C-N-O-P cycles. Long spans of pseudo-stability are a consequence of many intertwined cycles operating on incommensurate timescales: an atmosphere-ocean evolving over timescales spanning $10^{-2} - 10^{4}$ years struggles to find balance with geologic processes spanning $10^{7} - 10^{9}$ years. Major transitions in the biosphere catastrophically upend pseudo-stasis and force the entire system to shift towards a new balance; because of progressive oxygenation, a steady increase in solar flux, and the many magnitudes of scale spanned by dynamic natural processes, true equilibrium remains just beyond reach.

5.2 Suggested future research

There are several areas of future inquiry that stem directly from the work presented here. I demonstrated the importance of the mantle reductant outgassing forcing in chapter 3 (section 3.2.2). Different shapes for this decline would undoubtably change how the model is tuned to produce a well-timed GOE, and potentially suggest a wide range of oxygenation scenarios of varying realism. In a similar vein, one could keep f_{org} constant by making organic burial flux a function of carbonate burial. This approach would allow the user to better constrain how f_{org} actually relates to oxygenation, since the current treatment makes it impossible to discern whether organic carbon burial is a control over oxygenation or simply reflects oxygenation.

The significant role CO_2 plays in determining the timing and tempo of glaciations (section 4.5.3) suggests that the rate of continental emergence could be a major tuning parameter for resolving Paleoproterozoic glaciations. It would be simple to compare how non-linear treatments of continental silicate reservoir growth affect glaciations, and could address the discrepancy between Proterozoic glacial duration and timing in *EONS* versus the geologic record. In the same vein, one could modify mantle output and seafloor spreading in this model to simulate regularly occurring LIP events and tectonic slowdowns, which would undoubtably alter the timing of the GOE; this experiment would address some of my lingering questions regarding whether or not the prevailing tectonic influence over oxygenation is output of reductants (slowing oxygenation) or the punctuated growth of continental bodies (accelerating oxygenation).

EONS currently can address a great many questions regarding the Earth system's evolution, many more than have been covered in this work. I have demonstrated one potential scenario for the evolution of Earth's surface in chapter 3, but many scenarios are possible with different timings for biological evolutionary developments. For instance, if oxygenic photosynthesis instead evolved in the middle or late Archean, I would expect a lesser degree of mantle reductant decline to resolve the timing of the GOE. This work also touched upon how nutrient limitations shift over 4 billion years, but an interesting test of the Archean biosphere would be to impose phosphorus limitation (either by curtailing weathering transport or enhancing phosphorus precipitation onto iron oxides) to see how a “phosphate crisis” would affect the timing of the GOE and the evolution of organic carbon burial fraction (Bjerrum & Canfield, 2002).

5.3 Improving the *EONS* model

A good rule of thumb is that any model is inherently incomplete. *EONS* is in no way an exception to this rule. This model requires more validation against the geologic record through time. Adding in carbon and nitrogen isotope fractionation would allow a direct comparison to the best record of surface conditions available, as well as allow for direct comparison to other models like COPSE. The phosphorus cycle in this model is simplistic and includes limited species that do not capture the complexity of this nutrient. There is much interest regarding how phosphorus limitation has changed through time, and how that has, or has not, resulted in biospheric bottlenecks; *EONS* would greatly benefit from more development in this area.

The systems included in the current *EONS* model appear to be the most fundamental requirements for modelling the long-term biogeochemical evolution of Earth’s surface. But the systems included barely capture any relationship between the mantle and the surface, resulting in a major blindspot for this work. The evolution of the mantle, both chemically and thermally, has undoubtably exerted significant influence over not only the oxygenation of Earth’s surface but on the partitioning and sequestration of volatile species for carbon and nitrogen. Additionally, a more nuanced approach to continental bodies and subduction evolution is warranted; in particular, whether or not crustal materials are being efficiently recycled or acting as stagnant lids atop the mantle long into the Proterozoic seems to me to present two drastically different scenarios both for the GOE and for the glaciations that surround it. While I do not believe *EONS* is well suited to resolve paleogeography, an additional forcing for average continental weathering timescale would be a good first step to testing how equatorial arrangements could affect my preliminary results on climate destabilization. A more complicated history for mantle output and continental growth would almost certainly result in a different tuning to produce a nominal run, and would reveal which assumptions I make here are most strongly influencing these results.

Along with improved resolution of mantle-surface interactions, *EONS* would greatly benefit from the addition of sulphur and iron cycles. Without resolving the mantle or continental growth in more detail, and because of the not insubstantial time this effort would require, I have made no attempt to address these important cycles. Many other models of Earth's oxygenation include sulphur cycling, and without this cycle *EONS* will always differ from its cohort in a significant way. A reasonable *EONS* sulphur cycle could include degassing at mid-ocean ridges and in arc volcanism, pyrite formation and burial, photochemical oxidation, additional pathways of anoxygenic photosynthesis, and sulphate reduction in remineralization. The addition of another reducing species would address so many of my lingering questions regarding how oxygenation progresses and how strong the influence of the biosphere over the geosphere truly is. This would, of course, also require a more detailed approach to the biosphere, volcanism, atmospheric chemistry, and much more. Again, not an insubstantial proposition.

5.4 Successes of the *EONS* model

A major accomplishment of the *EONS* model is the ability to reproduce the broad trends of Earth's long term surface oxygenation. This model is capable of resolving how oxygenation occurs over 4 billion years with only a handful of boundary forcings. When it is compared to other models of its ilk, *EONS* is a big step forward in complexity, scope, and scale. This model significantly improves on other evolutionary biogeochemical box models by employing dynamic systems, reservoirs, and fluxes. Because of this, the *EONS* model reproduces interactions between the major nutrient cycles in much greater detail than its predecessors, and is a proof of concept that these systems can be modelled through time without being reduced to fixed flux interactions.

This model's design allows for extensive hypothesis testing. The utility of *EONS* is limited almost exclusively by the vision and creativity of those who use it. This model has proved itself to be robust and adaptable; modifying systems and feedbacks is relatively straightforward, and suggests that this model is flexible enough to allow for the addition of several new modular systems. Almost any question that originates in the Archean in theory could be addressed by this model, given sufficient constraints, additional parameters, and abundant patience.

5.5 Reflections

The process of building a model like *EONS* is circuitous. The last five years of my life I have devoted most of my days and a great many hours of non-sleep ruminating over this work, the Earth, and the pure insanity of this project's premise. Modelling Earth systems, or any single system, is fundamentally an attempt to reduce something complicated into separate, approachable components to see if the one's conceptions hold water. It turns out that my understanding was often riddled with holes. So it goes! As frustrating and nonlinear as this process has been, it has undeniably given me much deeper insight into the intricacies of our beautiful planet.

Bibliography

Ahm, A.-S. C., Bjerrum, C. J., Blättler, C. L., Swart, P. K., & Higgins, J. A. (2018, September 1). Quantifying early marine diagenesis in shallow-water carbonate sediments. *Geochimica et Cosmochimica Acta*. Chemistry of Oceans Past and Present: A Special Issue in Tribute to Harry Elderfield, *236*, 140–159. doi:10.1016/j.gca.2018.02.042

Alcott, L. J., Mills, B. J., Bekker, A., & Poulton, S. W. (2022). Earth's Great Oxidation Event facilitated by the rise of sedimentary phosphorus recycling. *Nature Geoscience*, *15*(3), 210–215.

Alcott, L. J., Mills, B. J., & Poulton, S. W. (2019). Stepwise Earth oxygenation is an inherent property of global biogeochemical cycling. *Science*, *366*(6471), 1333–1337.

Ali, S. N., Sharma, A., Agrawal, S., MG, Y., RA, J., Dubey, J., & Morthekai, P. (2020). Oxygen and deuterium isotope characteristics of Teesta river catchment from Sikkim Himalaya, India: Implications of different moisture sources. *Geochemical Journal*, *54*(5), 327–336.

Allan, J. R., & Matthews, R. K. (1990). Isotope signatures associated with early meteoric diagenesis. *Carbonate diagenesis*, 197–217.

Altermann, W., & Kazmierczak, J. (2003, November 1). Archean microfossils: A reappraisal of early life on Earth. *Research in Microbiology*, *154*(9), 611–617. doi:10.1016/j.resmic.2003.08.006

Anbar, A. D., Duan, Y., Lyons, T. W., Arnold, G. L., Kendall, B., Creaser, R. A., . . . Garvin, J. (2007). A whiff of oxygen before the great oxidation event? *Science*, *317*(5846), 1903–1906.

Anderson, L. A., & Sarmiento, J. L. (1994). Redfield ratios of remineralization determined by nutrient data analysis. *Global biogeochemical cycles*, *8*(1), 65–80.

Asael, D., Rouxel, O., Poulton, S. W., Lyons, T. W., & Bekker, A. (2018). Molybdenum record from black shales indicates oscillating atmospheric oxygen levels in the early Paleoproterozoic. *American Journal of Science*, *318*(3), 275–299.

Bekker, A., Holland, H. D., Wang, P. L., Rumble III, D., Stein, H. J., Hannah, J. L., . . . Beukes, N. J. (2004). Dating the rise of atmospheric oxygen. *Nature*, *427*(6970), 117.

Bellefroid, E. J., Hood, A. v. S., Hoffman, P. F., Thomas, M. D., Reinhard, C. T., & Planavsky, N. J. (2018). Constraints on Paleoproterozoic atmospheric oxygen levels. *Proceedings of the National Academy of Sciences*, *115*(32), 8104–8109.

Bergman, N. M., Lenton, T. M., & Watson, A. J. (2004). COPSE: A new model of biogeochemical cycling over Phanerozoic time. *American Journal of Science*, *304*(5), 397–437.

Berman-Frank, I., Chen, Y., Gao, Y., Fennel, K., Follows, M. J., Milligan, A. J., & Falkowski, P. G. (2008). Feedbacks between the nitrogen, carbon and oxygen cycles. *Nitrogen in the marine environment. 2nd ed. Burlington: Elsevier*, 1537–63.

Berman-Frank, I., Lundgren, P., & Falkowski, P. G. (2003). Nitrogen fixation and photosynthetic oxygen evolution in cyanobacteria. *Research in microbiology*, *154*(3), 157–164.

Berner, R. A. (1991). A model for atmospheric CO sub 2 over phanerozoic time. *American Journal of Science;(United States)*, *291*(4).

Berner, R. A., & Kothavala, Z. (2001). GEOCARB III: A revised model of atmospheric CO2 over Phanerozoic time. *American Journal of Science*, *301*(2), 182–204.

Berner, R. A. (2004). *The Phanerozoic carbon cycle: CO2 and O2*. Oxford University Press.

Berner, R. A. (2009). Phanerozoic atmospheric oxygen: New results using the GEOCARBSULF model. *American Journal of Science*, *309*(7), 603–606.

Bjerrum, C. J., & Canfield, D. E. (2002). Ocean productivity before about 1.9 Gyr ago limited by phosphorus adsorption onto iron oxides. *Nature*, *417*(6885), 159–162.

Bjerrum, C. J., & Canfield, D. E. (2004). New insights into the burial history of organic carbon on the early Earth. *Geochemistry, Geophysics, Geosystems*, *5*(8).

Bleeker, W. (2003). The late Archean record: A puzzle in ca. 35 pieces. *Lithos*, *71*(2-4), 99–134.

Blichert-Toft, J., & Albarede, F. (1994). Short-lived chemical heterogeneities in the Archean mantle with implications for mantle convection. *Science*, *263*(5153), 1593–1596.

Bond, D. P., & Grasby, S. E. (2020, May 18). Late Ordovician mass extinction caused by volcanism, warming, and anoxia, not cooling and glaciation. *Geology*, *48*(8), 777–781. doi:10.1130/G47377.1

Boudreau, B. P. (1996). The diffusive tortuosity of fine-grained unlithified sediments. *Geochimica et Cosmochimica Acta*, *60*(16), 3139–3142.

Boyd, E. S., Hamilton, T. L., & Peters, J. W. (2011). An alternative path for the evolution of biological nitrogen fixation. *Frontiers in microbiology*, *2*, 205.

Boyd, E. S., & Peters, J. W. (2013). New insights into the evolutionary history of biological nitrogen fixation. *Frontiers in microbiology*, *4*, 201.

Bradley, D. C. (2008). Passive margins through earth history. *Earth-Science Reviews*, *91*(1-4), 1–26.

Bradley, D. C. (2011). Secular trends in the geologic record and the supercontinent cycle. *Earth-Science Reviews*, *108*(1-2), 16–33.

Brady, P. V., & Carroll, S. A. (1994). Direct effects of CO2 and temperature on silicate weathering: Possible implications for climate control. *Geochimica et Cosmochimica Acta*, *58*(7), 1853–1856.

Brasier, M. D., & Lindsay, J. F. (1998). A billion years of environmental stability and the emergence of eukaryotes: New data from northern Australia. *Geology*, *26*(6), 555–558.

Braterman, P. S., Cairns-Smith, A. G., & Sloper, R. W. (1983, May). Photo-oxidation of hydrated Fe2+—significance for banded iron formations. *Nature*, *303*(5913), 163–164. doi:10.1038/303163a0

Budyko, M. I. (1969). The effect of solar radiation variations on the climate of the Earth. *tellus*, *21*(5), 611–619.

Burkhardt, S., Amoroso, G., Riebesell, U., & Sültemeyer, D. (2001). CO2 and HCO3 uptake in marine diatoms acclimated to different CO2 concentrations. *Limnology and Oceanography*, *46*(6), 1378–1391.

Butcher, S. S., Charlson, R. J., Orians, G. H., & Wolfe, G. V. (1992). *Global biogeochemical cycles*. Academic press London.

Byrne, B., & Goldblatt, C. (2014). Radiative forcing at high concentrations of well-mixed greenhouse gases. *Geophysical research letters*, *41*(1), 152–160.

Canfield, D. E., Poulton, S. W., & Narbonne, G. M. (2007). Late-Neoproterozoic deep-ocean oxygenation and the rise of animal life. *Science*, *315*(5808), 92–95.

Canfield, D. E. (1998). A new model for Proterozoic ocean chemistry. *Nature*, *396*(6710), 450–453.

Canfield, D. E., Glazer, A. N., & Falkowski, P. G. (2010). The evolution and future of Earth's nitrogen cycle. *science*, *330*(6001), 192–196.

Canfield, D. E., & Raiswell, R. (1999). The evolution of the sulfur cycle. *American Journal of Science*, *299*(7-9), 697–723.

Canfield, D. E., Zhang, S., Frank, A. B., Wang, X., Wang, H., Su, J., . . . Frei, R. (2018). Highly fractionated chromium isotopes in Mesoproterozoic-aged shales and atmospheric oxygen. *Nature Communications*, *9*(1), 2871.

Canuel, E. A., & Hardison, A. K. (2018). Carbon Cycle. *Encyclopedia of Geochemistry: A Comprehensive Reference Source on the Chemistry of the Earth; White, WM, Ed*, 191–194.

Carlson, R. W. (2005). *The Mantle and Core: Treatise on Geochemistry, Volume 2*. Elsevier.

Catling, D. C., & Zahnle, K. J. (2020). The Archean atmosphere. *Science Advances*, *6*(9), eaax1420.

Catling, D. C., Zahnle, K. J., & McKay, C. P. (2001). Biogenic methane, hydrogen escape, and the irreversible oxidation of early Earth. *Science*, *293*(5531), 839–843.

Charnay, B., Le Hir, G., Fluteau, F., Forget, F., & Catling, D. C. (2017). A warm or a cold early Earth? New insights from a 3-D climate-carbon model. *Earth and Planetary Science Letters*, *474*, 97–109.

Cheng, C., Busigny, V., Ader, M., Thomazo, C., Chaduteau, C., & Philippot, P. (2019, September 15). Nitrogen isotope evidence for stepwise oxygenation of the ocean during the Great Oxidation Event. *Geochimica et Cosmochimica Acta*, *261*, 224–247. doi:10.1016/j.gca.2019.07.011

Ciais, P., Sabine, C., Bala, G., Bopp, L., Brovkin, V., Canadell, J., . . . Heimann, M. (2014). Carbon and other biogeochemical cycles. In *Climate change 2013: The physical science basis. Contribution of Working Group I to the Fifth Assessment Report of the Intergovernmental Panel on Climate Change* (pp. 465–570). Cambridge University Press.

Ciborowski, T. Jake. R., & Kerr, A. C. (2016, March 1). Did mantle plume magmatism help trigger the Great Oxidation Event? *Lithos*, *246–247*, 128–133. doi:10.1016/j.lithos.2015.12.017

Claire, M. W., Catling, D. C., & Zahnle, K. J. (2006). Biogeochemical modelling of the rise in atmospheric oxygen. *Geobiology*, *4*(4), 239–269.

Claire, M. W., Kasting, J. F., Domagal-Goldman, S. D., Stüeken, E. E., Buick, R., & Meadows, V. S. (2014, September 15). Modeling the signature of sulfur mass-independent fractionation produced in the Archean atmosphere. *Geochimica et Cosmochimica Acta*, *141*, 365–380. doi:10.1016/j.gca.2014.06.032

Clift, P. D. (2017). A revised budget for Cenozoic sedimentary carbon subduction. *Reviews of Geophysics*, *55*(1), 97–125.

Cloud, P. (1972, June 1). A working model of the primitive Earth. *American Journal of Science*, *272*(6), 537–548. doi:10.2475/ajs.272.6.537

Cloud, P. E. (1968). Atmospheric and Hydrospheric Evolution on the Primitive Earth: Both secular accretion and biological and geochemical processes have affected earth's volatile envelope. *Science*, *160*(3829), 729–736.

Condie, K. C. (2002). The supercontinent cycle: Are there two patterns of cyclicity? *Journal of African Earth Sciences*, *35*(2), 179–183.

Condie, K. C., & Aster, R. C. (2010). Episodic zircon age spectra of orogenic granitoids: The supercontinent connection and continental growth. *Precambrian Research*, *180*(3-4), 227–236.

Condie, K. C., Davaille, A., Aster, R. C., & Arndt, N. (2015). Upstairs-downstairs: Supercontinents and large igneous provinces, are they related? *International Geology Review*, *57*(11-12), 1341–1348.

Condie, K. C., Pisarevsky, S. A., & Puetz, S. J. (2021). LIPs, orogens and supercontinents: The ongoing saga. *Gondwana Research*, *96*, 105–121.

Coogan, L. A., Gillis, K. M., Parrish, R. R., Austin-Giddings, W., Dosso, S. E., & Moore, A. (2013). The role of low temperature alteration of the oceanic crust in global carbon cycling. In *AGU Fall Meeting Abstracts* (Vol. 2013, B13B–0465).

Coogan, L. A., & Gillis, K. M. (2013). Evidence that low-temperature oceanic hydrothermal systems play an important role in the silicate-carbonate weathering cycle and long-term climate regulation. *Geochemistry, Geophysics, Geosystems*, *14*(6), 1771–1786.

Coogan, L. A., & Gillis, K. M. (2018). Low-temperature alteration of the seafloor: Impacts on ocean chemistry. *Annual Review of Earth and Planetary Sciences*, *46*, 21–45.

Cordani, U. G., D'Agrella-Filho, M. S., Brito-Neves, B. B. de, & Trindade, R. I. F. (2003). Tearing up Rodinia: The Neoproterozoic palaeogeography of South American cratonic fragments. *Terra Nova*, *15*(5), 350–359.

Cox, G. M., Halverson, G. P., Stevenson, R. K., Vokaty, M., Poirier, A., Kunzmann, M., . . . Macdonald, F. A. (2016). Continental flood basalt weathering as a trigger for Neoproterozoic Snowball Earth. *Earth and Planetary Science Letters*, *446*, 89–99.

Craddock, P. R., & Dauphas, N. (2011). Iron and carbon isotope evidence for microbial iron respiration throughout the Archean. *Earth and Planetary Science Letters*, *303*(1-2), 121–132. Retrieved October 24, 2023, from https://www.sciencedirect.com/science/article/pii/S0012821X10008186

Crockford, P. W., Hayles, J. A., Bao, H., Planavsky, N. J., Bekker, A., Fralick, P. W., . . . Wing, B. A. (2018). Triple oxygen isotope evidence for limited mid-Proterozoic primary productivity. *Nature*, *559*(7715), 613–616.

Crockford, P. W., On, Y. M. B., Ward, L. M., Milo, R., & Halevy, I. (2023). The geologic history of primary productivity. *Current Biology*, *33*(21), 4741–4750.

Crockford, P., & Halevy, I. (2022). Questioning the Paradigm of a Phosphate-Limited Archean Biosphere. *Geophysical research letters*, *49*(17), e2022GL099818.

Crowe, S. A., Døssing, L. N., Beukes, N. J., Bau, M., Kruger, S. J., Frei, R., & Canfield, D. E. (2013). Atmospheric oxygenation three billion years ago. *Nature*, *501*(7468), 535–538.

Crowe, S. A., Jones, C., Katsev, S., Magen, C., O'Neill, A. H., Sturm, A., . . . Sundby, B. (2008). Photoferrotrophs thrive in an Archean Ocean analogue. *Proceedings of the National Academy of Sciences*, *105*(41), 15938–15943.

Czaja, A. D., Johnson, C. M., Beard, B. L., Roden, E. E., Li, W., & Moorbath, S. (2013). Biological Fe oxidation controlled deposition of banded iron formation in the ca. 3770 Ma Isua Supracrustal Belt (West Greenland). *Earth and Planetary Science Letters*, *363*, 192–203. Retrieved October 24, 2023, from https://www.sciencedirect.com/science/article/pii/S0012821X1200711X

Czaja, A. D., Johnson, C. M., Roden, E. E., Beard, B. L., Voegelin, A. R., Nägler, T. F., . . . Wille, M. (2012). Evidence for free oxygen in the Neoarchean ocean based on coupled iron–molybdenum isotope fractionation. *Geochimica et Cosmochimica Acta*, *86*, 118–137.

Daines, S. J., Mills, B. J., & Lenton, T. M. (2017). Atmospheric oxygen regulation at low Proterozoic levels by incomplete oxidative weathering of sedimentary organic carbon. *Nature Communications*, *8*(1), 14379.

Dasgupta, R., Mallik, A., Tsuno, K., Withers, A. C., Hirth, G., & Hirschmann, M. M. (2013). Carbon-dioxide-rich silicate melt in the Earth's upper mantle. *Nature*, *493*(7431), 211.

de Wit, M. J., & Furnes, H. (2016). 3.5-Ga hydrothermal fields and diamictites in the Barberton Greenstone Belt—Paleoarchean crust in cold environments. *Science advances*, *2*(2), e1500368.

Derry, L. A. (2014). Organic carbon cycling and the lithosphere.

Derry, L. A. (2010, May 15). A burial diagenesis origin for the Ediacaran Shuram–Wonoka carbon isotope anomaly. *Earth and Planetary Science Letters*, *294*(1), 152–162. doi:10.1016/j.epsl.2010.03.022

Deutsch, C., & Weber, T. (2012). Nutrient Ratios as a Tracer and Driver of Ocean Biogeochemistry. *Annual Review of Marine Science*, *4*(1), 113–141. doi:10.1146/annurev-marine-120709-142821

Dewey, M., & Goldblatt, C. (2018). Empirical Evidence for Radiative-Convective Bi-Stability in Earth's Tropics. *Comparative Climatology of Terrestrial Planets III: From Stars to Surfaces*, *2065*.

Dhuime, B., Hawkesworth, C. J., Delavault, H., & Cawood, P. A. (2018). Rates of generation and destruction of the continental crust: Implications for continental growth. *Philosophical Transactions of the Royal Society A: Mathematical, Physical and Engineering Sciences*, *376*(2132), 20170403.

Di Giulio, M. (2003). The universal ancestor was a thermophile or a hyperthermophile: Tests and further evidence. *Journal of Theoretical Biology*, *221*(3), 425–436.

di Giulio, M. (2000). The universal ancestor lived in a thermophilic or hyperthermophilic environment. *Journal of theoretical biology*, *203*(3), 203–213.

Dickson, A. G. (1981). An exact definition of total alkalinity and a procedure for the estimation of alkalinity and total inorganic carbon from titration data. *Deep Sea Research Part A. Oceanographic Research Papers*, *28*(6), 609–623.

Dijkstra, N., Kraal, P., Kuypers, M. M. M., Schnetger, B., & Slomp, C. P. (2014, July 2). Are Iron-Phosphate Minerals a Sink for Phosphorus in Anoxic Black Sea Sediments? *PLOS ONE*, *9*(7), e101139. doi:10.1371/journal.pone.0101139

Dinçer, A. R., & Kargı, F. (2000). Kinetics of sequential nitrification and denitrification processes. *Enzyme and microbial technology*, *27*(1-2), 37–42.

Dos Santos, P. C., Fang, Z., Mason, S. W., Setubal, J. C., & Dixon, R. (2012). Distribution of nitrogen fixation and nitrogenase-like sequences amongst microbial genomes. *BMC genomics*, *13*, 1–12.

Duan, Y., Anbar, A. D., Arnold, G. L., Lyons, T. W., Gordon, G. W., & Kendall, B. (2010). Molybdenum isotope evidence for mild environmental oxygenation before the Great Oxidation Event. *Geochimica et Cosmochimica Acta*, *74*(23), 6655–6668.

Durand, B. (1980). *Kerogen: Insoluble organic matter from sedimentary rocks*. Editions technip.

Egger, M., Jilbert, T., Behrends, T., Rivard, C., & Slomp, C. P. (2015). Vivianite is a major sink for phosphorus in methanogenic coastal surface sediments. *Geochimica et Cosmochimica Acta*, *169*, 217–235.

Eguchi, J., Seales, J., & Dasgupta, R. (2020, January). Great Oxidation and Lomagundi events linked by deep cycling and enhanced degassing of carbon. *Nature Geoscience*, *13*(1), 71–76. doi:10.1038/s41561-019-0492-6

Elkins, L. J., Fischer, T. P., Hilton, D. R., Sharp, Z. D., McKnight, S., & Walker, J. (2006). Tracing nitrogen in volcanic and geothermal volatiles from the Nicaraguan volcanic front. *Geochimica et Cosmochimica Acta*, *70*(20), 5215–5235.

Emerson, S., & Hedges, J. (2008). *Chemical oceanography and the marine carbon cycle*. Cambridge University Press.

Erwin, D. H. (1994, January). The Permo–Triassic extinction. *Nature*, *367*(6460), 231–236. doi:10.1038/367231a0

Evans, D. A., Beukes, N. J., & Kirschvink, J. L. (1997). Low-latitude glaciation in the Palaeoproterozoic era. *Nature*, *386*(6622), 262–266. Retrieved October 26, 2023, from https://www.nature.com/articles/386262a0

Evans, M. E., & Muxworthy, A. R. (2019). Vaalbara palaeomagnetism. *Canadian Journal of Earth Sciences*, *56*(9), 912–916.

Falkowski, P. G. (1997). Evolution of the nitrogen cycle and its influence on the biological sequestration of CO2 in the ocean. *Nature*, *387*(6630), 272–275.

Falkowski, P. G. (2012). The global carbon cycle: Biological processes. *Fundamentals of Geobiology*, 5–19.

Falkowski, P. G., & Godfrey, L. V. (2008). Electrons, life and the evolution of Earth's oxygen cycle. *Philosophical Transactions of the Royal Society B: Biological Sciences*, *363*(1504), 2705–2716. doi:10.1098/rstb.2008.0054

Fani, R., Gallo, R., & Liò, P. (2000). Molecular evolution of nitrogen fixation: The evolutionary history of the nifD, nifK, nifE, and nifN genes. *Journal of molecular evolution*, *51*, 1–11.

Farquhar, J., Bao, H., & Thiemens, M. (2000). Atmospheric influence of Earth's earliest sulfur cycle. *Science*, *289*(5480), 756–758.

Farquhar, J., Savarino, J., Airieau, S., & Thiemens, M. H. (2001). Observation of wavelength-sensitive mass-independent sulfur isotope effects during SO2 photolysis: Implications for the early atmosphere. *Journal of Geophysical Research: Planets*, *106*(E12), 32829–32839.

Fennel, K., Follows, M., & Falkowski, P. G. (2005). The co-evolution of the nitrogen, carbon and oxygen cycles in the Proterozoic ocean. *American Journal of Science*, *305*(6-8), 526–545.

Feulner, G. (2012). The faint young Sun problem. *Reviews of Geophysics*, *50*(2).

Fischer, G., & Karakaş, G. (2009). Sinking rates and ballast composition of particles in the Atlantic Ocean: Implications for the organic carbon fluxes to the deep ocean. *biogeosciences*, *6*(1), 85–102.

Fischer, T. P. (2008). Fluxes of volatiles (H2O, CO2, N2, Cl, F) from arc volcanoes. *Geochemical Journal*, *42*(1), 21–38.

Froelich, P., Klinkhammer, G. P., Bender, M. L., Luedtke, N. A., Heath, G. R., Cullen, D., . . . Maynard, V. (1979). Early oxidation of organic matter in pelagic sediments of the eastern equatorial Atlantic: Suboxic diagenesis. *Geochimica et cosmochimica acta*, *43*(7), 1075–1090.

Gaillard, F., Scaillet, B., & Arndt, N. T. (2011, October). Atmospheric oxygenation caused by a change in volcanic degassing pressure. *Nature*, *478*(7368), 229–232. doi:10.1038/nature10460

Gallon, J. R. (1981). The oxygen sensitivity of nitrogenase: A problem for biochemists and micro-organisms. *Trends in Biochemical Sciences*, *6*, 19–23.

Galtier, N., Tourasse, N., & Gouy, M. (1999). A nonhyperthermophilic common ancestor to extant life forms. *Science*, *283*(5399), 220–221.

Garduño Ruíz, D. I., Goldblatt, C., & Ahm, A.-S. (2022). Photochemical modelling of the climate-redox evolution of the Great Oxidation Event: From a Snowball Earth to a Hot-Moist Greenhouse. In *2022 Goldschmidt Conference*, GOLDSCHMIDT.

Garduño Ruíz, D. I., Goldblatt, C., & Ahm, A.-S. (2023). Climate shapes the oxygenation of Earth's atmosphere across the Great Oxidation Event. *Earth and Planetary Science Letters*, *607*, 118071.

Gaucher, E. A., Kratzer, J. T., & Randall, R. N. (2010). Deep phylogeny—how a tree can help characterize early life on Earth. *Cold Spring Harbor Perspectives in Biology*, *2*(1), a002238.

Gillis, K. M., & Coogan, L. A. (2011). Secular variation in carbon uptake into the ocean crust. *Earth and Planetary Science Letters*, *302*(3-4), 385–392.

Glasspool, I. J., & Scott, A. C. (2010). Phanerozoic concentrations of atmospheric oxygen reconstructed from sedimentary charcoal. *Nature Geoscience*, *3*(9), 627–630.

Goddéris, Y., Donnadieu, Y., Nédélec, A., Dupré, B., Dessert, C., Grard, A., ... François, L. M. (2003). The Sturtian 'snowball'glaciation: Fire and ice. *Earth and Planetary Science Letters*, *211*(1-2), 1–12.

Godfrey, L. V., & Falkowski, P. G. (2009). The cycling and redox state of nitrogen in the Archaean ocean. *Nature Geoscience*, *2*(10), 725.

Goldblatt, C., Claire, M. W., Lenton, T. M., Matthews, A. J., Watson, A. J., & Zahnle, K. J. (2009). Nitrogen-enhanced greenhouse warming on early Earth. *Nature Geoscience*, *2*(12), 891.

Goldblatt, C., Lenton, T. M., & Watson, A. J. (2006). Bistability of atmospheric oxygen and the Great Oxidation. *Nature*, *443*(7112), 683–686.

Goldblatt, C., McDonald, V. L., & McCusker, K. E. (2021). Earth's long-term climate stabilized by clouds. *Nature Geoscience*, *14*(3), 143–150.

Goldblatt, C., & Zahnle, K. J. (2011). Faint young Sun paradox remains. *Nature*, *474*(7349), E1.

Goody, R. M., & Yung, Y. L. (1995). *Atmospheric radiation: Theoretical basis*. Oxford university press.

Gough, D. O. (1981). Solar interior structure and luminosity variations. In *Physics of Solar Variations: Proceedings of the 14th ESLAB Symposium held in Scheveningen, The Netherlands, 16–19 September, 1980* (pp. 21–34). Springer.

Gregory, B. S., Claire, M. W., & Rugheimer, S. (2021). Photochemical modelling of atmospheric oxygen levels confirms two stable states. *Earth and Planetary Science Letters*, *561*, 116818.

Grotzinger, J. P., & Knoll, A. H. (1999). Stromatolites in Precambrian carbonates: Evolutionary mileposts or environmental dipsticks? *Annual review of earth and planetary sciences*, *27*(1), 313–358.

Gruber, N. (2008). The marine nitrogen cycle: Overview and challenges. *Nitrogen in the marine environment*, *2*, 1–50.

Gumsley, A. P., Chamberlain, K. R., Bleeker, W., Söderlund, U., de Kock, M. O., Larsson, E. R., & Bekker, A. (2017). Timing and tempo of the Great Oxidation Event. *Proceedings of the National Academy of Sciences*, *114*(8), 1811–1816.

Hallam, A. (1987). End-Cretaceous mass extinction event: Argument for terrestrial causation. *Science*, *238*(4831), 1237–1242.

Halverson, G. P., Hoffman, P. F., Schrag, D. P., Maloof, A. C., & Rice, A. H. N. (2005). Toward a Neoproterozoic composite carbon-isotope record. *GSA bulletin*, *117*(9-10), 1181–1207.

Hardison, A. K., & Canuel, E. A. (2011). Carbon (Organic, Cycling). *Encyclopedia of Geobiology*, 230–234.

Harper, D. A. T., Hammarlund, E. U., & Rasmussen, C. M. Ø. (2014, May 1). End Ordovician extinctions: A coincidence of causes. *Gondwana Research*, *25*(4), 1294–1307. doi:10.1016/j.gr.2012.12.021

Hawkesworth, C., Cawood, P., Kemp, T., Storey, C., & Dhuime, B. (2009). A matter of preservation. *Science*, *323*(5910), 49–50.

Hayes, J. M., & Waldbauer, J. R. (2006). The carbon cycle and associated redox processes through time. *Philosophical Transactions of the Royal Society B: Biological Sciences*, *361*(1470), 931–950.

Haynes, W. M. (2014). *CRC handbook of chemistry and physics*. CRC press.

Heckman, D. S., Geiser, D. M., Eidell, B. R., Stauffer, R. L., Kardos, N. L., & Hedges, S. B. (2001). Molecular evidence for the early colonization of land by fungi and plants. *science*, *293*(5532), 1129–1133.

Herman, J. S., & White, W. B. (1985). Dissolution kinetics of dolomite: Effects of lithology and fluid flow velocity. *Geochimica et Cosmochimica Acta*, *49*(10), 2017–2026.

Hiatt, W. C., & Grady, C. P. (2008). An updated process model for carbon oxidation, nitrification, and denitrification. *Water Environment Research*, *80*(11), 2145–2156.

Hoffland, E., Kuyper, T. W., Wallander, H., Plassard, C., Gorbushina, A. A., Haselwandter, K., . . . Rosling, A. (2004). The role of fungi in weathering. *Frontiers in Ecology and the Environment*, *2*(5), 258–264.

Hoffman, P. F. (2013). The Great Oxidation and a Siderian snowball Earth: MIF-S based correlation of Paleoproterozoic glacial epochs. *Chemical Geology*, *362*, 143–156.

Hoffman, P. F. (2022). Glacial erosion on a snowball Earth: Testing for bias in flux balance, geographic setting, and tectonic regime. *Canadian Journal of Earth Sciences*.

Hoffman, P. F., Abbot, D. S., Ashkenazy, Y., Benn, D. I., Brocks, J. J., Cohen, P. A., . . . Warren, S. G. (2017). Snowball Earth climate dynamics and Cryogenian geology-geobiology. *Science Advances*, *3*(11), e1600983. doi:10.1126/sciadv.1600983

Hoffman, P. F., Kaufman, A. J., Halverson, G. P., & Schrag, D. P. (1998). A Neoproterozoic Snowball Earth. *science*, *281*(5381), 1342–1346.

Hoffman, P. F., & Schrag, D. P. (2002, June). The snowball Earth hypothesis: Testing the limits of global change. *Terra Nova*, *14*(3), 129–155. doi:10.1046/j.1365-3121.2002.00408.x

Holland, H. D. (2003). The geologic history of seawater. *Treatise on Geochemistry*, *6*, 625.

Holland, H. D. (2006, June 29). The oxygenation of the atmosphere and oceans. *Philosophical Transactions of the Royal Society B: Biological Sciences*, *361*(1470), 903–915. doi:10.1098/rstb.2006.1838

Holland, H. D. (2002). Volcanic gases, black smokers, and the Great Oxidation Event. *Geochimica et Cosmochimica acta*, *66*(21), 3811–3826.

Holloway, J. M., & Dahlgren, R. A. (2002). Nitrogen in rock: Occurrences and biogeochemical implications. *Global Biogeochemical Cycles*, *16*(4), 65–1.

Hunten, D. M. (1973). The escape of light gases from planetary atmospheres. *Journal of the Atmospheric Sciences*, *30*(8), 1481–1494.

Hurley, S. J., Wing, B. A., Jasper, C. E., Hill, N. C., & Cameron, J. C. (2021, January 6). Carbon isotope evidence for the global physiology of Proterozoic cyanobacteria. *Science Advances*, *7*(2), eabc8998. doi:10.1126/sciadv.abc8998

Husson, J. M., & Peters, S. E. (2017). Atmospheric oxygenation driven by unsteady growth of the continental sedimentary reservoir. *Earth and Planetary Science Letters*, *460*, 68–75.

Hyde, W. T., Crowley, T. J., Baum, S. K., & Peltier, W. R. (2000). Neoproterozoic 'snowball Earth'simulations with a coupled climate/ice-sheet model. *Nature*, *405*(6785), 425–429.

Ibarra, D. E., Rugenstein, J. K. C., Bachan, A., Baresch, A., Lau, K. V., Thomas, D. L., . . . Chamberlain, C. P. (2019). Modeling the consequences of land plant evolution on silicate weathering. *American Journal of Science*, *319*(1), 1–43.

Isley, A. E., & Abbott, D. H. (1999). Plume-related mafic volcanism and the deposition of banded iron formation. *Journal of Geophysical Research: Solid Earth*, *104*(B7), 15461–15477.

Isson, T. T., & Planavsky, N. J. (2018). Reverse weathering as a long-term stabilizer of marine pH and planetary climate. *Nature*, *560*(7719), 471.

Iversen, N., & Jørgensen, B. B. (1993). Diffusion coefficients of sulfate and methane in marine sediments: Influence of porosity. *Geochimica et Cosmochimica Acta*, *57*(3), 571–578.

Izon, G., Luo, G., Uveges, B. T., Beukes, N., Kitajima, K., Ono, S., . . . Summons, R. E. (2022). Bulk and grain-scale minor sulfur isotope data reveal complexities in the dynamics of Earth's oxygenation. *Proceedings of the National Academy of Sciences*, *119*(13), e2025606119.

Jahnke, R. A. (2000). The phosphorus cycle. *Earth system science: From biogeochemical cycles to global change, Elservier Academic Press, San Diego*, 360–376.

Jaisi, D. P., Blake, R. E., & Kukkadapu, R. K. (2010). Fractionation of oxygen isotopes in phosphate during its interactions with iron oxides. *Geochimica et Cosmochimica Acta*, *74*(4), 1309–1319.

Johnson, B., & Goldblatt, C. (2015). The nitrogen budget of Earth. *Earth-Science Reviews*, *148*, 150–173.

Johnson, B. W., & Goldblatt, C. (2017). *A secular increase in continental crust nitrogen during the Precambrian*. arXiv: 1709.02412

Johnson, B. W., & Goldblatt, C. (2018). EarthN: A new Earth system nitrogen model. *Geochemistry, Geophysics, Geosystems*, *19*(8), 2516–2542.

Johnson, B. W., & Wing, B. A. (2020). Limited Archaean continental emergence reflected in an early Archaean 18 O-enriched ocean. *Nature Geoscience*, *13*(3), 243–248.

Johnson, J. E., Gerpheide, A., Lamb, M. P., & Fischer, W. W. (2014). O2 constraints from Paleoproterozoic detrital pyrite and uraninite. *Bulletin*, *126*(5-6), 813–830.

Kaiser, S. I., Aretz, M., & Becker, R. T. (2016). The global Hangenberg Crisis (Devonian–Carboniferous transition): Review of a first-order mass extinction. *Geological Society, London, Special Publications*, *423*(1), 387–437.

Kanzaki, Y., & Kump, L. R. (2017). Biotic effects on oxygen consumption during weathering: Implications for the second rise of oxygen. *Geology*, *45*(7), 611–614.

Kappler, A., Pasquero, C., Konhauser, K. O., & Newman, D. K. (2005). Deposition of banded iron formations by anoxygenic phototrophic Fe (II)-oxidizing bacteria. *Geology*, *33*(11), 865–868.

Karhu, J. A., & Holland, H. D. (1996). Carbon isotopes and the rise of atmospheric oxygen. *Geology*, *24*(10), 867–870.

Kasting, J. F. (2005). Methane and climate during the Precambrian era. *Precambrian Research*, *137*(3-4), 119–129.

Kasting, J. F., Howard, M. T., Wallmann, K., Veizer, J., Shields, G., & Jaffrés, J. (2006). Paleoclimates, ocean depth, and the oxygen isotopic composition of seawater. *Earth and Planetary Science Letters*, *252*(1-2), 82–93.

Kaufman, A. J., & Knoll, A. H. (1995). Neoproterozoic variations in the C-isotopic composition of seawater: Stratigraphic and biogeochemical implications. *Precambrian research*, *73*(1-4), 27–49. Retrieved October 24, 2023, from https://www.sciencedirect.com/science/article/pii/0301926894000708

Kelly, E. F., Chadwick, O. A., & Hilinski, T. E. (1998). The effect of plants on mineral weathering. *Biogeochemistry*, *42*, 21–53.

Kendall, B., Anbar, A. D., Kappler, A., & Konhauser, K. O. (2012). The global iron cycle. *Fundamentals of geobiology*, *1*, 65–92.

Kendall, B., Reinhard, C. T., Lyons, T. W., Kaufman, A. J., Poulton, S. W., & Anbar, A. D. (2010). Pervasive oxygenation along late Archaean ocean margins. *Nature Geoscience*, *3*(9), 647–652.

Kendall, C., & Caldwell, E. A. (1998). Fundamentals of isotope geochemistry. In *Isotope tracers in catchment hydrology* (pp. 51–86). Elsevier.

Kennedy, M. J. (1996). Stratigraphy, sedimentology, and isotopic geochemistry of Australian Neoproterozoic postglacial cap dolostones; deglaciation, delta 13 C excursions, and carbonate precipitation. *Journal of sedimentary Research*, *66*(6), 1050–1064. Retrieved October 26, 2023, from https://pubs.geoscienceworld.org/sepm/jsedres/article-abstract/66/6/1050/98788

Kharecha, P., Kasting, J., & Siefert, J. (2005). A coupled atmosphere–ecosystem model of the early Archean Earth. *Geobiology*, *3*(2), 53–76.

Kipp, M. A., & Stüeken, E. E. (2017). Biomass recycling and Earth's early phosphorus cycle. *Science advances*, *3*(11), eaao4795.

Kirschvink, J. L. (1992). Late Proterozoic low-latitude global glaciation: The snowball Earth.

Kirschvink, J. L., Gaidos, E. J., Bertani, L. E., Beukes, N. J., Gutzmer, J., Maepa, L. N., & Steinberger, R. E. (2000). Paleoproterozoic snowball Earth: Extreme climatic and geochemical global change and its biological consequences. *Proceedings of the National Academy of Sciences*, *97*(4), 1400–1405.

Knauth, L. P. (2005). Temperature and salinity history of the Precambrian ocean: Implications for the course of microbial evolution. In *Geobiology: Objectives, concepts, perspectives* (pp. 53–69). Elsevier.

Knauth, L. P., & Kennedy, M. J. (2009, August). The late Precambrian greening of the Earth. *Nature*, *460*(7256), 728–732. doi:10.1038/nature08213

Knoll, A. H., Wörndle, S., & Kah, L. C. (2013). Covariance of microfossil assemblages and microbialite textures across an upper Mesoproterozoic carbonate platform. *Palaios*, *28*(7), 453–470.

Knudsen, A. C., & Gunter, M. E. (2002). Sedimentary phosphorites—An example: Phosphoria formation, southeastern Idaho, USA. *Reviews in Mineralogy and Geochemistry*, *48*(1), 363–389.

Koltermann, K. P., Gouretski, V., & Jancke, K. (2011). Hydrographic Atlas of the World Ocean Circulation Experiment (WOCE): Volume 3: Atlantic Ocean.

Konhauser, K. O., Amskold, L., Lalonde, S. V., Posth, N. R., Kappler, A., & Anbar, A. (2007a). Decoupling photochemical Fe (II) oxidation from shallow-water BIF deposition. *Earth and Planetary Science Letters*, *258*(1-2), 87–100.

Konhauser, K. O., Hamade, T., Raiswell, R., Morris, R. C., Ferris, F. G., Southam, G., & Canfield, D. E. (2002). Could bacteria have formed the Precambrian banded iron formations? *Geology*, *30*(12), 1079–1082. Retrieved October 24, 2023, from https://pubs.geoscienceworld.org/gsa/geology/article-abstract/30/12/1079/192275

Konhauser, K. O., Lalonde, S. V., Amskold, L., & Holland, H. D. (2007b). Was there really an Archean phosphate crisis? *Science*, *315*(5816), 1234–1234.

Kopp, G., & Lean, J. L. (2011). A new, lower value of total solar irradiance: Evidence and climate significance. *Geophysical Research Letters*, *38*(1). doi:10.1029/2010GL045777

Kopp, R. E., Kirschvink, J. L., Hilburn, I. A., & Nash, C. Z. (2005). The Paleoproterozoic snowball Earth: A climate disaster triggered by the evolution of oxygenic photosynthesis. *Proceedings of the National Academy of Sciences*, *102*(32), 11131–11136.

Korenaga, J. (2006). Archean geodynamics and the thermal evolution of Earth. *Geophysical Monograph-American Geophysical Union*, *164*, 7.

Kraal, P., Dijkstra, N., Behrends, T., & Slomp, C. P. (2017). Phosphorus burial in sediments of the sulfidic deep Black Sea: Key roles for adsorption by calcium carbonate and apatite authigenesis. *Geochimica et Cosmochimica Acta*, *204*, 140–158.

Krause, A. J., Mills, B. J., Merdith, A. S., Lenton, T. M., & Poulton, S. W. (2022). Extreme variability in atmospheric oxygen levels in the late Precambrian. *Science advances*, *8*(41), eabm8191.

Kriest, I., & Oschlies, A. (2008). On the treatment of particulate organic matter sinking in large-scale models of marine biogeochemical cycles. *Biogeosciences (BG)*, *5*, 55–72.

Krissansen-Totton, J., Arney, G. N., & Catling, D. C. (2018). Constraining the climate and ocean pH of the early Earth with a geological carbon cycle model. *Proceedings of the National Academy of Sciences*, *115*(16), 4105–4110.

Krissansen-Totton, J., Buick, R., & Catling, D. C. (2015). A statistical analysis of the carbon isotope record from the Archean to Phanerozoic and implications for the rise of oxygen. *American Journal of Science*, *315*(4), 275–316.

Krissansen-Totton, J., Kipp, M. A., & Catling, D. C. (2021, July). Carbon cycle inverse modeling suggests large changes in fractional organic burial are consistent with the carbon isotope record and may have contributed to the rise of oxygen. *Geobiology*, *19*(4), 342–363. doi:10.1111/gbi.12440

Krom, M. D., & Berner, R. A. (1980). The diffusion coefficients of sulfate, ammonium, and phosphate ions in anoxic marine sediments 1. *Limnology and Oceanography*, *25*(2), 327–337.

Kump, L. R. (2014). Hypothesized link between Neoproterozoic greening of the land surface and the establishment of an oxygen-rich atmosphere. *Proceedings* *of the National Academy of Sciences*, *111*(39), 14062–14065. doi:10.1073/pnas.1321496111

Kump, L. R., & Arthur, M. A. (1999). Interpreting carbon-isotope excursions: Carbonates and organic matter. *Chemical Geology*, *161*(1-3), 181–198.

Kump, L. R., & Barley, M. E. (2007). Increased subaerial volcanism and the rise of atmospheric oxygen 2.5 billion years ago. *Nature*, *448*(7157), 1033–1036.

Lambers, H. (2022). Phosphorus acquisition and utilization in plants. *Annual Review of Plant Biology*, *73*, 11–126.

Lee, C.-T. A., Yeung, L. Y., McKenzie, N. R., Yokoyama, Y., Ozaki, K., & Lenardic, A. (2016). Two-step rise of atmospheric oxygen linked to the growth of continents. *Nature Geoscience*, *9*(6), 417.

Lenton, T. M. (2000). Land and ocean carbon cycle feedback effects on global warming in a simple Earth system model. *Tellus B: Chemical and Physical Meteorology*, *52*(5), 1159–1188.

Lenton, T. M., Dahl, T. W., Daines, S. J., Mills, B. J., Ozaki, K., Saltzman, M. R., & Porada, P. (2016). Earliest land plants created modern levels of atmospheric oxygen. *Proceedings of the National Academy of Sciences*, *113*(35), 9704–9709.

Lenton, T. M., Daines, S. J., & Mills, B. J. (2018). COPSE reloaded: An improved model of biogeochemical cycling over Phanerozoic time. *Earth-Science Reviews*, *178*, 1–28.

Lenton, T. M., & Watson, A. J. (2000). Redfield revisited: 1. Regulation of nitrate, phosphate, and oxygen in the ocean. *Global Biogeochemical Cycles*, *14*(1), 225–248.

Lenton, T. M., & Watson, A. J. (2004). Biotic enhancement of weathering, atmospheric oxygen and carbon dioxide in the Neoproterozoic. *Geophysical Research Letters*, *31*(5). doi:10.1029/2003GL018802

Lepot, K. (2020, October 1). Signatures of early microbial life from the Archean (4 to 2.5 Ga) eon. *Earth-Science Reviews*, *209*, 103296. doi:10.1016/j.earscirev.2020.103296

Lewis, J. P., Weaver, A. J., & Eby, M. (2007). Snowball versus slushball Earth: Dynamic versus nondynamic sea ice? *Journal of Geophysical Research: Oceans*, *112*(C11).

Li, G., & Elderfield, H. (2013). Evolution of carbon cycle over the past 100 million years. *Geochimica et Cosmochimica Acta*, *103*, 11–25.

Li, H., Li, X., Xu, Z., Liang, S., Ding, Y., Song, D., & Guo, H. (2022). Nutrient budgets for the Bohai Sea: Implication for ratio imbalance of nitrogen to phosphorus input under intense human activities. *Marine Pollution Bulletin*, *179*, 113665.

Li, K., Li, L., Aubaud, C., & Muehlenbachs, K. (2020). Efficient carbon recycling at the Central-Northern Lesser Antilles Arc: Implications to deep carbon recycling in global subduction zones. *Geophysical Research Letters*, *47*(9), e2020GL086950.

Li, Y., & Keppler, H. (2014). Nitrogen speciation in mantle and crustal fluids. *Geochimica et Cosmochimica Acta*, *129*, 13–32.

Li, Z.-X., Evans, D. A. D., & Zhang, S. (2004). A 90 spin on Rodinia: Possible causal links between the Neoproterozoic supercontinent, superplume, true polar wander and low-latitude glaciation. *Earth and Planetary Science Letters*, *220*(3-4), 409–421.

Libes, S. (2011). *Introduction to marine biogeochemistry*. Academic Press.

Liss, P. S. (1974). Flux of gases across the air-sea interface. *Nature*, *247*, 181–184.

Liu, Y., Chen, C., He, D., & Chen, W. (2019, November). Deep carbon cycle in subduction zones. *Science China Earth Sciences*, *62*(11), 1764–1782. doi:10.1007/s11430-018-9426-1

Lodders, K., Fegley, B., & Lodders, F. (1998). *The planetary scientist's companion*. Oxford University Press on Demand.

Lovelock, J. (1972). Gaia as seen through the atmosphere. *Atmospheric Environment*, (6), 579–580.

Lovelock, J. E., & Margulis, L. (1974). Atmospheric homeostasis by and for the biosphere: The Gaia hypothesis. *Tellus*, *26*(1-2), 2–10.

Lowe, D. R., & Tice, M. M. (2007). Tectonic controls on atmospheric, climatic, and biological evolution 3.5–2.4 Ga. *Precambrian Research*, *158*(3-4), 177–197.

Lowenstein, T. K., Timofeeff, M. N., Brennan, S. T., Hardie, L. A., & Demicco, R. V. (2001). Oscillations in Phanerozoic seawater chemistry: Evidence from fluid inclusions. *Science*, *294*(5544), 1086–1088.

Lowman, J. P., & Jarvis, G. T. (1999). Effects of mantle heat source distribution on supercontinent stability. *Journal of Geophysical Research: Solid Earth*, *104*(B6), 12733–12746.

Lubnina, N. V., & Slabunov, A. I. (2011). Reconstruction of the Kenorland supercontinent in the Neoarchean based on paleomagnetic and geological data. *Moscow University Geology Bulletin*, *66*, 242–249.

Lucking, R., Huhndorf, S., Pfister, D. H., Plata, E. R., & Lumbsch, H. T. (2009). Fungi evolved right on track. *Mycologia*, *101*(6), 810–822.

Luo, G., Ono, S., Beukes, N. J., Wang, D. T., Xie, S., & Summons, R. E. (2016). Rapid oxygenation of Earth's atmosphere 2.33 billion years ago. *Science Advances*, *2*(5), e1600134.

Lutzoni, F., Nowak, M. D., Alfaro, M. E., Reeb, V., Miadlikowska, J., Krug, M., . . . Magallón, S. (2018, December 21). Contemporaneous radiations of fungi and plants linked to symbiosis. *Nature Communications*, *9*(1), 5451. doi:10.1038/s41467-018-07849-9

Lynch-Stieglitz, J., Stocker, T. F., Broecker, W. S., & Fairbanks, R. G. (1995). The influence of air-sea exchange on the isotopic composition of oceanic carbon: Observations and modeling. *Global Biogeochemical Cycles*, *9*(4), 653–665. doi:10.1029/95GB02574

Lyons, T. W., Reinhard, C. T., & Planavsky, N. J. (2014). The rise of oxygen in Earth's early ocean and atmosphere. *Nature*, *506*(7488), 307–315.

Mackenzie, F. T., Lerman, A., & Andersson, A. J. (2004). Past and present of sediment and carbon biogeochemical cycling models. *Biogeosciences*, *1*(1), 11–32.

Marais, D. J. D., Strauss, H., Summons, R. E., & Hayes, J. M. (1992). Carbon isotope evidence for the stepwise oxidation of the Proterozoic environment. *Nature*, *359*(6396), 605–609.

Marshall, A. O., Jehlička, J., Rouzaud, J.-N., & Marshall, C. P. (2014). Multiple generations of carbonaceous material deposited in Apex chert by basin-scale pervasive hydrothermal fluid flow. *Gondwana Research*, *25*(1), 284–289. Retrieved January 16, 2024, from https://www.sciencedirect.com/science/article/pii/S1342937X13001512

Martiny, A. C., Vrugt, J. A., Primeau, F. W., & Lomas, M. W. (2013a). Regional variation in the particulate organic carbon to nitrogen ratio in the surface ocean. *Global Biogeochemical Cycles*, *27*(3), 723–731.

Martiny, A. C., Pham, C. T., Primeau, F. W., Vrugt, J. A., Moore, J. K., Levin, S. A., & Lomas, M. W. (2013b). Strong latitudinal patterns in the elemental ratios of marine plankton and organic matter. *Nature Geoscience*, *6*(4), 279–283.

Marty, B., & Tolstikhin, I. N. (1998). CO2 fluxes from mid-ocean ridges, arcs and plumes. *Chemical Geology*, *145*(3-4), 233–248.

Masuda, Y., Yamanaka, Y., Smith, S. L., Hirata, T., Nakano, H., Oka, A., . . . Aita, M. N. (2023). Acclimation by diverse phytoplankton species determines oceanic carbon to nitrogen ratios. *Limnology and Oceanography Letters*, *8*(3), 519–528. doi:10.1002/lol2.10304

McCollom, T. M., & Seewald, J. S. (2013). Serpentinites, hydrogen, and life. *Elements*, *9*(2), 129–134.

Merz, M. U. (1992). The biology of carbonate precipitation by cyanobacteria. *Facies*, *26*, 81–101.

Mével, C. (2003). Serpentinization of abyssal peridotites at mid-ocean ridges. *Comptes Rendus Geoscience*, *335*(10-11), 825–852.

Mikhail, S., Barry, P. H., & Sverjensky, D. A. (2017). The relationship between mantle pH and the deep nitrogen cycle. *Geochimica et Cosmochimica Acta*, *209*, 149–160.

Mikhail, S., & Sverjensky, D. A. (2014). Nitrogen speciation in upper mantle fluids and the origin of Earth's nitrogen-rich atmosphere. *Nature Geoscience*, *7*(11), 816.

Millero, F. J. (1996). Chemical Oceanography. Boca Raton: CRC Press, 469 p.

Millero, F. J. (1995). Thermodynamics of the carbon dioxide system in the oceans. *Geochimica et Cosmochimica Acta*, *59*(4), 661–677.

Mills, B., Lenton, T. M., & Watson, A. J. (2014). Proterozoic oxygen rise linked to shifting balance between seafloor and terrestrial weathering. *Proceedings of the National Academy of Sciences*, *111*(25), 9073–9078.

Mills, B., Watson, A. J., Goldblatt, C., Boyle, R., & Lenton, T. M. (2011). Timing of Neoproterozoic glaciations linked to transport-limited global weathering. *Nature geoscience*, *4*(12), 861–864.

Montgomery, D. R., & Brandon, M. T. (2002, August 15). Topographic controls on erosion rates in tectonically active mountain ranges. *Earth and Planetary Science Letters*, *201*(3), 481–489. doi:10.1016/S0012-821X(02)00725-2

Morse, J. W., & Mackenzie, F. T. (1998). Hadean ocean carbonate geochemistry. *Aquatic Geochemistry*, *4*(3-4), 301–319.

Mukhopadhyay, J., Crowley, Q. G., Ghosh, S., Ghosh, G., Chakrabarti, K., Misra, B., . . . Bose, S. (2014). Oxygenation of the Archean atmosphere: New paleosol constraints from eastern India. *Geology*, *42*(10), 923–926.

Müller, R. D., Sdrolias, M., Gaina, C., & Roest, W. R. (2008). Age, spreading rates, and spreading asymmetry of the world's ocean crust. *Geochemistry, Geophysics, Geosystems*, *9*(4). doi:10.1029/2007GC001743

Murphy, M. A., & Salvador, A. (1999). International stratigraphic guide—an abridged version. *Episodes Journal of International Geoscience*, *22*(4), 255–271.

Nance, R. D. (2022). The supercontinent cycle and Earth's long-term climate. *Annals of the New York Academy of Sciences*, *1515*(1), 33–49.

Nance, R. D., & Murphy, J. B. (2013). Origins of the supercontinent cycle. *Geoscience Frontiers*, *4*(4), 439–448.

Nance, R. D., Murphy, J. B., & Santosh, M. (2014). The supercontinent cycle: A retrospective essay. *Gondwana Research*, *25*(1), 4–29.

Newman, M. J., & Rood, R. T. (1977). Implications of Solar Evolution for the Earth's Early Atmosphere. *Science*, *198*(4321), 1035–1037.

Nutman, A. P., Bennett, V. C., & Friend, C. R. (2017). Seeing through the magnetite: Reassessing Eoarchean atmosphere composition from Isua (Greenland) 3.7 Ga banded iron formations. *Geoscience Frontiers*, *8*(6), 1233–1240. Retrieved October 24, 2023, from https://www.sciencedirect.com/science/article/pii/S1674987117300464

O'Neil, J., Carlson, R. W., Francis, D., & Stevenson, R. K. (2008, September 26). Neodymium-142 Evidence for Hadean Mafic Crust. *Science*, *321*(5897), 1828–1831. doi:10.1126/science.1161925

Ohtomo, Y., Kakegawa, T., Ishida, A., Nagase, T., & Rosing, M. T. (2014, January). Evidence for biogenic graphite in early Archaean Isua metasedimentary rocks. *Nature Geoscience*, *7*(1), 25–28. doi:10.1038/ngeo2025

Olson, J. M. (2006). Photosynthesis in the Archean era. *Photosynthesis research*, *88*(2), 109–117.

Ouyang, Z., Collins, A., Li, Y., Qi, D., Arrigo, K. R., Zhuang, Y., . . . Murata, A. (2022). Seasonal Water Mass Evolution and Non-Redfield Dynamics Enhance CO2 Uptake in the Chukchi Sea. *Journal of Geophysical Research: Oceans*, *127*(8), e2021JC018326.

Ozaki, K., Cole, D. B., Reinhard, C. T., & Tajika, E. (2022). CANOPS-GRB v1. 0: A new Earth system model for simulating the evolution of ocean–atmosphere chemistry over geologic timescales. *Geoscientific Model Development*, *15*(20), 7593–7639.

Ozaki, K., & Reinhard, C. T. (2021). The future lifespan of Earth's oxygenated atmosphere. *Nature Geoscience*, *14*(3), 138–142.

Padhi, C. M., Korenaga, J., & Ozima, M. (2012). Thermal evolution of Earth with xenon degassing: A self-consistent approach. *Earth and Planetary Science Letters*, *341*, 1–9.

Palta, M. M., & Hartnett, H. (2018). Nitrogen cycle. In *Encyclopedia of Earth Sciences Series* (pp. 987–991). Springer Netherlands.

Partin, C. A., & Sadler, P. M. (2016). Slow net sediment accumulation sets snowball Earth apart from all younger glacial episodes. *Geology*, *44*(12), 1019–1022.

Pavlov, A. A., & Kasting, J. F. (2002). Mass-independent fractionation of sulfur isotopes in Archean sediments: Strong evidence for an anoxic Archean atmosphere. *Astrobiology*, *2*(1), 27–41.

Pavlov, A. A., Brown, L. L., & Kasting, J. F. (2001). UV shielding of NH3 and O2 by organic hazes in the Archean atmosphere. *Journal of Geophysical Research: Planets*, *106*(E10), 23267–23287.

Pavlov, A. A., Hurtgen, M. T., Kasting, J. F., & Arthur, M. A. (2003). Methane-rich Proterozoic atmosphere? *Geology*, *31*(1), 87–90.

Pavlov, A. A., Kasting, J. F., Brown, L. L., Rages, K. A., & Freedman, R. (2000). Greenhouse warming by CH4 in the atmosphere of early Earth. *Journal of Geophysical Research: Planets*, *105*(E5), 11981–11990.

Pearson, A. (2010). Pathways of carbon assimilation and their impact on organic matter values 13C. In *Handbook of hydrocarbon and lipid microbiology*.

Peck, W. H., Valley, J. W., Wilde, S. A., & Graham, C. M. (2001, November 15). Oxygen isotope ratios and rare earth elements in 3.3 to 4.4 Ga zircons: Ion microprobe evidence for high 18O continental crust and oceans in the Early Archean. *Geochimica et Cosmochimica Acta*, *65*(22), 4215–4229. doi:10.1016/S0016-7037(01)00711-6

Pehrsson, S. J., Buchan, K. L., Eglington, B. M., Berman, R. M., & Rainbird, R. H. (2014). Did plate tectonics shutdown in the Palaeoproterozoic? A view from the Siderian geologic record. *Gondwana Research*, *26*(3-4), 803–815.

Pellerin, A., Thomazo, C., Ader, M., Marin-Carbonne, J., Alleon, J., Vennin, E., & Hofmann, A. (2023, May). Iron-mediated anaerobic ammonium oxidation recorded in the early Archean ferruginous ocean. *Geobiology*, *21*(3), 277–289. doi:10.1111/gbi.12540

Peters, S. E., & Husson, J. M. (2017). Sediment cycling on continental and oceanic crust. *Geology*, *45*(4), 323–326.

Planavsky, N. J., Fakhraee, M., Bolton, E. W., Reinhard, C. T., Isson, T. T., Zhang, S., & Mills, B. J. (2022). On carbon burial and net primary production through Earth's history. *American Journal of Science*, *322*(3), 413–460.

Planavsky, N. J., Rouxel, O. J., Bekker, A., Lalonde, S. V., Konhauser, K. O., Reinhard, C. T., & Lyons, T. W. (2010). The evolution of the marine phosphate reservoir. *Nature*, *467*(7319), 1088.

Pollard, D. (2005). Snowball Earth: A thin-ice solution with flowing sea glaciers. *Journal of Geophysical Research*, *110*(C7), C07010. doi:10.1029/2004JC002525

Porder, S. (2019). How plants enhance weathering and how weathering is important to plants. *Elements: An International Magazine of Mineralogy, Geochemistry, and Petrology*, *15*(4), 241–246.

Porter, S. (2011, June 1). The rise of predators. *Geology*, *39*(6), 607–608. doi:10.1130/focus062011.1

Poulton, S. W., Bekker, A., Cumming, V. M., Zerkle, A. L., Canfield, D. E., & Johnston, D. T. (2021). A 200-million-year delay in permanent atmospheric oxygenation. *Nature*, *592*(7853), 232–236. Retrieved October 6, 2023, from https://www.nature.com/articles/s41586-021-03393-7

Poulton, S. W., & Canfield, D. E. (2011). Ferruginous conditions: A dominant feature of the ocean through Earth's history. *Elements*, *7*(2), 107–112. Retrieved October 24, 2023, from https://pubs.geoscienceworld.org/msa/elements/article-abstract/7/2/107/137888

Poulton, S. W., Fralick, P. W., & Canfield, D. E. (2004). The transition to a sulphidic ocean 1.84 billion years ago. *Nature*, *431*(7005), 173–177.

Rasmussen, B., Bekker, A., & Fletcher, I. R. (2013, November 15). Correlation of Paleoproterozoic glaciations based on U–Pb zircon ages for tuff beds in the Transvaal and Huronian Supergroups. *Earth and Planetary Science Letters*, *382*, 173–180. doi:10.1016/j.epsl.2013.08.037

Redfield, A. C., Ketchum, B. H., & Richards, F. A. (1963). The influence of organisms on the composition of seawater. *The sea*, *2*, 26–77.

Redfield, A. C. (1958). The biological control of chemical factors in the environment. *American scientist*, *46*(3), 230A–221.

Reimink, J. R., Davies, J. H., & Ielpi, A. (2021). Global zircon analysis records a gradual rise of continental crust throughout the Neoarchean. *Earth and Planetary Science Letters*, *554*, 116654.

Reinhard, C. T., Planavsky, N. J., Gill, B. C., Ozaki, K., Robbins, L. J., Lyons, T. W., . . . Konhauser, K. O. (2017). Evolution of the global phosphorus cycle. *Nature*, *541*(7637), 386–389.

Ren, T., Amaral, J. A., & Knowles, R. (1997). The response of methane consumption by pure cultures of methanotrophic bacteria to oxygen. *Canadian Journal of Microbiology*, *43*(10), 925–928.

Retallack, G. J. (2013, January). Ediacaran life on land. *Nature*, *493*(7430), 89–92. doi:10.1038/nature11777

Ridgwell, A., Hargreaves, J. C., Edwards, N. R., Annan, J. D., Lenton, T. M., Marsh, R., . . . Watson, A. (2007). Marine geochemical data assimilation in an efficient Earth System Model of global biogeochemical cycling. *Biogeosciences*, *4*(1), 87–104.

Rogers, J. J., & Santosh, M. (2003). Supercontinents in Earth history. *Gondwana Research*, *6*(3), 357–368.

Rogers, J. J., & Santosh, M. (2009). Tectonics and surface effects of the supercontinent Columbia. *Gondwana Research*, *15*(3-4), 373–380.

Rogers, J. J., & Santosh, M. J. G. R. (2002). Configuration of Columbia, a Mesoproterozoic supercontinent. *Gondwana Research*, *5*(1), 5–22.

Rolf, T., Coltice, N., & Tackley, P. J. (2014). Statistical cyclicity of the supercontinent cycle. *Geophysical Research Letters*, *41*(7), 2351–2358.

Rosing, M. T. (1999). 13C-depleted carbon microparticles in> 3700-Ma sea-floor sedimentary rocks from West Greenland. *Science*, *283*(5402), 674–676.

Rothman, D. H., Hayes, J. M., & Summons, R. E. (2003). Dynamics of the Neoproterozoic carbon cycle. *Proceedings of the National Academy of Sciences*, *100*(14), 8124–8129.

Rudnick, R. L., & Gao, S. (2003). Composition of the continental crust. *Treatise on geochemistry*, *3*, 659.

Rushby, A. J., Johnson, M., Mills, B. J., Watson, A. J., & Claire, M. W. (2018). Long-term planetary habitability and the carbonate-silicate cycle. *Astrobiology*, *18*(5), 469–480.

Ruttenberg, K. C. (2003). The global phosphorus cycle. *Treatise on geochemistry*, *8*, 682.

Sagan, C., & Chyba, C. (1997). The early faint sun paradox: Organic shielding of ultraviolet-labile greenhouse gases. *Science*, *276*(5316), 1217–1221.

Sagan, C., & Mullen, G. (1972). Earth and Mars: Evolution of Atmospheres and Surface Temperatures. *Science*, *177*(4043), 52–56.

Saito, M. A., Sigman, D. M., & Morel, F. M. (2003). The bioinorganic chemistry of the ancient ocean: The co-evolution of cyanobacterial metal requirements and biogeochemical cycles at the Archean–Proterozoic boundary? *Inorganica Chimica Acta*, *356*, 308–318.

Saltzman, M. R., & Thomas, E. (2012). Carbon isotope stratigraphy. *The geologic time scale*, *1*, 207–232.

Sander, R. (2015). Compilation of Henry's law constants (version 4.0) for water as solvent. *Atmospheric Chemistry & Physics*, *15*(8).

Santosh, M. (2010). Supercontinent tectonics and biogeochemical cycle: A matter of 'life and death'. *Geoscience Frontiers*, *1*(1), 21–30.

Schidlowski, M. (1988). A 3,800-million-year isotopic record of life from carbon in sedimentary rocks. *Nature*, *333*(6171), 313–318.

Schidlowski, M. (2001). Carbon isotopes as biogeochemical recorders of life over 3.8 Ga of Earth history: Evolution of a concept. *Precambrian Research*, *106*(1-2), 117–134.

Schidlowski, M., Eichmann, R., & Junge, C. E. (1976). Carbon isotope geochemistry of the Precambrian Lomagundi carbonate province, Rhodesia. *Geochimica et Cosmochimica Acta*, *40*(4), 449–455.

Schopf, J. W., Kudryavtsev, A. B., Czaja, A. D., & Tripathi, A. B. (2007, October 5). Evidence of Archean life: Stromatolites and microfossils. *Precambrian Research*. Earliest Evidence of Life on Earth, *158*(3), 141–155. doi:10.1016/j.precamres.2007.04.009

Schott, J., Berner, R. A., & Sjöberg, E. L. (1981). Mechanism of pyroxene and amphibole weathering—I. Experimental studies of iron-free minerals. *Geochimica et Cosmochimica Acta*, *45*(11), 2123–2135.

Schrag, D. P., Berner, R. A., Hoffman, P. F., & Halverson, G. P. (2002). On the initiation of a snowball Earth. *Geochemistry, Geophysics, Geosystems*, *3*(6), 1–21.

Schrag, D. P., Higgins, J. A., Macdonald, F. A., & Johnston, D. T. (2013). Authigenic carbonate and the history of the global carbon cycle. *science*, *339*(6119), 540–543.

Schrag, D. P., & Hoffman, P. F. (2001). Life, geology and snowball Earth. *Nature*, *409*(6818), 306–306.

Schulte, P., Alegret, L., Arenillas, I., Arz, J. A., Barton, P. J., Bown, P. R., . . . Cockell, C. S. (2010). The Chicxulub asteroid impact and mass extinction at the Cretaceous-Paleogene boundary. *Science*, *327*(5970), 1214–1218.

Scott, C. T., Bekker, A., Reinhard, C. T., Schnetger, B., Krapež, B., Rumble III, D., & Lyons, T. W. (2011). Late Archean euxinic conditions before the rise of atmospheric oxygen. *Geology*, *39*(2), 119–122.

Sellers, W. D. (1969). A global climatic model based on the energy balance of the earth-atmosphere system. *Journal of Applied Meteorology and Climatology*, *8*(3), 392–400. Retrieved October 10, 2023, from https://journals.ametsoc.org/view/journals/apme/8/3/1520-0450_1969_008_0392_agcmbo_2_0_co_2.xml

Selley, R. C. (2005, January 1). SEDIMENTARY ROCKS — Mineralogy and Classification. In R. C. Selley, L. R. M. Cocks, & I. R. Plimer (Eds.), *Encyclopedia of Geology* (pp. 25–37). doi:10.1016/B0-12-369396-9/00304-X

Sleep, N. H., Zahnle, K., & Neuhoff, P. S. (2001). Initiation of clement surface conditions on the earliest Earth. *Proceedings of the National Academy of Sciences*, *98*(7), 3666–3672.

Sleep, N. H., & Zahnle, K. (2001). Carbon dioxide cycling and implications for climate on ancient Earth. *Journal of Geophysical Research: Planets*, *106*(E1), 1373–1399.

Sperling, E. A., Wolock, C. J., Morgan, A. S., Gill, B. C., Kunzmann, M., Halverson, G. P., . . . Johnston, D. T. (2015). Statistical analysis of iron geochemical data suggests limited late Proterozoic oxygenation. *Nature*, *523*(7561), 451–454.

Stal, L. J. (2012). Cyanobacterial mats and stromatolites. In *Ecology of cyanobacteria II: Their diversity in space and time* (pp. 65–125). Springer.

Stanley, S. M. (2006). Influence of seawater chemistry on biomineralization throughout Phanerozoic time: Paleontological and experimental evidence. *Palaeogeography, Palaeoclimatology, Palaeoecology*, *232*(2-4), 214–236.

Stüeken, E. E., Buick, R., Guy, B. M., & Koehler, M. C. (2015a). Isotopic evidence for biological nitrogen fixation by molybdenum-nitrogenase from 3.2 Gyr. *Nature*, *520*(7549), 666–669.

Stüeken, E., Buick, R., Guy, B., & Koehler, M. (2015b). Constraining the origin and prevalence of biological N2 fixation in the Precambrian. In *EGU General Assembly Conference Abstracts* (p. 4183).

Swanner, E. D., Lambrecht, N., Wittkop, C., Harding, C., Katsev, S., Torgeson, J., & Poulton, S. W. (2020). The biogeochemistry of ferruginous lakes and past ferruginous oceans. *Earth-Science Reviews*, *211*, 103430.

Talley, L. D. (2007). *Hydrographic Atlas of the World Ocean Circulation Experiment (WOCE): Volume 2: Pacific Ocean*. WOCE International Project Office.

Tanioka, T., & Matsumoto, K. (2017). Buffering of ocean export production by flexible elemental stoichiometry of particulate organic matter. *Global Biogeochemical Cycles*, *31*(10), 1528–1542.

Thomazo, C., Ader, M., & Philippot, P. (2011). Extreme 15N-enrichments in 2.72-Gyr-old sediments: Evidence for a turning point in the nitrogen cycle. *Geobiology*, *9*(2), 107–120.

Thomazo, C., & Papineau, D. (2013). Biogeochemical cycling of nitrogen on the early Earth. *Elements*, *9*(5), 345–351.

Thompson, K. J., Kenward, P. A., Bauer, K. W., Warchola, T., Gauger, T., Martinez, R., . . . Reinhard, C. T. (2019). Photoferrotrophy, deposition of banded iron formations, and methane production in Archean oceans. *Science advances*, *5*(11), eaav2869.

Tiano, L., Garcia-Robledo, E., Dalsgaard, T., Devol, A. H., Ward, B. B., Ulloa, O., . . . Revsbech, N. P. (2014). Oxygen distribution and aerobic respiration in the north and south eastern tropical Pacific oxygen minimum zones. *Deep Sea Research Part I: Oceanographic Research Papers*, *94*, 173–183.

Tiwari, M., Singh, A. K., & Sinha, D. K. (2015, January 1). Chapter 3 - Stable Isotopes: Tools for Understanding Past Climatic Conditions and Their Applications in Chemostratigraphy. In Mu. Ramkumar (Ed.), *Chemostratigraphy* (pp. 65–92). doi:10.1016/B978-0-12-419968-2.00003-0

Torsvik, T. H. (2003). The Rodinia jigsaw puzzle. *Science*, *300*(5624), 1379–1381.

Treumann, R. A., LaBelle, J., & Bauer, T. M. (1995). Diffusion processes: An observational perspective. *Physics of the Magnetopause*, *90*, 331–341.

Tromp, T. K., Van Cappellen, P., & Key, R. M. (1995). A global model for the early diagenesis of organic carbon and organic phosphorus in marine sediments. *Geochimica et Cosmochimica Acta*, *59*(7), 1259–1284.

Van Cappellen, P., & Ingall, E. D. (1994). Benthic phosphorus regeneration, net primary production, and ocean anoxia: A model of the coupled marine biogeochemical cycles of carbon and phosphorus. *Paleoceanography*, *9*(5), 677–692.

van den Boorn, S. H., van Bergen, M. J., Nijman, W., & Vroon, P. Z. (2007). Dual role of seawater and hydrothermal fluids in Early Archean chert formation: Evidence from silicon isotopes. *Geology*, *35*(10), 939–942.

van Zuilen, M. A., Mathew, K., Wopenka, B., Lepland, A., Marti, K., & Arrhenius, G. (2005). Nitrogen and argon isotopic signatures in graphite from the 3.8-Ga-old

Isua Supracrustal Belt, Southern West Greenland. *Geochimica et Cosmochimica Acta*, *69*(5), 1241–1252.

Von Brunn, V., & Gold, D. J. C. (1993). Diamictite in the Archaean Pongola sequence of southern Africa. *Journal of African Earth Sciences (and the Middle East)*, *16*(3), 367–374.

Von Huene, R., & Scholl, D. W. (1991). Observations at convergent margins concerning sediment subduction, subduction erosion, and the growth of continental crust. *Reviews of Geophysics*, *29*(3), 279–316. doi:10.1029/91RG00969

Voss, M., Bange, H. W., Dippner, J. W., Middelburg, J. J., Montoya, J. P., & Ward, B. (2013). The marine nitrogen cycle: Recent discoveries, uncertainties and the potential relevance of climate change. *Philosophical Transactions of the Royal Society B: Biological Sciences*, *368*(1621), 20130121.

Wachholz, A., Dehaspe, J., Ebeling, P., Kumar, R., Musolff, A., Saavedra, F., . . . Graeber, D. (2023). Stoichiometry on the edge—humans induce strong imbalances of reactive C: N: P ratios in streams. *Environmental Research Letters*, *18*(4), 044016.

Walker, J. C. (1982). Climatic factors on the Archean Earth. *Palaeogeography, Palaeoclimatology, Palaeoecology*, *40*(1-3), 1–11.

Walker, J. C. (1985). Carbon dioxide on the early Earth. *Origins of Life and Evolution of the Biosphere*, *16*(2), 117–127.

Walker, J. C., Hays, P. B., & Kasting, J. F. (1981). A negative feedback mechanism for the long-term stabilization of Earth's surface temperature. *Journal of Geophysical Research: Oceans*, *86*(C10), 9776–9782.

Walker, J. C., Klein, C., Schidlowski, M., Schopf, J. W., Stevenson, D. J., & Walter, M. R. (1983). Environmental evolution of the Archean-early Proterozoic Earth. *IN: Earth's earliest biosphere: Its origin and evolution (A84-43051 21-51). Princeton, NJ, Princeton University Press, 1983, p. 260-290.* 260–290.

Wallmann, K., & Aloisi, G. (2012). The global carbon cycle: Geological processes. *Fundamentals of Geobiology*, 20–35.

Wallmann, K., Aloisi, G., Haeckel, M., Tishchenko, P., Pavlova, G., Greinert, J., . . . Eisenhauer, A. (2008). Silicate weathering in anoxic marine sediments. *Geochimica et Cosmochimica Acta*, *72*(12), 2895–2918.

Warke, M. R., Di Rocco, T., Zerkle, A. L., Lepland, A., Prave, A. R., Martin, A. P., . . . Claire, M. W. (2020). The great oxidation event preceded a paleoproterozoic “snowball Earth”. *Proceedings of the National Academy of Sciences*, *117*(24), 13314–13320.

Watson, A. J., & Orr, J. C. (2003). Carbon dioxide fluxes in the global ocean. In *Ocean Biogeochemistry* (pp. 123–143). Springer.

Wedepohl, K. H. (1995). The composition of the continental crust. *Geochimica et cosmochimica Acta*, *59*(7), 1217–1232.

Wegener, A. (1912). Die entstehung der kontinente. *Geologische Rundschau*, *3*(4), 276–292.

West, A. J., Galy, A., & Bickle, M. (2005). Tectonic and climatic controls on silicate weathering. *Earth and Planetary Science Letters*, *235*(1-2), 211–228.

Whiteside, J. H., Olsen, P. E., Eglinton, T., Brookfield, M. E., & Sambrotto, R. N. (2010, April 13). Compound-specific carbon isotopes from Earth’s largest flood basalt eruptions directly linked to the end-Triassic mass extinction. *Proceedings of the National Academy of Sciences*, *107*(15), 6721–6725. doi:10.1073/pnas.1001706107

Whitton, B. A. (2012). *Ecology of cyanobacteria II: Their diversity in space and time*. Springer Science & Business Media.

Williams, H., Hoffman, P. F., Lewry, J. F., Monger, J. W., & Rivers, T. (1991). Anatomy of North America: Thematic geologic portrayals of the continent. *Tectonophysics*, *187*(1-3), 117–134.

Williams, S. N., Schaefer, S. J., Calvache, V. M. L., & Lopez, D. (1992). Global carbon dioxide emission to the atmosphere by volcanoes. *Geochimica et Cosmochimica Acta*, *56*(4), 1765–1770.

Wilson, J. T. (1966, August 1). Did the Atlantic Close and then Re-Open? *Nature*, *211*(5050), 676–681. doi:10.1038/211676a0

Wilson, J. T. (1968). Static or mobile earth: The current scientific revolution. *Proceedings of the American Philosophical Society*, *112*(5), 309–320.

Wogelius, R. A., & Walther, J. V. (1992). Olivine dissolution kinetics at near-surface conditions. *Chemical Geology*, *97*(1-2), 101–112.

Wolf-Gladrow, D. A., Zeebe, R. E., Klaas, C., Körtzinger, A., & Dickson, A. G. (2007). Total alkalinity: The explicit conservative expression and its application to biogeochemical processes. *Marine Chemistry*, *106*(1-2), 287–300.

Wong, K., Mason, E., Brune, S., East, M., Edmonds, M., & Zahirovic, S. (2019). Deep carbon cycling over the past 200 million years: A review of fluxes in different tectonic settings. *Frontiers in Earth Science*, *7*, 263.

Yool, A., & Fasham, M. J. (2001). An examination of the "continental shelf pump" in an open ocean general circulation model. *Global Biogeochemical Cycles*, *15*(4), 831–844.

Young, G. M., Brunn, V. V., Gold, D. J., & Minter, W. E. L. (1998). Earth's oldest reported glaciation: Physical and chemical evidence from the Archean Mozaan Group (2.9 Ga) of South Africa. *The Journal of Geology*, *106*(5), 523–538.

Zahnle, K. J. (1986). Photochemistry of methane and the formation of hydrocyanic acid (HCN) in the Earth's early atmosphere. *Journal of Geophysical Research: Atmospheres*, *91*(D2), 2819–2834.

Zahnle, K., & Sleep, N. H. (2002). Carbon dioxide cycling through the mantle and implications for the climate of ancient Earth. *Geological Society, London, Special Publications*, *199*(1), 231–257.

Zalasiewicz, J., Bianca Cita, M., Hilgen, F., Pratt, B. R., Strasser, A., Thierry, J., & Weissert, H. (2013, March). Chronostratigraphy and geochronology: A proposed realignment. *GSA Today*, *23*(3), 4–8. doi:10.1130/GSATG160A.1

Zeebe, R. E. (2012). LOSCAR: Long-term ocean-atmosphere-sediment carbon cycle reservoir model v2. 0.4. *Geoscientific Model Development*, *5*(1), 149–166.

Zeebe, R. E., & Wolf-Gladrow, D. (2001). *CO2 in seawater: Equilibrium, kinetics, isotopes*. Gulf Professional Publishing.

Zegers, Wit, D., & Dann. (1998). Vaalbara, Earth's oldest assembled continent? A combined structural, geochronological, and palaeomagnetic test. *Terra Nova*, *10*(5), 250–259.

Zerkle, A. L., & Mikhail, S. (2017). The geobiological nitrogen cycle: From microbes to the mantle. *Geobiology*, *15*(3), 343–352.

Zerkle, A. L., House, C. H., Cox, R. P., & Canfield, D. E. (2006). Metal limitation of cyanobacterial N2 fixation and implications for the Precambrian nitrogen cycle. *Geobiology*, *4*(4), 285–297.

Zhang, S., Li, Z.-X., Evans, D. A., Wu, H., Li, H., & Dong, J. (2012). Pre-Rodinia supercontinent Nuna shaping up: A global synthesis with new paleomagnetic results from North China. *Earth and Planetary Science Letters*, *353*, 145–155.

Zhang, S., Wang, X., Wang, H., Bjerrum, C. J., Hammarlund, E. U., Costa, M. M., . . . Canfield, D. E. (2016). Sufficient oxygen for animal respiration 1,400 million years ago. *Proceedings of the National Academy of Sciences*, *113*(7), 1731–1736.

Appendix A

Parameterization and Reference Tables

This appendix details key information for the *EONS* model parameterization. All constants and parameters in the model are included in table A.1. For reservoirs not initialized at 0 moles, initial reservoir parameterizations are summarized in table A.2. References for all modern reservoirs and fluxes used in the chapter 3 nominal run plots are summarized in table A.3. I include a summary table of all model fluxes with unique chemical stoichiometries in table A.4.

A.1 Parameters and Constants

Table A.1: Model constants and parameters Reference abbreviations are **JG18** (Johnson & Goldblatt, 2018), **S15** (Sander, 2015), **CRC** (Haynes, 2014), **Ar5** (Ciais et al., 2014), **Z12** (Zeebe, 2012), **SZ01** (Sleep & Zahnle, 2001), **B02** (Bjerrum & Canfield, 2002), **B04**, (Bergman et al., 2004), **YF01** (Yool & Fasham, 2001), **BG14** (Byrne & Goldblatt, 2014), B01 (Burkhardt et al., 2001), **F05** (Fennel et al., 2005), **K07** (Konhauser et al., 2007a), **WA12** (Wallmann & Aloisi, 2012), **IP18** (Isson & Planavsky, 2018), **T14** (Tiano et al., 2014), **FK09** (Fischer & Karakaş, 2009), **BC94** (Brady & Carroll, 1994), **H85** (Herman & White, 1985), **C06** (Claire et al., 2006), **C08** (Crowe et al., 2008), **KO08** (Kriest & Oschlies, 2008), **R97** (Ren et al., 1997), **B92** (Butcher et al., 1992), **B96** (Boudreau, 1996), **T95** (Treumann et al., 1995)), **IJ93** (Iversen & Jørgensen, 1993), **KB80** (Krom & Berner, 1980), **GC11** (Gillis & Coogan, 2011), **M14** (Mills et al., 2014), **LF98** (Lodders et al., 1998), **LS74** (Liss, 1974), **DK00** (Dinçer & Kargı, 2000), **WOCE** (Talley, 2007), and **J10** (Jaisi et al., 2010). References accompanied by "This model" denote parameters derived from literature sources but modified in the tuning process.

Parameter & Definition	**Value**	**Units**	**Ref**
Atmosphere Constants			
Solar radiation constants			
S_M	1361	W/m^2	BG14
S_A	1020	W/m^2	This model
Average hydrogen diffusion constant			
k_Hesc	1.33×10^{16}	mol H/yr	C06
Thermal optical depth parameterization constants $(a_T T + b_T GF_t)$			
a_T	0.0075		This model
b_T	0.0175		This model
N_2 *pressure-broadening exponent*			
q	0.1257		This model
van't Hoff Temperature dependant Henry's law constants $(-\Delta_\mathrm{sol}H)/R$			
ν_O2	1700	K	S15
ν_CO2	2400	K	S15
ν_CH4	1900	K	S15
ν_N2	1300	K	S15
ν_NH3	4200	K	S15
Henry's Law constants at 298.15 K			
$\kappa_{0,\mathrm{O_2}}$	1.2×10^{-5}	mol/m^{3}Pa	S15
$\kappa_{0,\mathrm{CO_2}}$	3.3×10^{-4}	mol/m^{3}Pa	S15
$\kappa_{0,\mathrm{CH_4}}$	1.4×10^{-5}	mol/m^{3}Pa	S15

Table A.1 continued: Model constants and parameters

Parameter & Definition	Value	Units	Ref
$\kappa_{0,\mathrm{N_2}}$	6.4×10^{-6}	mol/m^{3}Pa	S15
$\kappa_{0,\mathrm{NH_3}}$	5.9×10^{-1}	mol/m^{3}Pa	S15
Gas diffusivity			
$D_{\mathrm{O_2}}$	1.78×10^{-5}	cm/s	CRC
$D_{\mathrm{CO_2}}$	1.45×10^{-5}	cm/s	CRC
$D_{\mathrm{CH_4}}$	1.55×10^{-5}	cm/s	CRC
$D_{\mathrm{N_2}}$	2.0×10^{-5}	cm/s	CRC
$D_{\mathrm{NH_3}}$	1.5×10^{-5}	cm/s	CRC
Modern atmospheric reservoirs			
$R_{\mathrm{O2},a,0}$	3.7×10^{19}	mol	JG18
$R_{\mathrm{CO2},a,0}$	5.3×10^{16}	mol	JG18
$R_{\mathrm{N2},a,0}$	1.4×10^{20}	mol	JG18
$R_{\mathrm{CH4},a,0}$	1.2×10^{14}	mol	JG18
$R_{\mathrm{NH3},a,0}$	1.7×10^{12}	mol	JG18
	Earth properties		
Mean albedo			
α	0.3		
Surface area of the Earth, ocean, continents, and continental sediments			
A_{E}	5.1×10^{14}	m^2	JG18
A_{oc}	3.4×10^{14}	m^2	JG18
A_{cont}	1.7×10^{14}	m^2	JG18
A_{shelf}	3.4×10^{12}	m^2	This model
Ocean, continental crust, oceanic crust, and upper mantle mass			
M_{oc}	1.4×10^{21}	kg	
M_{ccrust}	1.52×10^{22}	kg	LF98
M_{ocrust}	8.45×10^{21}	kg	LF98
M_{um}	1×10^{24}	kg	LF98
Specific heat capacity and density of ocean water			
c_p	4200	J/kgK	
ρ_{oc}	1027	kg/m^3	

Table A.1 continued: Model constants and parameters

Parameter & Definition	**Value**	**Units**	**Ref**
Depth of ocean boxes and stagnant boundary layer			
d_s	100	m	JG18
d_d	4000	m	JG18
d_{sl}	3.96×10^{-5}	m	LS74
Modern ocean dissolved silica			
$[Si]_0$	5×10^{-3}	mol/m^3	IP18, This model
Modern ocean dissolved phosphorus			
$[H_3PO_4]_0$	1.5×10^{-3}	mol/L	WOCE
Continental silicate reservoir			
$R_{sil,c,0}$	1×10^{22}	mol	This model
Fractions			
f_{Ashelf}	0.08		YF01
f_{Pshelf}	0.3		YF01
f_{sub}	0.05		This model
f_{melt}	0.85		This model
f_{acc}	0.1		This model
$f_{apatite}$	0.01		This model
f_{scav}	0.1		This model
f_{melt}	0.85		This model
$f_{acc,u}$	0.1		This model
$f_{acc,o}$	0.05		This model
$f_{sub,u}$	0.05		This model
$f_{sub,o}$	0.1		This model
$f_{volc,NH4}$	0.2125		This model
$f_{volc,ON}$	0.2125		This model
$f_{volc,CaCO3}$	0.85		This model
$f_{volc,OC}$	0.85		This model
$f_{cryst,NH4}$	0.6375		This model
$f_{cryst,ON}$	0.6375		This model
$f_{cryst,SP}$	0.85		This model

Table A.1 continued: Model constants and parameters

Parameter & Definition	Value	Units	Ref
$f_{\mathrm{cryst,OP}}$	0.85		This model
$f_{\mathrm{cryst,CP}}$	0.85		This model
$f_{\mathrm{cryst,Fe(OH3)}}$	0.85		This model
Population growth curve slopes			
$\epsilon_{\mathrm{photo}}$	2.76×10^{-7}	yr^{-1}	This model
$\epsilon_{\mathrm{fungi}}$	4.61×10^{-8}	yr^{-1}	This model
$\epsilon_{\mathrm{plant}}$	5.53×10^{-7}	yr^{-1}	This model
Biological Reaction constants $k_{j,x}$			
Half-saturation uptake of O_2 in ammonification			
$k_{\mathrm{ammon,O2}}$	8×10^{-3}	mol/m^3	CRC
Nitrification acidity inhibition factor			
$k_{\mathrm{nit,H}}$	6.3×10^{-5}	mol/m^3	DK00
Nitrification half-saturation uptake values			
$k_{\mathrm{nit,O2}}$	2×10^{-2}	mol/m^3	F05
Denitrification half-saturation uptake values			
$k_{\mathrm{denit,HNO3}}$	4.4×10^{-3}	mol/m^3	DK00
$k_{\mathrm{denit,O2}}$	2.05×10^{-4}	mol/m^3	T14
Nutrient assimilation half-saturation uptake values			
$k_{\mathrm{assim,fixN}}$	1.6×10^{-3}	mol/m^3	JG18
$k_{\mathrm{assim,H3PO4}}$	10^{-4}	mol/m^3	JG18
$k_{\mathrm{assim,DIC}}$	4.4×10^{-3}	mol/m^3	B01
Redfield sensitivity half-saturation constant			
$k_{\mathrm{assim,NP}}$	2		This model
Half reaction rate for N_2 fixation			
$k_{\mathrm{fix,N2}}$	3.73×10^{-2}	mol/m^3	JG18
Methanotrophy half-saturation uptake values			
$k_{\mathrm{mtrophy,O2}}$	5.7×10^{-3}	mol/m^3	R97
Oxygen limitation on anoxicity			
$k_{\mathrm{anox,O2}}$	6.2×10^{-3}	mol/m^3	C08
pH limitation on iron-phosphate sorption			

Table A.1 continued: Model constants and parameters

Parameter & Definition	Value	Units	Ref
$k_{\mathrm{sorb,pH}}$	7		K07
Biological Uptake ratios $r_{\frac{j}{j^*}}$			
Nutrient assimilation			
$r_{\frac{C}{P}}$	106 : 1		
$r_{\frac{C}{N}}$	106 : 16		
$r_{\frac{N}{P}}$	16 : 1		
Newly Fixed N Assimilation			
$r_{\frac{N2}{newN}}$	1 : 2		
$r_{\frac{CO2}{newN}}$	106 : 16		
$r_{\frac{H3PO4}{newN}}$	1 : 16		
$r_{\frac{O2}{newN}}$	118 : 16		
$r_{\frac{H2O}{newN}}$	130 : 16		
$r_{\frac{N2}{FeO}}$	8 : 472		
$r_{\frac{CO2}{FeO}}$	106 : 472		
$r_{\frac{H3PO4}{FeO}}$	1 : 472		
$r_{\frac{H2O}{FeO}}$	838 : 472		
Geochemical constants			
Activation energies for weathering dissolution			
E_{gran}	20.5	kcal/mol	BC94
E_{basa}	15	kcal/mol	BC94
E_{carb}	32	kJ/mol	H85
Rate power for $CaCO_3$ reactions			
η_{calc}	1.25		This model
η_{diss}	1.05		This model
Rate power for weathering reactions			

Table A.1 continued: Model constants and parameters

Parameter & Definition	Value	Units	Ref
η_w	0.3		SZ01
Normalization modifiers for weathering sensitivity			
a_w	10		This model
b_w	9		This model
Speciation constant for orthophosphate			
k_ads	0.07	$\mu\mathrm{M}^{-1}$	B02
Rate constant of reverse weathering			
k_rw	5.75×10^{12}	mol C/yr	IP18
Rate constant of seafloor weathering			
k_sfw	1.75×10^{12}	mol C/yr	GC11, M14
Rate constant of hydrothermal flow			
k_hyd	5.05×10^{13}	m^3/yr	JG17
Sediment diffusion constants			
λ_N2	6.28×10^{-2}	m^2/yr	B96
λ_NO3	1.58×10^{-2}	m^2/yr	B92
λ_NH4	2.21×10^{-2}	m^2/yr	B92
λ_PO4	9.5×10^{-3}	m^2/yr	B92
λ_O2	3.15×10^{-2}	m^2/yr	KB80
λ_CO2	4.57×10^{-2}	m^2/yr	CRC
λ_HCO3	1.61×10^{-2}	m^2/yr	T95
λ_CH4	2.74×10^{-2}	m^2/yr	IJ93
Timescales			
NH_3 photo-oxidation and photolysis			
$\tau_\mathrm{ammox,0}$	5	day	BG14
τ_pholys	10	yr	K82
Fe(II) Photo-oxidation			
τ_photox	1	yr	This model
Productivity			
τ_assim	180	day	F05
τ_fix	1825	day	F05

Table A.1 continued: Model constants and parameters

Parameter & Definition	Value	Units	Ref
τ_{death}	15	day	AR5
Ocean mixing, sinking, and sediment residence			
τ_{oc}	1000	yr	KO08
$\tau_{\text{sink,s}}$	50	day	KO08
$\tau_{\text{sink,d}}$	5000	day	FK09
$\tau_{\text{sink,n}}$	100	yr	This model
$\tau_{\text{sink,z}}$	1000	yr	This model
Aerobic remineralization			
$\tau_{\text{oxrm,s}}$	1.65	day	KO08, This model
$\tau_{\text{oxrm,d}}$	165	day	KO08, This model
$\tau_{\text{oxrm,n}}$	30	yr	KO08, This model
$\tau_{\text{oxrm,z}}$	300	yr	KO08, This model
Anaerobic remineralization and methanotrophy			
$\tau_{\text{axrm,s}}$	165	day	This model
$\tau_{\text{axrm,d}}$	825	day	This model
$\tau_{\text{axrm,n}}$	10	yr	This model
$\tau_{\text{axrm,z}}$	150	yr	This model
τ_{mtrophy}	0.1	yr	This model
Nitrification			
τ_{nit}	2.4×10^{-2}	yr	DK00, This model
Carbonate Precipitation and Dissolution			
τ_{precip}	25	yr	This model
$\tau_{\text{diss,s}}$	0.25	yr	This model
$\tau_{\text{diss,d}}$	0.25	yr	This model
$\tau_{\text{diss,n}}$	10	yr	This model
$\tau_{\text{diss,z}}$	100	yr	This model
Iron oxide P sorption and reduction			
τ_{sorb}	0.1	yr	J10
Weathering			
τ_{wsil}	5×10^{8}	yr	Z12

Table A.1 continued: Model constants and parameters

Parameter & Definition	Value	Units	Ref
τ_{woxi}	1×10^8	yr	B04
τ_{wcarb}	5×10^8	yr	Z12, WA12
Outgassing and subduction			
τ_{meta}	10^9	yr	WA12
τ_{subd}	10^8	yr	This model

Table A.2: Initial reservoirs summary All initialized reservoir sizes; we note present atmospheric levels (PAL; PAN denotes present atmospheres of nitrogen) and sources for certain values in the **Note** column. Citation keys are: **G21** (Goldblatt et al., 2021); **SC72** (Sagan & Chyba, 1997); **B02** (Bjerrum & Canfield, 2002); **F05** (Fennel et al., 2005); **S20** (Swanner et al., 2020); **R03** (Ruttenberg, 2003); **RG03** (Rudnick & Gao, 2003); **W95** (Wedepohl, 1995); **TGv2** (Carlson, 2005); **JG15** (Johnson & Goldblatt, 2015); *tuned* denotes initial conditions set to equilibrate high initial atmospheric CO_2 (for DIC, TA) or to achieve modern surface reservoirs at the end of the run, given a constant mantle outflux (for mantle reservoirs). "PAL" stands for present atmospheric level; "PCR" stands for present continental reservoir size; "PAN" stands for present atmospheric nitrogen level.

Reservoir	Species	Initial Size (mol)	Note	Ref
Atmosphere (*a*)	CO_2	5×10^{18}	150 PAL	MG1
	CH_4	1.2×10^{14}	1 PAL	
	N_2	1.38×10^{20}	1 PAL	
	NH_3	1.2×10^{11}	10 ppm	SM72
	H_2O	1×10^{18}		
Surface ocean (*s*)	DIC	2.6×10^{18}	7.5×10^{-2} mol/kg	*tuned*
	TA	2.4×10^{18}	7×10^{-2} mol/kg	*tuned*
	CH_4	1×10^{6}		
	N_2	3×10^{17}		
	RN	1×10^{14}		
	H_3PO_4	6.1×10^{12}	1.75×10^{-7} mol/kg	B02; F05
	FeO	3.5×10^{15}	1×10^{-4} mol/kg	S20
	H_2O	1×10^{19}		
Neritic sediments (*n*)	DIC	1.5×10^{14}	7.5×10^{-2} mol/kg	*tuned*
	TA	1.4×10^{14}	7×10^{-2} mol/kg	*tuned*
	CH_4	1×10^{6}		
	N_2	3×10^{17}		
	RN	1×10^{9}		
	H_3PO_4	3.4×10^{8}	1.75×10^{-7} mol/kg	B02; F05
	H_2O	1×10^{18}		
Deep ocean (*d*)	DIC	1×10^{20}	7.5×10^{-2} mol/kg	*tuned*
	TA	9.8×10^{19}	7×10^{-2} mol/kg	*tuned*
	CH_4	1×10^{6}		

Table A.2 continued: Initial reservoir summary

Reservoir	Species	Initial Size (mol)	Note	Ref
	N_2	3×10^{18}		
	RN	1×10^{15}		
	H_3PO_4	2.4×10^{14}	1.75×10^{-7} mol/kg	B02; F05
	FeO	1.4×10^{17}	1×10^{-4} mol/kg	S20
	H_2O	1×10^{20}		
Pelagic sediments (z)	DIC	1.7×10^{15}	7.5×10^{-2} mol/kg	*tuned*
	TA	1.6×10^{15}	7×10^{-2} mol/kg	*tuned*
	CH_4	1×10^{6}		
	N_2	3×10^{9}		
	RN	1×10^{9}		
	H_3PO_4	4×10^{8}	1.75×10^{-7} mol/kg	B02; F05
	H_2O	1×10^{18}		
Continental crust (c)	SP	1.5×10^{19}	5% PCR	R03; RG03
	Fe_2SiO_4	6.8×10^{20}	5% PCR	W95
	SiO_3	5×10^{20}	5% PCR	RG03
Mantle (m)	C	3.3×10^{22}	100 ppm	TGv2
	N	5.5×10^{20}	2-5 PAN	JG15
	P	4.6×10^{20}		*tuned*
	Fe	2×10^{22}		*tuned*
	SiO_3	3×10^{22}		*tuned*

A.2 Modern references

Table A.3: Modern References All references correspond to nominal run output plots in chapter 3, denoting the plot symbols for each point. Subplots without denoted references are excluded.

Subplot	Item	Symbol	Reference
Figure 3.1			
a	fixed N	○	Koltermann et al. (2011), Talley (2007)
	HNO_3	○	Koltermann et al. (2011), Talley (2007)
	NH_3+NH_4^+	○	Gruber (2008)
	H_3PO_4	○	Koltermann et al. (2011), Talley (2007)
b	oxygenic photosynthesis	○	Canuel and Hardison (2018)
	photoferrotrophy	○	Thompson et al. (2019)
c	oxygenic fixation	○	Palta and Hartnett (2018)
d	ammonification	○	Canuel and Hardison (2018)
	denitrification	○	Gruber (2008)
e	organic carbon burial fraction	○	Berner (2004)
Figure 3.3			
a	CO_2	○	Falkowski (2012)
	CH_4	○	Ciais et al. (2014)
	N_2	○	Wallmann and Aloisi (2012)
	NH_3	○	Byrne and Goldblatt (2014)
	O_2	○	Bergman et al. (2004)
b	CO_2	○	Byrne and Goldblatt (2014)
	CH_4	○	Byrne and Goldblatt (2014)
	NH_3	○	Byrne and Goldblatt (2014)
c	surface temperature	○	Lodders et al. (1998)
d	solar constant	○	Kopp and Lean (2011)
Figure 3.4			
a	$[O_2]_s$	○	Koltermann et al. (2011), Talley (2007)
	$[O_2]_d$	☆	Koltermann et al. (2011), Talley (2007)
c	$[RN]_s$	○	Gruber (2008)
	$[RN]_d$	☆	Gruber (2008)
d	$[HNO_3]_s$	○	Koltermann et al. (2011), Talley (2007)
	$[HNO_3]_d$	☆	Koltermann et al. (2011), Talley (2007)
e	$[H_3PO_4]_s$	○	Koltermann et al. (2011), Talley (2007)
	$[H_3PO_4]_d$	☆	Koltermann et al. (2011), Talley (2007)
f	$[OrgC]_n$	△	Mackenzie, Lerman, and Andersson (2004)

Table A.3 continued: Modern references

Subplot	Item	Symbol	Reference
	$[\mathrm{OrgC}]_z$	□	Mackenzie et al. (2004)
g	$[\mathrm{DIC}]_s$	○	Falkowski (2012)
	$[\mathrm{DIC}]_d$	☆	Falkowski (2012)
h	$[\mathrm{TA}]_s$	○	Millero (1996)
	$[\mathrm{TA}]_d$	☆	Millero (1996)
i	pH_s	○	Zeebe and Wolf-Gladrow (2001)
Figure 3.7			
a	silicate P	○	Jahnke (2000)
	carbonate P	○	Jahnke (2000)
	organic P	○	Falkowski (2012)
b	wSP	○	Jahnke (2000)
	wCP	○	Jahnke (2000)
c	$[\mathrm{HNO_3}]_s$	○	Koltermann et al. (2011), Talley (2007)
	$[\mathrm{HNO_3}]_d$	☆	Koltermann et al. (2011), Talley (2007)
d	export OP	○	Watson and Orr (2003)
f	zSP	□	Ruttenberg (2003)
	nCP	△	Ruttenberg (2003)
	zCP	□	Ruttenberg (2003)
	zOP	□	Mackenzie et al. (2004)
Figure 3.9			
a	N_2	○	Wallmann and Aloisi (2012)
	NH_3	○	Byrne and Goldblatt (2014)
c	NH_4	○	Wallmann and Aloisi (2012)
	ON	○	Falkowski (2012)
d	wON	○	Voss et al. (2013)
e	$\mathrm{sHNO_3}$	○	Koltermann et al. (2011), Talley (2007)
	$\mathrm{dHNO_3}$	☆	Koltermann et al. (2011), Talley (2007)
	$\mathrm{sNH_3\text{-}NH_4^+}$	○	Gruber (2008)
	$\mathrm{dNH_3\text{-}NH_4^+}$	☆	Gruber (2008)
f	export ON	○	Watson and Orr (2003)
h	nON	○	Mackenzie et al. (2004)
i	$\mathrm{oNH_4}$	☆	Goldblatt et al. (2009)
	uON	□	Goldblatt et al. (2009)
j	volc $\mathrm{oNH_4}$	□	Wallmann and Aloisi (2012)
	sub $\mathrm{oNH_4}$	☆	Goldblatt et al. (2009)
	volc uON	□	Wong et al. (2019)

Table A.3 continued: Modern references

Subplot	Item	Symbol	Reference
	sub uON	☆	Goldblatt et al. (2009)
		Figure 3.10	
a	CH_4	○	Ciais et al. (2014)
b	methox	○	Ciais et al. (2014)
	mantle	□	Bergman et al. (2004)
	H escape	○	Catling et al. (2001)
c	continental OC	○	Wallmann and Aloisi (2012)
d	weathering	○	Bergman et al. (2004)
	metamorphism	☆	Wallmann and Aloisi (2012)
f	export	○	Watson and Orr (2003)
	zSed	□	Watson and Orr (2003)
g	nOC	△	Mackenzie et al. (2004)
	zOC	□	Mackenzie et al. (2004)
h	nBur	△	Mackenzie et al. (2004)
	zBur	□	Mackenzie et al. (2004)
	nOxic	△	Mackenzie et al. (2004)
	zOxic	□	Mackenzie et al. (2004)
i	abyssal sediment OC	□	Clift (2017)
j	volcanism	□	Wong et al. (2019)
		Figure 3.11	
a	CO_2	○	Falkowski (2012)
b	methox	○	Ciais et al. (2014)
	mantle	□	Wallmann and Aloisi (2012)
c	$CaCO_3$	○	Falkowski (2012)
	SiO_3	○	Rudnick and Gao (2003)
d	wSil	○	Canuel and Hardison (2018)
	w$CaCO_3$	○	Wallmann and Aloisi (2012)
	metamorphism	☆	Wallmann and Aloisi (2012)
e	sDIC	○	Falkowski (2012)
	dDIC	☆	Falkowski (2012)
f	precip	○	Wallmann and Aloisi (2012)
	diss	☆	Wallmann and Aloisi (2012)
	nSed	△	Libes (2011)
	zSed	□	Mackenzie et al. (2004)
h	nBur	△	Libes (2011)
	zBur	□	Mackenzie et al. (2004)
	SFW	☆	Wallmann et al. (2008)

Table A.3 continued: Modern references

Subplot	Item	Symbol	Reference
	RW	□	Li and Elderfield (2013)
i	u$CaCO_3$	□	Wong et al. (2019)
	o$CaCO_3$	☆	Mackenzie et al. (2004)
j	volcanism	□	Wong et al. (2019)
	subduction	☆	Wong et al. (2019)

Table A.4: Model flux summary All model fluxes with unique stoichiometries

Flux Name	**Eq. #**	**Stoichiometry**	**Parameterization**	**Reservoirs**								
				a	**s**	**n**	**d**	**z**	**u**	**o**	**c**	**m**
		Photochemical Fluxes										
NH_3 Photolysis	2.52	$8\,NH_3 + 3\,CO_2 \xrightarrow{12h\nu} 4\,N_2 + 3\,CH_4 + 6\,H_2O$	$F_{\mathrm{pholys}} = \frac{R_{\mathrm{NH3,a}}}{\tau_{\mathrm{pholys}}}$	✓								
NH_3 Photo-oxidation	2.49	$2\,NH_3 + \frac{3}{2}O_2 \xrightarrow{6h\nu} N_2 + 3\,H_2O$	$F_{\mathrm{ammox}} = \frac{R_{\mathrm{NH3,a}}}{\tau_{\mathrm{ammox}}(O_2)}$	✓								
CH_4 Photo-oxidation	2.54	$CH_4 + 2\,O_2 \xrightarrow{4h\nu} CO_2 + 2\,H_2O$	$F_{\mathrm{methox}} = K_{\mathrm{eff}}([CH_4][O_2])^{\frac{1}{2}}$	✓								
NH_3 Hydrogen escape	2.58	$2\,NH_3 \xrightarrow{6h\nu} N_2 + 6\,H^+ \uparrow$	$F_{\mathrm{Hesc},NH3} = k_{\mathrm{Hesc}}[NH_3]\frac{1}{3}$	✓								
CH_4 Hydrogen escape	2.58	$CH_4 + H_2O \xrightarrow{4h\nu} \frac{1}{2}CO_2 + \frac{1}{2}CH_4 + 4\,H^+ \uparrow$	$F_{\mathrm{Hesc,CH4}} = k_{\mathrm{Hesc}}[CH_4]\frac{1}{4}$	✓								
		Biochemical Fluxes										
$CaCO_3$ Precipitation	2.61	$Ca^{2+} + 2\,HCO_3{}^- \xrightarrow{\Omega \geqslant 1} CaCO_3 + CO_2 + H_2O$	$F_{\mathrm{precip},i} = \frac{\left(\Omega_i - 1\right)^{\eta_{\mathrm{calc}}}[CO_3{}^{2-}]_i M_{\mathrm{oc},i}}{\tau_{\mathrm{precip}}}$		✓	✓	✓	✓				
$CaCO_3$ Dissolution	2.62	$CaCO_3 + CO_2 + H_2O \xrightarrow{\Omega < 1} Ca^{2+} + 2\,HCO_3{}^-$	$F_{\mathrm{diss},i} = \frac{\left(1 - \Omega_i\right)^{\eta_{\mathrm{diss}}} R_{\mathrm{CaCO3},i}}{\tau_{\mathrm{diss}}}$		✓	✓	✓	✓				
Nitrification	2.37	$NH_4{}^+ + 2\,O_2 \longrightarrow HNO_3 + H^+ + H_2O$	$F_{\mathrm{nit},i} = \frac{[NH_4{}^+]_i M_{\mathrm{oc},i}}{\tau_{\mathrm{nit}}} L_{\mathrm{nit,O2},i}(1 - L_{\mathrm{nit,H},i})$		✓	✓	✓	✓				
Abiotic Iron photo-oxidation	2.65	$4\,FeO + O_2 + 11\,H_2O \xrightarrow{4\,h\nu} 4\,Fe(OH)_3 + 5\,H_2O$	$F_{\mathrm{Fephotox}} = \frac{R_{\mathrm{FeO,s}}}{\tau_{\mathrm{photox}}} L_{\mathrm{O2,anox},s}$		✓							
Productivity by photosynthesis via NH_3 assimilation	2.26	$106\,CO_2 + 16\,NH_3 + H_3PO_4 + 106\,H_2O \xrightarrow{h\nu} (CH_2O)_{106}\,(NH_3)_{16}\,(H_3PO_4) + 106\,O_2$	$F_{\mathrm{assim,NH3}} = \frac{R_{\mathrm{H3PO4,s}}}{\tau_{\mathrm{assim}}} L_{\mathrm{assim,DIC}} L_{\mathrm{Redf}} \mathrm{r}_{\frac{C}{P}} \chi_{\mathrm{photo}}(t) f_{\mathrm{RN}}$		✓							

Table A.4 continued: Model flux summary

Flux Name	Eq. #	Stoichiometry			Parameterization	Reservoirs								
						a	s	n	d	z	u	o	c	m
Productivity by photosynthesis via HNO_3 Assimilation	2.26	$106\,CO_2 + 16\,HNO_3 + H_3PO_4 + 122\,H_2O$	$\xrightarrow{h\nu}$	$(CH_2O)_{106}\,(NH_3)_{16}\,(H_3PO_4) + 138\,O_2$	$F_{\text{assim,HNO3}} = \frac{R_{\text{H3PO4,s}}}{\tau_{\text{assim}}} L_{\text{assim,DIC}} L_{\text{Redf}}\, \mathrm{r}_{\frac{C}{P}}\, \chi_{\text{photo}}(t)\left(1 - f_{\text{RN}}\right)$		✓							
Productivity by Oxygenic N_2 Fixation	2.31	$106\,CO_2 + 8\,N_2 + H_3PO_4 + 130\,H_2O$	$\xrightarrow{h\nu}$	$(CH_2O)_{106}(NH_3)_{16}(H_3PO_4) + 118\,O_2$	$F_{\text{fix,newN}} = \frac{R_{\text{H3PO4,s}}}{\tau_{\text{fix}}} L_{\text{assim,DIC}} L_{\text{fix,N2}} (1 - L_{\text{Redf}})\, \chi_{\text{photo}}(t)\, \mathrm{r}_{\frac{N}{P}}$		✓							
Productivity by Anoxygenic N_2 Fixation	2.34	$106\,CO_2 + 8\,N_2 + H_3PO_4 + 472\,FeO + 1322\,H_2O$	$\xrightarrow{h\nu}$	$(CH_2O)_{106}(NH_3)_{16}(H_3PO_4) + 472\,Fe(OH)_3 + 484\,H_2O$	$F_{\text{fixation,FeO}} = \frac{R_{\text{FeO,s}}}{\tau_{\text{fix}}} L_{\text{assim,DIC}} L_{\text{assim,H3PO4}}\, L_{\text{fix,N2}} (1 - L_{\text{Redf}})(1 - \chi_{\text{photo}}(t))$		✓							
Productivity by Photoferrotrophy	2.28	$CO_2 + \frac{16}{106} NH_3 + \frac{1}{106} H_3PO_4 + 4\,FeO + 11\,H_2O$	$\xrightarrow{h\nu}$	$\frac{1}{106} (CH_2O)_{106}(NH_3)_{16}(H_3PO_4) + 4\,Fe(OH)_3 + 5\,H_2O$	$F_{\text{ferrotrophy}} = \frac{R_{\text{FeO,s}}}{\tau_{\text{assim}}} L_{\text{assim,DIC}} L_{\text{assim,fixN}}\, L_{\text{assim,H3PO4}} (1 - L_{\text{anox,O2},s})$		✓							
Remineralization by Ammonification	2.40	$(CH_2O)_{106}\,(NH_3)_{16}\,(H_3PO_4) + 106\,O_2$	$\longrightarrow$	$106\,CO_2 + 16\,NH_3 + H_3PO_4 + 106\,H_2O$	$F_{\text{ammon},i} = \frac{R_{\text{OC},i}}{\tau_{\text{oxrm},i}} L_{\text{ammon,O2},i}$		✓	✓	✓	✓				
Remineralization by Denitrification	2.43	$(CH_2O)_{106}\,(NH_3)_{16}\,(H_3PO_4) + \frac{424}{5} HNO_3$	$\longrightarrow$	$106\,CO_2 + \frac{212}{5} N_2 + 16\,NH_3 + H_3PO_4 + \frac{742}{5} H_2O$	$F_{\text{denit},i} = \frac{R_{\text{OC},i}}{\tau_{\text{axrm},i}} \left(1 - L_{\text{ammon,O2},i}\right) L_{\text{denit,HNO3},i}$		✓	✓	✓	✓				
Remineralization by Methanogenesis	2.44	$(CH_2O)_{106}\,(NH_3)_{16}\,(H_3PO_4)$	$\longrightarrow$	$53\,CO_2 + 53\,CH_4 + 16\,NH_3 + H_3PO_4$	$F_{\text{methgen},i} = \frac{R_{\text{OC},i}}{\tau_{\text{axrm},i}} \left(1 - L_{\text{ammon,O2},i}\right)\left(1 - L_{\text{denit,HNO3},i}\right)$		✓	✓	✓	✓				
Methanotrophy	2.46	$CH_4 + 2\,O_2$	$\longrightarrow$	$CO_2 + 2\,H_2O$	$F_{\text{mtrophy},i} = \frac{R_{\text{CH4},i}}{\tau_{\text{mtrophy}}} L_{\text{mtrophy,O2},i}$		✓	✓	✓	✓				

Table A.4 continued: Model flux summary

Flux Name	Eq. #	Stoichiometry	Parameterization	a	s	n	d	z	u	o	c	m
Phosphate scavenging	2.67	$(CH_2O)_{106}\,(NH_3)_{16}\,(H_3PO_4) \longrightarrow (CH_2O)_{106}\,(NH_3)_{16} + H_3PO_4\,(aq)$	$F_{\text{scav,i}} = \frac{R_{\text{OP},i}}{\tau_{\text{sink},i}}\left(1 - L_{\text{H3PO4,assim}}\right)\left(1 - L_{\text{O2,anox},i}\right) f_{\text{scav}}$			✓		✓				
Phosphate iron-sorption	2.69	$Fe(OH)_3 + H_3PO_4 \longrightarrow FePO_4 + 3\,H_2O$	$F_{\text{sorb},i} = \frac{R_{\text{FeOH3},i}}{\tau_{\text{sorb}}}[H_3PO_4]_i k_{\text{ads}}\left(1 - L_{\text{pH,sorb},i}\right)$		✓	✓	✓	✓				
		Geologic Fluxes										
Apatite burial	2.74	$H_3PO_4\,(aq) \longrightarrow H_3PO_4\,(u)$	$F_{\text{burial,PO4},i} = F_{\text{burial,CaCO3},i}\frac{[H_3PO_4]_i}{[H_3PO_4]_0} f_{\text{apatite}}$			✓		✓	✓			
Iron-oxide P burial	2.70	$FePO_4 + 3\,H_2O \longrightarrow Fe(OH)_3 + H_3PO_4$	$F_{\text{burial,FePO4},i} = \frac{R_{\text{FePO4},i}}{\tau_{\text{sink,i,0}}\chi_{\text{eros}}(t)}$			✓		✓	✓			
NH_4 subduction	2.76	$(NH_4)_2SiO_3\,(o) \longrightarrow 2\,NH_4\,(m) + SiO_2 + H_2O$	$F_{\text{subduct,NH4}} = \frac{R_{\text{NH4,o}}}{\tau_{\text{sub}}} f_{\text{sub,o}}$							✓		✓
$CaCO_3$ subduction	2.77	$CaCO_3\,(o) \longrightarrow CaO + CO_2\,(m)$	$F_{\text{subduct,CaCO3}} = \frac{f_{\text{sub,u}}R_{\text{CaCO3,u}} + f_{\text{sub,o}}R_{\text{CaCO3,o}}}{\tau_{\text{sub}}}$						✓	✓		✓
Carbonate Volcanism	2.82	$CaCO_3 + SiO_2 \xrightarrow{heat} CO_2\uparrow + CaSiO_3$	$F_{\text{volc,CaCO3}} = \frac{R_{\text{CaCO3,u}} + R_{\text{CaCO3,o}}}{\tau_{\text{sub}}} f_{\text{volc,CaCO3}}$	✓					✓			
Organic Volcanism	2.81	$(CH_2O)_{106}(NH_3)_{16}(H_3PO_4) \xrightarrow{heat} 53\,CO_2\uparrow + 53\,CH_4\uparrow + 16\,NH_3\uparrow + H_3PO_4$	$F_{\text{volc,OC}} = \frac{R_{\text{OC,u}}}{\tau_{\text{sub}}} f_{\text{volc,OC}}$	✓					✓			
NH_4 Volcanism	2.83	$(NH_4)_2SiO_3 \xrightarrow{heat} 2\,NH_3\uparrow + SiO_2 + H_2O$	$F_{\text{volc,NH4}} = \frac{R_{\text{NH4,o}}}{\tau_{\text{sub}}} f_{\text{volc,NH4}}$	✓						✓		
NH_4 recrystallization	2.85	$(NH_4)_2SiO_3\,(o) \longrightarrow (NH_4)_2SiO_3\,(c)$	$F_{\text{cryst,NH4}} = \frac{R_{\text{NH4,o}}}{\tau_{\text{sub}}} f_{\text{cryst,NH4}}$							✓	✓	
Carbonate Metamorphism	2.86	$CaCO_3 \xrightarrow{heat} CO_2\uparrow + CaO$	$F_{\text{meta,CaCO3}} = \frac{R_{\text{CaCO3,c}}}{\tau_{\text{meta}}}$	✓							✓	
Organic Metamorphism	2.86	$(CH_2O)_{106}(NH_3)_{16}(H_3PO_4) \xrightarrow{heat} 53\,CO_2\uparrow + 53\,CH_4\uparrow + 16\,NH_3\uparrow + H_3PO_4$	$F_{\text{meta,OC}} = \frac{R_{\text{OC,c}}}{\tau_{\text{meta}}}$	✓							✓	

Table A.4 continued: Model flux summary

Flux Name	Eq. #	Stoichiometry	Parameterization	Reservoirs a	s	n	d	z	u	o	c	m
NH_4 Metamorphism	2.86	$(NH_4)_2SiO_3 \xrightarrow{heat} 2\,NH_3\uparrow + 2\,H_2O + SiO_2$	$F_{\text{meta,NH4}} = \frac{R_{\text{NH4,c}}}{\tau_{\text{meta}}}$	✓							✓	
Carbonate weathering	2.96	$CaCO_3 + H_2O + CO_2 \longrightarrow Ca^{2+} + 2\,HCO_3{}^-$	$F_{\text{wthr,CaCO3}} = \frac{R_{\text{CaCO3,c}}}{\tau_{\text{wcarb}}} S_{\text{carb}}(t, T, CO_2)$	✓	✓						✓	
Apatite weathering	2.97	$H_3PO_4\,(c) \longrightarrow H_3PO_4\,(aq)$	$F_{\text{wthr,CP}} = \frac{R_{\text{CP,c}}}{\tau_{\text{wcarb}}/\chi_{\text{fungi}}(t)} S_{\text{carb}}(t, T, CO_2)$	✓	✓						✓	
Silicate weathering	2.102	$CaSiO_3(c) + H_2O + 2\,CO_2(a) \longrightarrow Ca^{2+} + 2\,HCO_3{}^-(aq) + SiO_2$	$F_{\text{wthr,sil}} = 2\frac{R_{\text{SiO3,c}}}{\tau_{\text{wsil}}} S_{\text{sil}}(t, T, CO_2)$	✓	✓						✓	
Silicate-bound P weathering	2.104	$H_3PO_4\,(c) \longrightarrow H_3PO_4\,(aq)$	$F_{\text{wthr,SP}} = \frac{R_{\text{SP,c}}}{\tau_{\text{wsil}}/\chi_{\text{fungi}}(t)} S_{\text{sil}}(t, T, CO_2)$	✓	✓						✓	
Ammonium weathering	2.103	$(NH_4)_2SiO_3 + 2\,CO_2(a) + H_2O \longrightarrow 2\,NH_4{}^+\,(aq) + SiO_2 + 2\,HCO_3{}^-\,(aq)$	$F_{\text{wthr,NH4}} = \frac{R_{\text{NH4,c}}}{\tau_{\text{wsil}}} S_{\text{sil}}(t, T, CO_2)$	✓	✓						✓	
Iron oxidative weathering	2.105	$Fe_2SiO_4 + CO_2(a) + H_2O + \frac{1}{2}O_2\,(a) \longrightarrow Fe_2O_3(c) + H_2CO_3(aq) + SiO_2$	$F_{\text{wthr,Feox}} = \frac{R_{\text{Fe2SiO4,c}}}{\tau_{\text{wsil}}} \sqrt{f_{O_2}} S_{\text{sil}}(t, T, CO_2)$	✓							✓	
Oxidative weathering	2.107	$(CH_2O)_{106}(NH_3)_{16}(H_3PO_4) + 106\,O_2 \longrightarrow 106\,CO_2 + 16\,NH_3 + H_3PO_4 + 106\,H_2O$	$F_{\text{wthr,OC}} = \frac{R_{\text{OC,c}}}{\tau_{\text{woxi}}} \sqrt{f_{O_2}}$	✓	✓						✓	
Reverse weathering	2.109	$Ca^{2+} + 2\,HCO_3{}^- + SiO_2 \longrightarrow CaSiO_3 + 2\,CO_2 + H_2O$	$F_{\text{revwthr},i} = 2k_{\text{rw},i}(\text{pH}_i)[\text{Si}]_i(\text{pH}_i)V_i$			✓		✓				
Seafloor weathering	2.112	$CO_2(aq) + CaSiO_3 \longrightarrow CaCO_3 + SiO_2$	$F_{\text{sfw}} = k_{\text{sfw}} S_{\text{sfw}}(t, [CO_2]_z)$					✓		✓		
Hydrothermal alteration	2.114	$2\,NH_4{}^+\,(aq) + SiO_2 + 2\,HCO_3{}^- \longrightarrow (NH_4)_2SiO_3 + 2\,CO_2(aq) + H_2O$	$F_{\text{hyd}} = [NH_4{}^+]_z \rho_{oc} k_{\text{hyd}} S_{\text{sfw}}(t, [CO_2]_z)$					✓		✓		
NH_3 mantle outgassing	2.116	$NH_3\,(m) \longrightarrow NH_3\,(a)$	$F_{\text{mantle,NH3}} = f_{\text{red}} F_{\text{mantle,N}}$	✓								✓
CH_4 mantle outgassing	2.116	$CH_4\,(m) \longrightarrow CH_4\,(a)$	$F_{\text{mantle,CH4}} = f_{\text{red}} F_{\text{mantle,C}}$	✓								✓

Table A.4 continued: Model flux summary

Flux Name	**Eq. #**	**Stoichiometry**	**Parameterization**	**Reservoirs**								
				a	**s**	**n**	**d**	**z**	**u**	**o**	**c**	**m**
N_2 mantle outgassing	2.117	N_2 (m) $\longrightarrow$ N_2 (a)	$F_{\text{mantle,N2}} = (1 - f_{\text{red}})F_{\text{mantle,N}}$	✓								✓
CO_2 mantle outgassing	2.117	CO_2 (m) $\longrightarrow$ CO_2 (a)	$F_{\text{mantle,CO2}} = (1 - f_{\text{red}})F_{\text{mantle,C}}$	✓								✓
FeO mantle outgassing	2.13	FeO (m) $\longrightarrow$ FeO (d)	$F_{\text{mantle,FeO}} = F_{\text{mantle,Fe,0}}\left(\chi_{\text{mantle}} + \frac{(1-\chi_{\text{mantle}})t}{4.5\times10^9}\right)$				✓					✓

Table A.5: All model speciation stoichiometries

Flux Name	**Eq. #**	**Stoichiometry**	**Parameterization**	**Reservoirs**								
				a	**s**	**n**	**d**	**z**	**u**	**o**	**c**	**m**
CO_2 speciation	2.8	$2\,H^+ + CO_3{}^{2-} \longrightarrow CO_2 + H_2O$	$[CO_2]_i = \frac{[DIC]_i}{\left(1+\frac{K_{1,i}}{[H^+]_i}+\frac{K_{1,i}K_{2,i}}{[H^+]_i^2}\right)}$		✓	✓	✓	✓				
$CO_3{}^{2-}$ speciation	2.9	$HCO_3{}^- \longrightarrow H^+ + CO_3{}^{2-}$	$[CO_3{}^{2-}]_i = \frac{[DIC]_i}{\left(1+\frac{[H^+]_i}{K_{2,i}}+\frac{[H^+]_i^2}{K_{1,i}K_{2,i}}\right)}$		✓	✓	✓	✓				
$HCO_3{}^-$ speciation	2.10	$CO_2 + H_2O \longrightarrow H^+ + HCO_3{}^-$	$[HCO_3{}^-]_i = \frac{[DIC]_i}{\left(1+\frac{[H^+]_i}{K_{1,i}}+\frac{K_{2,i}}{[H^+]_i}\right)}$		✓	✓	✓	✓				
NH_3 speciation	2.11	$NH_4{}^+ \longrightarrow NH_3 + H^+$	$[NH_3]_i = \frac{[RN]_i}{\left(1+\frac{[H^+]_i}{K_{N,i}}\right)}$		✓	✓	✓	✓				
$NH_4{}^+$ speciation	2.12	$NH_3 + H^+ \longrightarrow NH_4{}^+$	$[NH_4{}^+]_i = \frac{[NH_3]_i[H^+]_i}{K_{N,i}}$		✓	✓	✓	✓				

Appendix B

Extra Formulae

This appendix details formulations for chemical equilibria in the ocean (section B.1), and the calculation of temperature and greenhouse forcing parameters used in the model (section B.2).

B.1 Formulae for aqueous speciation

I summarize calculations for equilibrium speciation between ammonia-ammonium (section B.1.1), for dissolved inorganic carbon species and carbonate saturation state (section B.1.2), and provide the thermodynamic equilibrium constants for all speciation reactions (table B.1).

B.1.1 NH_3 and $NH_4{}^+$ speciation

Ammonia and ammonium exist in the ocean and reactive sedimentary reservoirs in equilibrium. The ammonium dissociation constant (K_{N}) depends on local salinity (S_i, in permil) and temperature (T_i, in Kelvin), and is based on an equation from Millero (1995).

$$\begin{aligned} K_{N,i} = \exp\Bigg(& \frac{-6285.33}{T_i} + 0.0001635 T_i - 0.25444 \\ & + \big(0.46532 - \frac{123.7184}{T_i}\big) S_i^{0.5} + \big(-0.01992 + \frac{3.17556}{T_i}\big) S_i \Bigg) \end{aligned} \tag{B.1}$$

B.1.2 Carbon Speciation

Carbon species (CO_2, $HCO_3{}^-$, and $CO_3{}^{2-}$) exist in equilibrium within the dissolved inorganic carbon (DIC) reservoir within the surface (*s*) and deep (*d*) ocean and in the porewaters of reactive sediments (*n* and *z*). Concentrations of hydrogen and hydroxyl ions ([H^+] and [OH^-]) are calculated assuming equilibrium hydration and protonation reactions and a sixth-order polynomial equation solved for the single set of positive roots; the acid dissociation constants for protonation, hydration, boric acid, and ion water product (K_1, K_2, K_B ,K_W) for these following equations depend on local salinity (S_i, in permil) and temperature (T_i, in Kelvin; Zeebe & Wolf-Gladrow, 2001). Pressure effects on the thermodynamic constants outlined below are treated the same as outlined in Zeebe & Wolf-Gladrow, 2001 appendix A.

$$K_{1,i} = \exp\Bigg(2.83655 - \frac{2307.1266}{T_i} - 1.5529413 ln(T_i) - \big(0.207608410 + \frac{4.0484}{T_i} S_i^{0.5}\big) + 0.0846834 S_i - 0.00654208 S_i^{1.5} + ln(1 - 0.001005 S_i)\Bigg) \tag{B.2}$$

$$K_{2,i} = \exp\Bigg(- 9.226508 - \frac{3351.6106}{T_i} - 0.2005743 ln(T_i) - \Big(0.106901773 + \frac{23.9722}{T_i} S_i^{0.5}\Big) + 0.1130822 S_i - 0.00846934 S_i^{1.5} + ln(1 - 0.001005 S_i)\Bigg) \tag{B.3}$$

$$K_{B,i} = \exp\Bigg(- 8966.9 - 2890.53 S_i^{0.5} - 77.942 S_i + 1.728 S_i^{1.5} - \frac{0.0996 S_i^2}{T_i} + 148.0248 + 137.1942 S_i^{0.5} + 1.62142 S_i - \big(24.4344 + 25.085 S_i^{0.5} + 0.2474 S_i\big) ln(T_i) + 0.053105 S_i^{0.5} T_i\Bigg) \tag{B.4}$$

$$K_{W,i} = \exp\left(148.96502 - \frac{13847.26}{T_i} - 23.6521 ln(T_i) + \frac{118.67}{T_i} - 5.977 \right. \\ \left. + 1.0495 ln(T_i) S_i^{0.5} - 0.01615 S_i\right) \tag{B.5}$$

The following sixth-order polynomial equation has been modified from the fifth-order polynomial in appendix A of Zeebe and Wolf-Gladrow (2001), to add in the effects of ammonia-ammonium speciation on total alkalinity. This equation is solved for hydrogen concentration for reservoir *i*:

$$[\mathrm{DIC}]_i\left(\frac{K_{1,i}}{[\mathrm{H}^+]_i} + 2\frac{K_{1,i}K_{2,i}}{[\mathrm{H}^+]_i^2}\right) \\ = \\ \left([\mathrm{TA}]_i - \frac{K_{B,i}[B_T]_i}{K_{B,i} + [\mathrm{H}^+]_i} - \frac{K_{W,i}}{[\mathrm{H}^+]_i} + [\mathrm{H}^+]_i - \frac{[RN]_i K_{N,i}}{K_{N,i} + [\mathrm{H}^+]_i}\right)\left(1 + \frac{K_{1,i}}{[\mathrm{H}^+]_i} + \frac{K_{1,i}K_{2,i}}{[\mathrm{H}^+]_i^2}\right) \tag{B.6}$$

where $[B_T]_i$ is the total dissolved boron concentration in the ocean, taken to be a constant approximately equal to $4.16 \times 10^{-4} \frac{S_i}{35}$ (Zeebe & Wolf-Gladrow, 2001).

Calcium carbonate saturation state, Ω, is a product of $[\mathrm{CO_3}^{2-}]$ and a fixed $[\mathrm{Ca}^{2+}]$ divided by the aragonite solubility constant (K_a) which is dependant on local temperature (T_i), salinity (S_i), and pressure (P_i; Millero, 1995).

$$K_{\mathrm{a},i} = 10^{\left(-171.945 - 0.077993 T_i + \frac{2903.293}{T_i} + 71.595 log(T_i) \right. \\ \left. + (-0.068393 + 0.0017276 T_i + \frac{88.135}{T_i}) S_i^{0.5} - 0.10018 S_i + 0.0059415 S_i^{1.5}\right)} \tag{B.7}$$

Table B.1: Thermodynamic equilibrium speciation constants for the *EONS* model. Note: pK_x terms denote reaction rate constants, while K_x terms denote equilibrium dissociation constants.

Parameter	Definition	Value	Units
Ammonia equilibrium reaction: $NH_4{}^+ \rightleftharpoons NH_3 + H^+$			
$pK_{N,s}$	surface ocean reaction rate	-9.2562	
$pK_{N,n}$	neritic sediments rate	-9.2562	
$pK_{N,d}$	deep ocean rate	-10.0243	
$pK_{N,z}$	pelagic sediments rate	-10.0834	
$K_{N,s}$	surface ocean dissociation	5.5434×10^{-10}	mol/kg
$K_{N,n}$	neritic sediments dissociation	5.5434×10^{-10}	mol/kg
$K_{N,d}$	deep ocean dissociation	9.4553×10^{-11}	mol/kg
$K_{N,z}$	pelagic sediments dissociation	8.2537×10^{-11}	mol/kg
Protonation reaction: $HCO_3{}^- \rightleftharpoons CO_3{}^{2-} + H^+$			
$pK_{1,s}$	surface ocean reaction rate	-5.8563	
$pK_{1,n}$	neritic sediments reaction rate	-5.8563	
$pK_{1,d}$	deep ocean reaction rate	-6.0675	
$pK_{1,z}$	pelagic sediments reaction rate	-6.0837	
$K_{1,s}$	surface ocean dissociation	1.4048×10^{-6}	mol/kg
$K_{1,n}$	neritic sediments dissociation	1.4048×10^{-6}	mol/kg
$K_{1,d}$	deep ocean dissociation	1.3134×10^{-6}	mol/kg
$K_{1,z}$	pelagic sediments ocean dissociation	1.2718×10^{-6}	mol/kg
Hydration reaction: $CO_2 + H_2O \rightleftharpoons H_2CO_3$			
$pK_{2,s}$	surface ocean reaction rate	-8.9249	
$pK_{2,n}$	neritic sediments reaction rate	-8.9249	
$pK_{2,d}$	deep ocean reaction rate	-9.3116	
$pK_{2,z}$	deep sediment reaction rate	-9.3409	
$K_{2,s}$	surface ocean dissociation	1.1967×10^{-9}	mol/kg
$K_{2,n}$	neritic sediments dissociation	1.1967×10^{-9}	mol/kg
$K_{2,d}$	deep ocean dissociation	6.4591×10^{-10}	mol/kg

Table B.1 continued

Parameter	Definition	Value	Units
$K_{2,z}$	pelagic sediments dissociation	6.0476×10^{-10}	mol/kg
	Boric acid reaction: $B(OH)_4 \rightleftharpoons B(OH)_3 + OH^-$		
$pK_{B,s}$	surface ocean reaction rate	-8.5975	
$pK_{B,n}$	neritic sediments reaction rate	-8.5975	
$pK_{B,d}$	deep ocean reaction rate	-8.8625	
$pK_{B,z}$	deep sediment reaction rate	-8.8829	
$K_{B,s}$	surface ocean dissociation	2.5545×10^{-9}	mol/kg
$K_{B,n}$	neritic sediments dissociation	2.5545×10^{-9}	mol/kg
$K_{B,d}$	deep ocean dissociation	2.2530×10^{-9}	mol/kg
$K_{B,z}$	pelagic sediments dissociation	2.1635×10^{-9}	mol/kg
	Ion water product reaction: $H_2O \rightleftharpoons H^+ + OH^-$		
$pK_{W,s}$	surface ocean reaction rate	-13.2173	
$pK_{W,n}$	neritic sediments reaction rate	-13.2173	
$pK_{W,d}$	deep ocean reaction rate	-14.1249	
$pK_{W,z}$	pelagic sediments reaction rate	-14.1960	
$K_{W,s}$	surface ocean dissociation	6.1075×10^{-14}	mol/kg
$K_{W,n}$	neritic sediments dissociation	6.107×10^{-14}	mol/kg
$K_{W,d}$	deep ocean dissociation	1.0392×10^{-14}	mol/kg
$K_{W,z}$	pelagic sediments dissociation	8.8603×10^{-15}	mol/kg

B.2 Temperature and greenhouse forcing

Greenhouse gases CO_2, CH_4, and NH_3 trap thermal IR radiation in the atmosphere, heating the planet. The amount of greenhouse gas required to heat the surface of the Earth by 1 W/m^2, as calculated by the line-by-line radiative transfer analysis by Byrne & Goldblatt (2014) is shown in figure B.1a. To figure out what level of CO_2 is required to sufficiently warm the Earth's surface in the Archean, I define the greenhouse forcing using radiative forcings and fitted parameters a_{RF} and b_{RF}:

$$GF_t = a_{\mathrm{RF}} RF_t^{b_{\mathrm{RF}}} \tag{B.8}$$

Equilibrium temperature is a balance the influx of solar energy (F_s), thermal retention from greenhouse gases (F_{IR}) and outgoing radiation (F_{bb}):

$$0 = F_s + F_{IR} - F_{bb} \tag{B.9}$$

I can solve for the required greenhouse forcing to balance incoming and outgoing energy:

$$F_{IR} = F_{bb} - F_s \tag{B.10}$$

For the Archean, the energy balance at this planetary surface temperature is:

$$F_{IR,\mathrm{A}} = \sigma(289K)^4 - \frac{S_{\mathrm{A}}}{4}\big(1 - \alpha\big) \tag{B.11}$$

where S_{A} is the solar constant in the Archean, approximately 1088 W/m^2 and $F_{IR,\mathrm{A}}$ is the resulting greenhouse forcing. Modern greenhouse forcing is therefore:

$$F_{\mathrm{IR,M}} = \sigma(289K)^4 - \frac{S_{\mathrm{M}}}{4}\big(1 - \alpha\big) \tag{B.12}$$

where S_{M} is the modern solar constant, approximately 1361 W/m^2. As such, the difference in the outgoing and incoming radiation for the Archean and modern Earth is:

$$\begin{aligned} F_{IR,\mathrm{A}} &= 205\ \mathrm{W}/m^2 \\ F_{IR,\mathrm{M}} &= 157\ \mathrm{W}/m^2 \end{aligned} \tag{B.13}$$

Greenhouse gases CO_2, CH_4, and NH_3 balance this radiative deficit. The change in temperature associated with changing greenhouse gas partial pressures is found in an ordinary differential equation (equation 2.9.10); in this equation, γ_{IR} is the thermal optical depths, a function of greenhouse forcing:

$$\gamma_{IR} = f_{\mathrm{N2}}^{q}\Big(a_T T + b_T GF_t\Big) \tag{B.14}$$

where constants a_T and b_T are fitted to the radiative transfer model output from Byrne and Goldblatt (2014). This fit assumes the Archean Earth had enough greenhouse forcing to maintain a habitable surface temperature of 289 K (i.e. $T_{\mathrm{A}} = T_{\mathrm{M}}$) with no pressure broadening effects from elevated N_2 (i.e. $f_{\mathrm{N2}} = 1$). Temperature is balanced with respect to incoming (right side) and outgoing (left side) radiation (equation B.9):

$$F_{bb} = F_s(1 + \frac{3}{4}\gamma_{IR}) \tag{B.15}$$

Substituting in modern radiative values:

$$F_{bb,\mathrm{M}} = F_{s,\mathrm{M}}\left(1 + \frac{3}{4}\gamma_{IR,\mathrm{M}}\right) \tag{B.16}$$

Rearranging allows calculation of the modern day thermal optical depth term:

$$\gamma_{IR,\mathrm{M}} = \frac{4}{3}\left(\frac{F_{bb,\mathrm{M}}}{F_{s,\mathrm{M}}} - 1\right) \tag{B.17}$$

where the modern solar ($F_{s,\mathrm{M}}$) and black body ($F_{bb,\mathrm{M}}$) radiation fluxes are, in W/m^2:

$$\begin{aligned} F_{s,\mathrm{M}} &= (1-\alpha)\frac{S_{\mathrm{M}}}{4} \\ F_{bb,\mathrm{M}} &= \sigma T_{\mathrm{M}}^4 \end{aligned} \tag{B.18}$$

I correspondingly solve for the thermal optical depth in the Archean knowing the value for solar ($F_{s,\mathrm{A}}$) radiation and ensuring that outgoing radiative flux equivalent to modern ($F_{bb,\mathrm{A}} = F_{bb,\mathrm{M}}$); i.e. I assume the elevated Archean greenhouse keeps the surface temperature at 289 K.

$$\begin{aligned} F_{s,\mathrm{A}} &= (1-\alpha)\frac{S_{\mathrm{A}}}{4} \\ F_{bb,\mathrm{A}} &= \sigma T_{\mathrm{M}}^4 = F_{bb,\mathrm{M}} \end{aligned} \tag{B.19}$$

The thermal optical depth term in the Archean is therefore:

$$\gamma_{IR,\mathrm{A}} = \frac{4}{3}\left(\frac{F_{bb,\mathrm{a}}}{F_{s,\mathrm{a}}} - 1\right) \tag{B.20}$$

The equations for thermal optical depth in both the modern (left) and Archean (right) eras can be rearranged to solve for their common terms:

$$\begin{aligned} \gamma_{IR,\mathrm{M}} &= a_T T + b_T F_{IR,\mathrm{M}} \quad \text{and} \quad \gamma_{IR,\mathrm{A}} = a_T T + b_T F_{IR,\mathrm{A}} \\ a_T T &= \gamma_{IR,\mathrm{M}} - b_T F_{IR,\mathrm{M}} \quad \text{and} \quad a_T T = \gamma_{IR,\mathrm{A}} - b_T F_{IR,\mathrm{A}} \end{aligned} \tag{B.21}$$

The $a_T T$ terms cancel, allowing further simplification:

$$\begin{aligned} \gamma_{IR,\mathrm{M}} - b_T F_{IR,\mathrm{M}} &= \gamma_{IR,\mathrm{A}} - b_T F_{IR,\mathrm{A}} \\ \gamma_{IR,\mathrm{M}} - \gamma_{IR,\mathrm{A}} &= b_T \left(F_{IR,\mathrm{M}} - F_{IR,\mathrm{A}} \right) \end{aligned} \tag{B.22}$$

Solving for b_T:

$$b_T = \frac{\gamma_{IR,\mathrm{M}} - \gamma_{IR,\mathrm{A}}}{F_{IR,\mathrm{M}} - F_{IR,\mathrm{A}}} \tag{B.23}$$

I use this formula for b_T and equation B.14 to solve for a_T, still assuming no pressure broadening from elevated N_2 (i.e. $f_{\mathrm{N2}} = 1$):

$$\begin{aligned} \gamma_{IR} &= a_T T + b_T F_{IR} \\ a_T T &= \gamma_{IR} - b_T F_{IR} \\ a_T &= (\gamma_{IR} - b_T F_{IR}) \frac{1}{T} \end{aligned} \tag{B.24}$$

These values are provided in table A.1.

Pressure broadening of absorption spectra with changing atmospheric N_2 reservoirs (f_{N2}^{q}) depends on the size of the atmospheric N_2 reservoir with respect to the modern day and constant q fitted to the pressure broadening relationship from Goldblatt et al. (2009); these authors found that for an Archean $f_{\mathrm{N2}} = 2$, there was a corresponding 4.4°C increase in surface temperature. Incorporating this into my equation for thermal optical depth and knowing the constants a_T and b_T, I can solve for the unknown constant q. First, I modify the equation for thermal optical depth (B.17) with Archean values:

$$\begin{aligned} \frac{4}{3}\left(\frac{F_{bb,\mathrm{A}}}{F_{s,\mathrm{A}}} - 1 \right) &= \gamma_{IR,\mathrm{A}} \\ &= f_{\mathrm{N2}}^{q} \Big(a_T T + b_T F_{IR,\mathrm{A}} \Big) \end{aligned} \tag{B.25}$$

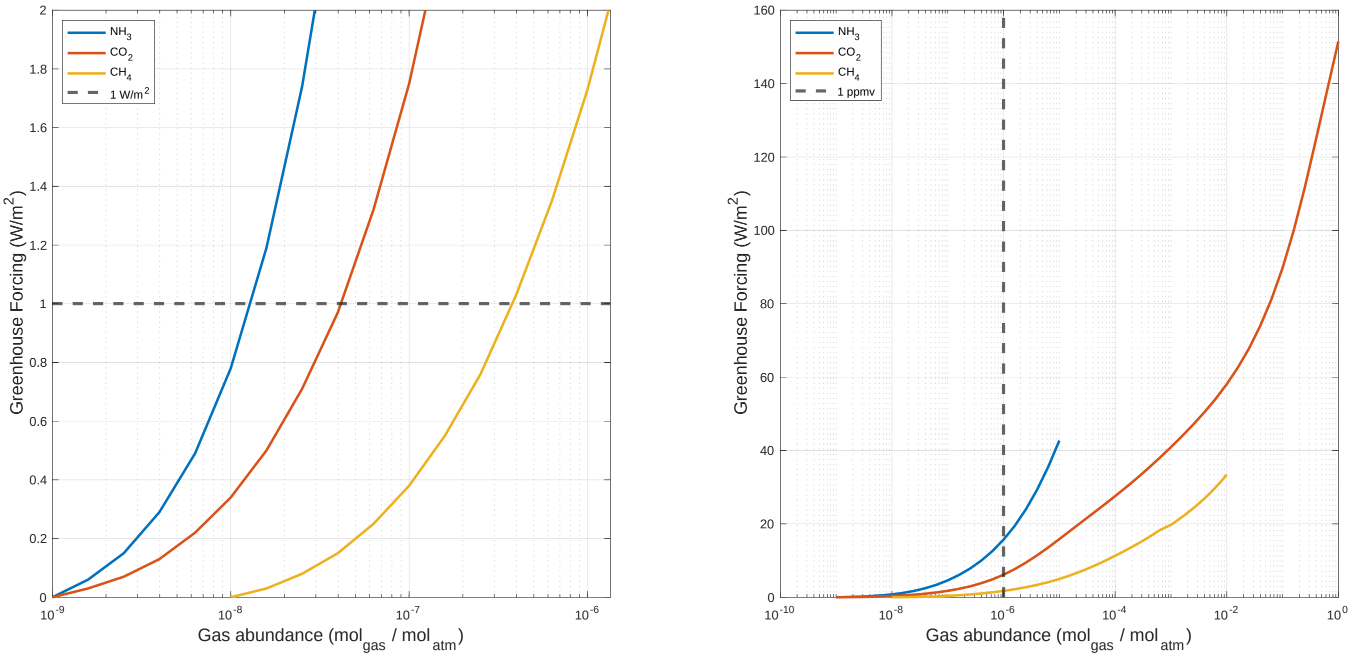

(a) **(b)**

Figure B.1: Greenhouse forcing curves a The greenhouse forcing curves of NH_3, CO_2, and CH_4 in the atmosphere, highlighting the required partial pressures to absorb 1 W/m^2; **b** illustrating the greenhouse forcing by partial pressures of 1 ppm in a modern atmosphere (HITRAN model output compilation from Byrne & Goldblatt, 2014).

I then calculate the effect of doubling N on the outgoing radiative flux ($F_{bb,2\text{PAN}}$):

$$F_{bb,2\text{PAN}} = \sigma(T + 4.4)^4 \tag{B.26}$$

This new outgoing radiative flux allows us to solve for q given $f_{\text{N2}} = 2$:

$$\begin{aligned}
\frac{4}{3}\left(\frac{F_{bb,2\text{PAN}}}{F_{s,\text{A}}} - 1\right) &= 2^q\left(a_T T + b_T F_{IR,\text{A}}\right)\\
\frac{4}{3}\left(\frac{F_{bb,2\text{PAN}}}{F_{s,\text{A}}} - 1\right)\frac{1}{a_T T + b_T F_{IR,\text{A}}} &= 2^q\\
\log\left(\frac{4}{3}\left(\frac{F_{bb,2\text{PAN}}}{F_{s,\text{A}}} - 1\right)\frac{1}{a_T T + b_T F_{IR,\text{A}}}\right) &= q\log(2)\\
\log\left(\frac{4}{3}\left(\frac{F_{bb,2\text{PAN}}}{F_{s,\text{A}}} - 1\right)\frac{1}{a_T T + b_T F_{IR,\text{A}}}\right)\frac{1}{\log(2)} &= q
\end{aligned} \tag{B.27}$$

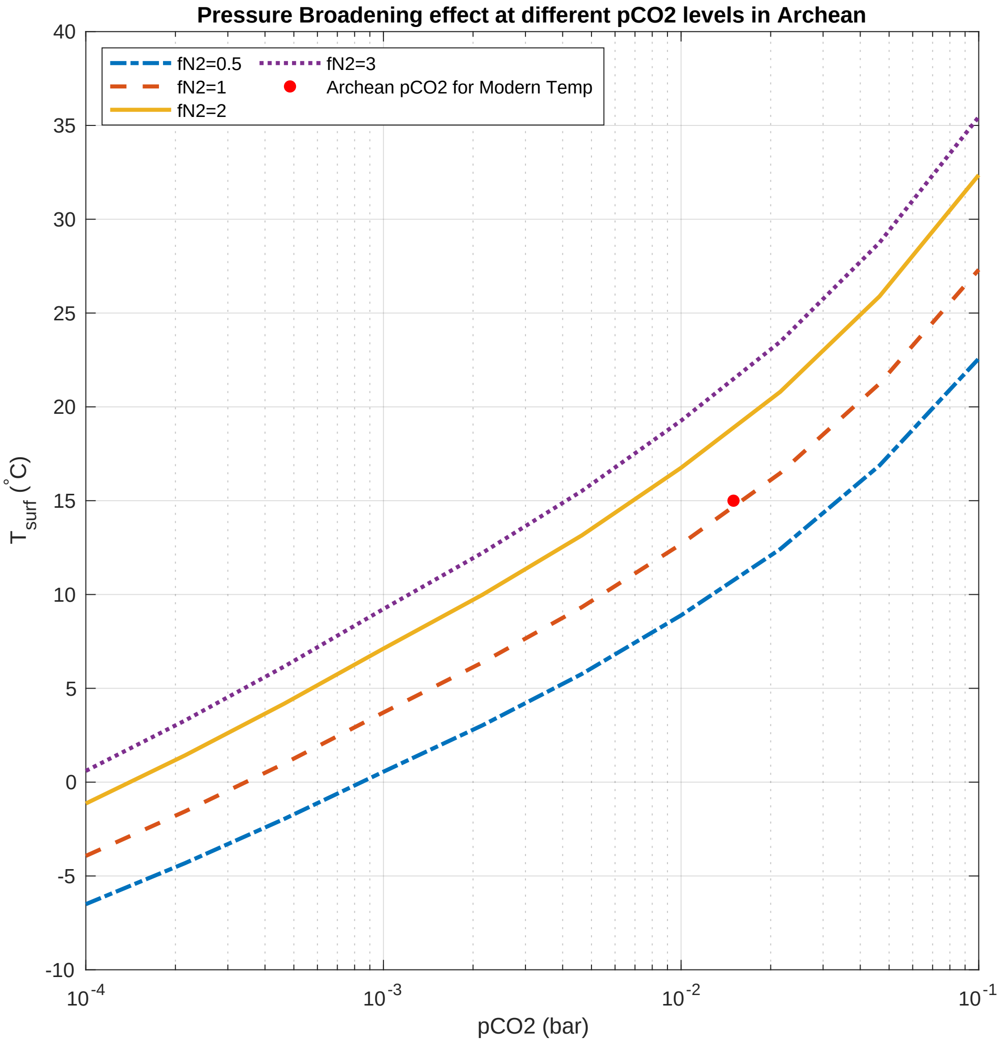

Figure B.2: Pressure broadening by N_2 The effect of pressure-broadening by changing fN_2 (fraction of modern day reservoir) at various pCO_2 levels in the Archean.